INVESTIGATION OF THE STRUCTURE OF OXY-FUEL FLAMES USING RAMAN LASER DIAGNOSTICS

ALEXIS SEVAULT

Thesis for the degree of philosophiae doctor

Trondheim, May 2012

Norwegian University of
Science and Technology
Faculty of Engineering Science and Technology
Department of Energy and Process Engineering

NTNU – Trondheim
Norwegian University of
Science and Technology

NTNU
Norwegian University of Science and Technology

Thesis for the degree of philosophiae doctor

Faculty of Engineering Science and Technology
Department of Energy and Process Engineering

ISBN 978-82-471-3623-2 (printed ver.)
ISBN 978-82-471-3624-9 (electronic ver.)
ISSN 1503-8181

Doctoral Theses at NTNU, 2012:166

To Maria and my family.

ABSTRACT

In the current context of climate change and global energy policy, CO_2 capture and storage (CCS) technologies are expected to play a major role in the mitigation of CO_2 emissions in a close future. The present PhD work is a part of the BIGCO2 project, aiming at exploring the different CCS technologies. Oxy-combustion burning natural gas is one of them and research about it has been relatively scarce. The present experimental investigation aims at bridging the gap by building up fundamentals on the structure of CO_2-dilluted oxy-fuel flames from different simple flame configurations and generating data-libraries from experiments.

Laser Raman scattering (LRS) measurements were performed and allowed capturing radial profiles of the temperature and concentrations of the main flame species. A complete LRS setup was especially designed at NTNU for the experimental investigation. The Hybrid method was used for Raman calibration and data-processing, and its application was reported in detail. The use of LRS in CO_2-diluted oxy-fuel flames proved to be challenging, due to CO_2 properties compared to N_2, and is not well documented in the available literature,. Among the main induced difficulties: protection from mixing with ambient air, Joule-Thomson effects onto CO_2 supply, quenching effects, heat radiation, CO_2* chemiluminescence, high range of flame temperature, radical pool, Raman cross-talks from H_2 Raman rotational bands onto CO_2 and from CO_2 onto O_2 in recorded Raman spectra.

The investigated configurations are:

- Laminar premixed $CH_4/O_2/CO_2$ flat flames,
- Laminar premixed $H_2/O_2/CO_2$ flat flames,
- Transitional non-premixed H_2 – O_2/CO_2 jet flames,
- Turbulent non-premixed H_2/CH_4 – O_2/CO_2 jet flames.

The laminar premixed flat flames enable to isolate the chemical processes specific to oxy-fuel flames. The transitional non-premixed jet flames contribute to knowledge on specific mixing processes. Using H_2 as fuel allows evaluating the degree of participation of CO_2 in the chemical processes. The turbulent non-premixed jet flames highlight the interactions between turbulence and chemistry. The latter flame

configuration was investigated using the Raman/Rayleigh laser diagnostics setup at Sandia National Laboratories.

Parametric studies were systematically carried out for each flame configuration, notably varying equivalence ratio, oxygen content in the oxidizer, hydrogen content in fuel and jet Reynolds number. Most results were compared to similar air-fired conditions, and in some cases, to corresponding non-reacting mixtures. Observations for each configuration are supported by laminar flame calculations.

Experimental results are of good quality and generally agree reasonably well with laminar flame calculations. A complete analysis of the results points out the similarities and differences with air-fired conditions. Among the main observations:

- CO_2 primarily participates in the reaction through the reverse rate of the CO burnout reaction leading to larger local levels of CO than in comparable air-fired flames.
- The near-field of non-premixed oxy-fuel jet flames experiences increased flame stability and strong laminarisation effects while increasing the oxygen content in the oxidizer.
- In the near-field of turbulent non-premixed jet flames, the degree of localized extinction increases while increasing the jet Reynolds number or decreasing H_2-dilution of the fuel.
- Differential diffusion effects play a significant role in the mixing processes in the near-field of non-premixed jet flames while increasing the H_2-dilution of the fuel, especially at low to moderate jet Reynolds numbers.

The obtained results constitute a library of species and temperature data over various flame configurations that can be used to benchmark models and numerical simulations in oxy-fuel conditions. The data library is available upon request.

PUBLICATIONS

Journal publication

On the Structure of the Near Field of Oxy-Fuel Jet Flames Using Raman/Rayleigh Laser Diagnostics, Sevault, A., Barlow R. S., Dunn M., Ditaranto M., Combustion and Flame (2012), http://dx.doi.org/10.1016/j.combustflame.2012.06.017

Oral presentations

Investigation of Turbulent Oxy-Fuel Jet Flames Using Raman/Rayleigh Laser Diagnostics, Sevault, A., Barlow R. S., Dunn M., Ditaranto M., Sixth Trondheim CO_2 Capture and Storage Conference, Norway, June 2011.

Investigation of Turbulent Oxy-Fuel Jet Flames Using Raman/Rayleigh Laser Diagnostics, Sevault, A., Barlow R. S., Dunn M., Ditaranto M., Seventh Mediterranean Combustion Symposium, Chia Laguna, Italy, September 2011.

Investigation of CO_2-diluted Oxy-Fuel Flames Using Laser Raman Scattering, Sevault, A., Ditaranto M., Sixth Trondheim CO_2 Capture and Storage Conference, Norway, June 2011. Presented by M. Ditaranto.

Visual presentation

On Turbulent Oxy-Fuel Jet Flames Using Raman/Rayleigh Laser Diagnostics, Sevault, A., Barlow R. S., Dunn M., Ditaranto M., European Combustion Meeting 2011, Cardiff, United Kingdom, June 2011.

ACKNOWLEDGEMENTS

Among the reasons that convinced me for taking this PhD position, working within a large international project aiming at concrete and global solutions to CO_2 emissions was undoubtedly the main one. I will never be thankful enough to my supervisors, Mario Ditaranto and Inge R. Gran, who offered me this priceless opportunity. In addition, I want to acknowledge He Zhao and Sven Tollak Munkejord, who granted me a great insight into experimental research, while supervising my final internship at SINTEF, prior to the PhD position.

Another round of acknowledgements is deserved for Mario Ditaranto, who made the completion of this PhD work possible, supported me in many ways since the very first day and always came out with the exact advice I needed when I struggled.

I am extremely grateful to Robert S. Barlow, Matthew Dunn and Robert Harmon for all I learnt from them and the wonderful work we achieved together during my 6-month stay at Sandia National Laboratories (Livermore, CA, USA). Special thanks go Robert S. Barlow who made this fruitful collaboration possible and has always been present when I needed help since then.

I am also grateful to Peter Kutne and Claudio Dem, who welcomed me for a short visit at DLR Stuttgart (Germany) during my first year, in order to get my first insight into laser Raman scattering diagnostics. Every time I met Peter Kutne since then, we have had very interesting discussions, systematically ending up with his very useful advice to my work.

I am deeply grateful to Julien Nicoloso and Denis Rondeau, who performed their final internships with me, striving in the laboratory to finally make the laser Raman scattering setup work. They significantly contributed as well to the data-processing software suite. Without them, I would not have been able to achieve the great results reported in this PhD thesis.

Håvard Rekstad and Arnt-Egil Kolstad helped me the whole way from the design to the realisation of the oxy-fuel combustion rig. This was completely new to me and they simply made it smoother. This is the reason why I would like to thank them. I am also grateful to all the technicians from the Thermal Laboratory at NTNU who took part in the experimental work.

The administrative and IT personnel from the department of Energy and Process Engineering at NTNU deserves my acknowledgements, especially Gerd Randi Fremstad, Eugen Uthaug, Ole-Martin Hansen and Anita Yttersian, who have always been extremely kind and helpful to me.

The PhD students from the department also merit my true acknowledgements. They all know that the PhD road is full of ups and downs, and some PhD students know how to make you forget the downs; I sincerely thank them for this.

In addition, I would like to thank all the people I met during the journeys, conferences, courses and exchanges, who have been a great source of inspiration and energy for my research. Some became very good friends and will recognize themselves.

I am extremely thankful to the colleagues from the Combustion group at SINTEF Energy, who accompanied me since day 1 and gave me tons of valuable advice every time I came to them. I am also very grateful to them for welcoming me in their team after the PhD and enabling me to keep working with combustion research in such a great environment.

Despite the distance with my family and my friends from France, my time in Trondheim has been unbelievable so far. I have met friends from all horizons and learnt about cultures from many countries. All those who have counted for me will recognize themselves: I thank them all for their marvellous friendship and all the unforgettable moments we have had together.

Despite the distance, I can always count on my friends from France whatever I ask for. This is the most valuable quality to my view and I am truly thankful to them.

My family undeniably deserves my deepest acknowledgements for their constant support and sacrifices all along my life. My devotion to this PhD research is the legacy of their fantastic education. I owe them what I am now and will never be thankful enough for this. To my two nieces, Victoire and Céleste, I sincerely hope the time I could not spend playing with you and watching you growing up during the last years was worthy and I will be able to catch it up one day.

Lastly, because nothing would be possible without her, I would like to express how grateful I am to my girlfriend, Maria. She has been sharing my ups and downs, cheering me up, discussing, asking, inspiring me and dragging me off the office when long working hours would have made me insane. She has even thoroughly read every single page of this thesis to help me with the corrections. Most importantly, I learnt from her how not to focus on only one thing but rather live in the present moment and use time in what really matters. For all these reasons and because you are simply the best, quérote!

The present publication forms a part of the BIGCO2 project, performed under the strategic Norwegian research program Climit and coordinated by SINTEF. The author acknowledges the partners: Statoil, GE Global Research, Statkraft, Aker Kværner, Shell, TOTAL, ConocoPhillips, ALSTOM, the Research Council of Norway (178004/I30 and 176059/I30) and Gassnova (182070) for their support.

The cooperation with R. S. Barlow at the Combustion Research Facility from Sandia National Laboratories was supported by the United States Department of Energy. Sandia National Laboratories is a multi-program laboratory operated by Sandia Corporation, a Lockheed Martin company, for the United States Department of Energy under contract DE-AC04-94-AL85000.

CONTENTS

NOMENCLATURE

Roman letters

a	Strain rate (s^{-1})
$C_{i,j}$	Mean signal intensities recorded over spectral bandwidth i, due to contribution of species j (CCD counts.W^{-1})
d	Nozzle diameter (m)
e	Euler's number / exponential number
E	Energy level (Joules)
f	Focal length (m)
F_B	Mixture fraction, according to Bilger's definition
$f_i(T)$	Bandwidth factor accounting for temperature-dependent distribution of molecules in their allowed quantum states
FL	Fluctuation level
G_i	Coefficient linking RAMSES spectra library and calibration measurement of species i
h	Planck's constant ($6.626068.10^{-34}$ m^2.kg.s^{-1})
IL	Intensity level
K	Matrix of Raman calibration coefficients
K_1, K_2	Coefficients for data pre-processing algorithms
K_i	Factor dependent on vibrational Raman cross-section, wavelength, geometry, and optical collection efficiency
$k^*_{i<<j}$	Temperature-dependent coefficient obtained by Raman calibration (in m^3.mol^{-1} or in CCDcounts.m^3.mol^{-1}.W^{-1} with Q_r in CCD counts)
l	Probe length (m)
m	Mass (kg)
M	Molar weight (g.mol^{-1})
M	Third body (in chemical reactions)
n	Number of moles (mol)
$[N]$	Number density of scattering species (molecules.m^{-3})
p	Pixel index

p	Pressure (Pa)
Q_1	Incident laser power (W)
Q_i	Scattered Raman power over species *i*'s bandwidth (W)
Q_{iC}	Corrected intensity integrated over species *i*'s bandwidth (Joules)
Q_r	Scattered Raman power (W)
R	Ideal gas constant (8.314 $J.mol^{-1}.K^{-1}$)
Re_f	Jet Reynolds number
$R_{i,j}$	Temperature-dependent signal intensities from species *j* over species *i*'s bandwidth (CCD counts.W^{-1})
s	Spatial coordinate
S	Three-dimensional matrix containing recorded Raman signals
S_L	Flame speed ($m.s^{-1}$)
t	Time (s)
T	Temperature (K)
T_{Ad}	Adiabatic flame temperature (K)
$T_{c,j}$	Temperature corresponding to the calibration measurement involving species *j* (K)
T_{new}, T_{old}	Temperatures used in Raman iterative resolution algorithm (K)
V	Velocity ($m.s^{-1}$)
X	Molar fraction
X_R	Molar fraction of one species in its corresponding RAMSES spectra library
X_C	Molar fraction of one species in its calibration measurement
Y	Mass fraction

Greek letters

α	Thermal diffusivity ($m^2.s^{-1}$)
Δ	Interval
ϵ	Collection efficiency accounting for losses in optical collection system
φ_{O2}	Oxygen molar fraction in the oxidizer stream
φ_{H2}	Hydrogen molar fraction in the fuel stream
Φ	Equivalence ratio
λ_L	Incident laser wavelength (nm)
$\lambda_{Pi,j}$	Wavelength corresponding to Raman peak of vibrational frequency *j* from species *i* (nm)
ν	Kinematic viscosity ($m^2.s^{-1}$)

ν	Frequency (s^{-1})
$\overline{\nu_{i,j}}$	Raman vibrational frequency *j* from species *i* (cm^{-1})
Ω	Scattering solid angle (Sr)
ζ	Stoichiometric coefficient
$\left(\frac{\partial\sigma}{\partial\Omega}\right)$	Raman cross-section (cm^2/Sr)

Subscripts and superscripts

-	Mean
''	Fluctuations from Favre decomposition
1	Fuel stream
2	Oxidizer stream
f	Fuel
Favre	Favre-averaged
i	Species *i*
mol	On molar basis
mix	Mixture
o	Oxidizer
st	Stoichiometric conditions
tot	Total
vol	On volume basis

Abbreviations

ADC	Analog-to-digital converter
ASU	Air separation unit
bck	Background spectral bandwidth
C_2	Carbon compounds inducing fluorescence interferences in LRS
ca.	From Latin "circa", means around, approximately
CAD	Computer-aided design
CCD	Charge-coupled device
CCS	CO_2 capture and storage
CLC	Chemical-looping combustion
CH_4	Methane
CO	Carbon monoxide

CO_2	Carbon dioxide
CRF	Combustion Research Facility
EDT	Equal diffusivities transport
FGR	Flue gas recirculation
FMCT	Full multi-component transport
FWHM	Full width at half maximum
GRI	Gas Research Institute
GUI	Graphical user interface
H_2	Hydrogen
H_2O	Water
ICCD	Intensified charge-coupled device
IR	Infra-red
LEL	Lower explosion limit
LIF	Laser-induced fluorescence
LRS	Laser Raman Scattering
MFC	Mass flow controller
N_2	Nitrogen
Nd:YAG	Neodymium YAG laser
NO_x	Nitric oxides
NTNU	Norges teknisk-naturvitenskapelige universitet
O_2	Oxygen
PAH	Polycyclic aromatic hydrocarbons
RAMSES	RAMan Spectrum Efficient Simulation
RMS	Root mean square
SNL	Sandia National Laboratories
SNR	Signal-to-noise ratio
TNF	Turbulent Non-premixed Flames
UEL	Upper explosion limit
UV	Ultra-violet
YAG	Yttrium Aluminium Garnet

PART I

BACKGROUND OF THE INVESTIGATION

1. MOTIVATIONS

1.1. Facing a global environment challenge

1.1.1. Status of carbon emissions

Over the two last centuries, the use of combustion processes in industry has increased exponentially, due to the developing exploitation of fossil fuels. Currently, nearly 87 % of the global primary energy still relies on fossil fuels [*BP* 2011]. Since the industrial revolutions, most research investigations on combustion have focused on improving efficiency. However, the environmental impact of combustion had been set aside until the last two decades. Today, particulate matter, nitric oxides, sulphur oxides and carbon dioxide are well-known pollutants that are systematically considered in any combustion process. Whereas the three first pollutants are relatively well handled, neutralizing carbon dioxide (CO_2) emissions has not been a priority until today, since the molecule represented the least health hazard.

Processes involving fossil fuels represent the major source of human-related CO_2 emissions, which have been exponentially increasing over the two last centuries [*Metz* 2005, *GCP* 2011]. The emissions are found to be stored in natural CO_2-sinks, mainly in land, atmosphere and ocean. None of these CO_2-sinks have an infinite capacity. Consequently, as with any other stable system, a perturbation may cause a shift of the equilibrium. In this context, this shift of the equilibrium is generally associated to the concept of climate change and its impact is typically global.

Whereas it is relatively complex to personally sense the climate change and to imagine how everyday's life can have such a global impact, a large share of the specialists agree on the link between CO_2 emissions from human activity and climate change [*IPCC* 2007]. Some people will always be sceptical and debate upon this statement, but one can hardly ignore the danger of releasing within years billions tons of carbon that have been accumulating over hundreds of thousands years. Today, CO_2 emissions represent ca. 30 Gt CO_2/year and keep increasing steeply along with the global energy needs. Some scenarios predict that those levels would double by 2050 if no solutions are applied to cut CO_2 emissions [*IEA* 2009].

1.1.2. Perspectives

Climate change and CO_2 emissions are now becoming a major topic in global energy policy. To face the global environment challenge, three main ways are being explored [*IEA* 2009]:

- Optimizing processes and infrastructures to reduce the needs in energy,

- Decreasing the share of fossil in the energy mix in favour of the development of renewable energies,

- Developing industrial CO_2 capture and storage technologies (CCS).

The current investigation is a part of the BIGCO2 project, aiming at building up knowledge and technologies on gas power-generation employing CCS at industrial scale [*SINTEF* 2012]. Therefore, the focus of the present investigation is especially set on CCS technologies. According to predictions described in [*Metz* 2005, *IEA* 2009], in a context of large global increase in energy demand, combining the three ways to explore would significantly contribute to the global mitigation of CO_2 emissions in a close future. In this context, CCS technologies are expected to account for ca. 20 % of the mitigation of carbon dioxide emissions. The trend can be explained by the current predominance of fossil fuels in the global primary energy and the high cost of technologies based on alternative energy sources.

1.1.3. CO_2 capture and storage technologies

1.1.3.1. Principle

As illustrated in Figure I.1, the basic principle of CCS technologies is to keep on using fossil fuels in industrial plants, while safely handling the induced CO_2 emissions. CCS necessarily implies a reduction of efficiency compared to the current industrial plants, which results in an extra cost. Consequently, another issue at stake is to value CO_2 emissions by developing an appropriate global CO_2 trade policy to ensure the viability of CCS infrastructures in a close future.

CO_2 can be captured by different ways throughout the combustion processes. After purification, the resulting CO_2 stream can be compressed for transport and stored in geological reservoirs on the continent or off-shore, depending on the geographical location of the industrial site.

CO_2 capture through combustion processes is based upon three main routes, mainly derived from technologies established in the oil and gas industry: post-combustion, pre-combustion, oxy-combustion. A brief description of each technology is

given in the following paragraphs. Though they are also key elements of the CCS chain, transport and storage technologies are not further detailed, since they are out of the scope of the present investigation on oxy-fuel combustion. Detailed reviews on CCS technologies can be found in [*IEA* 2009].

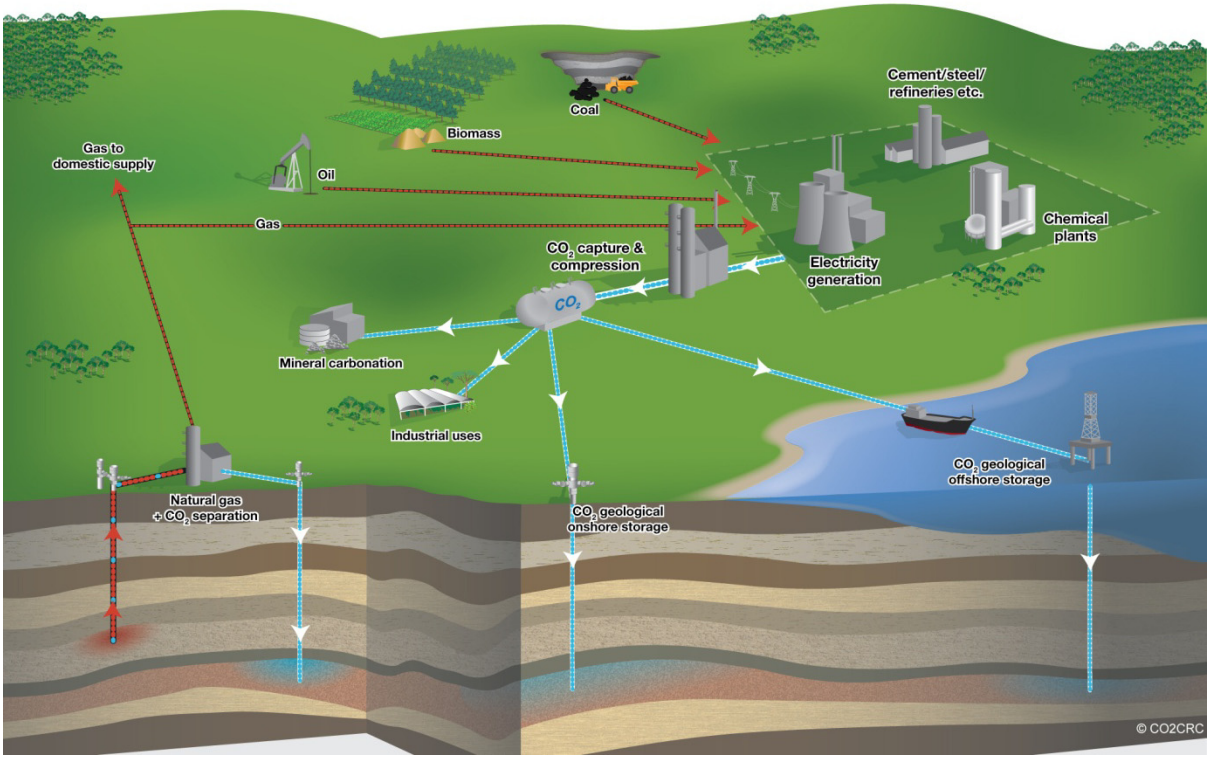

Figure I.1: Representation of the network of CCS facilities. [CO2CRC 2012]

1.1.3.2. Post-combustion

Post-combustion achieves CO_2 separation directly from the flue gas. There has already been a large interest in this technology due its great potential for retrofitting CO_2 separation units onto existing plants. Most investigations in that field focus on performing CO_2 separation from other flue gas constituents through membranes and amine scrubbing.

1.1.3.3. Pre-combustion

Pre-combustion consists in converting fuel into a synthesis gas, composed of carbon monoxide (CO) and hydrogen (H_2). Synthesis gas can be generated from natural gas through steam reforming, or from coal or biomass through partial oxidation. CO can then react with water to form H_2 and CO_2 through the water-gas shift reaction. CO_2 is readily captured and H_2 is used in other processes to generate heat, power and eventually by-products.

1.1.3.4. Oxy-combustion

In the CCS context, oxy-combustion consists in using an oxidizer mixture mainly composed of oxygen and carbon dioxide, instead of air. In these conditions, the products of combustion with any fuel are mostly CO_2 and water steam, which eases the CO_2 capture process.

Another concept, often associated to oxy-combustion, is the chemical-looping combustion (CLC). It consists of two combined loops. Reactive metal particles circulate in the first loop and separate oxygen from the incoming air through oxidation reactions. They are then transferred to the second loop where they are reduced by the fuel through an exothermic chemical process. Reduced metal particles are then sent back to the first loop to get oxidized in air.

1.2. Oxy-combustion technology

Oxy-combustion is the main scope of the present investigation. Therefore, the following paragraphs further detail the principle, advantages and limitations of the technology.

1.2.1. Principle

Figure I.2 gives an overview of the oxy-combustion process. The process includes a large-scale air separation unit (ASU) achieving oxygen separation from the air. Oxygen is then carried to the combustion chamber where it burns with the fuel. The reacting mixture is generally diluted by flue gas recirculation (FGR), which enables to control the flame temperature over a large range. Nitrogen being theoretically absent from the reacting mixture, flue gas is mainly composed of CO_2 and water. Water can be readily separated from CO_2 through condensation, providing a relatively pure CO_2 stream. Part of the CO_2 stream is sent back to the combustion chamber for FGR, while the rest is compressed for transport. Depending on the purity of the fuel and the oxygen supply, a supplementary CO_2 purification stage may be required to filter out other constituents from the flue gas, such as oxygen, argon, nitrogen, sulfur oxides or nitric oxides, for instance. The general configuration shown in Figure I.2 corresponds to oxy-fuel boilers [*Buhre* 2005], where the main purpose is to use the heat of combustion to generate steam and run a turbine. Another configuration of interest while firing natural gas is to use the products of combustion directly as a working fluid in a turbine, since those have a relatively high density due to their high CO_2 content [*Bolland* 1992, *Bolland* 1998].

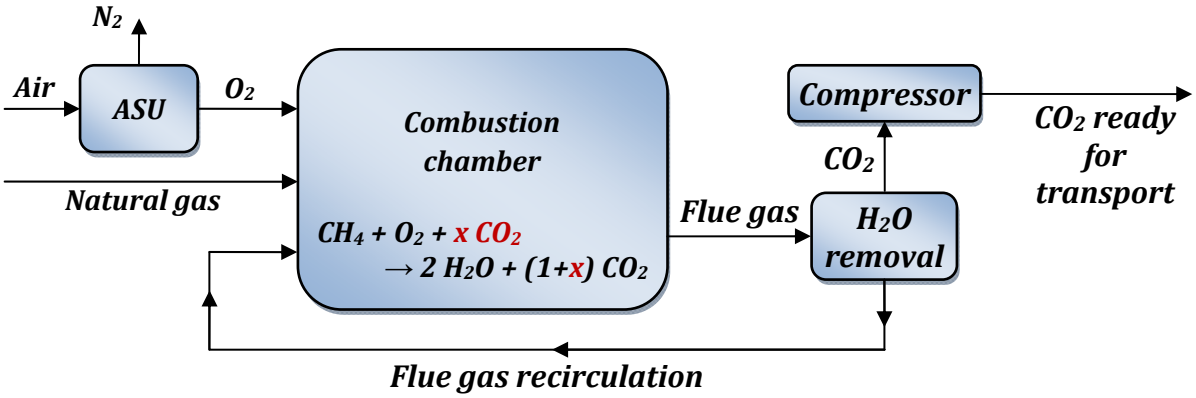

Figure I.2: Schematic of oxy-combustion process using CH_4 as fuel.

1.2.2. Status

Oxy-combustion has been primarily used in glass-melting and metal industries due to the high temperature requirements. The implementation of FGR has enabled to consider a larger number of applications due to the wider range of flame temperatures reached in the combustion chamber. Studies have shown that flame temperatures similar to those from air-fired conditions can be achieved with 25 – 40 $\%_{vol}$ O_2 in the oxidizer [*Buhre* 2005, *Ditaranto* 2011, *Kutne* 2011].

Due to the high amount of coal power plants across the world, oxy-combustion using pulverized coal as a fuel has been widely studied, pilot-scale plants have already been tested and full-scale projects are in progress [*Buhre* 2005, *Toftegaard* 2010, *Lupion* 2011].

Literature on CO_2-diluted oxy-combustion firing natural gas is still scarce in comparison, though results from existing numerical and laboratory-scale investigations are promising (cf. Section 3). Only a limited number of pilot-scale projects are currently in progress, such as, for instance, the CO_2 pilot in Lacq (France) [*Cieutat* 2009]. This field of investigation is likely to grow much more industrial interest in the close future as a significant global shift from coal to natural gas is expected for future power generation [*Metz* 2005].

1.2.3. Advantages

The main advantages of oxy-combustion using FGR compared to other CCS technologies have been listed in various design investigations and reviews [*Bolland* 1992, *Bolland* 1998, *Tan* 2002, *Buhre* 2005, *Plasynski* 2009]. Among them:

- Wide range of flame temperature by varying rate of FGR,

- Possibility to retrofit oxy-fuel boilers on existing plants,
- Decreased flue gas volume compared to air-fired plants,
- Much higher CO_2 fraction in the flue gas than in air-fired plants,
- Great potential to reduce emissions of pollutants and comply with purity requirements of CO_2 transport.

In other words, oxy-combustion using FGR offers a great potential for short-term feasibility and provides optimum operating conditions for CO_2 scrubbers, which eventually reduce the cost of CO_2 capture.

1.2.4. Limitations

As pointed out by most cited references in this section, the main limitation of the technology is the requirement of a large-scale, energy-intensive ASU. Typically, the power consumption to separate oxygen from air exponentially increases with the level of purity of the oxygen stream. The ASU still represents more than half of the power consumption for CO_2 capture, though significant optimizations are still in progress to reduce this rate.

Most current operational ASU are based on cryogenic processes, and achieve oxygen purity in the range 85 – 98 % [*Tranier* 2011]. A trade-off should be found between oxygen purity and filtering of pollutants in the post-combustion stages to achieve the best overall efficiency. Promising alternative technologies are in development and may potentially improve space- and energy-related issues [*Bredesen* 2004, *Burdyny* 2010].

Another limitation is the excess oxygen in the reacting mixture that generates a significant energy penalty [*Toftegaard* 2010]. In air-fired conditions, air is readily available and is typically in excess in the reacting mixture (fuel-lean conditions) to allow full combustion of the fuel. In oxy-fuel conditions, the power consumption of the ASU is directly proportional to the amount of oxygen carried to the reacting mixture.

1.3. Research topic

1.3.1. Motivations of the PhD work

Through the BIGCO2 project, different technologies for gas power-generation employing CCS at industrial scale have been explored to enhance the available knowledge and pave the ground for demonstration plants. As mentioned above, a limited number of investigations of oxy-combustion firing natural gas can be found in the literature compared to oxy-coal combustion. The major motivation of the present experimental investigation has been to contribute to this research field by gathering fundamental observations and data from the flame structure of oxy-fuel flames performed at laboratory scale.

In that respect, natural gas can be reduced to fuel mixtures composed of methane and hydrogen, while the oxidizer mixture can consist of oxygen and carbon dioxide only. In addition, simple, well-known burners can be used to simplify the flame geometry. These simplifications enable to generate flames whose features can be compared to results from equivalent air-fired conditions to highlight the main differences. There is a particular interest in improving knowledge from parametric studies where oxidizer composition, fuel composition and jet Reynolds number (Re_f) are varied. The described oxy-combustion conditions are in line with previous investigations carried out by Dr. Ditaranto at SINTEF (Norway), whose focus has mainly been set on flame structure and heat flux distribution [*Ditaranto* 2006, *Ditaranto* 2011].

Another major motivation for the present investigation has been to design a complete combustion rig enabling to perform non-premixed CO_2-diluted oxy-fuel jet flames while performing laser Raman scattering (LRS) diagnostics. This method provides radial profiles of quasi-instantaneous scalar measurements of the temperature and the main flame species concentrations. It is also very adapted to monitor changes in the flame structure while varying different flames conditions. Results from the measurements are used to support observations and discussions made on the investigated flames. Generated quantitative data can also be used to validate combustion models dealing with oxy-fuel flames, since such experimental results are not yet available in the literature.

Part of the PhD work took place at the Combustion Research Facility (CRF) at Sandia National Laboratories (SNL) in Livermore (California, USA). The exchange aimed at performing experiments with the advanced Raman/Rayleigh laser diagnostics setup on more complex oxy-fuel flames than those investigated at NTNU.

1.3.2. Present contribution

The scope of the PhD work is to experimentally study the flame structure of oxy-fuel flames using LRS diagnostics and to produce a data library of various flame conditions to eventually contribute to combustion code validation. The focus is especially set on laminar premixed flat flames and non-premixed jet flames burning fuel mixtures of H_2 and/or CH_4 in O_2/CO_2 oxidizer mixtures.

A complete **combustion rig** able to withstand high flame temperatures at atmospheric pressure has been designed for that purpose. It includes a 200 x 200 mm square-based combustion chamber to protect the flames from early mixing with ambient air. The latter is adapted to most combustion laser diagnostics and mounted on a 2-axis moving table. It integrates a 95-mm coflow burner with a centred jet fuel nozzle enabling non-premixed jet flames for various fuel and oxidizer mixtures.

A functional **LRS diagnostics setup** has been fully designed around the combustion rig and enables quasi-instantaneous radial profile measurements of the temperature and mole fractions of all main flame species (CO_2, O_2, N_2, CO, CH_4, H_2O and H_2). A dedicated software suite has been designed for pre-processing, processing and post-processing data and for Raman calibration. Though optimized for oxy-fuel flames, the LRS setup and the software suite can be used with any type of flames or non-reacting mixtures. This feature enables to perform air-fired flames with similar conditions to oxy-fuel flames for comparison. The setup allows measurements using a 532-nm laser at 530 mJ/pulse with pulse duration of 400 ns. The spatial resolution is 0.262 mm along a ~5.5-mm section of the focused laser beam.

LRS measurements in **laminar premixed flat flames** have been performed using a Hencken burner positioned on the 2-axis moving table, for the following mixtures:

- **CH_4/air** with equivalence ratio, Φ, ranging from 0.7 to 1.15,
- **$CH_4/O_2/CO_2$** with Φ from 0.5 to 0.9 and from 35 to 55 $\%_{mol}$ O_2 in the oxidizer,
- **$H_2/O_2/CO_2$** with Φ from 0.5 to 0.9 and from 15 to 40 $\%_{mol}$ O_2 in the oxidizer.

LRS measurements of full radial profiles of scalars have been performed in **transitional non-premixed jet flames** for the following mixtures:

- **H_2 – air** with jet Reynolds number, Re_f = 1600 and coflow speed of 0.23 $m.s^{-1}$,
- **H_2 – O_2/CO_2** with Re_f = 1600, coflow speed of 0.22 $m.s^{-1}$ and from 15 to 70 $\%_{mol}$ O_2 in the oxidizer.

During the exchange at SNL, LRS measurements of full radial profiles of scalars have been performed in **turbulent non-premixed jet flames** using Raman/Rayleigh laser diagnostics setup for the following mixtures:

- **$H_2/CH_4 - O_2/CO_2$** with 32 $\%_{mol}$ O_2 in the oxidizer, Re_f = 15,000, and from 37 to 55 $\%_{mol}$ H_2 in the fuel,
- **$H_2/CH_4 - O_2/CO_2$** with 32 $\%_{mol}$ O_2 in the oxidizer, Re_f ranging from 12,000 to 18,000 and 55 $\%_{mol}$ H_2 in the fuel.

In most cases, measurements have been performed in **non-reacting mixtures** as well, either for calibration purpose or to analyse the jet development in the case of the non-premixed jets.

Laminar flame calculations using Chemkin-Pro [*Reaction-Design* 2008] have been performed in each case to support the analysis and highlight the main features of the flame structures and the chemical processes.

A complete description and discussion of the ensemble of results is given in **Part III**, with a special focus on general observations, flame structure and products of combustion. The major particularities of performing LRS measurements in oxy-fuel conditions have been discussed to highlight the differences with regular air-fired conditions.

Most experimental data are available upon request. This also includes scalar fluctuations and conditional statistics from the turbulent non-premixed oxy-fuel flames performed at SNL.

1.3.3. Structure of the thesis

The structure of the thesis logically follows the chronological development of the PhD work. It starts with a theoretical background on combustion and oxy-fuel flames, is followed by the experimental developments and finishes with the results analysis.

Part I - Background of the investigation

After defining topic and motivations of the PhD work, Part I provides selected definitions from the combustion field, in order to better apprehend the present study on oxy-fuel flame structure. The typical flame structures corresponding to the investigated flame configurations are also presented. Then follows a review of the main features observed in oxy-fuel flames and reported in the available literature. The list of the investigated flames is revealed and justified at the end of Part I.

Part II – Development of laser Raman scattering methods for oxy-fuel flames

Background on LRS diagnostics is first given in Part II, followed by a detailed explanation on the application of the LRS calibration and data-processing methods to the present investigation. Then, the design of the experimental setup at NTNU is described along with the signal optimization procedure leading to the optimum experimental settings and final uncertainties. A description follows of the experimental setup at SNL, where measurements in turbulent oxy-fuel jet flames were achieved during an exchange. Part II ends with a list of the major challenges encountered while applying LRS diagnostics in oxy-fuel flames.

Part III – Results and discussion

After specifying each set of flame conditions, the results of LRS measurements in oxy-fuel flames are reported and discussed. The analysis goes from the most simple flame configuration to the most complex. Therefore, the focus is first set on laminar premixed flat flames. Air-fired conditions are described as a reference case, prior to the CO_2-diluted oxy-fuel cases with methane and hydrogen as fuels. Results from non-premixed jet flames are then revealed, starting with the transitional flames and finishing with the turbulent flames. Results in laminar non-premixed H_2-air jet flames and in selected non-reacting mixtures are also presented for comparison. For all reported flames, laminar flame calculations have systematically been included in the analysis to support the observations.

Part IV - Appendices

- Appendix A describes the algorithms used in the data pre-processing code to filter out the Raman spectra corrupted by optical breakdowns and correct for cosmic ray events.
- Appendix B reveals the developments related to safety issues for the different items composing the experimental setup at NTNU.
- Appendix C contains supplementary experimental results from the LRS measurements in transitional non-premixed H_2 – O_2/CO_2 jet flames.
- Appendix D is a journal publication written in collaboration with SNL and dealing with the results from turbulent non-premixed H_2/CH_4 – O_2/CO_2 jet flames achieved during a 6-month exchange at SNL.

2. FUNDAMENTALS OF COMBUSTION

2.1. Introduction

This chapter essentially focuses on definitions and concepts whose knowledge is recommended to apprehend the following chapters of the investigation. A special interest is given to the concepts related to laminar premixed flat flames and non-premixed jet flames, which are the types of flames considered in this investigation. Most of the following definitions are greatly inspired from the recommended textbooks dealing with combustion [*Turns* 2000, *Warnatz* 2000, *McAllister* 2011].

2.2. Definitions

2.2.1. Definition of combustion

As defined by [*Turns* 2000], combustion consists in a more or less rapid oxidation reaction, accompanied by heat and light, whose intensities can greatly vary with the reacting mixture. The spontaneous luminosity does not necessarily occur in the visible spectral range. Heat and light are released from the transformation of the energy stored in chemical bonds and can be utilized in a variety of ways. In line with the definition, a flame is a self-sustaining propagation of a localized combustion zone**.**

2.2.2. Combustion regimes

Flames can be classified into two main categories: premixed and non-premixed flames. The following paragraphs provide a brief description of those two categories.

2.2.2.1. Premixed flames

Premixed flames correspond to a combustion reaction occurring when fuel and oxidizer reach the flame front after complete molecular mixing upstream. Since the reactants are readily available, the flame front appears relatively thin (~1 mm). With fuel-rich conditions, a secondary flame often burns the remaining fuel farther downstream.

Premixed flames are generally associated to the concept of flame speed, which measures the rate of expansion of the flame front. With a laminar flow of reactants, the flame speed of the premixed flames is dominated by the chemical processes. Therefore, if the flow rate of reactants is equal to the flame speed, a stationary flat flame front will take place over a plane normal to the flow direction. If the flow rate is greater than the flame speed, the flame will display a conical shape, characterized by the component of the flow velocity normal to the flame front equal to the flame speed. The latter type of flames can be found in spark-ignition engines or Bunsen burners, for instance. If the flow rate is lower than the flame speed, the flame front will move upstream, until the mixture is out of its flammability limits or until the flame is quenched due to changes in flow conditions. Flame flashback, eventually leading to explosion, is considered as one of the main hazards with premixed flames.

2.2.2.2. Non-premixed flames

In non-premixed flames, fuel and oxidizer are separated until they burn at the mixing interface where the mixture reaches stoichiometric conditions. Therefore, rather than the reaction rates, molecular transport dominates in these flames, either by diffusion or through turbulent mixing. The exact location and thickness of the flame front can greatly vary, depending on the flow conditions and the composition of the reactants. Non-premixed flames generally burn slower than premixed flames and the longer residence time tends to promote the presence of soot.

Non-premixed flames often originate from a fuel jet issued from a pipe (or nozzle), burning in an oxidizer environment, as with lighters or candles, for instance. This configuration is limited by the rate of available oxygen in the surrounding air. When the power of the flame is at stake, it is generally of interest to accompany the fuel jet by coflowing the oxidizer, whose flow rate can be controlled. This enables to monitor the amount of oxygen required for the combustion, as in the diesel engines, for instance. Since fuel and oxidizer keep separated up to the flame front, non-premixed flames are considered safer than premixed flames.

2.2.3. Equivalence ratio

Premixed flames are generally characterized by the equivalence ratio, Φ, which indicates whether a reacting mixture is fuel-lean ($\Phi < 1$), stoichiometric ($\Phi = 1$) or fuel-rich ($\Phi > 1$). In a system at stoichiometric conditions, the amount of oxygen molecules exactly matches the amount required to consume all fuel molecules, giving a so-called complete combustion. The equivalence ratio of a system is defined as the ratio of the fuel-to-oxidizer ratio to the stoichiometric fuel-to-oxidizer ratio, as given in Eq. I.1.

$$\phi = \frac{m_f/m_o}{\left(m_f/m_o\right)_{st}} = \frac{n_f/n_o}{\left(n_f/n_o\right)_{st}} \qquad \textit{Eq. I.1}$$

With:

m	Mass
n	Number of moles
f	Subscript for fuel
o	Subscript for oxidizer
st	Subscript for stoichiometric conditions

By determining whether the reacting mixture is fuel-lean, stoichiometric or fuel-rich, one can guess the major species composing the flame products. Suppose a premixed CH_4/air flame, depending on the equivalence ratio, besides N_2, the flame products are mainly composed of:

- H_2O, CO_2 and O_2, if $\Phi < 1$,
- H_2O and CO_2, if $\Phi = 1$,
- H_2O, CO_2, H_2 and CO, if $\Phi > 1$.

O_2 appears in fuel-lean conditions, since the amount of fuel molecules is not sufficient to react with all O_2 molecules. Inversely, in fuel-rich conditions, the amount of O_2 is not sufficient to fully oxidize the fuel into H_2O and CO_2, and therefore, species such as H_2 and CO appear. The actual equivalence ratio enables to calculate the exact composition of the flame products at equilibrium.

2.2.4. Number density, molar fraction and mass fraction

In combustion, compositions of reacting mixtures are mainly quantified using the concepts of number density, molar fraction or mass fraction.

- **Number density** qualifies a quantity of species in a given finite volume. Number densities are often expressed in [mol.m^{-3}], for instance.

- The **molar fraction**, X_i, of species i is defined as the ratio of the number of moles, n_i, from species i to the total number of moles, n_{tot}, in the multi-component mixture, as given in Eq. I.2.

$$X_i = \frac{n_i}{n_1 + \cdots + n_i + \cdots} = \frac{n_i}{n_{tot}} \qquad \textit{Eq. I.2}$$

- The **mass fraction**, Y_i, of species i is defined as the ratio of the mass, m_i, from species i to the total mass, m_{tot}, in the multi-component mixture, as given in Eq. I.3.

$$Y_i = \frac{m_i}{m_1 + \cdots + m_i + \cdots} = \frac{m_i}{m_{tot}} \qquad \textit{Eq. I.3}$$

By definition, the sum of the molar fractions or mass fractions from all the components of a reacting mixture is equal to unity, as given in Eq. I.4 and Eq. I.5.

$$\sum_i X_i = 1 \qquad \textit{Eq. I.4}$$

$$\sum_i Y_i = 1 \qquad \textit{Eq. I.5}$$

The equation given in Eq. I.6 relates molar fraction and mass fraction of species i to convert them from one to another, using the molar weight, M_i, of species i and the average molar weight of the mixture, M_{mix}.

$$Y_i = X_i \frac{M_i}{M_{mix}} \qquad \textit{Eq. I.6}$$

2.2.5. Mixture fraction

The concept of equivalence ratio is not sufficient in non-premixed flames, since the composition of the reacting mixture greatly varies spatially and temporally in the flames, from pure fuel or oxidizer to mixtures of products and reactants. Instead, the concept of mixture fraction is rather used when the reactants are initially separated. It is a conserved scalar, enabling to monitor the degree of mixing of the reactants with only one variable, under a certain set of simplifying assumptions.

Considering a flow system restricted to a single inlet stream of pure fuel together with a single stream of pure oxidizer, which react to form a single product, mixture fraction is defined as the ratio of the mass of molecules from the fuel stream, to the total mass of the mixture [*Turns* 2000]. Consequently, mixture fraction is unity in the pure fuel stream and is zero in the pure oxidizer stream. Within the flow field, any mixture of fuel, oxidizer and products should correspond to a mixture fraction between 0 and unity.

In non-premixed flames, the combustion reaction theoretically occurs where the mixture of reactants reaches stoichiometric conditions. Therefore, the flame front is theoretically located in mixture fraction space at the locus of the stoichiometric

conditions, also known as stoichiometric mixture fraction. Figure I.3, adapted from [*Warnatz* 2000], illustrates an idealized composition of burning mixture from a non-premixed CH_4 – O_2 flame in mixture fraction space. In this system, flame products gradually appear in the mixture up to the stoichiometric conditions where they reach a maximum as the reactants are fully consumed.

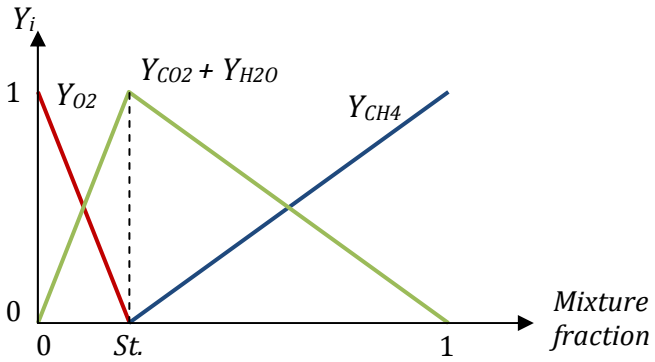

Figure I.3: Idealized composition of the reacting mixture from a non-premixed CH_4 – O_2 flame in mixture fraction.

Most definitions of the mixture fraction are based on a single elemental mixture fraction, i.e. based on only one atomic element, generally either hydrogen or carbon atoms, to monitor the mixing within the reacting mixture. The benefit is to reduce the species equations into one single equation of a conserved scalar, enabling to monitor the composition of the reacting mixture with only one variable. However, this assumption is only valid if all species have the same diffusivities. Though this assumption is sufficient in most applications, it is not necessarily verified in the near-field of flames at laboratory scale and at low to moderate jet Reynolds numbers [*Drake* 1982, *Smith* 1995, *Barlow* 2005]. A definition of the mixture fraction was determined in [*Bilger* 1990], and accounts for effects of non-equal diffusivities by combining the elemental mixture fractions of C, H and O elements into one single equation (cf. Eq. I.7). In the expression of the mixture fraction, F_B, subscripts *C, H* and *O* refer to the corresponding atomic elements, while *1* and *2* refer to the fuel stream and the oxidizer stream, respectively.

$$F_B = \frac{\frac{2(Y_C - Y_{C,2})}{M_C} + \frac{(Y_H - Y_{H,2})}{2M_H} - \frac{(Y_O - Y_{O,2})}{M_O}}{\frac{2(Y_{C,1} - Y_{C,2})}{M_C} + \frac{(Y_{H,1} - Y_{H,2})}{2M_H} - \frac{(Y_{O,1} - Y_{O,2})}{M_O}} \qquad \textit{Eq. I.7}$$

The stoichiometric mixture fraction, $F_{B,St}$, can be calculated using Eq. I.8 found in [Skeen 2009], with ζ_{O2} and ζ_f the stoichiometric coefficients of O_2 and fuel, respectively, in the overall equation of the combustion reaction. Consequently, pure fuel burning in diluted oxygen results in a relatively low $F_{B,St}$, while diluted fuel in pure oxygen results in relatively high $F_{B,St}$.

$$F_{B,St} = \left(1 + \frac{\zeta_{O2} M_{O2}}{\zeta_f M_f} \frac{Y_{f,1}}{Y_{O2,2}}\right)^{-1} \qquad \textit{Eq. I.8}$$

2.2.6. *Finite rate of chemistry*

The idealized case shown in Figure I.3 follows the assumption of fast chemistry, which means that the chemical reaction rates are infinitely fast and the reactants burn as they mix. Following this assumption, O_2 cannot exist in the fuel-rich side, since each O_2 molecule is supposed to immediately react with each encountered fuel molecule. The same applies for CH_4 molecules in the fuel-lean side. This corresponds to a basic chemical equilibrium calculation. In most cases, the assumption of finite-rate chemistry should be followed instead. With the latter assumption, the chemical reactions are not necessarily complete and the coexistence of fuel and oxidizer is possible. Figure I.4, inspired by [*Warnatz* 2000], gives an illustration of the composition of the burning mixture from a non-premixed CH_4 – O_2 flame in mixture fraction space, following the assumption of finite reaction rates. Compared to Figure I.3, two main differences have to be noted: fuel and oxidizer can coexist, and the peak of mass fraction of products displays a departure from the idealized case of fast chemistry.

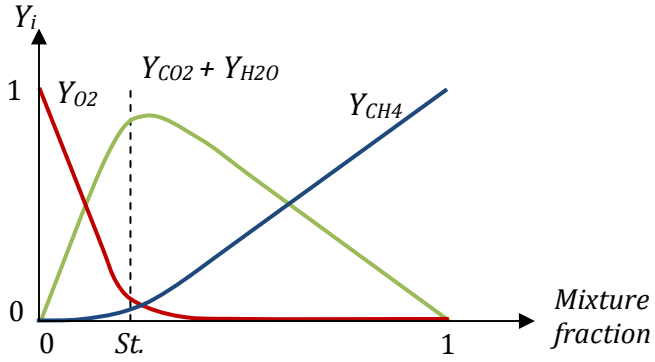

Figure I.4: Composition of the reacting mixture from a non-premixed CH_4 – O_2 flame in mixture fraction space, following the assumption of finite reaction rates.

As detailed in [*Warnatz* 2000], as the mixing rate increases in non-premixed flames, chemical processes depart from chemical equilibrium, until the main energy releasing reactions compete with the mixing rates. Further increase in the mixing rates leads to a temperature departure from equilibrium solution. At higher mixing rates, the main energy releasing reactions are not anymore able to sustain the chemical processes, leading to a sudden global flame extinction.

2.2.7. Turbulence – Reynolds number

As defined in [*Turns* 2000], turbulent flows results when instabilities in a flow are not sufficiently damped by viscous action and the fluid velocity at each point in the flow exhibits random fluctuations.

Besides the fluid velocity, most flow properties (temperature, mixture fraction, pressure, etc.) present random fluctuations in turbulent flows. The most common way to express the flow properties in turbulent flows is to follow the Reynolds decomposition, consisting in defining mean and fluctuating quantities. An example of the calculation of the mean quantity is given for any flow property A in Eq. I.9, considering a sufficiently large time interval, $\Delta t = t_2 - t_1$. $\bar{A}$ is also named Reynolds-averaged quantity *A*.

$$\bar{A} = \frac{1}{\Delta t}\int_{t_1}^{t_2} A(t)dt \qquad \textit{Eq. I.9}$$

The fluctuating quantity, $A'(t)$, corresponds to the difference between instantaneous value of the property, $A(t)$, and the mean value, $\bar{A}$, as given in Eq. I.10.

$$A(t) = \bar{A} + A'(t) \qquad \textit{Eq. I.10}$$

The most common way to mathematically characterize whether a flow is laminar or turbulent is to express the Reynolds number of the corresponding flow. In the case of non-premixed flames issued by a coflow burner, the jet Reynolds number, Re_f, is generally used and corresponds to the Reynolds number of the fuel jet at the outlet of the fuel nozzle. The jet Reynolds number is defined as shown in Eq. I.11.

$$Re_f = \frac{\bar{V}d}{\nu} \qquad \textit{Eq. I.11}$$

With:

$\bar{V}$ Mean speed at the fuel nozzle outlet ($m.s^{-1}$)

d Nozzle diameter at the outlet (m)

ν Kinematic viscosity ($m^2.s^{-1}$)

2.2.8. Localized extinction

In turbulent non-premixed flames, localized extinction is observed when the mixing rates are locally sufficiently high to compete with the critical rates of chemical

reactions. This instability induces local temperature drops due to increasing heat removal from convection and diffusion, along with decreasing chemical reaction rates [*Warnatz* 2000].

Figure I.5 shows the scatter plots of temperature from one turbulent non-premixed H_2/CH_4 – O_2/CO_2 jet flame displaying evidences of localized extinction. Each red dot represents one single-shot measurement from a Raman/Rayleigh scattering setup, providing quasi-instantaneous scalar measurements. At one diameter above the fuel nozzle (Figure I.5, left), the bulk of the temperature measurements gathers around a narrow band close to chemical equilibrium. Farther downstream, at 5 diameters above the fuel nozzle (Figure I.5, right), most temperature measurements are scattered, away from chemical equilibrium, which characterizes the rapid mixing between fuel and oxidizer. The departure from chemical equilibrium is significantly more pronounced than for Figure I.4. A further increase in mixing rates would lead to flame extinction.

The oxidizer temperature from a coflow burner plays a major role on the degree of localized extinction. The degree of localized extinction is generally found to increase while the oxidizer temperature decreases, as more energy is required to reach the ignition temperature. A small change in oxidizer temperature can have a large impact of the degree of localized extinction.

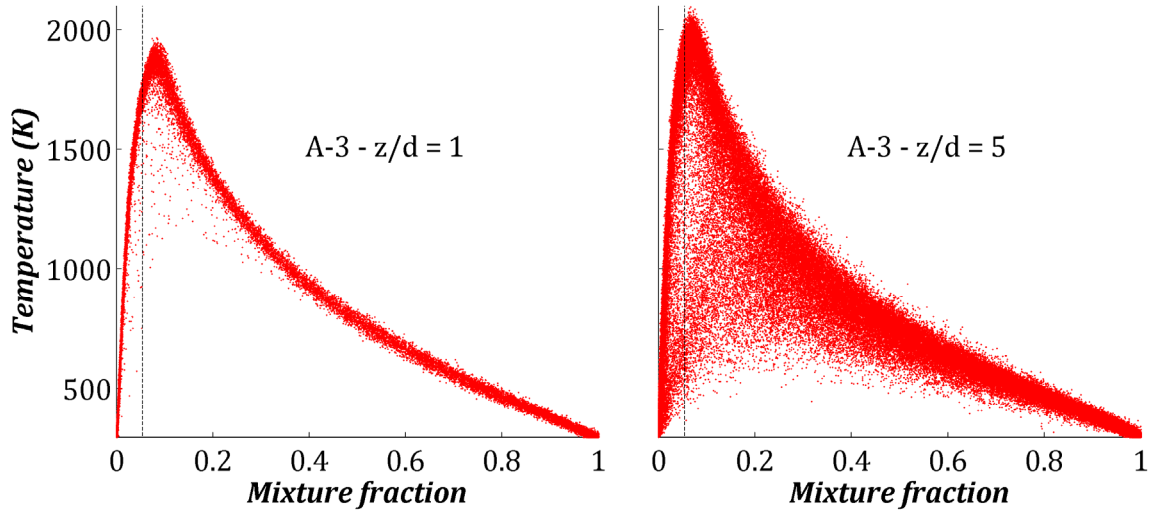

Figure I.5: Scatter plots of temperature from flame A-3 (cf. Table III.6) measured at 1 and 5 diameters above the fuel nozzle, using the simultaneous line imaging of Raman/Rayleigh scattering setup at Sandia National Laboratories (SNL).

2.2.9. Dissociation reactions

As mentioned in [*Turns* 2000], at high temperatures, the products of hydrocarbon combustion generally do not consist only of CO_2 and H_2O, which are the typical products from flames at stoichiometric conditions. Instead, CO, H_2 and

eventually minor species such as O, H and OH radicals, for instance, appear within the composition of the flame products. In these conditions, the latter species mainly originate from dissociation of CO_2 and H_2O. The minor species can potentially end up reaching a significant part of the composition of the flame products at sufficiently high temperatures.

The increase in the degree of dissociation of the flame products with the temperature is to be related to the principle of Le Châtelier. According to this principle, any system initially in a state of equilibrium, which is affected by a change (increasing pressure or temperature, for instance) will react by shifting its composition to minimize the change [*Turns* 2000]. For instance, an increase of temperature will be balanced by an increased rate in endothermic reactions. An example is the reaction absorbing heat while dissociating CO_2 into CO and O_2.

2.2.10. Molecular mixing

In non-premixed flames, molecular mixing is mainly achieved through convection and diffusion. Concerning molecular mixing through convection, natural convection is not of interest for this investigation, since only the near-field of the flames is considered, where buoyancy has only negligible effects [*Turns* 2000]. Due to the relatively high velocities of the fresh gas mixtures, forced convection, driven by velocity gradients, is rather considered and is associated to the concept of turbulent mixing rates. The turbulent mixing rates operate an intense macroscopic mixing, regardless of the species. Their influence onto the reacting mixture can be readily identified in the radial profiles of mixture composition by intense scalar fluctuations.

Molecular diffusion, as detailed in [*Turns* 2000], mainly consists of four distinct modes of mass diffusion:

- Ordinary diffusion, driven by concentration gradients (Fick's Law),
- Thermal (or Soret) diffusion, driven by temperature gradients,
- Pressure diffusion, driven by pressure gradients,
- Forced diffusion, driven by unequal body forces per unit mass among the species.

The present investigation focuses on open (or quasi-open) flames at atmospheric pressure. Therefore, pressure gradients can be neglected. Forced diffusion generally results from charged species (ions) interacting with an electric field. Since ions are supposedly present at sufficiently small concentrations in the present flames, forced diffusion can generally be neglected.

Consequently, molecular mixing can be reduced to only turbulent mixing, ordinary diffusion and thermal diffusion. In flame calculations, turbulent mixing can be handled by a variety of models, depending on the chosen degree of simplification [*Veynante* 2002]. Molecular diffusion is generally the dominating transport regime in the near-field of laminar non-premixed jet flames. In non-premixed turbulent flames, molecular diffusion is also generally the dominating transport regime in the near-field but competes with the turbulent mixing rates, which dominate farther downstream. There are generally two alternatives to account for molecular diffusion in flame calculations: full multi-component transport (FMCT) or equal diffusivities transport (EDT) regimes.

FMCT takes into account that all species have their own diffusivity and considers the effects from thermal diffusion, and consequently provides closer results to reality. The consequent computational time is generally considerable, which limits the application of FMCT in some cases. To greatly simplify the calculations, EDT considers diffusivities equal for all species and does not account for thermal diffusion. Though it may be sufficient in most applications, this assumption is known to be potentially inaccurate in the near field of simple jet flames at low to moderate jet Reynolds numbers, where molecular diffusion has the strongest influence on the mixing process [*Drake* 1982, *Smith* 1995, *Barlow* 2005].

The difference between both transport regimes is mostly seen in presence of species whose molar masses are very different from the mean molar mass. This leads to differential diffusion effects. A typical example is that small species, such as H radicals, are expected to diffuse faster than large species, such as CO_2. Differential diffusion effects may consequently affect the flame structure locally. The phenomenon might be especially of interest in oxy-fuel flames involving H_2 and CO_2 in large proportions.

2.2.11. Soot inception

Soot generally appears at relatively high flame temperatures in hydrocarbon flames. It is responsible for the yellow colour of the flame tip, which generates the thermal radiation encountered in most combustion applications in daily life (candles, wood oven, etc). Soot consists of small particles primarily based on carbon atoms. The particles are found in fuel-rich premixed flames, where the available oxygen is not sufficient to fully oxidize the available fuel in the reaction zone. Soot often appears in non-premixed flames as well, due to the longer residence times, which promote the formation of soot particles. The level of soot is very dependent on the type of fuel.

Figure I.6 shows a schematic view of the soot formation process as a function of the reaction time. Unburned hydrocarbons form polycyclic aromatic hydrocarbons (PAH). PAH are widely accepted as soot precursors [*Glassman* 1989, *Turns* 2000,

Warnatz 2000]. PAHs grow into large molecules up to reaching a critical size where they are rather identified as particles. The particles then agglomerate while travelling into the flame until they are oxidized where a larger amount of oxygen is available.

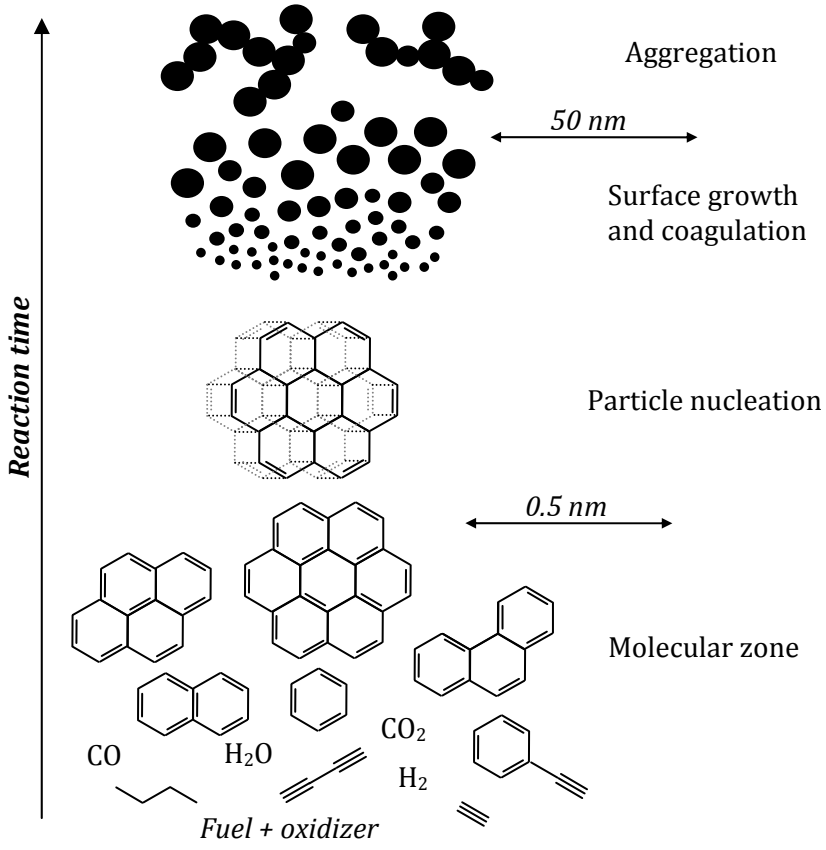

Figure I.6: Schematic view of the soot formation process. Adapted from [Bockhorn 1994].

2.3. Typical flame structures

The following paragraphs give a brief overview of the typical flame structures encountered in the present investigation: laminar premixed flat flames and non-premixed jet flames.

2.3.1. Laminar Premixed flat flames

Laminar premixed flat flames are widely used in combustion investigations due to their simplicity and their wide range of flame conditions. A laminar premixed flat flame stabilizes on a burner if the reactants penetrate the flame with a velocity approximately equal to the flame propagation speed.

Figure I.7 illustrates the flame structure of such stabilized flames, considering the fresh gas mixture flowing from left to right. The unburned mixture first gets preheated by a small part of the released heat from the reaction zone downstream. The molar fraction of the reactants decreases as they diffuse towards the reaction zone, due to the species concentration gradients. As the preheated mixture reaches its ignition temperature, the reaction starts, releases the bulk of the chemical energy and forms products. In the reaction zone, the reaction rate steeply increases and then decreases, as most of the fuel molecules are consumed. The reaction zone is generally very thin (~1 mm) and is characterized by a very fast chemistry dominated by bimolecular reactions. Farther downstream, products reach the post-flame region, which is considerably thicker than the reaction zone. This zone is dominated by slower reactions of three-body radical recombinations. In hydrocarbon flames, the final burnout of CO into CO_2 occurs in this zone. The temperature of the products is close to the adiabatic flame temperature in the post-flame zone.

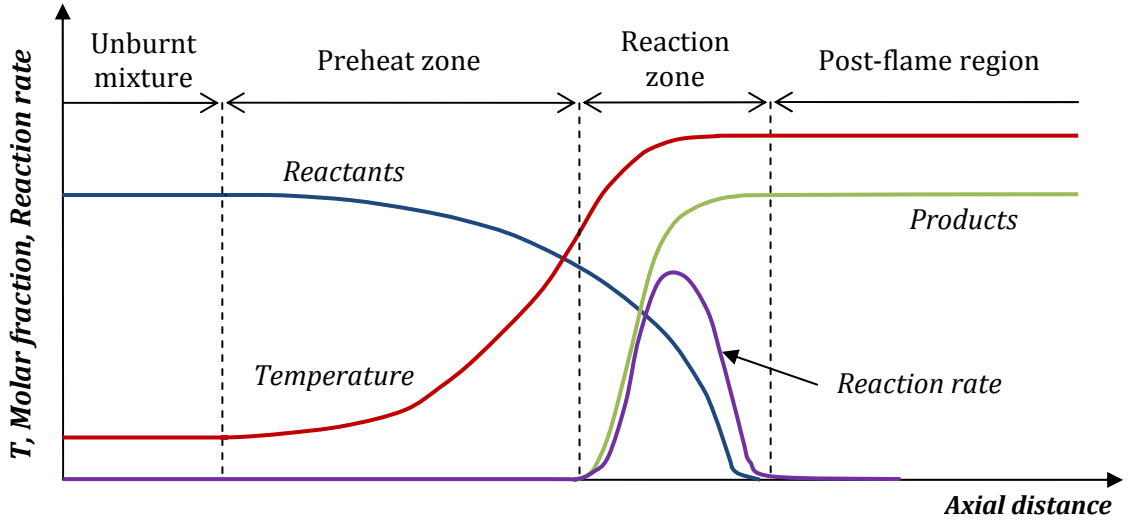

Figure I.7: Schematic structure of laminar premixed flat flames.

2.3.2. Non-premixed jet flames

2.3.2.1. Overview

Non-premixed jet flames can be divided into three different regimes: laminar, transitional and turbulent jet flames. The jet Reynolds number (cf. Eq. I.11) is generally used to determine the regime followed by a jet flame.

Figure I.8 gives an overview of the progressive change in flame regime with an increasing jet Reynolds number, adapted from [*Hottel* 1949]. At low jet Reynolds numbers, the jet flame is laminar and dominated by molecular diffusion. Its flame length monotonically increases with the jet Reynolds number. As Re_f reaches ca. 1000 – 2000,

the flame enters the transition region, where its flame length decreases with Re_f. While the near field remains laminar, turbulent structures dominate downstream. The proportion of the flame dominated by the turbulent structures increases with Re_f. Fully developed turbulent flames appear from Re_f of ca. 3000 – 4000, even if a short part of the flames remains laminar in the near-field. The flame length of fully developed turbulent jet flames first gently decreases with Re_f and then remains constant at high Re_f. For the three different regimes, the typical composition of the reacting mixture from non-premixed jet flames in mixture fraction space is similar to the one shown in Figure I.4.

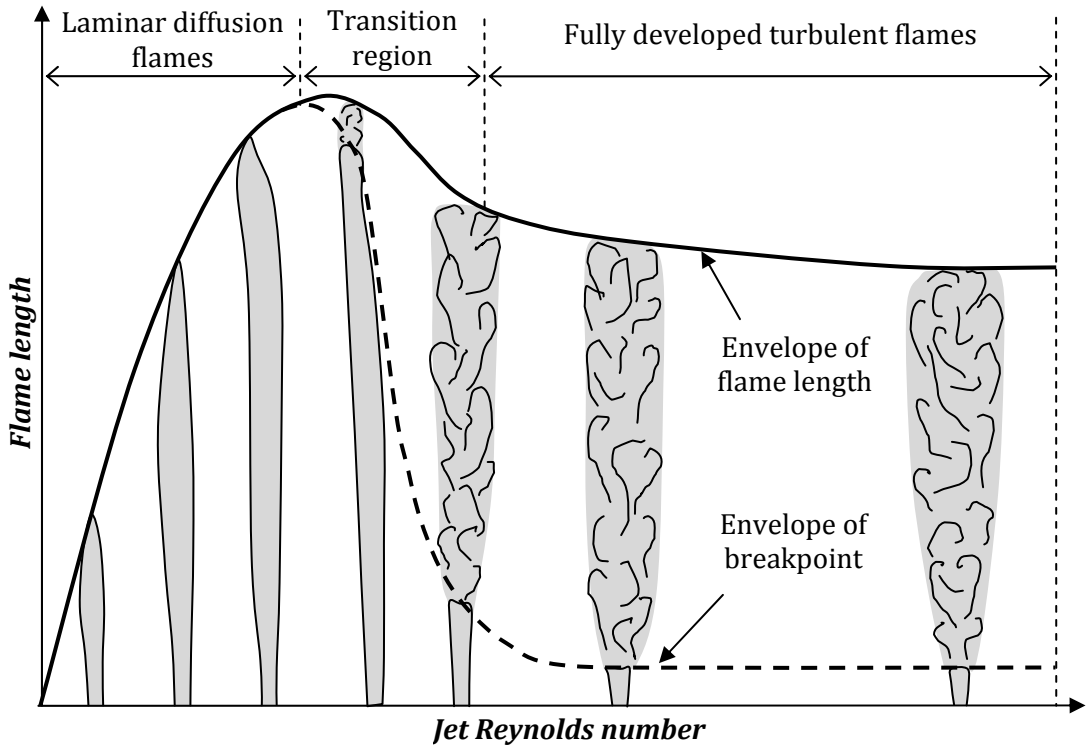

Figure I.8: Schematic of the progressive change in flame regime with an increasing jet Reynolds number. Adapted from [Hottel 1949].

2.3.2.2. Laminar non-premixed jet flames

Laminar non-premixed jet flames are characterized by relatively low jet outlet velocities and molecular transport dominated by diffusion processes. The importance of the diffusion processes in these flames justifies that they are often also called diffusion flames. A schematic of the typical flame structure of vertical non-premixed laminar jet flames is shown in Figure I.9, adapted from [*Turns* 2000].

As the fuel exits from the nozzle along the central axis, it diffuses radially outward, in the direction of the oxidizer. Similarly, the oxidizer diffuses radially inward, towards to the fuel jet. This can be seen as the radial profiles of mass fraction for both

fuel and oxidizer start to curve immediately after the nozzle outlet. The flame zone appears where fuel and oxidizer mix and meet stoichiometric conditions. This marks the peak of flame products and temperature. Flame products diffuse both inward and outward. The reaction zone is generally quite narrow and evolves along the central axis with an annular cross section, until the flame tip is reached. In the upper regions, most of the fuel is consumed and the concentration of hot flame products is sufficient, so that buoyant forces become important. This causes an acceleration of the flow upward, which tends to narrow the flame. Due to the relatively slow reaction and long residence time, soot may form in the fuel-rich side of the reaction zone and is consumed while reaching the oxidizer region.

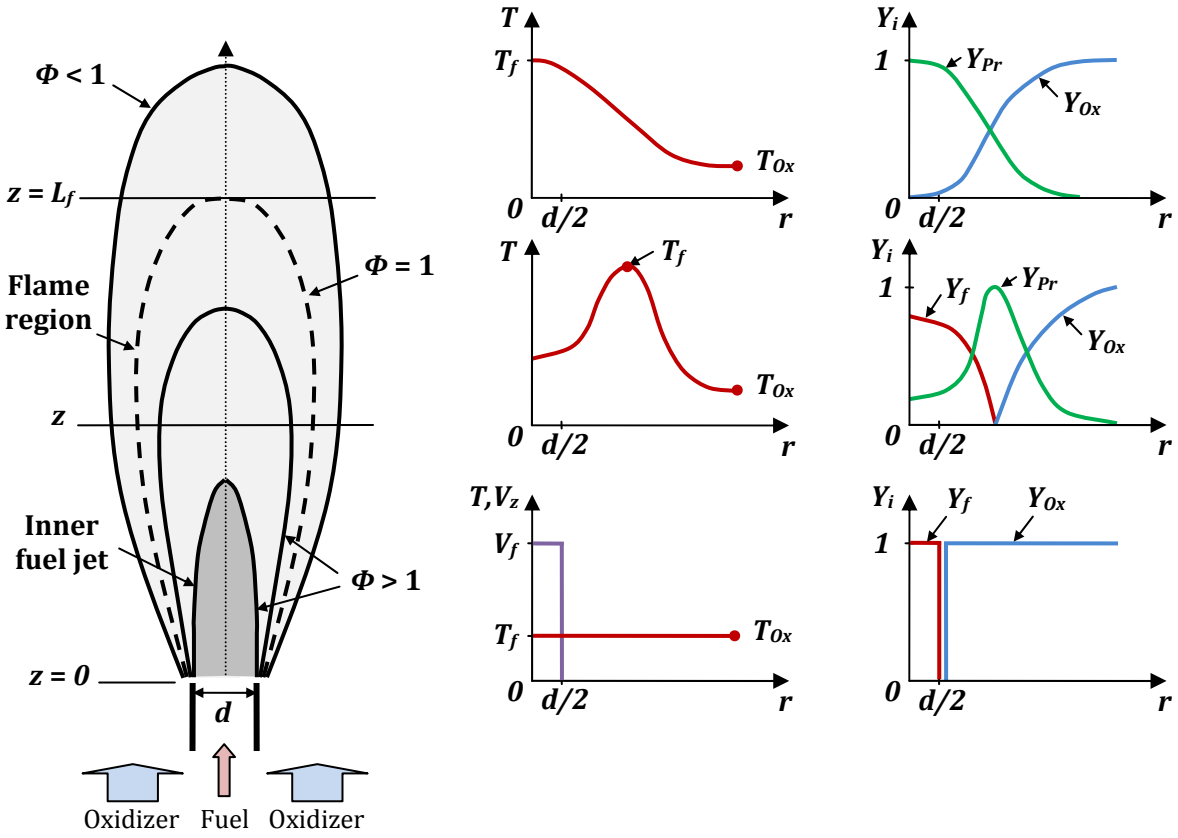

Figure I.9: Schematic of the laminar non-premixed jet flame structure. Adapted from [Turns 2000]

2.3.2.3. Turbulent non-premixed jet flames

Turbulent non-premixed jet flames represent a very popular research topic since those flames are widely found in industrial applications. They are also very complex, especially since the length scales of the turbulent structures vary over a large range. In addition, their time scales are generally very short and challenge the current experimental diagnostics. One of the main characteristics of turbulent jet flames is that the turbulent motion of fluid elements allows momentum, species and energy to be transported in the cross-stream direction farther and much more rapidly than is

possible by diffusion [*Turns* 2000]. This has a considerable influence on the rate of reactions and thus, on the flame structure.

A simple representation of the turbulent structures consists in considering a two-dimensional flame/vortex interaction, as shown in Figure I.10, adapted from [*Renard* 2000]. On each side of the fuel stream, a small perturbation of the velocity field at the rim of the nozzle outlet generates a Kelvin-Helmholtz instability. A high velocity difference at the shear layer between fuel and oxidizer is sufficient to trigger this instability, which generates vortices affecting both oxidizer and fuel layers. The amplitude of the vortices grows with the axial distance, while they are transported downstream, until they dissipate the energy inducing their motion. As they grow, they entrain higher amounts of oxidizer into the jet inner core. To some extent, this may create oxidizer engulfment into the jet inner core, eventually leading to localized extinction. Reciprocally, higher amounts of fuel are entrained into the oxidizer side, which may create flame islands out of the jet inner core. The growing amplitude of the vortices illustrates the wide variety of length scales seen in turbulent combustion.

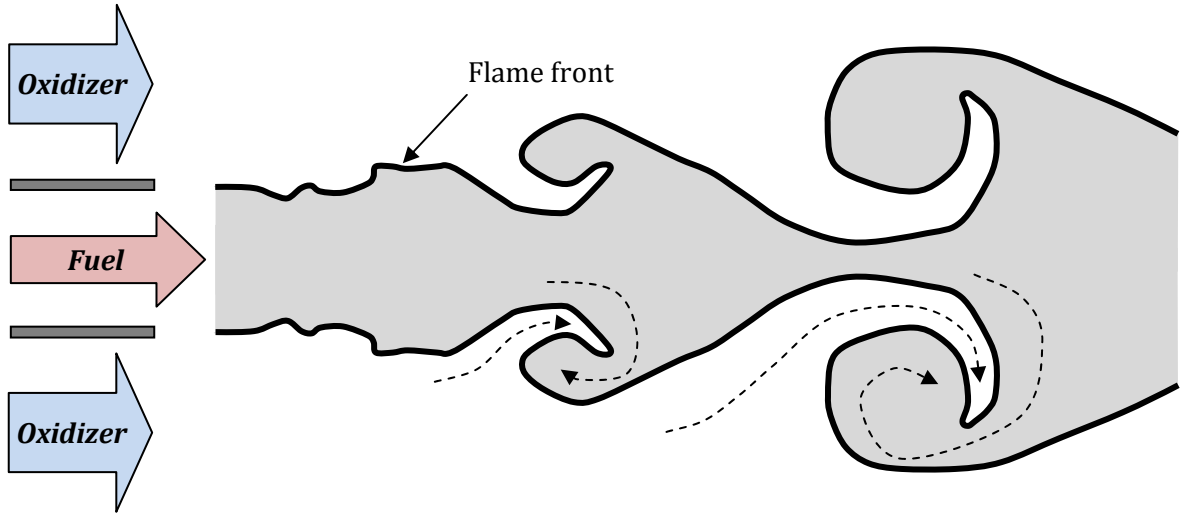

Figure I.10: Flame/vortex interaction as found in a non-premixed jet flame. Adapted from [Renard 2000].

In practice, the flame/vortex interaction is three-dimensional, starting as a vortex ring (thoroid/doughnut shape). Its shape can be affected by any parameter such as, for instance, the geometry of the burner, or the background flow, which can possibly destroy the ring before it interacts with the flame [*Renard* 2000]. Combustion processes also strongly modify the instability mechanism, and generally delay the amplification of the length scales of the vortices. This is due to a laminarisation effect, operated by the increasing temperature, which increases the local kinematic viscosity of the mixture and helps dampen the turbulent structures [*Hottel* 1949, *Takagi* 1980, *Takagi* 1981, *Takeno* 1994]. Another important aspect is that the time scales of the turbulent structures are very short. Consequently, the pattern seen in Figure I.10 rather corresponds to an

instantaneous picture. The intermittence of the vortex rings and their constant rotation make the edges of turbulent flames visually appear brushy or fuzzy [*Turns* 2000].

Two main distinct instability modes were evidenced in turbulent non-premixed non-reacting jet flows and jet flames [*Becker* 1983, *Mungal* 1989, *Mungal* 1991]: axisymmetric and helical (also called sinuous) modes. A double-helical mode is also mentioned in the literature [*Mungal* 1989, *Mungal* 1991], though its nature is very similar to the helical mode of instability. The axisymmetric mode is composed of a regular succession of axisymmetric contractions, similarly to the pattern observed in Figure I.10. The helical mode reveals a sinuous pattern of vortices instead, suggesting a vortex line helically rolled around the jet inner core and expanding with the axial distance [*Mungal* 1989, *Yoda* 1994, *Ditaranto* 2001]. Helical modes of instability are especially found in flames using swirl burners [*Shtork* 2008, *Stöhr*]. In non-premixed jet flames, both modes of instability can be seen intermittently in the same flame [*Mungal* 1989].

The averaged radial profiles of composition of the reacting mixture are similar to the two lowest profiles shown in Figure I.9. Farther downstream, the intense turbulent mixing rates dominate the molecular transport, and tend to flatten the radial profiles of all scalars. The instantaneous radial profiles are generally much more scattered, and the degree of discrepancy increases with the axial distance, as the amplitude of the turbulent structures increases.

Figure I.11 shows an example of Favre-averaged radial profiles of the temperature, T_{Favre}, and the corresponding fluctuations, T'', for a turbulent non-premixed $CH_4/H_2/N_2$ – air jet flame [*Meier* 2000]. Favre statistics are calculated by decomposing an instantaneous parameter into its mean part and its fluctuating part, using a mass density-weighted average. The temperature profile can be used to monitor the evolution of the reaction zone. The reaction zone greatly expands radially outward with the axial distance, as the turbulent structures expand as well. The expansion also occurs inward, until the maximum flame temperature attains the central axis. In this case, the fluctuations of temperature correspond to the variations from one single-shot measurement (quasi-instantaneous) to another and can be considered as mostly induced by turbulence. Fluctuations are seen to peak around the steep gradients of temperature, marking the fluctuations of the flame zone radial location. In addition, though the fluctuations remain low on the right side (oxidizer side), those from the central axis (fuel stream) increase with the axial distance. This marks the development of the fine-scale turbulent structures from the jet inner core with the axial distance, entraining more oxidizer and achieving the radial inward expansion of the flame zone.

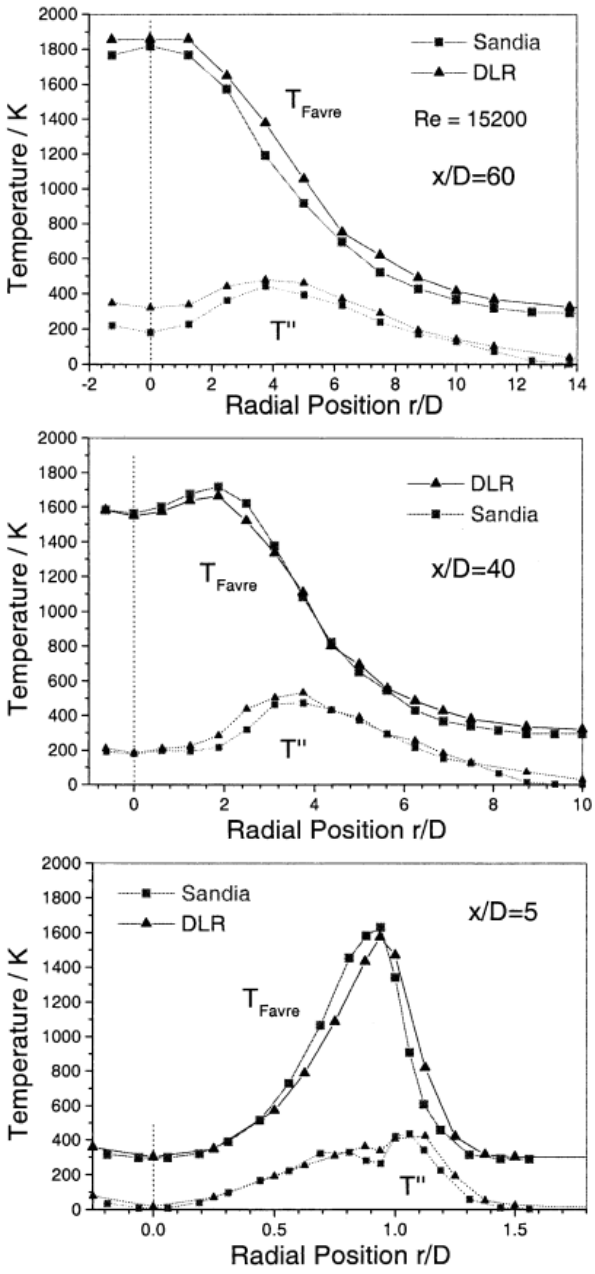

Figure I.11: Comparison of Favre-averaged radial profiles of temperature and the corresponding fluctuations for a non-premixed turbulent $CH_4/H_2/N_2$ – air jet flame. [Meier 2000]

Early investigations of the structure of turbulent non-premixed jet flames revealed two main zones within the reaction region: an endothermic pyrolysis zone and an exothermic zone at the location of the stoichiometric conditions [*Bilger* 1977, *Chen* 1986, *Takahashi* 1996]. The two zones are separated by the high-viscosity flame front. The outer zone mainly preheats the oxidant, while the inner zone is composed of the jet inner core and the mixing layer. Large-scale turbulent structures take place in the outer zone, while the fine-scale turbulent structures of the mixing layer grow with the axial distance. As soon as the flame front is no longer able to dampen the growing turbulent structures, coalescence occurs, achieving the radial inward expansion of the flame zone.

2.3.2.4. Transitional non-premixed jet flames

The structure of transitional non-premixed jet flames has been widely investigated over the last 60 years [*Hottel* 1949, *Scholefield* 1949, *Grant* 1975, *Takagi* 1980, *Takahashi* 1982, *Eickhoff* 1989, *Mungal* 1991, *Katta* 1993, *Takeno* 1994, *Warnatz* 2000, *Agrawal* 2005]. These flames are characterized by a laminar part in the near-field, followed downstream by a turbulent part. The transition between the two parts is marked by a breakpoint whose height varies with the flow conditions. The transition is also associated to Kelvin-Helmholtz instabilities of the jet flow. Such flames tend to happen for coflow jet flames with Re_f ranging from 1350 to about 2000. Therefore, the composition profiles of the reacting mixtures mainly consist of a combination of patterns from laminar and turbulent non-premixed flames.

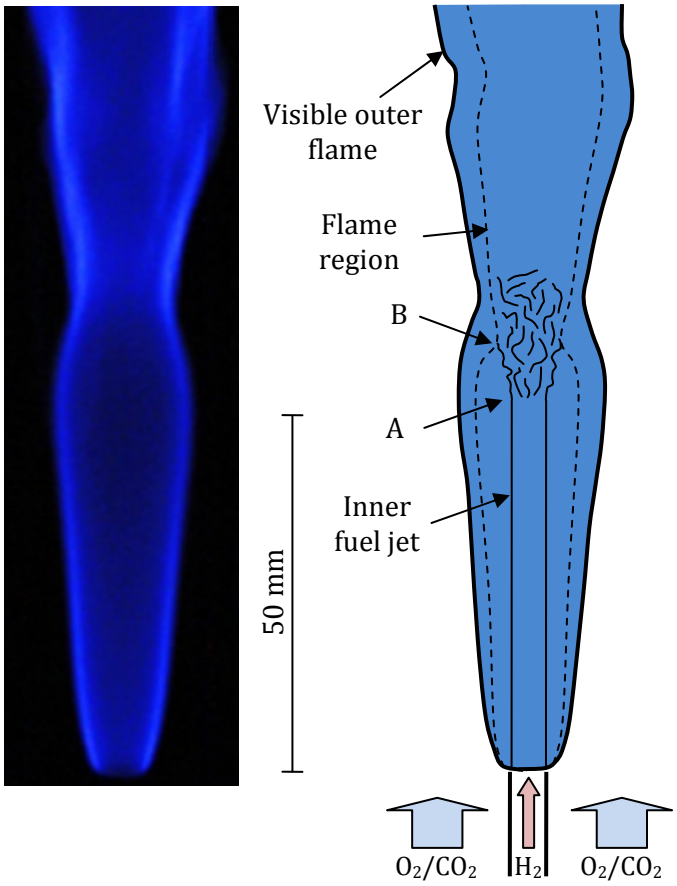

Figure I.12: Left: photograph of the near-field of a non-premixed transitional H_2 – O_2/CO_2 jet flames (Re_f = 1600, 22 $\%_{mol}$ O_2 in the oxidizer); ISO: 1600, exposure time: 1/100 s. Right: schematic of the transitional flame structure, adapted from [Takahashi 1982]; A: breakpoint of the inner fuel jet; B: breakpoint of the outer flame zone.

Figure I.12 shows a typical example of transitional non-premixed jet flames with a pure hydrogen jet flames performed in a narrow nozzle (3.6-mm inside diameter) and Re_f = 1600. As described in [*Takahashi* 1982], after a laminar jet development, the inner fuel jet breaks down into a turbulent flow (point A in Figure

I.12), due to instabilities in the inner jet boundary layer. The consequent turbulent zone spreads out downstream with an inverted cone pattern, typical of a turbulent jet. Up to this point, the sequence is relatively similar to non-reacting transitional flows, though the onset of the breakpoint is generally shifted downstream by combustion processes, as mentioned in Section 2.3.2.3. As the inner turbulent jet spreads out, the flame region shifts inward and becomes turbulent as the two regions meet (point B in Figure I.12). As described in most investigations cited above, the onset of the breakpoint shifts upstream as the jet Reynolds number increases, until the transition stagnates very close to the nozzle outlet, at the blow-off stability of the flames. When this limit is reached, flames are considered as turbulent.

3. CO_2-DILUTED OXY-FUEL FLAMES

3.1. Reacting mixtures

The overall chemical reaction of oxy-fuel flames using methane is given in Eq. I.12. Instead of air, pure oxygen is used to burn methane and, ideally, the flame products are only composed of carbon dioxide and water at stoichiometric conditions. In air, oxygen is only present at ca. 20.9 $\%_{vol}$ and the rest mostly consists of inert gases, which greatly contribute to mitigate the flame temperatures. Using pure oxygen, flame temperatures can reach up to 3000 K or more.

$$CH_4 + 2O_2 \rightarrow CO_2 + 2H_2O \qquad \textit{Eq. I.12}$$

In most practical applications, to comply with the upper temperature limits provided by the equipments, oxygen dilution by an inert gas is required. Flue gas recirculation (FGR) enables to dilute the oxygen with a mixture mostly consisting of carbon dioxide and water. The water is generally condensed before recirculation, which enables to have an almost pure stream of CO_2 available for recirculation. To simplify, the overall chemical reaction corresponding to oxy-flames with FGR is given in Eq. I.13. φ_{O2} is the molar fraction of oxygen in the oxidizer, so that the rest of the oxidizer only consists of carbon dioxide. This parameter brings one more degree of freedom compared to air-fired conditions, and has not been much investigated considering a CO_2-dilution of the oxidizer. Evidently, the flame temperature increases with the oxygen content in the oxidizer, as the degree of CO_2 dilution decreases.

$$CH_4 + \frac{2}{\varphi_{O2}}(\varphi_{O2}O_2 + (1-\varphi_{O2})CO_2) \rightarrow \left(\frac{2}{\varphi_{O2}} - 1\right)CO_2 + 2H_2O \qquad \textit{Eq. I.13}$$

Another interest of operating FGR with oxy-fuel flames is to enhance the CO_2 concentration in the flue gas. This eases the CO_2 capture process and makes it relatively inexpensive compared to CO_2 scrubbing methods used with air-fired conditions [*Bolland* 1998, *Buhre* 2005, *Skeen* 2009, *Li* 2011].

Practically, the flames of interest in the present investigation also consist of fuel mixtures of methane and hydrogen, or pure hydrogen only, as given in Eq. I.14 and Eq. I.15, respectively. φ_{H2} is the molar fraction of hydrogen in the fuel, so that the rest of the fuel only consists of methane.

$$CH_4 + \left(\frac{4+\varphi_{H2}}{2\varphi_{O2}}\right)[\varphi_{O2}O_2 + (1-\varphi_{O2})CO_2] + \varphi_{H2}H_2 \rightarrow \left(\frac{1}{\varphi_{O2}}\left(2+\frac{\varphi_{H2}}{2}\right) - \frac{\varphi_{H2}}{2} - 1\right)CO_2 + (2+\varphi_{H2})H_2O \quad \textit{Eq. I.14}$$

$$H_2 + \frac{1}{2\varphi_{O2}}[\varphi_{O2}O_2 + (1-\varphi_{O2})CO_2] \rightarrow H_2O + \left(\frac{1-\varphi_{O2}}{2\varphi_{O2}}\right)CO_2 \quad \textit{Eq. I.15}$$

Following the success in glass and metal industries of oxy-fuel furnaces running with pure oxygen and the latest process developments involving FGR, CO_2-diluted oxy-fuel has been a more popular research topic for the last decades. Most investigations tend to focus on flame conditions similar to air-fuel flames, since those are well known and existing equipments can be re-used. However, replacing nitrogen by carbon dioxide induces major differences compared to air-fired conditions. The following paragraphs give a brief overview of the main features observed in oxy-fuel flames, as described in the available literature. The focus is especially set on the general observations, the flame structure and the specific chemistry.

3.2. General observations

3.2.1. Stability domain

As a diluent, carbon dioxide achieves a higher degree of quenching than nitrogen, especially through its heat transfer properties. Therefore, considering fresh oxidizer mixtures at ambient temperature, O_2/CO_2 mixtures with ca. 21 $\%_{vol}$ O_2 (as in air) generally give different flame conditions than comparable air-fuel flames. Adiabatic flame temperatures are typically lower and the flammability limits are narrower. Most investigations found in the literature report that higher oxygen contents in the oxidizer than 21 $\%_{vol}$ O_2 are required to achieve air-flame like stability and temperatures [*Coppens* 2008, *Ditaranto* 2011].

Using a coflow burner, the poor degree of mixing between fuel and oxidizer typically prevents from reaching stable anchored flames at lower oxygen contents in the oxidizer than ca. 35 $\%_{vol}$ in laminar methane flames [*Ditaranto* 2011], for instance. Lower oxygen contents in the oxidizer generally lead to flame instabilities, lift-off and ultimately blow-off. Burners achieving a higher degree of mixing [*Kutne* 2011] or using preheated oxidizer mixtures can evidently lower this limit.

3.2.2. Flame length

The flame length is generally defined as the length from the base of the flame to the leading edge along the centerline, which is generally the highest point. Measurements can be performed using a simple video camera or using the excited OH* chemiluminescence, seen simply by adding a UV filter to the camera. The latter is generally seen as a concrete reference of the combustion reaction location.

The flame length of non-premixed oxy-fuel jet flames has been of interest in various studies [*Ditaranto* 2001, *Sautet* 2001, *Kim* 2006, *Kim* 2007a, *Ditaranto* 2011]. All cited authors agree that an increase in oxygen content in the oxidizer leads to shorter flames. Figure I.13 shows the flame lengths from oxy-fuel flames at various oxygen contents in the oxidizer and various jet Reynolds numbers, as measured by [*Ditaranto* 2011]. The increase in oxygen content in the oxidizer increases the stoichiometric mixture fraction, shifting the flame zone closer to the inner fuel jet, where the degree of mixing between fuel and oxidizer is lower. In addition, the momentum of the coflowing oxidizer decreases as the oxygen content in the oxidizer increases, which improves the local mixing [*Sautet* 2001].

Another feature seen in Figure I.13 is that the flame length monotonically increases with the jet Reynolds up to $Re_f = 2340$. This value generally corresponds to the transitional regime of non-premixed air-fuel flames, where the flame length supposedly decreases while increasing Re_f (cf. Section 2.3.2.1). The oxygen-enrichment of the oxidizer somehow shifts the transitional regime to higher Re_f. The phenomenon is due to the higher flame temperatures inducing higher kinematic viscosity and thus, a higher degree of flow laminarisation [*Ditaranto* 2011]. The effects of flow laminarisation will be further detailed in Section 3.3.2.

According to the authors of Figure I.13, the measured flame lengths for the three lowest jet Reynolds numbers shown in Figure I.13 are in good agreement with the 2/5 Froude law in the pure buoyancy driven flame regime given in [*Delichatsios* 1993].

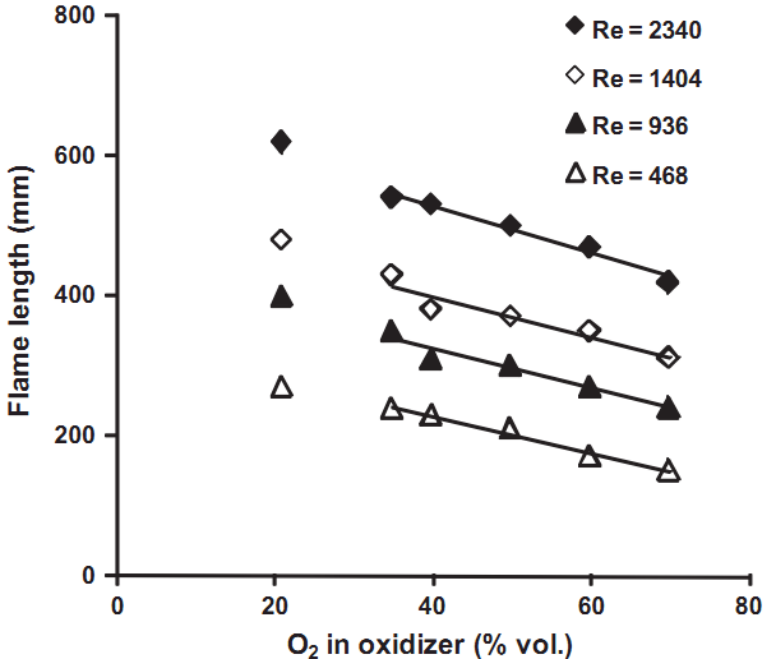

Figure I.13: Flame length at varying oxygen contents in the oxidizer and jet Reynolds numbers. [Ditaranto 2011]

3.2.3. Soot inception

The soot inception rate is considerably sensitive to the oxygen content in the oxidizer and can lead to enhanced levels of soot at high oxygen contents compared to similar air-fired conditions [*Linow* 2002]. On the one hand, the soot inception rate and the surface growth rate locally increase with the oxygen content in the oxidizer [*Lee* 2000, *Beltrame* 2001]. This is due to the induced temperature increase, which promotes the formation of aromatics (soot precursors) in the fuel pyrolysis zone. On the other hand, the CO_2 dilution decreases the soot nucleation rate and the surface growth distance [*Liu* 2001, *Oh* 2006]. This is due to the lower flame temperatures and the shorter residence time in the inception regions. In addition, radicals such as O, H and OH can take a significant share of the flame products composition at high oxygen contents in the oxidizer (cf. Section 3.4.2) and are known to enhance the soot oxidation process [*Bradley* 1985].

The dependence of the stoichiometric mixture fraction on the soot inception limits was investigated in [*Kumfer* 2008]. It was concluded that increasing the stoichiometric mixture fraction reduces, or eventually eliminates, the soot formation in oxy-fuel flames. In this case, increasing the stoichiometric mixture fraction means achieving a higher fuel dilution with inert gas and/or lower oxidizer dilution with inert gas (cf. Eq. I.8). In addition, increasing the stoichiometric mixture fraction above $F_{B,St}$ = 0.2 shifts the sooting limits to higher temperatures.

3.2.4. Thermal radiation

The level of thermal radiation in oxy-fuel flames is seen to increase with the oxygen content in the oxidizer, up to reaching overall levels higher than in comparable air-fired conditions [*Baukal* 1997, *Naik* 2002, *Ditaranto* 2011]. Thermal radiation originates mainly from soot formation and radiative gases in the flame products. As detailed above, the soot formation rate increases with the oxygen content in the oxidizer and can explain the difference with the air-fuel flames. In addition, while radiative gases account for 10 – 20 % of the flame products (mainly H_2O and CO_2) in air-fired conditions, they constitute the majority of the flame products of CO_2-diluted oxy-fuel flames.

An investigation was carried out in [*Ditaranto* 2011] on radiative heat flux from non-premixed CH_4 – O_2/CO_2 flames at various oxygen contents in the oxidizer. Measurements were also performed in air-fuel flames with similar conditions. Measured heat flux distributions are shown in Figure I.14 for air-fuel flames and oxy-fuel flames with 35 to 70 $\%_{vol}$ O_2 in the oxidizer. The increase in overall heat flux is clearly visible as the oxygen enrichment increases. The maximum heat flux shifts upstream as the flame shortens. The heat flux distribution with 35 $\%_{vol}$ O_2 in the oxidizer is quite comparable to the air-fired case, despite a relatively higher adiabatic flame temperature (2302 K versus 2226 K). It can also be seen that the air-fuel flame appears longer than any of the oxy-fuel flames.

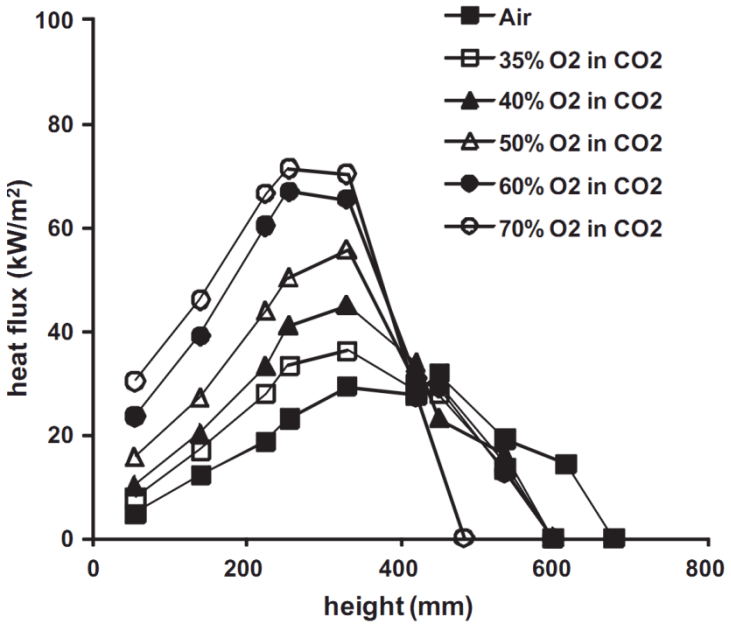

Figure I.14: Axial heat flux distribution for non-premixed CH_4 jet flames at Re_f = 2340. [Ditaranto 2011]

The high thermal radiation can be seen as an advantage, since large concentrations of H_2O and CO_2 enhance the heat transfer across the flame, producing a

uniform temperature distribution. On the other hand, thermal radiation towards the surroundings of the flame contributes to the quenching effects and the narrowing of the flame stability domain due to the heat losses.

3.2.5. Spontaneous flame luminosity

Some of the flame species become molecularly excited at high temperatures in the reaction zone and spontaneously emit radiations with their own spectral signatures. The phenomenon generally corresponds to chemical reactions releasing photons characteristic to the species involved. Such reactions are known as chemiluminescence reactions.

A spectral investigation was performed in [*Ditaranto* 2011] in non-premixed CH_4 – O_2/CO_2 jet flames from 30 to 50 $\%_{vol}$ O_2 in the oxidizer, and in the comparable air-fired conditions, as shown in Figure I.15. The spontaneous flame luminosity displays higher overall levels while increasing the oxygen content in the oxidizer, until reaching higher levels than in comparable air-fired conditions. The spectra mainly consist of the OH* chemiluminescence band (280 – 320 nm), the CH* chemiluminescence band at 431.5 nm and the combined broadband emissions from soot black body and CO_2* chemiluminescence. The degree of CH* chemiluminescence does not seem affected by the oxygen enrichment, unlike the OH* chemiluminescence whose intensity considerably increases with the oxygen content in the oxidizer. The latter observation also appears in [*De Leo* 2007], where it is added that the thermal excitation is the dominant excitation mechanism of OH* chemiluminescence at oxygen contents above 35 % in the oxidizer. Due to the large concentration of CO_2 in the reacting mixture, CO_2* chemiluminescence is assumed to take a great part of the broadband emissions. A comprehensive description of the CO_2* chemiluminescence mechanism can be found in [*Samaniego* 1995].

OH* chemiluminescence imaging can be applied in oxy-fuel flame to visualize the flame structure. In addition, the influence of the broadband signal related to CO_2* chemiluminescence and soot black body emission is relatively limited within this spectral region, which enhances the signal quality of OH* chemiluminescence. For instance, Figure I.16 shows a series of images from partially premixed swirl stabilized CH_4 – O_2/CO_2 flames at various oxygen contents in the oxidizer, presented in [*Kutne* 2011]. All images were applied similar background and normalization corrections, so that intensities are comparable between the images. The increase in intensity of the OH* chemiluminescence with the oxygen content in the oxidizer is considerable. This suggests an increasing presence of OH radicals in the reacting mixtures. As the oxidizer mixture gets closer to 100 % oxygen, the OH* chemiluminescence band is expected to dominate the combined broadband emissions from soot black body and CO_2* chemiluminescence [*Ditaranto* 2001]. This is especially due to the increasing flame

temperature and OH concentration, combined to the decreasing CO_2 concentration. Note also how the flame zone shifts upstream with the increasing oxygen content in the oxidizer in Figure I.16.

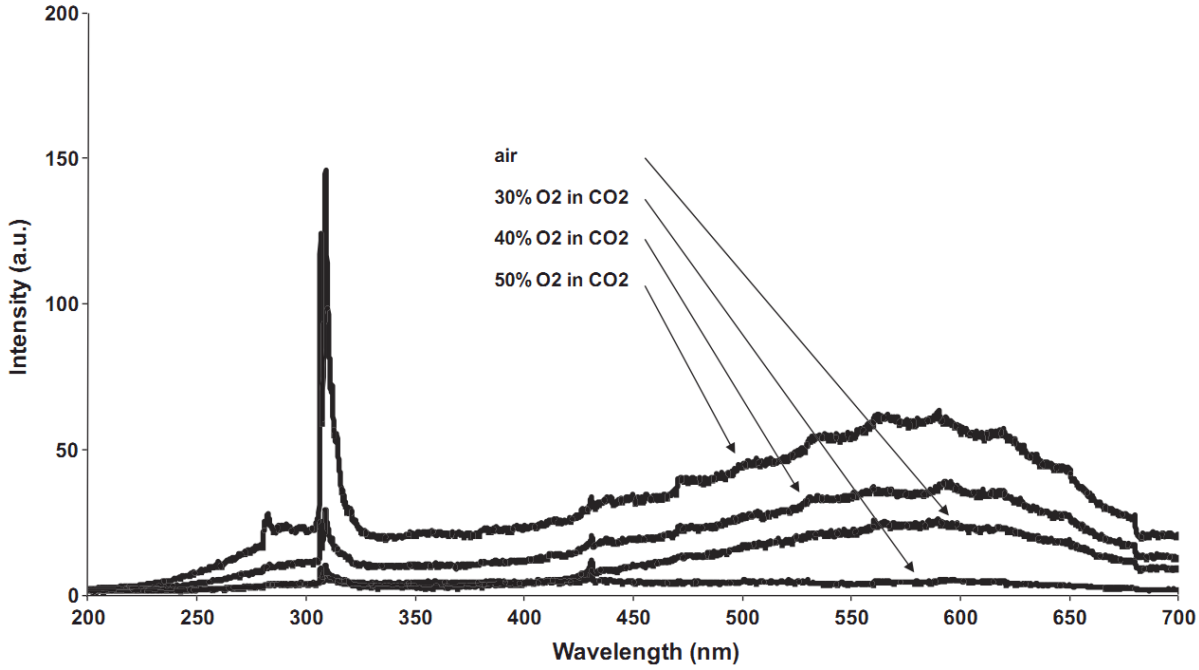

Figure I.15: Ultraviolet and visible spectra at varying oxidizer compositions, Re_f = 936. Spectra are not corrected for the optical path transfer function. [Ditaranto 2011]

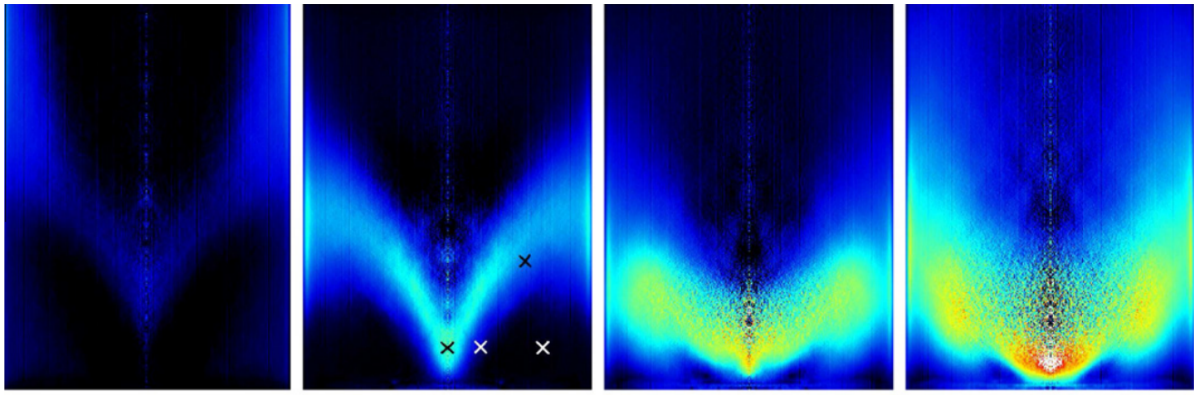

Figure I.16: Abel-deconvoluted OH chemiluminescence images showing average flame structure at power of 21.4 kW and Φ = 0.71 for various oxygen contents in the oxidizer from partially premixed swirl stabilized CH_4 – O_2/CO_2 flames. [Kutne 2011]*

3.3. Flame structure

3.3.1. Flame speed

Investigations on flame speed (burning velocity) revealed significant differences between regular air-fuel flames and oxygen-enhanced or CO_2-diluted flames. Compared to air-fuel flames [*Zhu* 1989, *Law* 1993], flame speed was found to increase with the oxygen enrichment of the oxidizer as a combined effect of higher flame temperatures and lower inert-dilution [*Ruan* 2001, *Kim* 2006]. This contributes to the enhanced flame stability and the flame zone shift upstream from oxy-flames at increasing oxygen content in the oxidizer (cf. Figure I.16).

On the other hand, the effect of the CO_2 dilution is seen to decrease the flame speed [*Law* 1993, *Ju* 1998, *Liu* 2003]. The addition of CO_2 affects the flame speed through three main mechanisms: change of transport and thermal properties of the reacting mixture, participation of CO_2 in chemical reactions and enhanced heat radiation transfer by CO_2 [*Liu* 2003].

Figure I.17, found in [*Liu* 2003], illustrates the different ranges of calculated flame speeds for methane and hydrogen flames, plotted with the equivalence ratio. Results are displayed for three oxidizer mixtures: air, 30 % N_2 in air replaced by CO_2 and O_2/CO_2. Results from [*Zhu* 1989] and [*Law* 1993] are also included for comparison. The case with 30 % N_2 in air replaced by CO_2 exhibits lower flame speeds with both fuels than in comparable air-fired conditions. The cases with O_2/CO_2 oxidizer mixtures display even lower flame speeds.

The authors of Figure I.17 also performed calculations of flame speeds with 30 % N_2 in air replaced by an artificial species FCO_2 with identical thermal and transport properties to CO_2. Unlike CO_2, FCO_2 is purposely excluded from the chemical reactions, though it was assigned the same third-body collision efficiency as CO_2 in all relevant reactions. Results shown in Figure I.17 highlight the considerable impact of the participation of CO_2 in chemical reactions. Flame speeds are found significantly higher with no participation to the chemical reactions.

The previous cases correspond to relatively low oxygen contents in the oxidizer, similar to those in air. Combining the opposite effects of CO_2 and O_2, similar flame speeds to methane/air flames can be obtained with O_2/CO_2 mixtures consisting of ca. 40 $\%_{vol}$ O_2 [*Ditaranto* 2006]. In such oxy-fuel flames, the adiabatic flame temperature is ca. 2400 K, which is about 200 K higher than in methane/air flames.

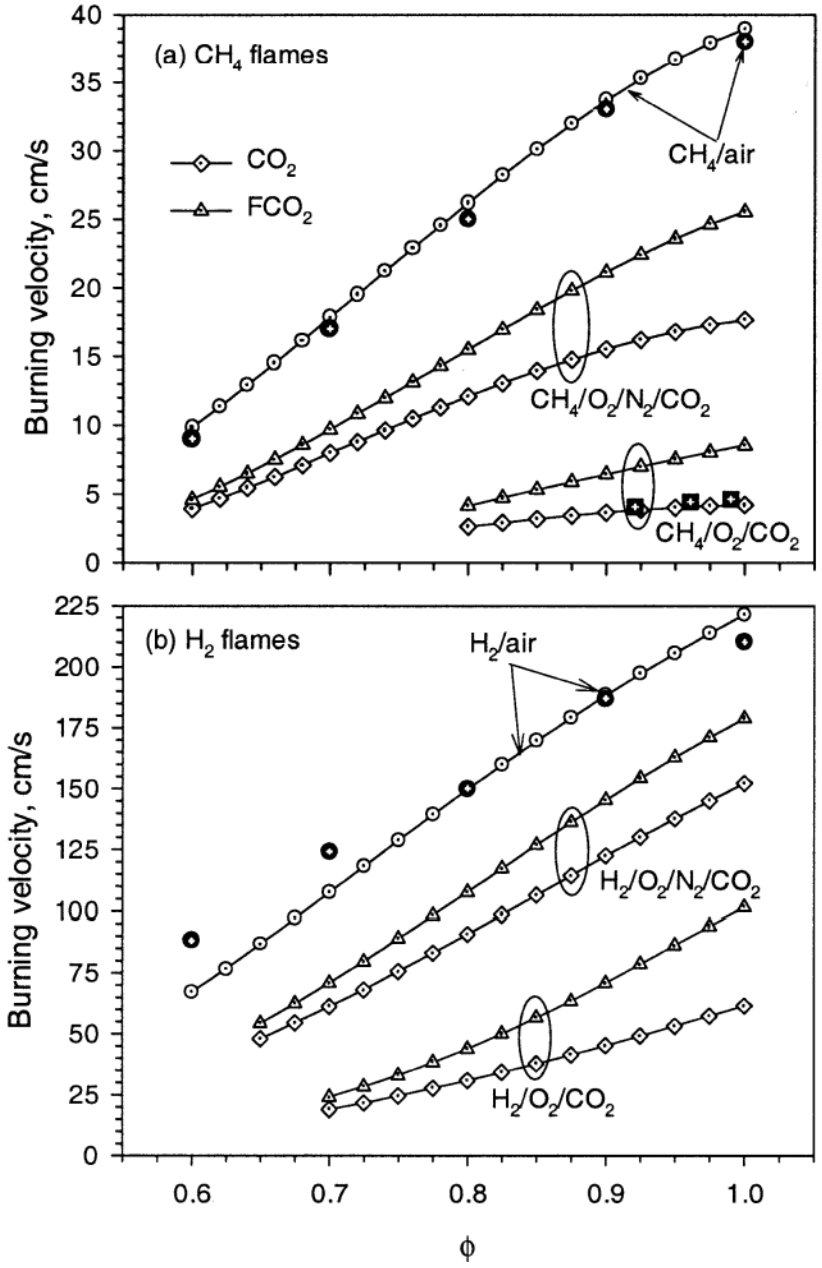

Figure I.17: Burning velocities of CH_4 and H_2 flames. Experimental data from [Zhu 1989] and [Law 1993] are also plotted in methane and hydrogen mixtures, respectively, as filled symbols. [Liu 2003]

3.3.2. Flame laminarisation

As described in Section 2.3.2, non-premixed jet flames always exhibit a laminar-like development in the near-field. This laminar part of the flames represents the required distance for the turbulent structure to fully dominate the mixing process. Relatively longer laminar-like developments have been reported in oxy-fuel flames with high oxygen contents in the oxidizer compared to similar air-fuel jet flames [*Sautet* 2001, *Kim* 2007a, *Ditaranto* 2011]. A stronger laminarisation of the reaction zone is achieved due to the higher flame temperature and the induced higher local kinematic

viscosity. The local viscosity helps dampen the developing turbulent structures. The phenomenon plays a significant role in the enhanced flame stability and the wider flammability limits of oxy-fuel flames with high oxygen content in the oxidizer.

Calculated kinematic viscosities for various flame compositions at equilibrium are shown in Figure I.18 and Figure I.19. Results illustrate that higher kinematic viscosities can be expected using oxidizer at high oxygen contents in the oxidizer. However, below 35 $\%_{mol}$ oxygen in the oxidizer, the kinematic viscosity is lower than in the air case. This observation can account for the difficulty to stabilize non-premixed CH_4 – O_2/CO_2 jet flames in coflow burners with less than 35 $\%_{mol}$ O_2 in the oxidizer (cf. Section 3.2.1).

In non-premixed jet flames at low jet Reynolds numbers, mixtures with higher kinematic viscosity generally exhibit much thicker flames in the laminar near-field than in comparable air-fuel flames. However flames are thinner in the turbulent zone downstream, due to the suppression of turbulent fluctuations in the highly viscous thin side [*Kim* 2007a].

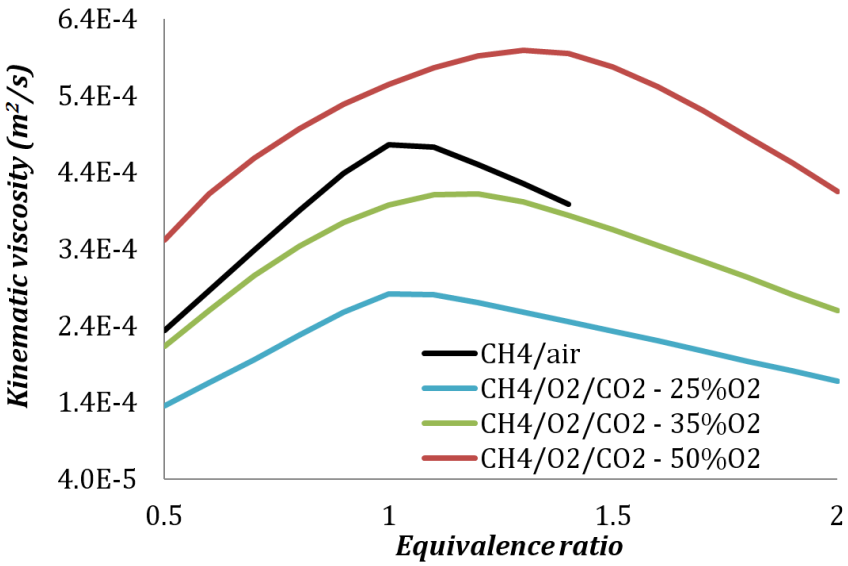

Figure I.18: Calculated kinematic viscosities for various methane flame compositions at equilibrium, using Gaseq.

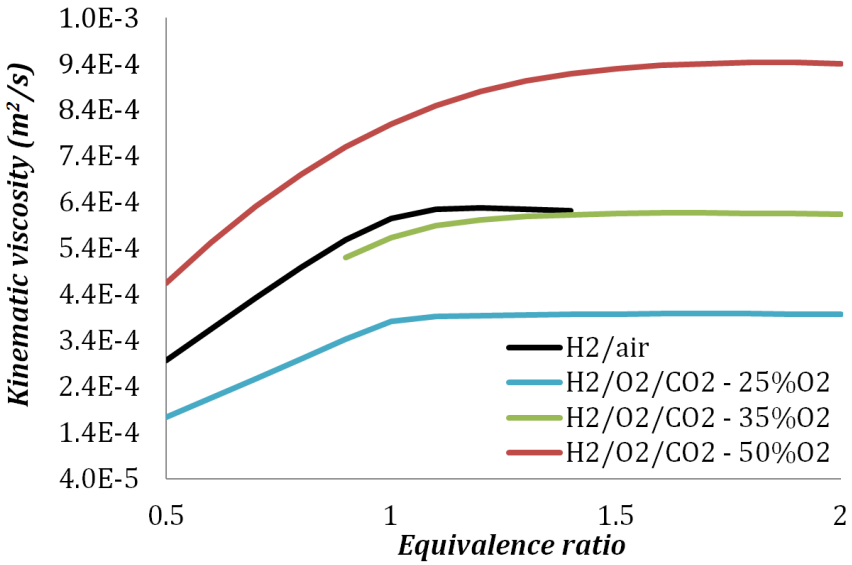

Figure I.19: Calculated kinematic viscosities for various hydrogen flame compositions at equilibrium, using Gaseq.

3.4. Specific chemistry

3.4.1. CO levels

The production of CO is a great matter of concern in combustion. Considering an industrial scale, the presence of CO in the flue gas represents a non-optimum efficiency. This is due to the missing oxidation step in the combustion reaction to convert CO into CO_2, which is considerably exothermic. Another concern, especially within the CCS perspective, is the requirement of extremely low CO contents in the CO_2 pipeline specifications because of the potential corrosion from CO. In addition, CO is characterized by a high health hazard, due to its capacity to substitute oxygen in the hemoglobin, affecting the oxygen-carrying capacity of the blood. Consequently, it is generally intended to keep the CO levels as low as possible.

Most investigations on oxy-fuel flames have reported higher local CO levels than in comparable air-fired conditions, for various kinds of burners and flame regimes [*Masri* 1992, *Tan* 2002, *Richards* 2005, *Czakiert* 2006, *Kim* 2007a, *Park* 2007, *Glarborg* 2008, *Choi* 2009, *Hjartstam* 2009, *Amato* 2011, *Heil* 2011, *Liu* 2012, *Seepana* 2012]. This trend is mainly due to the high CO_2-dilution and the slower burnout of CO, though CO levels also tend to increase with the oxygen content on the oxidizer through the high flame temperatures [*Breussin* 2000, *Kim* 2007a, *Amato* 2011, *Yin* 2011, *Liu* 2012].

Investigations have been carried out on the chemical effects of high CO_2 concentrations in methane flames and have mainly highlighted the enhanced

participation of CO_2 in the reverse direction of the CO burnout reaction given in Eq. I.16 [*Masri* 1992, *Liu* 2001, *Liu* 2003, *Glarborg* 2008].

$$CO + OH \rightarrow CO_2 + H \qquad \textit{Eq. I.16}$$

The different routes to the high CO levels have been numerically investigated in [*Glarborg* 2008]. Though not as strong as triple bonds of N_2, double bonds of CO_2 are sufficiently strong to require high temperatures and/or presence of very reactive free radicals to break them. The reaction given in Eq. I.16 is relatively fast, even at medium temperatures, and is mainly limited by the rate of available free H radicals. It is expected to be the dominating reaction in establishing a CO/CO_2 partial equilibrium under combustion processes and to be sufficiently significant to compete with O_2 for hydrogen free radicals. At higher flame temperatures, dissociation mechanisms mitigating the flame temperature (cf. Section 2.2.9) contribute to the high CO levels (cf. reaction given in Eq. I.17). However, they are potentially slower and act at a lower degree than the reaction given in Eq. I.16. Reactions of CO_2 with hydrocarbons radicals might also take part in the formation of CO.

$$CO_2\ (+M) \rightarrow CO + 0.5\ O_2\ (+M) \qquad \textit{Eq. I.17}$$

Whereas local CO levels can be relatively high in oxy-fuel flames, a few authors reported that CO levels were found rather low in the exhaust gas, and in some cases, lower than for comparable air-fuel flames [*Tan* 2002, *Hjartstam* 2009]. Pressure or inlet temperatures of the reactants can also have a significant influence on the CO levels in the flames [*Amato* 2011, *Liu* 2012], though this is beyond the scope of the present investigation.

3.4.2. Radical pool

The radical pool, especially O, H and OH radicals, has been reported as taking a significant share of the composition of the reaction mixtures at high oxygen contents in the oxidizer [*Breussin* 2000, *Linow* 2002, *Frassoldati* 2009, *Seepana* 2012]. The share is generally higher than in air-fired conditions and increases with the oxygen content in the oxidizer.

The phenomenon is particularly related to the flame temperature, which promotes the endothermic dissociation reactions (cf. Section 2.2.9). For instance, the onset of dissociation of water and other stable species is at temperatures slightly above the temperature of air-fuel flames [*Linow* 2002]. Consequently, the radical pool, which can potentially be ignored in air-fired conditions, should be taken into account in the composition of the reacting mixture above a given oxygen content in the oxidizer. The threshold depends on the flame conditions and the targeted accuracy.

3.4.3. Nitric oxides

Concerning industrial applications, one of the main advantages of oxy-fuel combustion is the potential reduction of NO_x emissions. Supplying pure fuel and oxidizer is not economically viable. Instead, reactant streams generally contain a few percents of nitrogen, and other trace species to reduce the production costs. Air leakages might also occur in the process and let some nitrogen into the reactant streams. The impact of those few percents of nitrogen in oxy-fuel flames has been widely investigated in the view of the NO_x emissions in various flame conditions [*Breussin* 2000, *Beltrame* 2001, *Ditaranto* 2001, *Liu* 2001, *Tan* 2002, *Kim* 2007b, *Park* 2007, *Hjartstam* 2009, *Krishnamurthy* 2009, *Seepana* 2009].

Most cited authors agree that even a small amount of nitrogen in oxy-fuel at high oxygen contents in the oxygen can lead to considerable levels of NO_x due to the thermal mechanism (Zeldovich), dominant at high temperatures. Inversely, the dilution with CO_2 can lead to NOx emissions far below those from comparable air-fired conditions. Through its chemical effects, CO_2 reduces the formation and destruction of NO_x through the Fenimore mechanism and decreases the NO_x formation through the thermal mechanism [*Park* 2007].

4. INVESTIGATED FLAMES

4.1. Scope

The aim of the PhD work is to experimentally investigate turbulent CO_2-diluted non-premixed oxy-fuel jet flames using laser Raman scattering (LRS). Ideally, the fuel should be close to the Norwegian-like natural gas, composed of ca. 92 % methane, 6 % various hydrocarbons, 1.5 % nitrogen and less than 1 % carbon dioxide, in export pipelines from Norway to southern Europe [*NTNU* 2004]. Since quantitative LRS in combustion is only achievable with small molecules (less than 6 atoms [*Eckbreth* 1996]), the fuel can ideally be simplified to pure methane. Hydrogen is also used as a fuel in the present investigation, as it brings interesting features for fundamentals on CO_2-diluted oxy-fuel combustion. Results from LRS can provide great insights into the flame structure and main differences with conventional air-fired combustion. Furthermore, the creation of data library on the studied flames is of great interest for validation of turbulent combustion models, or optimization of existing ones to oxy-fuel combustion.

4.2. Limitations from the soot levels

As detailed in Section 3.2.3, turbulent non-premixed CH_4 – O_2/CO_2 jet flames may generate relatively high levels of soot using a coflow burner. The level of soot is sufficiently high, so that laser-induced fluorescence (LIF) from soot precursors and hydrocarbons appears on Raman spectra. LIF interference mainly arises from the C_2 Swan band system and also occurs in near-sooting, rich flame zones. The phenomenon stands for one of the greatest limitations of LRS techniques in non-premixed flames [*Dibble* 1987, *Dibble* 1990, *Eckbreth* 1996, *Dreyer* 2004]. Spontaneous chemi-luminescence emission of excited C_2* (not laser-induced) also contributes to interferences in the same spectral region.

Using a 532-nm laser beam, the resonance of the vibrational system of C_2 Swan bands leads to two strong peaks at ca. 510 and 560 nm on the spectra (cf. Figure I.20 and Figure II.3). In non-premixed methane flames, the intensity of the bands may be up to several orders of magnitude higher than the Raman bands of the main flames species and saturate the whole spectra. Methane can be diluted with hydrogen to reduce the content of hydrocarbon species and mitigate the issue. Figure I.20 shows two averaged

Raman spectra. The top one has been recorded in a transitional non-premixed H_2/CH_4 – O_2/CO_2 jet flame at z/d = 3, and the bottom one, in the post-flame region of a non-sooting laminar premixed $CH_4/O_2/CO_2$ flat flame. In the top one, the two C_2 Swan bands dominate the spectrum, while none of them appears in the post-flame region of the premixed flat flame for comparison. Considering the fuel dilution with 70 $\%_{mol}$ H_2, the C_2 Swan band at ca. 560 nm still displays a non-negligible cross-talk onto the two CO_2 peaks but can be partly corrected during data-processing. Another main limitation from the C_2 Swan bands is that their overall intensity increases with the axial distance from the fuel nozzle, since more and more carbon compounds are formed. Consequently, LRS investigations in non-premixed flames are generally limited to the near-field.

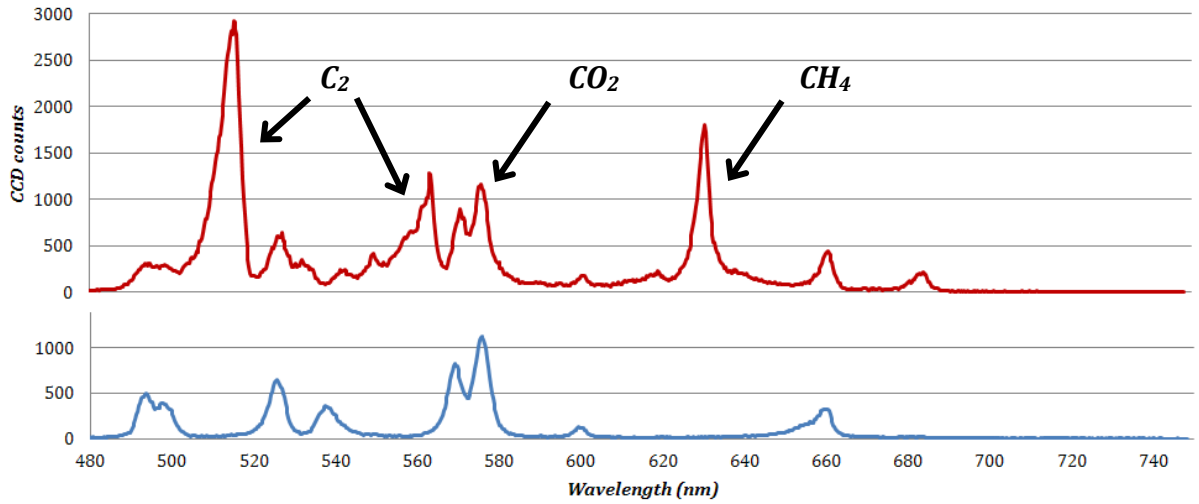

Figure I.20: Averaged Raman spectra. Top: flame region of a transitional non-premixed jet flame (fuel: 70 $\%_{mol}$ H_2 / 30 $\%_{mol}$ CH_4 – oxidizer: 35 $\%_{mol}$ O_2 / 65 $\%_{mol}$ CO_2). Bottom: post-flame region of a laminar premixed $CH_4/O_2/CO_2$ flat flame (PF-CH_4-OF-0.5-35, cf. Table III.2).

Since the species inducing C_2 LIF signals are not quantified by LRS, the correction is generally tedious. The soot level is especially linked to the high local concentrations of methane creating fuel-rich zones. A better mixing of the reactants with a swirl burner, for instance, would significantly reduce the local soot levels [*Kutne* 2011]. Nevertheless, the purpose is to use a coflow burner, due its simple geometry and to complete previous experimental datasets with a similar burner at SINTEF/NTNU [*Ditaranto* 2011].

4.3. Determination and role of each flame

In order to enrich the investigation and improve the knowledge on CO_2-diluted oxy-fuel flames, various types of flames have been studied. Figure I.21 gives an overview of the flames selected for the investigation and the way they are linked together. The main advantage of using different types of flames is to decouple the different features found in typical industrial turbulent flames. For each type of flames,

parametric studies have been carried out to highlight the characteristics features of oxy-fuel flames.

Laminar premixed flat flames have been achieved using a Hencken burner to isolate the effects of chemical processes in oxy-fuel combustion. They are naturally more stable than non-premixed jet flames, and allow varying the oxygen content in the oxidizer over a wide range. Only the post-flame zone is measured. As illustrated in Figure I.21, laminar premixed $CH_4/O_2/CO_2$ flat flames provide information on specific chemical processes from oxy-CH_4 flames. They can also be compared to laminar premixed CH_4-air flat flames to emphasize their particularities. Laminar premixed $H_2/O_2/CO_2$ flat flames have also been performed. They have not been compared to similar air-fired conditions since hydrogen/air flames are hardly visible and their stability could not be confidently monitored. The main interest of using H_2 as a fuel in CO_2-diluted oxy-fuel flames is to isolate the participation of CO_2 in the chemical processes (cf. Section 3.4.1). For both types of flames, a parametric study has been carried out by varying the oxygen content in the oxidizer and by varying the equivalence ratio. Note that premixed oxy-fuel flat flames have mostly been performed in fuel-lean conditions to reduce the levels of soot and prevent flames to be attached to the Hencken burner.

LRS measurements in transitional non-premixed CO_2-diluted oxy-H_2 jet flames have been performed and have provided great results on the specific flame structure and mixing effects. Similar air-fired flames have been measured by LRS for comparison. The main objective with these flames is to isolate the effects of the CO_2-dilution on the mixing processes by comparing them with measurements in similar air-fired conditions and in non-reacting jets. The parametric study of the flames has been carried out by varying the oxygen content in the oxidizer.

Turbulent non-premixed CO_2-diluted oxy-fuel jet flames using a varying mixture of methane and hydrogen have been achieved at SNL. The higher maturity of the diagnostic setup and the fuel dilution by H_2 have enabled to overcome the issue related to local soot levels. The main interest of such flames is to study the interaction between turbulence and chemical processes. The parametric study of the flames has been carried out through two parameters: jet Reynolds number and fuel dilution by hydrogen.

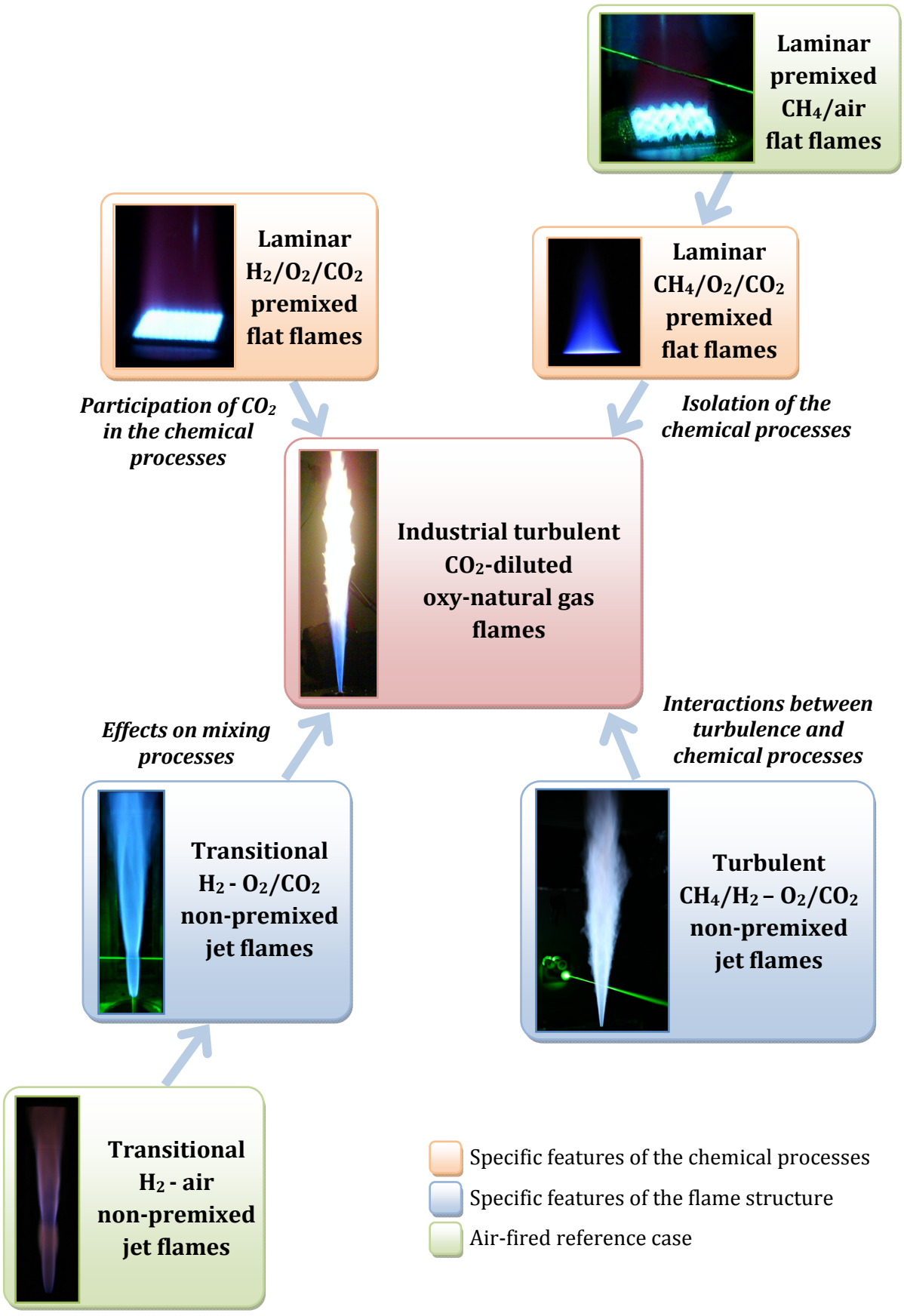

Figure I.21: Role of the different investigated flames.

SUMMARY OF PART I

The focus of Part I is set on providing the required background of the present PhD work to better understand the issues at stake and the different features found in oxy-fuel flames.

Motivations

In the context of the global energy policy on CO_2 emissions, CCS technologies are expected to contribute to ca. 20 % of the mitigation of CO_2 emissions by 2050. Among the CCS technologies, oxy-fuel combustion firing natural gas develops a growing industrial interest and is still relatively unexplored.

Fundamentals of combustion

Definitions and observations have been gathered as a recommended reading before apprehending the following investigation of oxy-fuel flames. Typical flame structures have been described, with a particular focus on laminar premixed flat flames and non-premixed flames.

CO_2-diluted oxy-fuel flames

The main features of CO_2-diluted oxy-fuel flames reported in the available literature have been summarized. The major differences with air-fired conditions have been highlighted.

- CO_2-diluted oxy-fuel flames offer a supplementary degree of freedom compared to air-fuel flames, through the oxygen content in the oxidizer.

- More than $21\%_{vol}$ O_2 is generally required to achieve air-flame like stability, due to the quenching effects of CO_2.

- While increasing the O_2 content on the oxidizer, the flame length of non-premixed jet flames decreases and the flame region shifts towards the inner fuel jet.

- The soot inception rate increases with the oxygen content in the oxidizer and can lead to higher levels than in air-fired conditions.

- The level of thermal radiation increases with the oxygen content in the oxidizer, up to reaching overall levels higher than in comparable air-fired conditions.

- The overall level of spontaneous flame luminosity increases with the oxygen content in the oxidizer, up to reaching overall levels higher than in comparable air-fired conditions. The trend is especially dominated by emissions from soot black body and OH* and CO_2* chemiluminescence bands.

- The flame speed increases with the oxygen content in the oxidizer, while the CO_2 dilution achieves the opposite effect.

- As the flame temperature increases with the oxygen content in the oxidizer, the local kinematic viscosity increases, leading to higher degree of laminarisation of the flame zone.

- CO_2 participates to the chemical processes, notably yielding higher local CO levels than in similar air-fired conditions. Local CO levels tend to increase with the oxygen content in the oxidizer, through the higher flame temperatures.

- As the flame temperature increases with the oxygen content in the oxidizer, the radical pool takes a larger share of the composition of the reacting mixture, generally higher than in similar air-fired conditions.

- Considering a few percents of nitrogen in CO_2-diluted reacting mixtures, NO_x levels are found far below those in comparable air-fired conditions.

Investigated flames

- The investigated flames have been selected relatively to their relevance to the study of oxy-fuel flames and their feasibility with the LRS diagnostics.

- The analysis of different types of oxy-fuel flames enable to decouple the different features found in typical industrial turbulent flames, such as features related to specific chemical processes or flame structures.

- The four different types of CO_2-diluted oxy-fuel flames investigated in the present PhD work by parametric study are as follows:
    - Laminar $CH_4/O_2/CO_2$ premixed flat flames

- Laminar $H_2/O_2/CO_2$ premixed flat flames
- Transitional H_2 - O_2/CO_2 non-premixed jet flames
- Turbulent H_2/CH_4 - O_2/CO_2 non-premixed jet flames

References

[*Agrawal* 2005] *Effects of buoyancy on transitional hydrogen gas-jet diffusion flames*, Agrawal, A.K., Albers B.W., and Alammar K.N. Combustion Science and Technology, 2005. 177(2): p. 305-322.

[*Amato* 2011] *Measurements and analysis of CO and O_2 emissions in $CH_4/CO_2/O_2$ flames*, Amato, A., Hudak B., D'Souza P., D'Carlo P., Noble D., Scarborough D., Seitzman J., and Lieuwen T. Proceedings of the Combustion Institute, 2011. 33(2): p. 3399-3405.

[*Barlow* 2005] *Piloted methane/air jet flames: Transport effects and aspects of scalar structure*, Barlow, R.S., Frank J.H., Karpetis A.N., and Chen J.Y. Combustion and Flame, 2005. 143(4): p. 433-449.

[*Baukal* 1997] *Oxygen-enhanced/natural gas flame radiation*, Baukal, C.E. and Gebhart B. International Journal of Heat and Mass Transfer, 1997. 40(11): p. 2539-2547.

[*Becker* 1983] *Soot Emission, Thermal-Radiation, and Laminar Instability of Acetylene Diffusion Flames*, Becker, H.A. and Liang D. Combustion and Flame, 1983. 52(3): p. 247-256.

[*Beltrame* 2001] *Soot and NO formation in methane-oxygen enriched diffusion flames*, Beltrame, A., Porshnev P., Merchan-Merchan W., Saveliev A., Fridman A., Kennedy L.A., Petrova O., Zhdanok S., Amouri F., and Charon O. Combustion and Flame, 2001. 124(1-2): p. 295-310.

[*Bilger* 1977] *Reaction-Rates in Diffusion Flames*, Bilger, R.W. Combustion and Flame, 1977. 30(3): p. 277-284.

[*Bilger* 1990] *On Reduced Mechanisms for Methane Air Combustion in Nonpremixed Flames*, Bilger, R.W., Starner S.H., and Kee R.J. Combustion and Flame, 1990. 80(2): p. 135-149.

[*Bockhorn* 1994] *Soot formation in combustion: mechanisms and models*. Bockhorn, H. 1994, Springer-Verlag - 596 pp.

[*Bolland* 1992] *New Concepts for Natural-Gas Fired Power-Plants Which Simplify the Recovery of Carbon-Dioxide*, Bolland, O. and Saether S. Energy Conversion and Management, 1992. 33(5-8): p. 467-475.

[*Bolland* 1998] *Comparison of two CO_2 removal options in combined cycle power plants*, Bolland, O. and Mathieu P. Energy Conversion and Management, 1998. 39(16-18): p. 1653-1663.

[*BP* 2011] *BP Statistical Review of World Energy, June 2011*, BP. 2011.

[*Bradley* 1985] *The oxidation of graphite powder in flame reaction zones*, Bradley, D., Dixon-Lewis G., El-din Habik S., and Mushi E.M.J. Symposium (International) on Combustion, 1985. 20(1): p. 931-940.

[*Bredesen* 2004] *High-temperature membranes in power generation with CO_2 capture*, Bredesen, R., Jordal K., and Bolland A. Chemical Engineering and Processing, 2004. 43(9): p. 1129-1158.

[*Breussin* 2000] *Computing of Oxy-Natural Gas Flames using Both a Global Combustion Scheme and a Chemical Equilibrium Procedure*, Breussin, F., Lallemant N., and Weber R. Combustion Science and Technology, 2000. 160(1): p. 369-397.

[*Buhre* 2005] *Oxy-fuel combustion technology for coal-fired power generation*, Buhre, B.J.P., Elliott L.K., Sheng C.D., Gupta R.P., and Wall T.F. Progress in Energy and Combustion Science, 2005. 31(4): p. 283-307.

[*Burdyny* 2010] *Hybrid membrane/cryogenic separation of oxygen from air for use in the oxy-fuel process*, Burdyny, T. and Struchtrup H. Energy, 2010. 35(5): p. 1884-1897.

[*Chen* 1986] *Visualization of Jet Flames*, Chen, L.D. and Roquemore W.M. Combustion and Flame, 1986. 66(1): p. 81-86.

[*Choi* 2009] *Structure of the edge flame in a methane-oxygen mixing layer*, Choi, S.K., Kim J., Chung S.H., and Kim J.S. Combustion Theory and Modelling, 2009. 13(1): p. 39-56.

[*Cieutat* 2009] *The Oxy-combustion burner development for the CO_2 pilot at Lacq*, Cieutat, D., Sanchez-Molinero I., Tsiava R., Recourt P., Aimard N., and Prebende C. Greenhouse Gas Control Technologies 9, 2009. 1(1): p. 519-526.

[*CO2CRC* 2012] *CCS facilities.* CO2CRC. Accessed on May 23rd, 2012; http://www.co2crc.com.au/imagelibrary3/general.php.

[*Coppens* 2008] *The effects of enrichment by H_2 on propagation speeds in adiabatic flat and cellular premixed flames of CH_4+O_2+CO_2*, Coppens, F.H.V. and Konnov A.A. Fuel, 2008. 87(13-14): p. 2866-2870.

[*Czakiert* 2006] *Fuel conversion from oxy-fuel combustion in a circulating fluidized bed*, Czakiert, T., Bis Z., Muskala W., and Nowak W. Fuel Processing Technology, 2006. 87(6): p. 531-538.

[*De Leo* 2007] *OH and CH luminescence in opposed flow methane oxy-flames*, De Leo, M., Saveliev A., Kennedy L.A., and Zelepouga S.A. Combustion and Flame, 2007. 149(4): p. 435-447.

[*Delichatsios* 1993] *Transition from momentum to buoyancy-controlled turbulent jet diffusion flames and flame height relationships*, Delichatsios, M.A. Combustion and Flame, 1993. 92(4): p. 349-364.

[*Dibble* 1987] *The Spontaneous Raman-Scattering Technique Applied to Nonpremixed Flames of Methane*, Dibble, R.W., Masri A.R., and Bilger R.W. Combustion and Flame, 1987. 67(3): p. 189-206.

[*Dibble* 1990] *An Improved Method of Data Aquisition and Reduction for Laser Raman-Rayleigh and Fluorescence Scattering from Multispecies*, Dibble, R.W., Starner S.H., Masri A.R., and Barlow R.S. Applied Physics B-Photophysics and Laser Chemistry, 1990. 51(1): p. 39-43.

[*Ditaranto* 2001] *Structural aspects of coaxial oxy-fuel flames*, Ditaranto, M., Sautet J.C., and Samaniego J.M. Experiments in Fluids, 2001. 30(3): p. 253-261.

[*Ditaranto* 2006] *Combustion instabilities in sudden expansion oxy-fuel flames*, Ditaranto, M. and Hals J. Combustion and Flame, 2006. 146(3): p. 493-512.

[*Ditaranto* 2011] *Radiative heat flux characteristics of methane flames in oxy-fuel atmospheres*, Ditaranto, M. and Oppelt T. Experimental Thermal and Fluid Science, 2011. 35(7): p. 1343-1350.

[*Drake* 1982] *Raman measurements and conserved scalar modeling in turbulent diffusion flames*, Drake, M.C., Bilger R.W., and Stårner S.H. Proceedings of the Combustion Institute, 1982. 19: p. 459-467.

[*Dreyer* 2004] *Raman scattering at 532 and 355 nm in atmospheric pressure propane/air flames, with and without liquid fuels*, Dreyer, C., Parker T., and Linne M.A. Applied Physics B: Lasers and Optics, 2004. 79(1): p. 121-130.

[*Eckbreth* 1996] *Laser Diagnostics for Combustion Temperature and Species*, Eckbreth, A.C. 1996: Gordon and Breach Publishers.

[*Eickhoff* 1989] *Azimuthal instability in jet diffusion flames*, Eickhoff, H., Winandy A., and Natarajan R. Experiments in Fluids, 1989. 7(6): p. 420-421.

[*Frassoldati* 2009] *Simplified kinetic schemes for oxy-fuel combustion* Frassoldati, A., Cuoci A., Faravelli T., Ranzi E., Candusso C., and Tolazzi D. 1st International Conference on Sustainable Fossil Fuels for Future Energy – S4FE 2009 2009.

[*GCP* 2011] *Global Carbon Project (2011) Carbon budget and trends 2010.* GCP. Released on December 4th, 2011; www.globalcarbonproject.org/carbonbudget.

[*Glarborg* 2008] *Chemical effects of a high CO_2 concentration in oxy-fuel combustion of methane*, Glarborg, P. and Bentzen L.L.B. Energy & Fuels, 2008. 22(1): p. 291-296.

[*Glassman* 1989] *Soot formation in combustion processes*, Glassman, I. Symposium (International) on Combustion, 1989. 22(1): p. 295-311.

[*Grant* 1975] *Low-frequency diffusion flame oscillations*, Grant, A.J. and Jones J.M. Combustion and Flame, 1975. 25(0): p. 153-160.

[*Heil* 2011] *Experimental investigation on the effect of O_2 and CO_2 on burning rates during oxyfuel combustion of methane*, Heil, P., Toporov D., Forster M., and Kneer R. Proceedings of the Combustion Institute, 2011. 33: p. 3407-3413.

[*Hjartstam* 2009] *Combustion characteristics of lignite-fired oxy-fuel flames*, Hjartstam, S., Andersson K., Johnsson F., and Leckner B. Fuel, 2009. 88(11): p. 2216-2224.

[*Hottel* 1949] *Diffusion in laminar flame jets*, Hottel, H.C. and Hawthorne W.R. Symposium on Combustion and Flame, and Explosion Phenomena, 1949. 3(1): p. 254-266.

[*IEA* 2009] *International Energy Agency: Technology Roadmaps - Carbon Capture and Storage, 2009*, IEA. 2009.

[*IPCC* 2007] *Climate Change 2007: The Physical Science Basis. Contribution of Working Group I to the Fourth Assessment Report of the Intergovernmental Panel on Climate Change*, IPCC, Solomon S., Qin M.M., D., Chen Z., Marquis M., Averyt K.B., Tignor M., and Miller H.L. 2007.

[*Ju* 1998] *Effects of radiative emission and absorption on the propagation and extinction of premixed gas flames*, Ju, Y., Masuya G., and Ronney P.D. Symposium (International) on Combustion, 1998. 27(2): p. 2619-2626.

[*Katta* 1993] *Role of inner and outer structures in transitional jet diffusion flame*, Katta, V.R. and Roquemore W.M. Combustion and Flame, 1993. 92(3): p. 274-282.

[*Kim* 2006] *Emission characteristics of the 0.03 MW oxy-fuel combustor*, Kim, H.K., Kim Y., Lee S.M., and Ahn K.Y. Energy & Fuels, 2006. 20(5): p. 2125-2130.

[*Kim* 2007a] *Studies on combustion characteristics and flame length of turbulent oxy-fuel flames*, Kim, H.K. and Kim Y. Energy & Fuels, 2007a. 21(3): p. 1459-1467.

[*Kim* 2007b] *NO reduction in 0.03-0.2 MW oxy-fuel combustor using flue gas recirculation technology*, Kim, H.K., Kim Y., Lee S.M., and Ahn K.Y. Proceedings of the Combustion Institute, 2007b. 31: p. 3377-3384.

[*Krishnamurthy* 2009] *Studies on low-intensity oxy-fuel burner*, Krishnamurthy, N., Paul P.J., and Blasiak W. Proceedings of the Combustion Institute, 2009. 32(2): p. 3139-3146.

[*Kumfer* 2008] *Soot inception limits in laminar diffusion flames with application to oxy-fuel combustion*, Kumfer, B.M., Skeen S.A., and Axelbaum R.L. Combustion and Flame, 2008. 154(3): p. 546-556.

[*Kutne* 2011] *Experimental Analysis of the Combustion Behaviour of Oxyfuel Flames in a Gas Turbine Model Combustor*, Kutne, P., Kapadia B.K., Meier W., and Aigner M. Proceedings of the Combustion Institute, 2011. 33(2): p. 3383-3390.

[*Law* 1993] *A Compilation of Experimental Data on Laminar Burning Velocities*, Law, C., N. Peters and B. Rogg, Editors. 1993, Springer Berlin / Heidelberg. p. 15-26.

[*Lee* 2000] *Soot formation effects of oxygen concentration in the oxidizer stream of laminar coannular nonpremixed methane/air flames*, Lee, K.O., Megaridis C.M., Zelepouga S., Saveliev A.V., Kennedy L.A., Charon O., and Ammouri F. Combustion and Flame, 2000. 121(1-2): p. 323-333.

[*Li* 2011] *Technologies for increasing CO_2 concentration in exhaust gas from natural gas-fired power production with post-combustion, amine-based CO2 capture*, Li, H.L., Ditaranto M., and Berstad D. Energy, 2011. 36(2): p. 1124-1133.

[*Linow* 2002] *Measurement of temperature and concentration in oxy-fuel flames by Raman/Rayleigh spectroscopy*, Linow, S., Dreizler A., Janicka J., and Hassel E.P. Measurement Science & Technology, 2002. 13(12): p. 1952-1961.

[*Liu* 2012] *Characteristics of oxy-fuel combustion in gas turbines*, Liu, C.Y., Chen G., Sipöcz N., Assadi M., and Bai X.S. Applied Energy, 2012. 89(1): p. 387-394.

[*Liu* 2003] *The chemical effect of CO_2 replacement of N_2 in air on the burning velocity of CH_4 and H_2 premixed flames*, Liu, F., Guo H., and Smallwood G.J. Combustion and Flame, 2003. 133(4): p. 495-497.

[*Liu* 2001] *The chemical effects of carbon dioxide as an additive in an ethylene diffusion flame: Implications for soot and NOx formation*, Liu, F.S., Guo H.S., Smallwood G.J., and Gulder O.L. Combustion and Flame, 2001. 125(1-2): p. 778-787.

[*Lupion* 2011] *CIUDEN CCS Project: Status of the CO_2 capture technology development plant in power generation*, Lupion, M., Diego R., Loubeau L., and Navarrete B. Energy Procedia, 2011. 4(0): p. 5639-5646.

[*Masri* 1992] *Chemical Kinetic Effects in Nonpremixed Flames of H_2/CO_2 Fuel*, Masri, A.R., Dibble R.W., and Barlow R.S. Combustion and Flame, 1992. 91(3-4): p. 285-309.

[*McAllister* 2011] *Fundamentals of Combustion Processes*. McAllister, S., Chen J.Y., and Fernandez-Pello A.C. 2011, Springer Science+Business Media, LLC 2011.

[*Meier* 2000] *Raman/Rayleigh/LIF measurements in a turbulent $CH_4/H_2/N_2$ jet diffusion flame: Experimental techniques and turbulence-chemistry interaction*, Meier, W., Barlow R.S., Chen Y.L., and Chen J.Y. Combustion and Flame, 2000. 123(3): p. 326-343.

[*Metz* 2005] *IPCC, 2005: IPCC Special Report on Carbon Dioxide Capture and Storage. Prepared by Working Group III of the Intergovernmental Panel on Climate Change.*, Metz, B., Davidson O., De Coninck H., Loos M., and Meyer L. 2005.

[*Mungal* 1989] *Visual observations of a turbulent diffusion flame*, Mungal, M.G. and O'Neil J.M. Combustion and Flame, 1989. 78(3–4): p. 377-389.

[*Mungal* 1991] *The Visible Structure of Turbulent Jet Diffusion Flames - Large-Scale Organization and Flame Tip Oscillation*, Mungal, M.G., Karasso P.S., and Lozano A. Combustion Science and Technology, 1991. 76(4-6): p. 165-185.

[*Naik* 2002] *Quantitative laser-saturated fluorescence measurements of nitric oxide in counter-flow diffusion flames under sooting oxy-fuel conditions*, Naik, S.V. and Laurendeau N.M. Combustion and Flame, 2002. 129(1-2): p. 112-119.

[*NTNU* 2004] *Composition of Natural Gas in Export Pipelines From Norway to Continental Europe and United Kingdom in 2004.* NTNU. Accessed on May 12th, 2012; http://www.ipt.ntnu.no/~jsg/undervisning/naturgass/GasCompositionExamplesTransport.pdf.

[*Oh* 2006] *The effect of oxygen and carbon dioxide concentration on soot formation in non-premixed flames*, Oh, K.C. and Shin H.D. Fuel, 2006. 85(5-6): p. 615-624.

[*Park* 2007] *NO emission behavior in oxy-fuel combustion recirculated with carbon dioxide*, Park, J., Park J.S., Kim H.P., Kim J.S., Kim S.C., Choi J.G., Cho H.C., Cho K.W., and Park H.S. Energy & Fuels, 2007. 21(1): p. 121-129.

[*Plasynski* 2009] *Progress and New Developments in Carbon Capture and Storage*, Plasynski, S.I., Litynski J.T., McIlvried H.G., and Srivastava R.D. Critical Reviews in Plant Sciences, 2009. 28(3): p. 123-138.

[*Reaction-Design* 2008] *CHEMKIN-PRO*, Reaction-Design. 2008: San Diego, 2008.

[*Renard* 2000] *Dynamics of flame/vortex interactions*, Renard, P.H., Thévenin D., Rolon J.C., and Candel S. Progress in Energy and Combustion Science, 2000. 26(3): p. 225-282.

[*Richards* 2005] *CO_2 and H_2O diluted oxy-fuel combustion for zero-emission power*, Richards, G.A., Casleton K.H., and Chorpening B.T. Proceedings of the Institution of Mechanical Engineers Part a-Journal of Power and Energy, 2005. 219(A2): p. 121-126.

[*Ruan* 2001] *Combined effects of nongray radiation and pressure on premixed $CH_4/O_2/CO_2$ flames*, Ruan, J., Kobayashi H., Niioka T., and Ju Y. Combustion and Flame, 2001. 124(1–2): p. 225-230.

[*Samaniego* 1995] *CO_2* Chemiluminescence in Premixed Flames*, Samaniego, J.M., Egolfopoulos F.N., and Bowman C.T. Combustion Science and Technology, 1995. 109: p. pp. 183-203.

[*Sautet* 2001] *Length of natural gas-oxygen non-premixed flames*, Sautet, J.C., Salentey L., Ditaranto M., and Samaniego J.M. Combustion Science and Technology, 2001. 166: p. 131-150.

[*Scholefield* 1949] *The structure and stability of diffusion flames*, Scholefield, D.A. and Garside J.E. Symposium on Combustion and Flame, and Explosion Phenomena, 1949. 3(1): p. 102-110.

[*Seepana* 2009] *Flame structure and NO generation in oxy-fuel combustion at high pressures*, Seepana, S. and Jayanti S. Energy Conversion and Management, 2009. 50(4): p. 1116-1123.

[*Seepana* 2012] *Flame structure investigations of oxy-fuel combustion*, Seepana, S. and Jayanti S. Fuel, 2012. 93(0): p. 52-58.

[*Shtork* 2008] *On the identification of helical instabilities in a reacting swirling flow*, Shtork, S.I., Vieira N.F., and Fernandes E.C. Fuel, 2008. 87(10–11): p. 2314-2321.

[*SINTEF* 2012] *BIGCO2 Project.* SINTEF. Accessed on May 21st, 2012; http://www.sintef.no/Projectweb/BIGCO2/.

[*Skeen* 2009] *Characteristics of non-premixed oxygen-enhanced combustion: I. The presence of appreciable oxygen at the location of maximum temperature*, Skeen, S.A., Yablonsky G., and Axelbaum R.L. Combustion and Flame, 2009. 156(11): p. 2145-2152.

[*Smith* 1995] *Laser Raman-Scattering Measurements of Differential Molecular-Diffusion in Turbulent Nonpremixed Jet Flames of H_2/CO_2 Fuel*, Smith, L.L., Dibble R.W., Talbot L., Barlow R.S., and Carter C.D. Combustion and Flame, 1995. 100(1-2): p. 153-160.

[*Stöhr* 2012] *Experimental study of vortex-flame interaction in a gas turbine model combustor*, Stöhr, M., Boxx I., Carter C.D., and Meier W. Combustion and Flame, 2012(0).

[*Takagi* 1980] *Local laminarization in turbulent diffusion flames*, Takagi, T., Shin H.-D., and Ishio A. Combustion and Flame, 1980. 37(0): p. 163-170.

[*Takagi* 1981] *Properties of turbulence in turbulent diffusion flames*, Takagi, T., Shin H.-D., and Ishio A. Combustion and Flame, 1981. 40(0): p. 121-140.

[*Takahashi* 1982] *Transition from laminar to turbulent free jet diffusion flames*, Takahashi, F., Mizomoto M., and Ikai S. Combustion and Flame, 1982. 48(0): p. 85-95.

[*Takahashi* 1996] *Vortex-flame interactions and extinction in turbulent jet diffusion flames*, Takahashi, F., Schmoll W.J., Trump D.D., and Goss L.P. Symposium (International) on Combustion, 1996. 26(1): p. 145-152.

[*Takeno* 1994] *Transition and structure of jet diffusion flames*, Takeno, T. Symposium (International) on Combustion, 1994. 25(1): p. 1061-1073.

[*Tan* 2002] *CO_2 capture using oxygen enhanced combustion strategies for natural gas power plants*, Tan, Y., Douglas M.A., and Thambimuthu K.V. Fuel, 2002. 81(8): p. 1007-1016.

[*Toftegaard* 2010] *Oxy-fuel combustion of solid fuels*, Toftegaard, M.B., Brix J., Jensen P.A., Glarborg P., and Jensen A.D. Progress in Energy and Combustion Science, 2010. 36(5): p. 581-625.

[*Tranier* 2011] *Air Separation, flue gas compression and purification units for oxy-coal combustion systems*, Tranier, J.P., Dubettier R., Darde A., and Perrin N. 10th International Conference on Greenhouse Gas Control Technologies, 2011. 4: p. 966-971.

[*Turns* 2000] *An Introduction to Combustion: Concepts and Applications*. Turns, S.R. Second edition ed., ed. M.s. McGraw-Hill Education, 2000 - 676 pp. 2000.

[*Veynante* 2002] *Turbulent combustion modeling*, Veynante, D. and Vervisch L. Progress in Energy and Combustion Science, 2002. 28(3): p. 193-266.

[*Warnatz* 2000] *Combustion*. Warnatz, J., Maas U., and Dibble R.W. Springer. Vol. 3rd Edition. 2000.

[*Yin* 2011] *Chemistry and radiation in oxy-fuel combustion: A computational fluid dynamics modeling study*, Yin, C., Rosendahl L.A., and Kær S.K. Fuel, 2011. 90(7): p. 2519-2529.

[*Yoda* 1994] *Instantaneous three-dimensional concentration measurements in the self-similar region of a round high-Schmidt-number jet*, Yoda, M., Hesselink L., and Mungal M.G. Journal of Fluid Mechanics, 1994. 279: p. p.313-350.

[*Zhu* 1989] *Experimental and numerical determination of laminar flame speeds of methane/(Ar, N_2, CO_2)-air mixtures as function of stoichiometry, pressure, and flame temperature*, Zhu, D.L., Egolfopoulos F.N., and Law C.K. Symposium (International) on Combustion, 1989. 22(1): p. 1537-1545.

PART II

DEVELOPMENT OF LASER RAMAN SCATTERING METHODS FOR OXY-FUEL FLAMES

INTRODUCTION OF PART II

The current project aims at investigating the structure of oxy-fuel flames. By structure, it is meant temperature field and major species concentrations within the flame. Experimentally, laser-based techniques are the most suitable measurement methods for this study. The main advantages, as listed in [*Eckbreth* 1996], are that these techniques are remote and non-intrusive, ideally adapted for application to recirculation zones, confined locations, and in situ measurements. They are also capable of simultaneous high spatial and temporal resolutions, and they do not reach upper temperature limits in their applicability since they are non-intrusive. Additionally, laser techniques are not limited to equilibrium situations, and hence, can be employed to diagnose non-equilibrium phenomena.

The present investigation mostly deals with the combustion of methane and hydrogen in an atmosphere composed of oxygen and carbon dioxide. The reacting molecules and those produced during the early steps of the combustion mainly consist of O_2, CO_2 H_2, CH_4 N_2, H_2O and CO. Therefore, the measurement of the main species concentration and temperatures tends to suit best to laser spectroscopic techniques such as laser Raman scattering techniques (LRS), as those molecules are all sensitive to Raman scattering.

The present chapter gathers definitions, information from the literature and personal observations about theory, applications, calibration, processing methods and limitations of the diagnostic technique. An explanation follows regarding the calibration and data-processing technique that were implemented. Then, a thorough description of the experimental setup used in Trondheim is given, with a particular accent on the combustion chamber design, capabilities of the main parts of the setup, signal optimization, level of uncertainties and safety considerations. Lastly, the setup used at Sandia National Laboratories is described with a focus on the motivations for the exchange, the experimental configuration, the level of uncertainties and the main differences with the setup designed at NTNU.

5. LASER RAMAN SCATTERING DIAGNOSTICS

5.1. Background on Laser Raman scattering diagnostics

5.1.1. Theory

In 1928, C. V. Raman and his student, K. S. Krishnan, brought into the light an inelastic scattering phenomenon, known as Raman scattering. The discovery granted him the Nobel Prize of Physics in 1930 [*Singh* 2002].

When light encounters certain molecules in the air, the most visible effect is the elastic mode of scattering, called Rayleigh scattering. Lord Rayleigh successfully showed this effect while attempting to explain the blue colour of the sky. Rayleigh scattering also enables to visualize a laser beam in the air when the laser output energy is sufficiently high. Raman scattering happens in similar conditions and is generally complicated to separate from the intense Rayleigh scattering, since it is several orders of magnitude weaker in intensity.

Figure II.1 shows the different changes in the energy level diagram occurring when a photon encounters a molecule. The photon interacts with the bonds and the cloud of electrons of the molecule, and generally excites the molecule to a virtual energy state. The molecule can then de-excite in three different ways:

- By releasing the energy elastically, which brings the molecule back to its initial energy state, giving the so-called Rayleigh scattering phenomenon. This phenomenon represents more than 99 % of the scattered light, which explains its high intensity compared to Raman scattering.

- By releasing only part of the energy while de-exciting to a higher vibrational state than the initial one, giving an inelastic phenomenon so-called Stokes Raman scattering. The resulting photon of lower energy generates then a Stokes line on the red side of the incident wavelength.

- By releasing slightly more energy while de-exciting to a lower vibrational state than the initial one, giving another inelastic phenomenon so-called Anti-Stokes

Raman scattering. The resulting photon is shifted towards the blue side of the spectrum.

For a given sample at thermal equilibrium, the relative number of molecules in states of different energies follows a Boltzmann distribution, so that most molecules populate the lowest energy states. Thus, within a given sample, elastic scattering events are more likely to happen than inelastic scattering events, inducing the strong Rayleigh signals compared to Raman signals. Based on the same assumption, Stokes Raman scattering events are more likely to happen than anti-Stokes Raman scattering events. Consequently, it is more convenient to monitor Stokes lines than anti-Stokes lines.

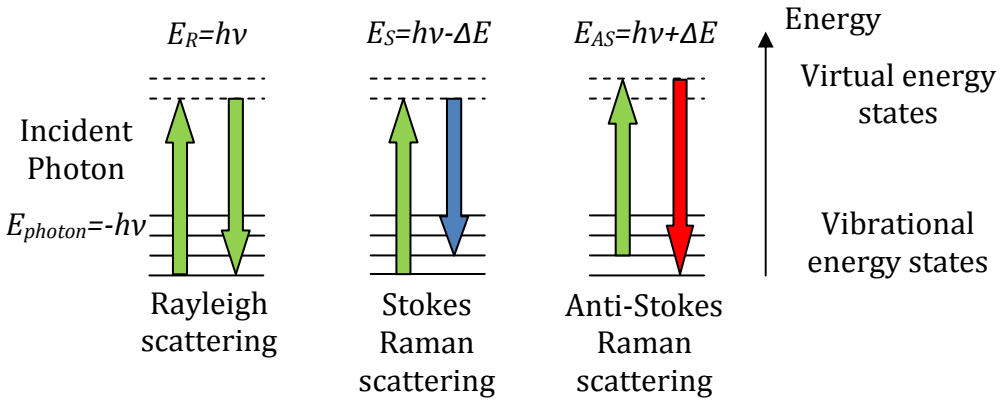

Figure II.1: Energy level diagram showing the three main scattering modes occuring when a molecule receives an incident photon (h is Planck's constant, ν is the light frequency).

The Raman sensitivity that induces the final intensity of the scattering is related to the molecular polarization potential of the molecules, i.e. the amount of deformation of the electron cloud. Each species has its own pattern of frequency shift induced by its coordinates for the vibrational and rotational states. Thus, for a given excitation wavelength emitted through a transparent optical medium, Raman scattering enables to identify the present species, as long as they are Raman active (by definition, all molecules made of two atoms or more).

The non-intrusive and remote characters of the laser-based techniques using Raman scattering enable measurements in extreme conditions. Applications using Raman spectroscopy are numerous: species identification in chemistry, respiratory gas mixtures control during surgery, planet characterisation in astronomy, crystal analysis in solid state physics, and monitoring scalar measurements in combustion, for instance. LRS is particularly adapted for measurements of major species (above 1 $\%_{mol}$ in the gas mixture) and temperatures in turbulent flames, though it is still limited to non-sooting conditions [*Eckbreth* 1996].

Mie scattering should also be mentioned. It corresponds to the scattered light from particles whose size is in the same range or larger than the excitation wavelength. Its intensity is a few orders of magnitude stronger than the intensity from Rayleigh

scattering. The presence of particles such as dusts or large soot particles in the gas phase is typically the source of Mie scattering signals.

5.1.2. Typical experimental setup and applications

LRS shows great advantages compared to any other laser diagnostic in combustion. First, the spectral response is shifted from the laser line and this response is inherent to each Raman active species. Thus, it is possible to identify on the spectra different Raman-active molecules, such as the most common small molecules found in hydrocarbon flames: CO_2, O_2, CO, N_2, CH_4, H_2O and H_2. Besides, Raman signals are linear with the species' number density and are not affected by collisional quenching. The temperature can be estimated using the ideal gas law once the number densities of the main species are known. However, Raman signals are generally so weak that they could suffer from any source of interferences. Therefore, the optical collection setup generally becomes quite complex to achieve a suitable detection of Raman signals.

Figure II.2 shows a typical laser Raman scattering setup. A laser system, usually with high output energy, emits a beam towards the test object. A focusing lens is placed on the trajectory to concentrate the laser energy in the probe volume. A camera coupled to a spectrometer records signals in a normal plan from the laser beam. Using an intensified camera generally compensates for the weakness of Raman signals at the expense of higher electronic noise.

A collection lens is used in front of the spectrometer to get a sharp focus of the probe volume at the slit of the spectrometer. A notch filter is placed between the probe volume and the spectrometer to reject the intense Rayleigh scattering. Laser output energy can also be continuously monitored if it significantly fluctuates over time.

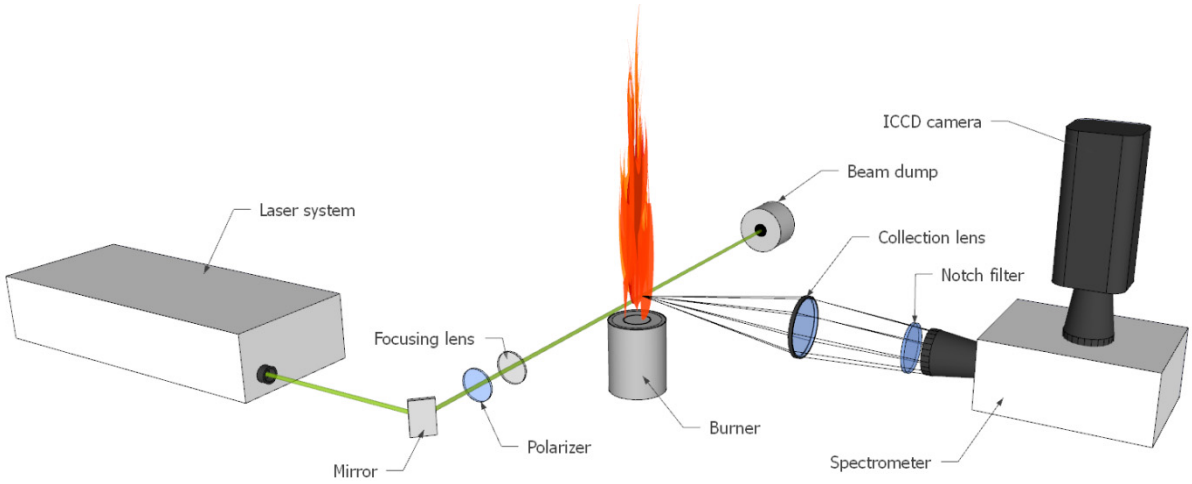

Figure II.2: Typical laser Raman scattering setup.

5.1.3. Limits

An investigation of the use of LRS techniques for gas turbine flames was carried out in [*Wehr* 2007]. The authors reported that it has not been used often, because of several difficulties. He listed the following as potential difficulties:

- For single-shot Raman measurements, high laser output energies in the order of 1 J/pulse are needed. With typical pulse durations from Nd:YAG or Excimer lasers of 10 ns, optical breakdowns or window damages pose a severe problem.

- Quantitative Raman measurements need calibration measurements over a large temperature range for all species to be detected. While this can be well arranged in unconfined flames, it is much harder in confined gas turbine configurations for large test rigs.

- In order to collect sufficient signal, a large solid angle of detection is necessary. However, large windows in the test rig are difficult to combine with high temperature combustion.

- It is difficult to keep the windows of the combustion chamber sufficiently clean, especially with sooty flames. The heat load onto the windows at high temperature and possible contaminations from supply lines make it hard to keep the windows and their coating clean and highly transparent. Window staining can lead to decreasing or non-uniform detection efficiency and/or damages by laser light absorption.

5.1.4. Background on calibration and data processing methods

Measured Raman signals are found to be dependent on the intensity of the incident laser beam, the chemical composition of the sample, the Raman cross-section of each species present in the sample, the sample pressure and temperature, the solid angle used by the collection system, the dispersion of the spectrograph, and the efficiency of the optical system. The scattered Raman power, Q_r, is defined in [*Eckbreth* 1996] using Eq. II.1 as follows:

$$Q_r = Q_1[N]\left(\frac{\partial\sigma}{\partial\Omega}\right)\Omega l\epsilon \qquad \textit{Eq. II.1}$$

With:

Q_1 Incident laser power

$[N]$ Number density of scattering species

$\left(\frac{\partial\sigma}{\partial\Omega}\right)$ Raman cross-section

Ω Scattering solid angle

l Probe length

ϵ Collection efficiency accounting for losses in optical collection system

To simplify the quantification of the scattered signals, consider a Stokes Raman signal integrated over the spectral region where Raman peaks from species *i* are found, giving the scattered Raman power Q_i. As adapted from an equation found in [*Eckbreth* 1996] and [*Dibble* 1990], Eq. II.2 is a general equation governing the behaviour of Raman signals.

$$Q_i = K_i Q_1 [N_i] f_i(T) \qquad \textit{Eq. II.2}$$

With:

K_i Factor dependent on vibrational Raman cross-section, wavelength, geometry, and optical collection efficiency. K_i is ultimately determined by calibration.

$[N_i]$ Number density of Raman active species *i*.

$f_i(T)$ Bandwidth factor accounting for temperature-dependent distribution of molecules in their allowed quantum states, depending on spectral location, shape and bandwidth of the detection system, laser beam profile and bandwidth.

Each molecule is identified by its own Raman shift from the incident wavelength depending on its Raman active bonds and polarizability. Raman shifts themselves are independent from the incident wavelength. Peak locations on spectra are found by subtracting Raman shift wave number from incident wave number, using Eq. II.3. Results are shown in Table II.1. Figure II.3 shows the variation of the vibrational Raman scattering with the laser wavelength using Eq. II.3. It can be seen that, at lower laser wavelength, Raman peaks would be closer to each other and, most likely, harder to distinguish. A benefit from a 532-nm exciting wavelength, as used in the present setup, is that the absorption lines of the C_2 Swan band system, inducing intense fluorescence signals when hydrocarbons are present, do not overlap with major species found in CO_2-diluted oxy-fuel flames [*Dibble* 1987]. More details on the determination of the Raman vibrational frequencies can be found in [*Eckbreth* 1996].

$$\frac{1}{\lambda_{Pi,j}} = \frac{1}{\lambda_L} - \nu_{i,j} \qquad \textit{Eq. II.3}$$

With:

$\lambda_{Pi,j}$ Wavelength corresponding to Raman peak of vibrational frequency *j* from species *i*

λ_L Incident laser wavelength

$\overline{\nu_{i,J}}$ Vibrational frequency *j* from species *i* (taken as the inverse of a length)

Table II.1: Raman vibrational frequencies and cross-sections, and peak locations on spectra corresponding to the major species seen in hydrocarbon flames using a 532-nm laser. [Eckbreth 1996]

Species	*Vibrational frequency (cm^{-1})*	*Vibrational cross-section at 532 nm ($10^{-30} cm^2/Sr$)*	*Peak wavelength on spectrum (nm)*
CO_2	ν_1: 1388	0.6	574.4
	$2\nu_2$: 1285	0.45	571.0
O_2	1556	0.65	580.0
CO	2145	0.48	600.5
N_2	2330.7	0.46	607.3
CH_4	ν_1: 2915	2.6	629.6
	ν_3: 3017	1.7	633.7
H_2O	3657	0.9	660.5
H_2	4160.2	0.94	683.2

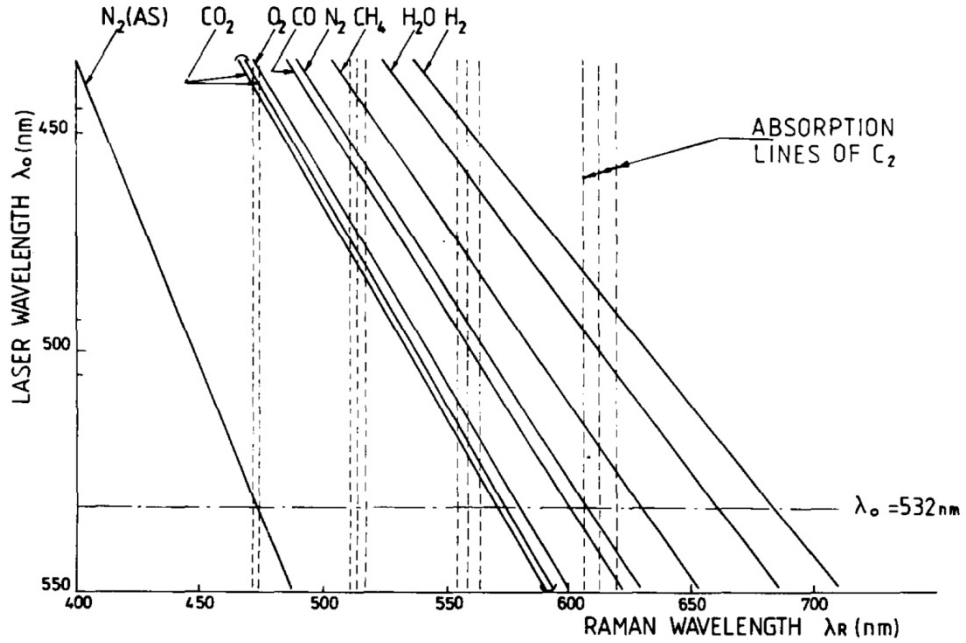

Figure II.3: Variation of the vibrational Raman scattering wavelengths for major hydrocarbons flames species with the laser wavelength. Dashed lines are the absorption bands of C_2. [Dibble 1987]

Optical systems generally operate a convolution leading to peaks on the spectrum which appear more dispersed than ideal Dirac-like peaks. Besides, as the distribution of the molecules populating different energy states is governed by a Boltzmann law, more molecules populating higher energy levels are found at higher temperatures. This leads to lower and more spread out peaks on the spectrum, since the number of populated energy states increases, but remains centred on the main Raman

shift. Peaks more remote from the one induced by the main Raman shift can also appear as more vibrational and rotational energy states get populated at higher temperatures. An example from air measurements can be seen in Figure II.4.

Cross-talk phenomena occur when signals from two Raman active species intersect and lead to unclear distinction between their spectral regions (see N_2 and O_2 at 1100 K in Figure II.4). For the reasons explained above, cross-talks are found to be temperature-dependent, and thus, require calibration over a wide temperature range to properly perform LRS in flames. This probably constitutes the most challenging aspect of LRS, since calibration and data processing methods cannot ignore those phenomena.

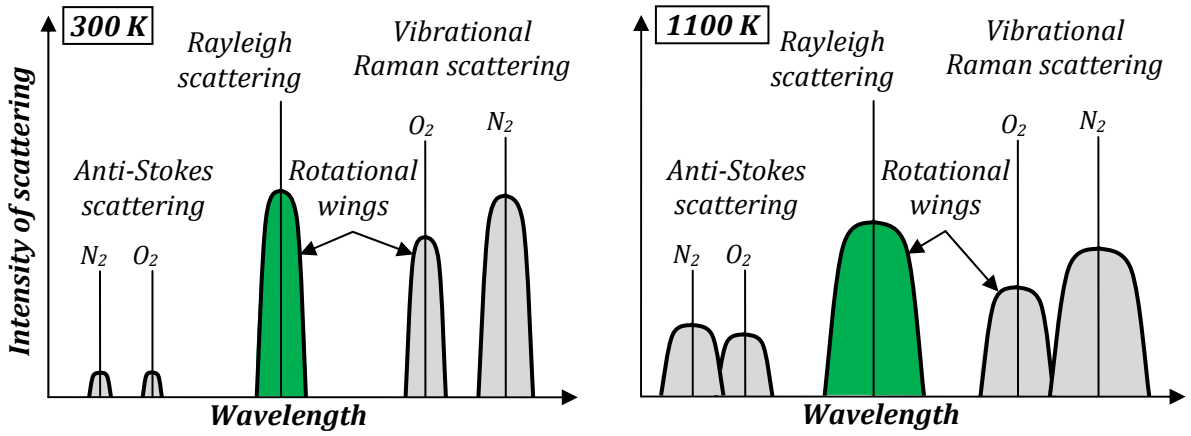

Figure II.4: Schematic of anti-Stokes, Rayleigh and Stokes signals from air measured at two different temperatures (left: 300 K, right: 1100 K). Adapted from [Chigier 1991].

5.1.5. Matrix formulation and matrix inversion method

The matrix formulation was first detailed in [*Dibble* 1990] and known as the Matrix Inversion method. More than a theory, this is the most common data processing method used so far with LRS. It is directly based on the Raman phenomenology governed by Eq. II.2. It relies on Raman signals, laser-induced fluorescence and background signals, integrated over fixed spectral regions to form a signal vector. The system takes into account the different cross-talks and can be solved as a linear equation requiring a matrix inversion providing the different species' number densities within the probe volume.

As described in [*Dibble* 1990], signals are integrated over well-defined spectral bandwidths, typically one per species. When species *j* has a cross-talk onto species *i*'s bandwidth, the contribution from species *j* can be handled as shown in Eq. II.4.

$$Q_{iC} = Q_i - k^*_{i \ll j} Q_j \qquad \text{Eq. II.4}$$

With:

Q_{iC}	Corrected intensity integrated over species *i*'s bandwidth
Q_i	Intensity integrated over species *i*'s bandwidth
$k^*_{i<<j}$	Temperature-dependent coefficient obtained by calibration
Q_j	Intensity integrated over species *j*'s bandwidth

A well calibrated system should then consider each contribution from one species to another. Those are induced either by spectral behaviour, or simply by bandwidth definition. Bandwidths are not overlapping but can be adjacent. The matrix formulation is a way to describe the system in only one equation taking into account all cross-talks and that can be solved linearly. Eq. II.5 is the proper formulation for such a system.

$$Q_i = \Sigma\, K_{i,j} Q_1[N_i] f_{i,j}(T) = \Sigma\, k_{i,j} Q_1[N_i] \qquad \textit{Eq. II.5}$$

Here, $k_{i,j}$ are the temperature-dependent coefficients that are to be defined by calibration and can be assembled in a square matrix with as many rows and columns as the number of observed species. Q and $[N]$ are vertical vectors with as many rows as the number of observed species. To simplify, Eq. II.5 can also be written as in Eq. II.6.

$$Q = K Q_1[N] \qquad \textit{Eq. II.6}$$

Figure II.5 shows a simple view of the matrix of calibration coefficients, that will be named matrix *K*. Notation $k_{j<<i}$ stands for the temperature-dependent Raman coefficient corresponding to the cross-talk from species *i* onto species *j*'s bandwidth. Matrix *K* has to be inversed to be solved in the linear system described by Eq. II.5. Therefore, diagonal coefficients (bold-faced in Figure II.1) should be non-zeros. Off-diagonal coefficients could be zeros if there is no cross-talk induced by quantum physics or system definition. Besides, all coefficients in matrix *K* should be positive to be physically realistic.

Contribution

Species' bandwidth

$$\begin{pmatrix}
\boldsymbol{k_1} & k_{1<<2} & \dots & k_{1<<i} & k_{1<<j} & \dots & k_{1<<N} \\
k_{2<<1} & \boldsymbol{k_2} & \dots & \dots & \dots & \dots & \dots \\
\dots & \dots & \dots & \dots & \dots & \dots & \dots \\
k_{i<<1} & \dots & \dots & \boldsymbol{k_i} & k_{i<<j} & \dots & k_{i<<N} \\
k_{j<<1} & \dots & \dots & k_{j<<i} & \boldsymbol{k_j} & \dots & k_{j<<N} \\
\dots & \dots & \dots & \dots & \dots & \dots & \dots \\
k_{N<<1} & \dots & \dots & k_{N<<i} & k_{N<<j} & \dots & \boldsymbol{k_N}
\end{pmatrix}$$

Figure II.5: Simple view of the matrix K containing the temperature-dependent Raman coefficients.

Virtual species can be added to matrix K to represent the interaction from intense signals, such as induced fluorescence from hydrocarbons and other soot precursors, or broadband flame luminosity. It is possible, for instance, to define the system as a 9 x 9 matrix including one index for hydrocarbon fluorescence and one index corresponding to a background bandwidth, where no Raman signals are recorded but which is affected by broadband luminosity.

Ideally, the calibration of the temperature-dependent coefficient $k_{j<<i}$ is done by interpolating measured intensities on species *j*'s bandwidth from pure samples of species *i* over a wide range of temperature. In fact, for most species, this cannot be done. For instance, pure water in the gas phase does not exist at ambient pressure and temperature, and it is technically complicated to get a pure sample of water in gas phase at higher temperatures anyway.

Eventually, about half of the off-diagonal coefficients are equal to zero. Thus, it will be possible, for instance, to calibrate any mixture of O_2 and N_2 since they have no cross-talk onto each other. Knowing the exact composition of air, measurements can be performed at different temperatures to calibrate simultaneously O_2 and N_2.

However, measurements in flames should be performed to calibrate the system for higher temperatures. Laminar premixed flat flames using Mac Kenna or Hencken burners are generally used for such purpose since their behaviour is well-known and flat flames can be readily simulated. The aim is to generate series of flat flames with different equivalence ratios, so that most species can be calibrated at flame temperatures. Evidently, the calibration of one species cannot be totally reliable if performed in presence of other species displaying Raman cross-talks onto its spectral bandwidth.

Properly calibrating the system only by direct measurements is consequently very time-consuming and requires some more equipment, such as flat flame burner and gas heater for instance. Besides, some of the species cannot be experimentally calibrated for some ranges of temperatures. Extrapolation of the calibration curves is generally achieved in this case [*Dibble* 1990]**.**

5.1.6. Hybrid method

A solution was needed to simplify the calibration and data-processing procedures induced by the Matrix Inversion method. A code called RAMSES (standing for RAMan Spectrum Efficient Simulation) has been developed at TU Darmstadt over the last two decades, enabling the prediction of the Raman spectral behaviour of the main species seen in hydrocarbon flames [*Geyer* 2005]**.** The RAMSES code generates spectra libraries of the main flame species based on the parameters of the experimental

collection system. An alternative method for LRS calibration and data-processing, so-called Spectral Fitting [*Geyer* 2005], relies on the RAMSES code. The method consists of fitting measured resolved spectra with the large theoretical spectra library based on quantum theories and experimental setup parameters. The fitting enables qualifying the present species in the medium and quantifying them. More details can be found in the cited references.

Pros and cons of the two previous methods have been listed in [*Fuest* 2011] who described the recently developed hybrid method, as collaboration between SNL and TU Darmstadt. The hybrid method is based on using the RAMSES code to generate spectra libraries instead of performing the whole set of calibration measurements required for each species over the temperature range.

Ideally, a comparison with only one LRS measurement (with known temperature, pressure and composition) for each species is sufficient to correlate the Raman spectra libraries to an equivalent of a complete set of calibration measurements. The hybrid method is made so that one gain factor per species should be enough for the correlation. Then, the linear equation from the matrix formulation (cf. Eq. II.6) is solved using temperature-dependent coefficients found by processing the adapted RAMSES spectra libraries. A list of the main pros and cons from the three methods is shown in Table II.2.

Table II.2: Pros and cons from the three main data-processing method adapted to LRS.

Matrix Inversion	***Spectral Fitting***	***Hybrid***
Pros: - Flexible control of the calibration curves, - Fast data-processing, - Accuracy especially depends on calibration measurements, - Processing code relatively easy.	***Pros:*** - Noise contribution is rejected during processing, - Fast calibration.	***Pros:*** - Relatively fast calibration, - As accurate as calibration measurements are performed and detection system parameters are known, - Simple processing code, - Fast data-processing.
Cons: - Very time-consuming calibration, - Signal-to-noise ratio (SNR) should be high, - Requires well-defined corrections for broadband flame luminescence and laser-induced fluorescence.	***Cons:*** - Requires totally well-defined and stable detection setup, - Time-consuming processing, - Requires strong and thorough processing codes, - Does not account for CH_4 and some of the cross-talk coefficients.	***Cons:*** - Requires totally well-defined and stable detection setup, - Requires well-defined corrections for broadband flame luminescence and laser-induced fluorescence, - SNR should be high.

RAMSES code requires a totally well characterized detection system to be properly used. Besides, since there is a lack of detailed spectroscopic description of the Raman behaviour for molecules with more than three atoms at high temperatures, CH_4 coefficients require calibration measurements over the whole temperature range. Some of the cross-talk coefficients also need further adjustments (cf. Section 5.2.1). The hybrid method has been selected for the present experiments.

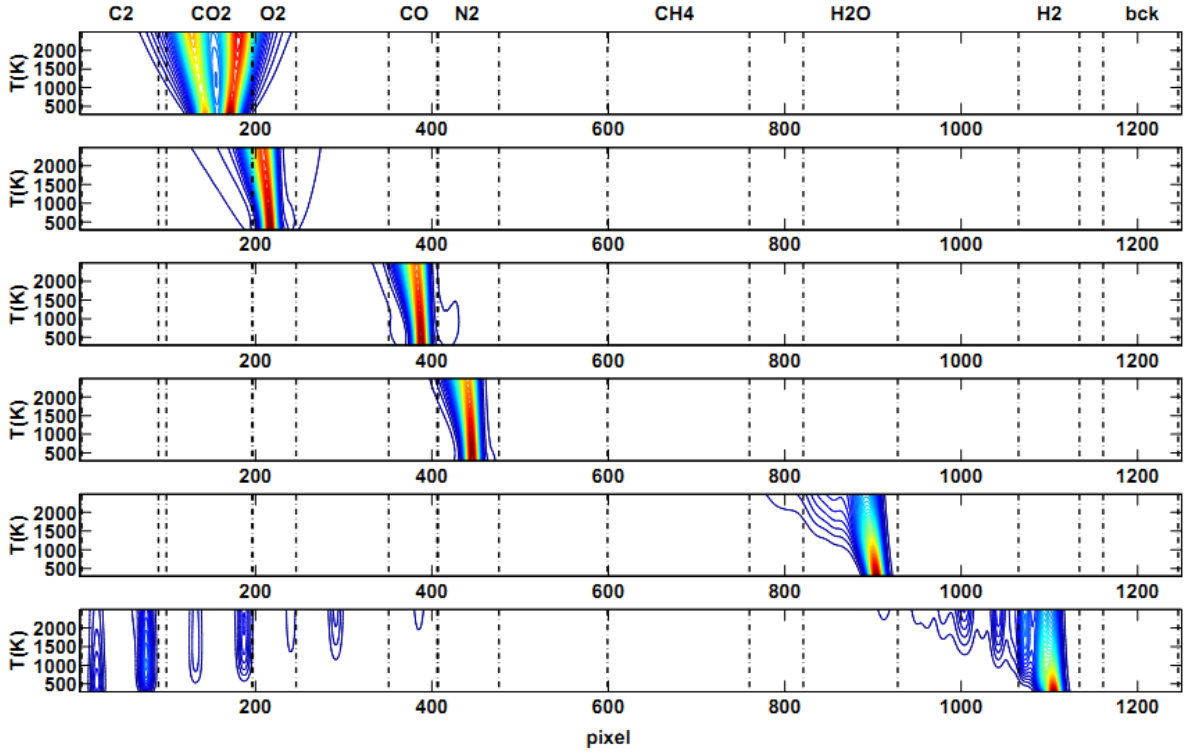

Figure II.6: Calculated temperature dependence of relative Raman scattering spectral intensities from CO_2, O_2, CO, N_2, H_2O, and H_2 using RAMSES code. Dashed vertical lines indicate an example of pixel boundaries for on-chip binning regions (Raman species' bandwidths) used in experiments. [Fuest 2011]

Figure II.6 from [*Fuest* 2011] gives an overview of the effects induced by cross-talks onto other species in his configuration. Data were found using the RAMSES code. Bandwidths are delimited by dashed vertical lines. "C2" stands for the regions where fluorescence signals from the C_2 Swan band system are recorded. "bck" stands for the region where background is constantly recorded. As written previously, the higher the temperature, the greater the effects induced by cross-talks. However, it can be seen that for most species, cross-talk effects only affect neighbouring bandwidths. Hydrogen shows widespread cross-talks onto the whole spectral region of interest, even though their Raman signal intensity is generally around an order of magnitude lower than the main Raman signals from the other observed species.

5.2. Application of the calibration and data-processing methods

As detailed in Section 5.1.4, performing calibration and data-processing for LRS is quite complex and involves a high number of variables. Besides, no tools or detailed procedures are available for this task, since each LRS system is unique and the method cannot be integrated. Dedicated procedures and tools have to be developed and tested to reach optimum results. The whole resolution method used at NTNU is greatly inspired by the matrix inversion method [*Dibble* 1990], the hybrid method [*Fuest* 2011], and the current resolution tools from SNL developed for their LRS setup.

A software suite has been designed using Matlab, which offers the advantages of fast data-processing and convenient tools to design graphical user interfaces (GUI). The software suite consists of four parts: pre-processing, calibration, data-processing and post-processing tools. The main advantage is to be able to use each part independently. For instance, the data-processing software could virtually be used for any other LRS setup, given that the pre-processing software reduces the raw data into the proper format. The post-processing tools have actually been first used with experimental data from SNL. A complete description of the designed tools and the operating procedures for the setup at NTNU is given in the present section.

5.2.1. Background on calibration measurements

As detailed in Section 5.1.4 and especially in Figure II.5, matrix K may display until 81 coefficients if hydrocarbon fluorescence and broadband background are implemented. Besides, each of these coefficients might be temperature dependent, which means that as many as 81 functions might have to be determined to solve LRS spectra. Nonetheless, experience and previous research found in the literature [*Dibble* 1987, *Dibble* 1990, *Nooren* 2000, *Fuest* 2011] enable to reduce the problem to about 50 functions.

Figure II.7 shows how the resulting matrix K is built up and the sensitivity of each Raman cross-talk coefficients for the current system. The diagonal components are the main coefficients, as they represent the main species. They have generally the highest coefficients and enable processing the highest peaks from the spectra. The cross-talks are by definition off-diagonal. Those represented by the contributions with a red colour in Figure II.7, are almost as essential as the main coefficients and require a fine determination. Orange coefficients are also important to bring more consistency to the results. Yellow coefficients enable to refine the results. Cross-talks can come from two main origins: adjacent Raman bands, as for O_2 onto CO_2 for instance, or remote secondary Raman bands, as for H_2 onto all other species. All of those coefficients are

potentially temperature-dependent and available calibration measurements may not be enough to solve them.

Ideally, each diagonal coefficient should be solved by experimentally measuring the Raman signal of a pure species along the whole temperature range. In addition, this would provide information regarding the cross-talk from this pure species onto the other spectral bandwidths. Measurements can be performed at ambient temperature for all species except water, but the possibilities of looking at higher temperatures are limited. A custom-made gas heater could provide reliable temperatures up to ca. 700 K. However, the only way to reach higher temperatures is to use flames, though this involves mixing several species and independent measurements are not possible any more.

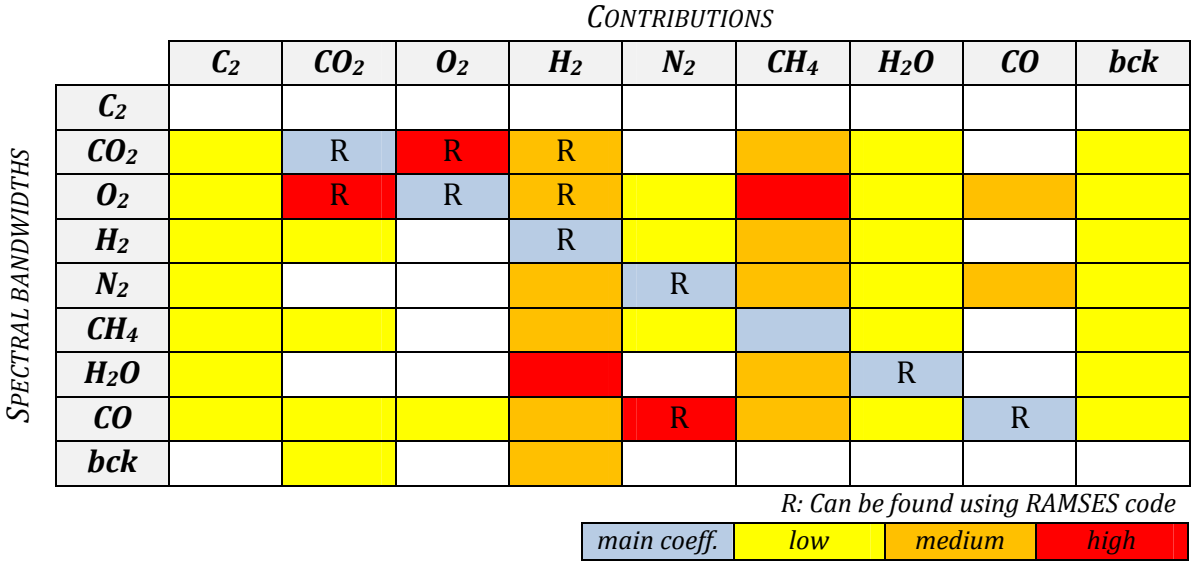

Figure II.7: Different components of matrix K and their sensitivity in the LRS setup.

A way to circumvent the issue is to use the hybrid method [*Fuest* 2011] relying on the RAMSES code [*Geyer* 2005], as described in Section 5.1.6. RAMSES code enables to create spectra libraries concerning six of the seven species of concern, over the whole temperature range. One calibration measurement at a given temperature allows scaling the corresponding library to the experimental values for the whole temperature range. Up to 11 coefficients are determined through RAMSES: CO_2, O_2, O_2 onto CO_2, CO_2 onto O_2, N_2, CO, N_2 onto CO, H_2O, H_2, H_2 onto CO_2 and H_2 onto O_2. Though they are among the most important coefficients, those for CH_4 and most cross-talks remain to be determined experimentally.

Measurements at ambient temperature and using the gas heater enable to solve most of the missing coefficients in the lower temperature range (300 - 700 K). However, measurements in flames cannot be avoided for the higher range of temperatures (1800 - 2200 K). Out of these ranges of temperature, extrapolation and refinements through

experience have to be performed to solve the coefficients. This can be conveniently achieved using the data-processing software, as will be detailed in Section 5.2.5.

For the higher temperature range, calibration flames require stable and well-known compositions and temperatures. Another requirement is to obtain a flat field of measurements, i.e. a field of stable and constant composition over a larger length than the probe length. This allows performing a spatial normalization for each spectral bandwidth over the spatial axis of the CCD chip. Those characteristics can be fulfilled by using a Hencken burner (cf. Figure II.24), known as a reliable calibration burner. The burner has three inlets: one for the fuel, one for the oxidizer and one for the surrounding shroud flow, which protects the main flow from early mixing with ambient air. The two reactants only mix at the burner outlet, exiting from a arrangement of adjacent capillary tubes. This configuration enables to operate in safe conditions and to reach laminar premixed flat flame regimes slightly above the burner, giving quasi-adiabatic conditions, since there is no conductive heat transfer with the burner. Thus, flames issued from Hencken burners can be efficiently simulated with available combustion codes.

Table II.3 shows the methane-air flame conditions used for calibration, enabling stable, slightly lifted premixed flat flames. The purpose is to keep the same range of flow rate through the burner to give comparable results. Consequently, the air flow rate is kept constant, while the methane flow rate is gradually increased by small steps. With these conditions, equivalence ratios lower than 0.7 lead to unstable lifted flames, while equivalence ratios above 1.1 lead to flames attached to the burner, invalidating the adiabatic assumption. Fuel-rich conditions were especially used for scaling the CO Raman spectra library, since no fresh CO gas was available for calibration measurements. The previous measurements can also be used to refine the coefficients found with the RAMSES code.

Table II.3: Methane-air laminar premixed flat flames conditions for Hencken burner.

			Flow rates (Nl.min^{-1})		
Name	***Equivalence ratio***	***T_{Ad} (K)***	***CH_4***	***Air***	***N_2 (shroud)***
PF-CH_4–air-1	0.70	1734	2.1	28.5	32.0
PF-CH_4–air-2	0.80	1908	2.4	28.5	32.0
PF-CH_4–air-3	0.90	2031	2.7	28.5	32.0
PF-CH_4–air-4	0.95	2098	2.8	28.5	32.0
PF-CH_4–air-5	1.00	2194	3.0	28.5	32.0
PF-CH_4–air-6	1.05	2201	3.1	28.5	32.0
PF-CH_4–air-7	1.10	2196	3.3	28.5	32.0

Simulations of the previous premixed flat flames were performed with Chemkin-Pro [*Reaction-Design* 2008], using the laminar premixed stabilized burner and

the GRI-Mech 3.0 kinetic mechanism [*Smith* 1999]. Full multi-component transport regime, thermal diffusion effect (Soret effect) and radiative heat loss were used in the calculations for more accuracy. All results showed that the flame front is located within the first centimetre above the burner, and that the post-flame gas composition remains constant over a few more centimetres. Consequently, the laser probe is positioned 25 mm above the burner, enabling reliable and repeatable results. Raman coefficients are then adjusted while comparing the results from the laminar flames calculations to the experimental results, as detailed in Section 5.2.5.

Another advantage of using a Hencken burner is its ability of also providing a flat field with non-reacting flows at ambient temperature. By flat field it is meant a field of uniform composition and temperature over the whole cross-section of the flow above the burner. One major drawback is the requirement of having a flow rate of about 30 - 40 Nl.min^{-1} in the main outlet to obtain a flat field above the burner. For safety reasons with non-reacting flows, it is preferred to avoid flowing pure species from the main output (except nitrogen) and to rather dilute mixtures with 75 $\%_{mol}$ nitrogen.

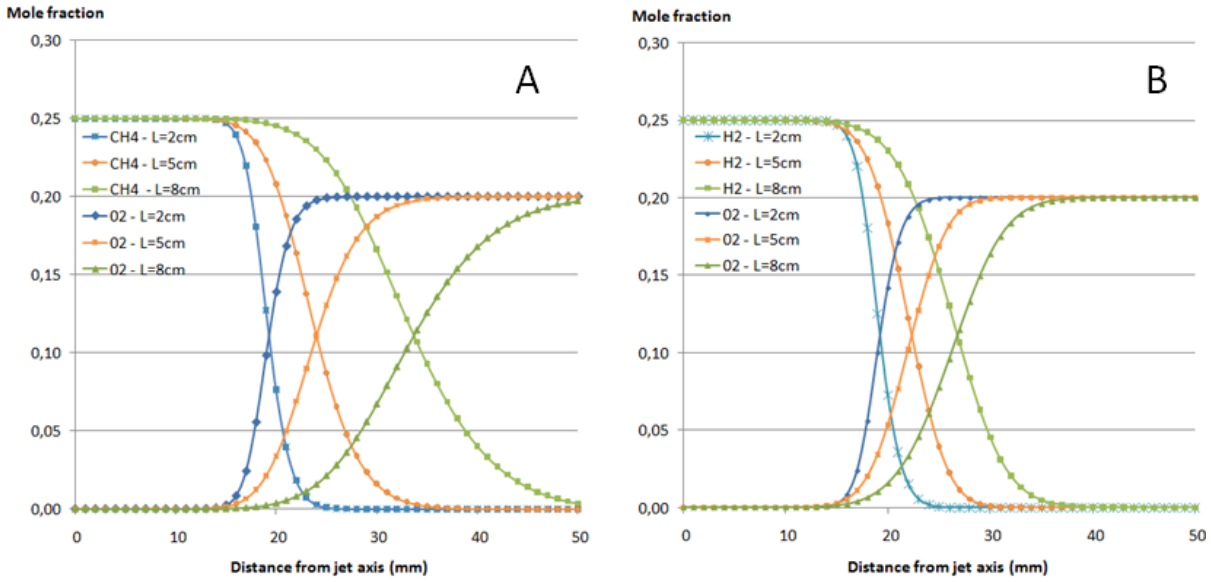

Figure II.8: Radial profiles of moles fractions resulting from simulation using Fluent and the Hencken burner configuration at three different heights above the burner (2, 5 and 8 cm). Central flow: 10 Nl.min^{-1} CH_4 (A) or H_2 (B) and 30 Nl.min^{-1} N_2. Shroud: 40 Nl.min^{-1} air. [Rondeau 2011]

While performing safety investigations using Fluent for non-reacting flows in the Hencken burner (cf. Appendix B), it was possible to focus on the burner output and to define the maximum distance at which the composition of the mixture starts to change due to mixing with surroundings.

Figure II.8 shows the results for two different mixtures, CH_4/N_2 and H_2/N_2, at three axial locations above the burner output, using Fluent. The molar fraction is used to monitor from where the central flow starts mixing with the surrounding air. Results

show that the composition of the central flow seems to remain unaffected by the surrounding air within the first 8 cm above the burner, and over a radius of about 12 mm, for both mixtures. These results confirm the assumption of achieving flat fields in non-reacting flows with the probe volume 25 mm above the Hencken burner.

5.2.2. Calibration measurements routine

Though plenty of measurements can be performed to solve and refine the calibration coefficients, performing measurements and processing data are time-consuming tasks. In addition, small movements within the detection system over time can have a large impact on the results. Typically, calibration coefficients keep over time a very similar shape in temperature space, but are not constant. From one day to another, some coefficients have to be corrected by 10 - 20 %. This is due to day-to-day small movements of optics, room temperature effects on optics, or laser energy profiles, for instance. The system response may also change on an hour-to-hour basis. These different sources of uncertainties can be minimized by performing a series of calibration measurements every day of experiments, and by repeating some of them several times along the day.

Figure II.9 shows the main daily layout of the calibration routine. First, a “dark” measurement, i.e. with neither laser nor ambient light, nor flames, is recorded to be subtracted as a background from the following measurements. Then, LRS measurements of non-reacting flows are performed at ambient temperature with the Hencken burner. It starts with a flow of pure nitrogen, and is followed by mixtures of nitrogen and, respectively, carbon dioxide, oxygen, hydrogen and methane. Nitrogen at ambient temperature gives a large Raman signal and displays only low levels of cross-talks on the species added in the rest of the measurements at ambient temperature. Consequently, the presence of nitrogen does not interfere much in the determination of the Raman coefficients of the other species at ambient temperature. Besides, it mitigates the danger of high contents of methane, hydrogen or carbon dioxide, in the laboratory or the ventilation system. It also brings more similar proportions to flames measurements. Air measurements are often performed, since they are costless and have well-known composition and temperature.

Laminar premixed CH_4/air flat flames are then performed with equivalence ratios varying from 0.7 to 1.1, as detailed in Table II.3. They are preceded by non-reacting measurements of four of the mixtures, to evaluate the accuracy of the mass flow controllers. This also allows adjusting the comparison with the results from the laminar flame calculations during the refinement of the Raman coefficients. In addition, laminar premixed $CH_4/O_2/CO_2$ flat flames are performed and compared to laminar flame calculations. Non-reacting mixtures are also measured, as well as spontaneous flame luminosity, i.e. measurements of light emissions from flames without laser beam.

In this case, the flame luminosity is mainly due to CO_2^* chemiluminescence appearing as a strong broadband background signal on spectra (cf. Section 3.2.5). Those flames especially help refining Raman calibration coefficients linked to CO_2 at flames temperatures, which has a significant influence on results accuracy.

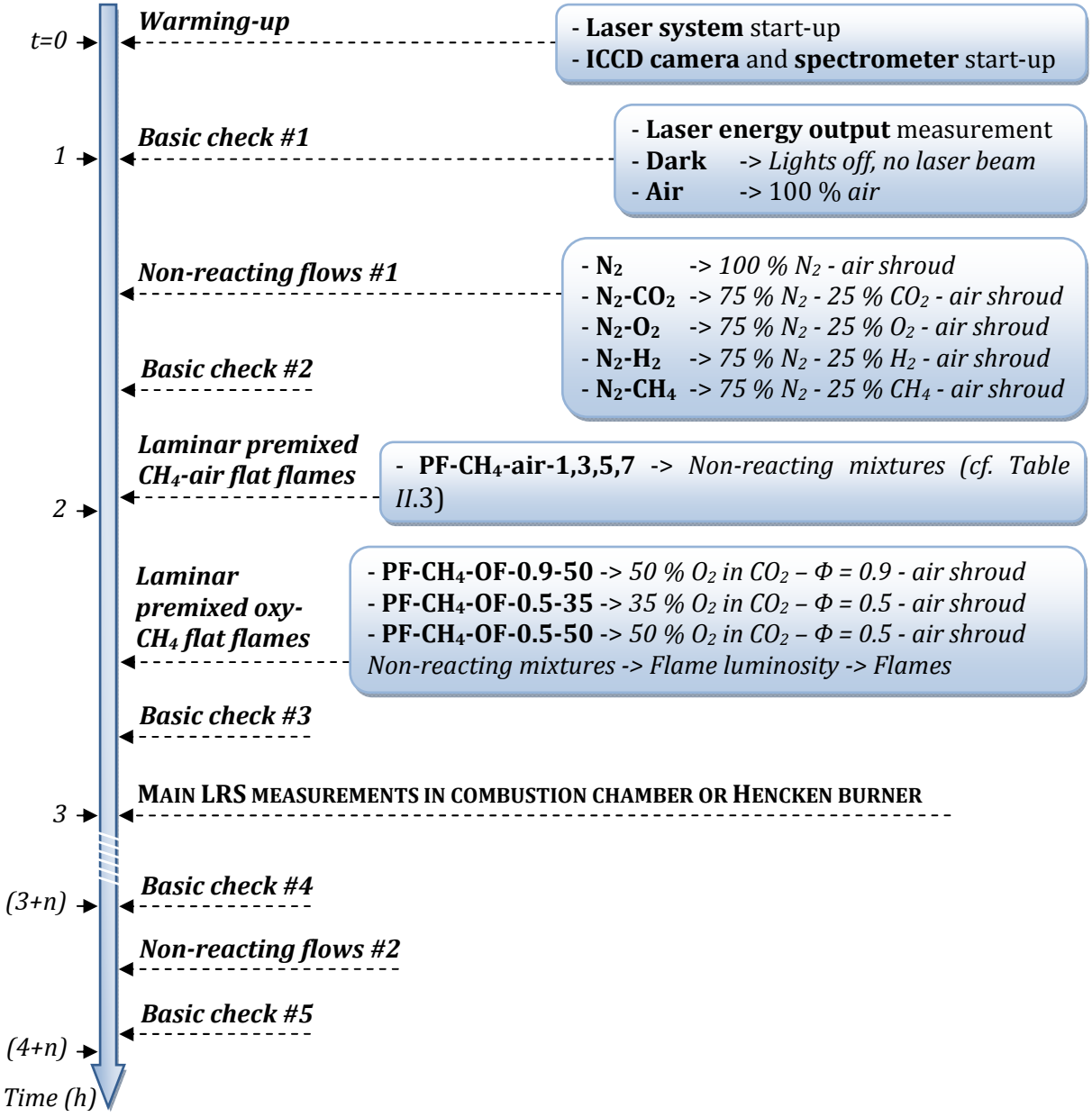

Figure II.9: Layout of the calibration measurements routine, performed with Hencken burner.

Air and dark measurements are frequently performed as basic checks during a typical day of experiments, to monitor any change in the system response over time. Laser energy output is also regularly measured, as it is an essential variable, since Raman signals are linear with the laser energy. The regularity of the measurements considerably reduces the uncertainties in the results. The calibration routine typically takes ca. 3 hours at the beginning of the day, and ca. 1 hour at the end of the day. This

considerably reduces the time for the main measurements, within one day of experiments.

5.2.3. Pre-processing software

Raw files are recorded as *.SPE* spectra files from Winspec, the data acquisition platform. Those contain information on experimental conditions and on recorded data over three dimensions: spectral, spatial and temporal dimensions. Spatial binning (lines of 10 pixels combined into 1 superpixel) is directly applied on CCD to improve the SNR and to reduce the processing time in Winspec by reducing the total volume of data by a factor 10. Though on-CCD binning may be applied as well on the spectral dimension, by reducing the 1024 pixels to a dozen of superpixels corresponding to the Raman species bandwidths, the priority is given instead to spectrally-resolved data, to gain on flame spectroscopy knowledge in oxy-fuel flames. Spectral binning would also prevent clear distinction of the influence of broadband flame luminosity or the cross-talk origins, for instance. A pre-processing code is thus required to apply the spectral binning on the raw files, while keeping the original files.

The pre-processing code offers the opportunity of filtering the raw files from erroneous measurements due to both optical-breakdowns and cosmic ray events. Details of the development of the two algorithms for filtering can be found in Appendix A, based upon [*Rondeau* 2011].

The software uses a GUI designed with Matlab, controls the spectral binning and applies two algorithms aiming at detecting optical breakdowns and cosmic ray events. Figure II.10 gives an overview of the structure of the software. Raw *.SPE* files are read by software and converted into data matrices. The two algorithms are then applied on data matrices and correct or delete erroneous measurements. Spectral binning follows, as an integration of the spectra over the Raman species spectral bandwidths. The resulting data matrices are finally converted into new *.SPE files*, associated to updated data information. The pre-processing code is systematically applied for all raw Raman measurements.

Supplementary functions have been developed with the GUI. First, the parameters used in the GUI are saved in a *.txt* files, being read as the GUI starts. This allows keeping in memory different sets of parameters. The GUI also allows multi-selection of files, so that a series of files can be treated in a row, which has proved to be significantly time-saving. Besides, the efficiency of the detection process could be monitored in real-time in the GUI, to highlight any mistake or any corrupted file. Another function allows removing a given number of temporal frames at both temporal ends of the raw files, since the two first and two last frames happen to show inconsistent results. The same function can be applied to remove pixels at both ends of

the spatial dimension, since the optical response is generally significantly attenuated there.

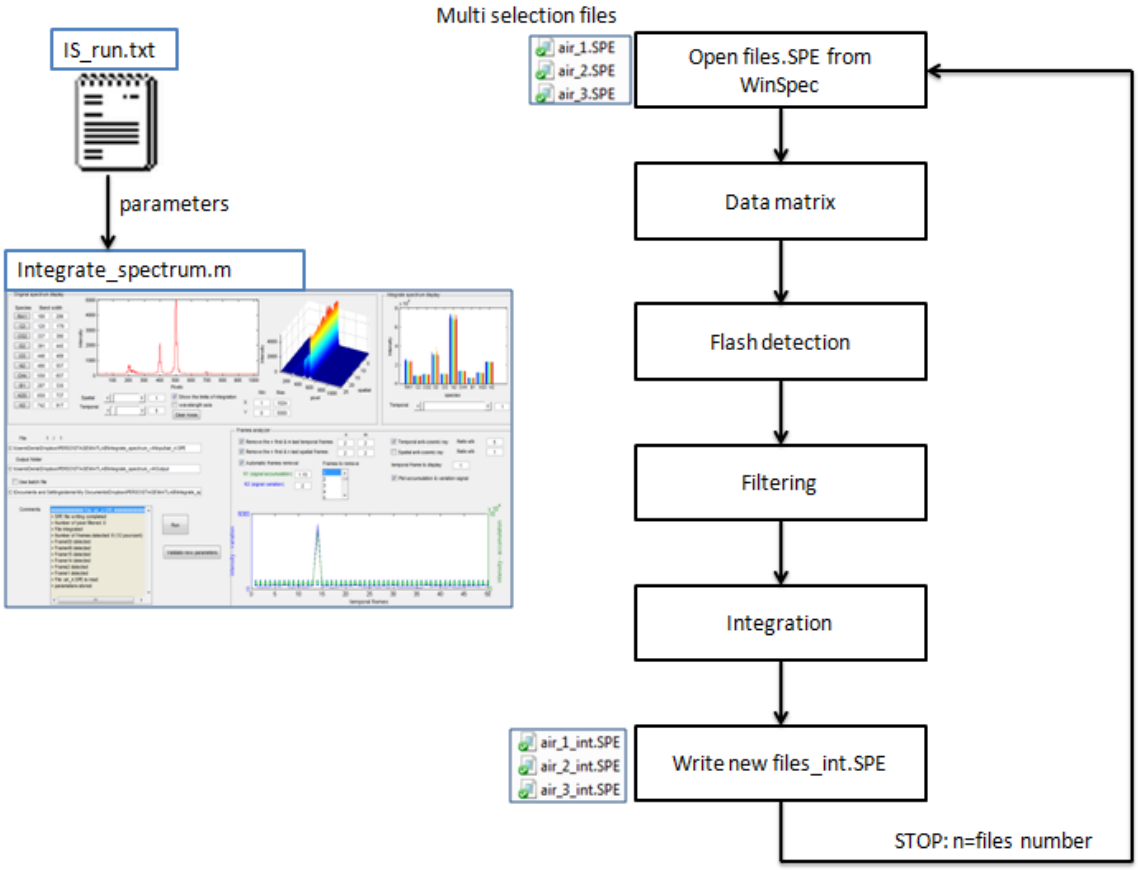

Figure II.10: Overview of the structure of the pre-processing software. [Rondeau 2011]

5.2.4. Calibration software

The calibration software, designed in Matlab, is used to produce the basic files and information required during data-processing. Three main goals are given to the code: creating a spatial normalization matrix to be applied to all raw spectra files later, calculating SNR from calibration files, and calculating the temperature-dependent Raman calibration coefficients by scaling the calibration files to the RAMSES spectra libraries.

5.2.4.1. Spatial normalization

Typically one file per species of interest is picked out of the calibration measurements detailed in Figure II.9**,** read by the Matlab code and transformed into data matrices. Ideally, each file should correspond to a configuration in which the species of interest is present in the same range of molar fraction as expected in the main Raman measurements. Once transformed into matrices, a time-averaged background

(also called dark) measurement is subtracted, and final intensities should ideally be constant over the spatial dimension, since calibration measurements were performed with supposedly flat fields.

Though the Hencken burner can be trusted for operating a proper gas mixing at the operating flow rate, spatial profiles do not appear completely flat. Even in the case of air flows, nitrogen and oxygen spatial profiles are generally not flat. This is mostly due to inhomogeneous efficiency from each pixel of CCD chip and irregularities from the optics. However, those issues are systematic and can be mostly corrected by applying a spatial normalization matrix to all results. Note that the same irregularity happens along the spectral dimension, but the correction is directly made through the Raman calibration coefficients.

Each of those spatial profiles can be corrected by a vector. The spatial normalization matrix is built up from all the correcting vectors. Figure II.11 shows a colour-map view of a typical spatial normalization matrix. All vectors are using the spatial strip #13 (out of the remaining 21 binned pixels along the spatial dimension) as a reference value for the correction. The strip #13 has been chosen since it is located close to the centre of the chip, where the intensity is generally the highest, and because there, the chip showed no impaired pixels or significant irregularities in the dark measurements.

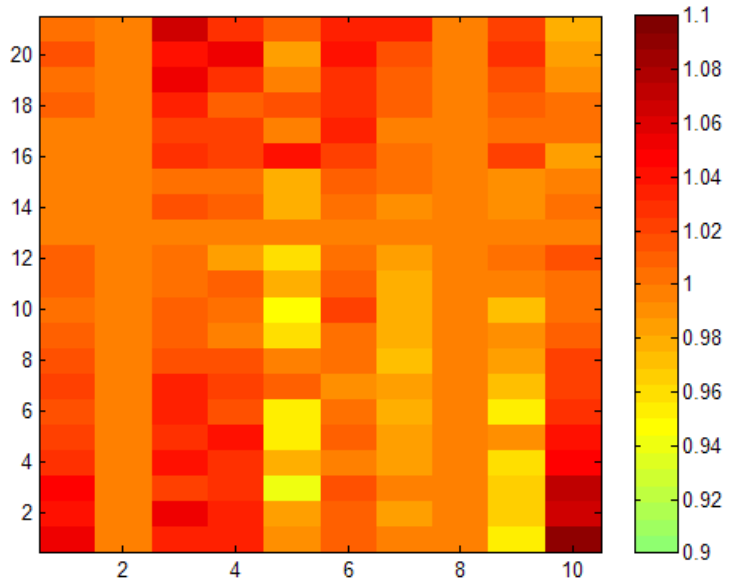

Figure II.11: Colour-map view of a typical spatial normalization matrix, where the horizontal axis represents the 10 spectral bandwidths and the vertical axis is the spatial dimension reduced to 21 binned pixels.

5.2.4.2. SNR estimates

The SNR can be conveniently estimated at this step of the data-processing since calibration measurements involving each species are already in the system. The SNR is calculated as the ratio of the mean temporal signal taken at the reference spatial strip (#13 here), to the standard deviation of the same signal.

Table II.4: Typical SNR estimates as found with the calibration software.

CO_2	O_2	CO	N_2	CH_4	H_2O	H_2
22	18	4.0	28	47	7.0	17

Five of the seven species are calibrated from cold flows, and the two remaining ones, CO and H_2O, with laminar methane-air premixed flat flames. CO was not available as fresh gas in the present experimental configuration and gaseous H_2O requires higher temperatures. SNR issued from the cold measurements detailed in Figure II.9, can be compared one to another since they all correspond to the same molar fraction (25 %). They are also much higher than those taken from flame measurements, since noise levels are generally higher in flames, and the molar fractions of CO and H_2O are lower than 25 %. However, it gives the opportunity to monitor the SNR from the calibration files over time. Table II.4 gives a typical estimate form the SNR found in the calibration software.

5.2.4.3. Determination of Raman calibration coefficients using the RAMSES code

The RAMSES code provides spectra libraries of 6 out of 7 species of interest, as a function of temperature over the range 290 - 2500 K. Figure II.6 gives an overview of the variation of Raman species spectra with temperature. The RAMSES code does not provide a reliable set of spectra for CH_4, as it is not a diatomic or tri-atomic molecule like the other species, and no theory provides a correct approximation of the inelastic behavior at high temperatures of such molecule yet. The RAMSES code requires a great knowledge of the experimental setup, as many experimental parameters have to be inputted in the code to better match the reality. Those parameters are, for instance, wavelength of the exciting laser, laser energy per pulse, solid angle of the optical device, length of the probe volume, quantum efficiency of digital camera, efficiency of mirrors or collection lens efficiency. Though part of the parameters is well-known, those remaining may add uncertainties. Thus, the spectra libraries have to be considered as a great approximation, which can still be improved with experience on the setup.

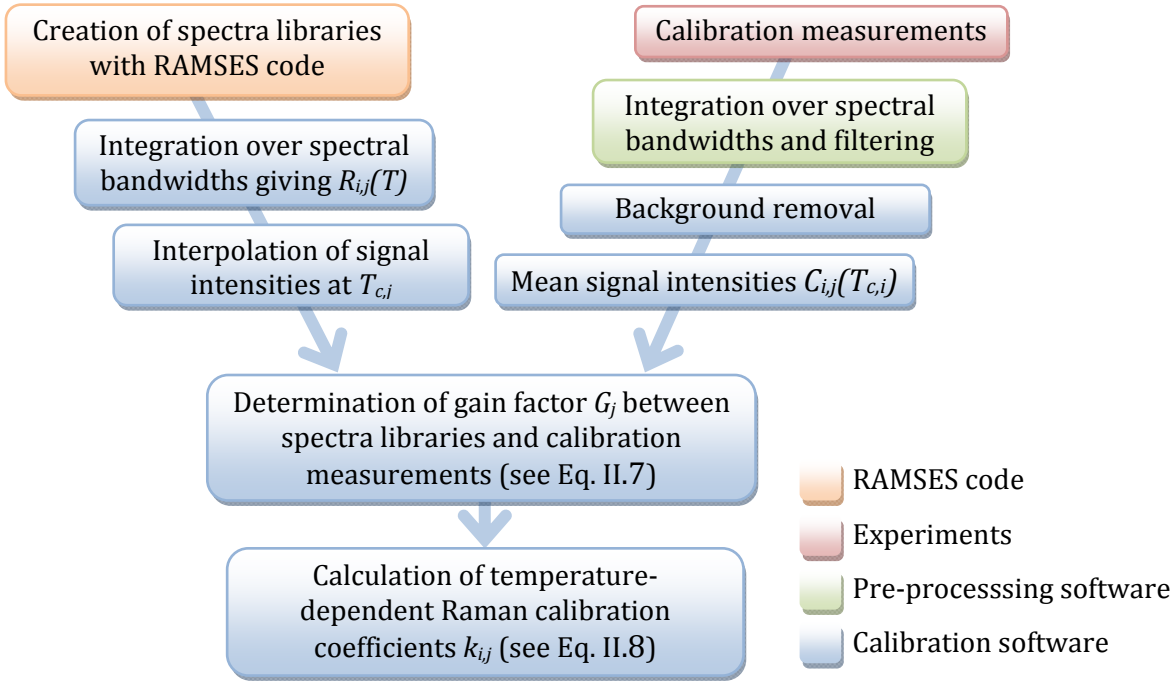

Figure II.12: Procedure to obtain Raman calibration coefficients from RAMSES spectra libraries using calibration measurements.

Figure II.12 shows the procedure to obtain Raman calibration coefficients from RAMSES spectra libraries using calibration measurements. Pre-processed calibration measurements are averaged after background removal (by use of dark measurements), resulting in coefficients $C_{i,j}$, mean signal intensities recorded over spectral bandwidth i, due to contribution of species j. In parallel, spectra libraries are generated from the RAMSES code using parameters from the experimental setup. Those are integrated over the species spectral bandwidths, with the same spectral coordinates as in the pre-processing software. Spectra libraries are thus converted into temperature-dependent signal intensities $R_{i,j}$ from species j over species i's bandwidth.

The purpose is then to link $C_{i,j}$ and $R_{i,j}$ to scale the RAMSES spectra libraries to the actual experimental results. This is performed by interpolating $R_{i,j}$ at the temperature $T_{c,j}$ corresponding to the calibration measurement involving species j. A gain coefficient G_j can be calculated, as shown in Eq. II.7. To simplify, it is assumed that only one gain coefficient per species is sufficient, instead of considering one different gain coefficient for each cross-talk. It is also considered that the gain coefficient is constant over the whole temperature range.

$$G_j = \frac{X_R C_{j,j}}{X_C R_{j,j}(T_{C,j})} \qquad \text{Eq. II.7}$$

With:

X_R Molar fraction of species j in its corresponding RAMSES spectra library

X_C Molar fraction of species j in its calibration measurement

In this particular case, RAMSES spectra libraries are generated as if only one species was present, which gives $x_R = 1$. x_C is inputted into the calibration software and corresponds either to what is indicated for the cold flow measurements in Figure II.9, or to the results of the laminar flames calculations in the case of CO and H_2O. Consequently, all coefficients G_j correspond to calibration of the RAMSES library to fit the experimental measurements as if those were performed with pure species.

Up to 11 Raman calibration coefficients are determined through RAMSES: CO_2, O_2, N_2, CO, H_2O, H_2, cross-talk from O_2 onto CO_2, CO_2 onto O_2, N_2 onto CO, H_2 onto CO_2 and H_2 onto O_2. The Raman calibration coefficients $k_{i,j}$ are calculated as shown in Eq. II.8. Note that the coefficients implicitly include the laser output power in this case.

$$k_{i,j}(T) = G_j \frac{RT}{p} R_{i,j}(T) \qquad \textit{Eq. II.8}$$

With:

R	Ideal gas constant (8.314 J.mol^{-1}.K^{-1})
p	Pressure (Pa) (only tested at atmospheric pressure)
T	Temperature as computed with the RAMSES code (K)

Ideal gas law is used to determine the number density of species *j* at temperature *T*, as species *j* virtually has a molar fraction equal to 1, by construction. This assumption of the ideal gas law is a fair approximation since the pressure is low and there is no (or entirely negligible) intermolecular forces between the molecules. Due to this procedure, using the coefficients $k_{i,j}$ in the Raman coefficients matrix *K* will provide results as number density in [mol.m^{-3}]. This is especially convenient to compare the results to laminar flames calculations for instance.

The 11 temperature-dependent coefficients $k_{i,j}$ are saved in a *.txt* file. Each of them appears as its value for about hundred temperatures regularly distributed between 290 and 2500 K, to keep good accuracy when using them in the data-processing software.

5.2.5. Data-processing software

The data-processing software is the keystone to solve Raman spectra. The software has been designed using Matlab and is operated through a GUI, greatly inspired by the Labview data-processing software developed by SNL for their LRS setup. Many functions have been implemented over time to ease the use of the GUI. An effort has also been made to keep the software virtually independent of the LRS experimental setup, so that it can be brought to any other LRS setup. The pre-processing code can be

readily adapted to any other input file format and still provide the proper output format of data to be used in the data-processing software.

5.2.5.1. Overview

Figure II.13 and Table II.5 give an overview of the GUI designed with Matlab and its components. Besides running the resolution algorithm for Raman spectra, many functions have been embedded to ease and optimize the data-processing. Most of them are relatively complex, interconnected and hidden behind the GUI. A few functions are especially of interest:

- **Real-time display**. The results from data-processing are displayed in real-time within the GUI. Mean, RMS, and scatter plots can be plotted to monitor the results. Outliers can also be spotted in the central plot. The variables on the *x*- and *y*-axis can be chosen among all available variables written in the output *.txt* files. Plots can be scaled by the operator or displayed with an auto-scale option.

- **Input parameters storage**. Most input parameters are read from a *.txt* file when the software is started. This enables storing inputs parameters from different configurations and to keep memory of which parameters are used to process a series of raw files. Up to 35 inputs parameters are saved in the *.txt* file.

- **Raw files selection**. The GUI can run in three different modes: with one raw file only, with a selection of several raw files, or with a batch file. The first mode is the simplest one based on a single raw file. For the second mode, the file selection box allows multi-selection of raw files. Raw files are then read and processed one after the other, to save on operating time. The number of raw files is not limited since the computer memory will only see one raw file at the time. The third mode is based on a batch file, which can also be used to read series of raw files with changing processing parameters. If the box shown in Figure II.13 (index #6) is selected, the code will read the corresponding batch *.txt* file, and find through it the required information to process the raw files. It contains some common parameters for the whole series of raw files, such as Raman calibration coefficients filename, dark measurement filename, and output directory. It also contains specific parameters to each raw file, such as its filename, spatial normalization filename, averaged laser output energy, or gas flow rates to calculate the mixture fraction, for example. Using such file is extremely time saving for long series of measurements that often happen to be entirely processed many times to refine the results.

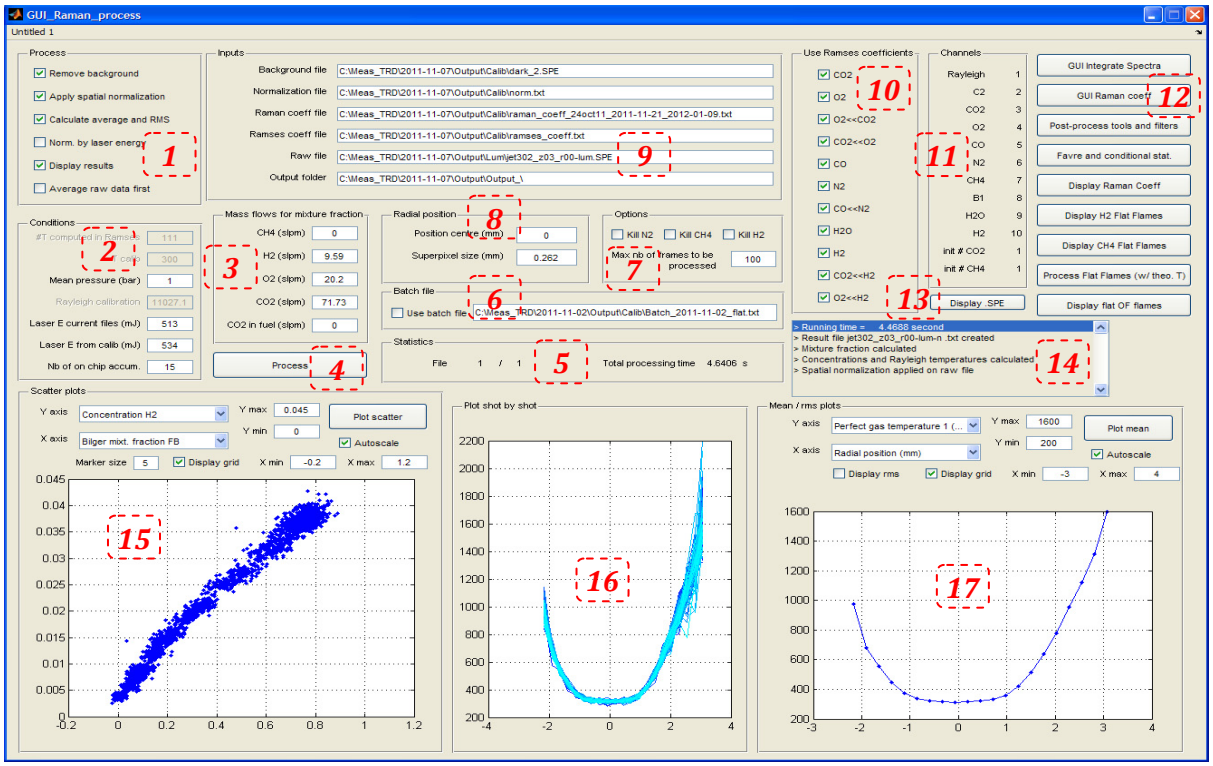

Figure II.13: Overview of the data-processing GUI.

Table II.5: Description of the main components of the data-processing GUI.

Index	Description
1	**Process options**, (e.g. background removal, spatial normalization and raw data averaging)
2	**Experimental conditions** (e.g. mean pressure and laser energy)
3	**Volumetric flow rates** from reactants, for mixture fraction calculation
4	**Process button**
5	**Statistics** (current file index in series, running time for a series of files)
6	**Batch file** selection and filename
7	**Kill species options**
8	**Radial position parameters**
9	**Inputs/outputs** filenames and directories
10	**Switch between RAMSES and classic coefficients**
11	**Bandwidth index display**
12	**Shortcuts to other tools** from the software suite
13	**Averaged raw files display**
14	**Status box**
15	**Real-time scatter plots display**
16	**Real-time shot-by-shot plots display**
17	**Real-time mean and RMS plots display**

- **Raw file averaging**. The processing time is closely linked to the number of temporal frames recorded in a raw file. A raw file containing 100 frames will take roughly 100 times longer than a raw file containing a single frame. One way to speed-up the processing time, is to average the raw signals as soon as they are read by the data-processing software. When the measured field is quite steady, the result is generally very close to the typical method of averaging processed data. The drawback is of course that individual shots will not appear in the results, though it is very convenient during the refinement of the Raman calibration coefficients if raw files have to be repeatedly processed.

- **Kill species function**. It may happen that some Raman calibration coefficients are not perfectly tuned and let slight amounts of one species appear in the results, while this one cannot be physically present. It could be the case of nitrogen in laminar premixed $CH_4/O_2/CO_2$ flat flames, for instance. Generally, those amounts are very low in number density, but they induce errors, which propagate through cross-talks or mass fraction calculations. When it is known that a species cannot physically appear in the results, a function enables to neutralize all Raman calibration coefficients related to this species. The function is available for N_2, CH_4 and H_2. This is especially useful when refining the results.

- **Laser energy normalization**. In case the laser output energy would significantly vary along one series of measurements, a function was implemented to normalize each frame to the same energy reference. In this case, shot-to-shot laser output energy measurements have to be synchronized with the spectra measurements. This function is not used in the present configuration, thanks to the steadiness of the laser energy output (cf. Section 6.1.2). Nevertheless, the laser output energy slightly decreases over time. Thus, a correction is applied using the ratio of the averaged laser output energy measured during calibration, to the current averaged value.

5.2.5.2. Raman calibration coefficients

As shown in Figure II.7, about 50 temperature-dependent Raman calibration coefficients have to be defined to solve the Raman spectra. Most are found iteratively while processing the calibration measurements. Since they have to be stored together and remain editable, values for 100 temperatures cannot be kept for each coefficient, as for those issued from the RAMSES code. A way to circumvent this issue is to reduce the number of temperatures to the minimum, without affecting much the shape of each coefficient over the whole temperature range. Depending on the coefficients, 5 or 6 temperatures are sufficient. Figure II.14 shows an example of one coefficient, as stored

in the Raman calibration coefficients *.txt* file. In this case, the values of the coefficient are indicated for 6 temperatures along the range 290 - 2500 K.

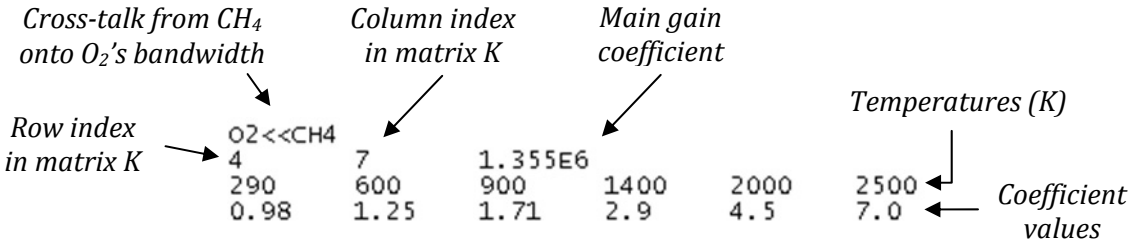

Figure II.14: Example of one of the coefficients stored in the Raman calibration coefficients .txt file.

The "spline" fitting function in Matlab enables to retrieve a smooth curve from those six values, or to efficiently interpolate the coefficients at intermediate temperatures. Based on comparison with measurements, coefficients can then be intuitively shaped in temperature space by tuning those values.

5.2.5.3. Main resolution scheme

Figure II.15 shows an overview of the main Raman data-processing scheme. Pre-processed experimental measurements are corrected with the dark measurements and spatially normalized. In the mean time, files containing the calibration coefficients issued from the RAMSES code and the classic Raman coefficients are read. Both files are combined into the temperature-dependent matrix *K*, respectively to the switches in the GUI, enabling to select either RAMSES or classical Raman coefficients (cf. Figure II.13, index #10).

An iterative resolution is required since both temperatures and number density of the main species have to be found from the recorded Raman signals. A first guess on temperature (T_{old}) is needed to start the iterative resolution. The value of T_{old} is not determinant on the final results, as long as it remains in the range 290 - 2500 K, where the Raman calibration coefficients are defined. The next step is to interpolate matrix K at the guessed temperature T_{old}. Matrix K can now be inverted while solving Eq. II.5 using a vector Q of the corrected signals recorded on each species bandwidth, and the laser output energy Q_1. The laser output energy is actually included in the Raman calibration coefficients in the present configuration.

The sum of the species number density can be found from the resulting vector of number densities [N]. Combined to the ideal gas law, a new temperature T_{new} can be calculated. The ideal gas law gives a fair approximation, since the pressure is low and there is no (or entirely negligible) intermolecular forces between the molecules. Due to the use of the ideal gas law, T_{new} is generally called ideal gas temperature.

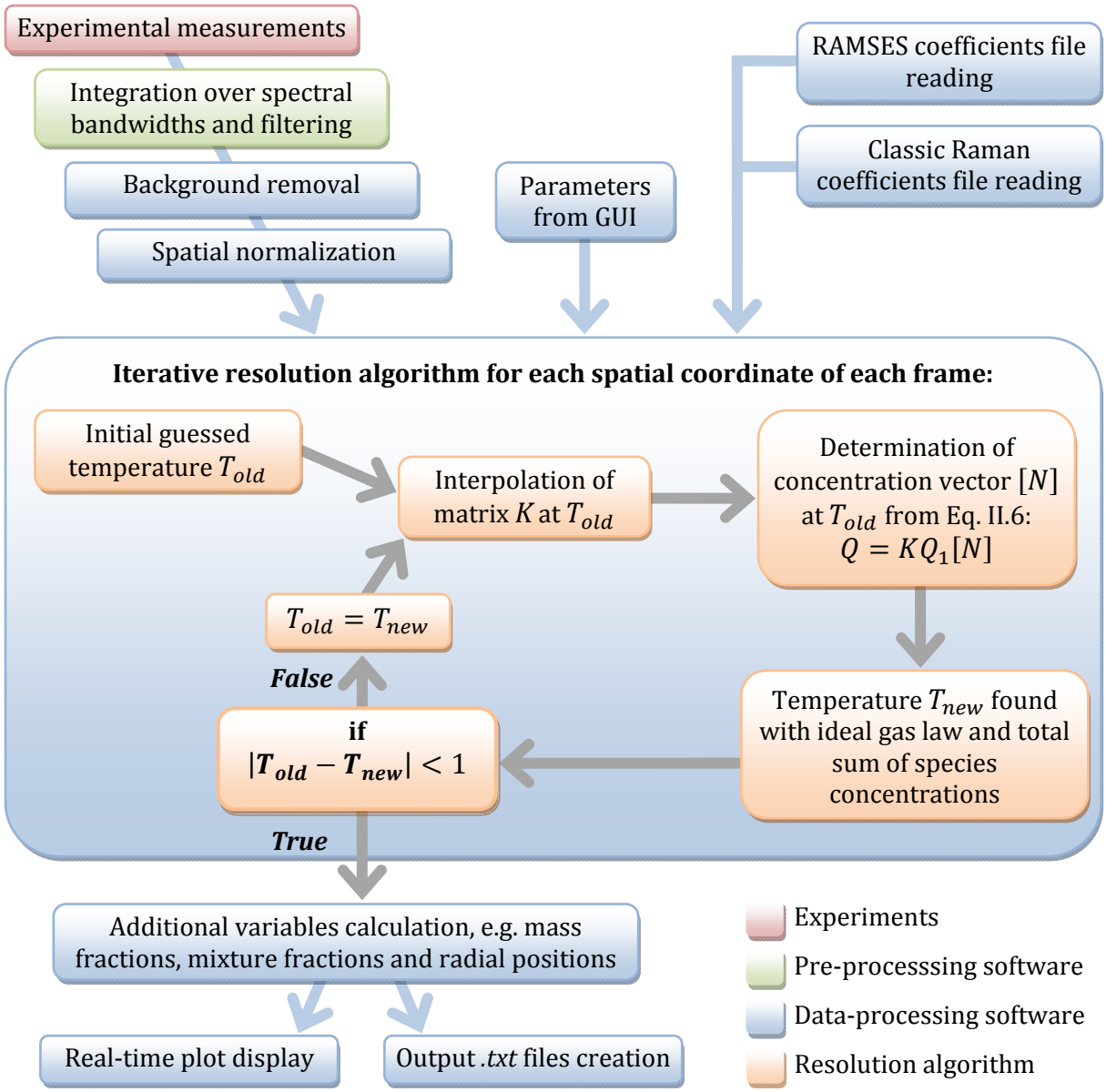

Figure II.15: Overview of the main Raman data-processing scheme.

At this point, the two temperatures are compared, and if the difference is less than 1 K, iterations can be stopped. Otherwise, a new loop starts with the value of the new temperature to replace the initial guess. The algorithm generally converges in less than 10 iterations. The algorithm is run for each spatial location of each temporal frame. Once a whole raw file is solved, a supplementary set of variables can be calculated from the resulting number densities. They include mass fractions, mixture fractions, radial positions, elemental mixture fractions of H and C atoms and densities. Then, the results are displayed in the GUI and an output *.txt* file is written.

5.2.5.4. Refinement of Raman calibration coefficients

Though Raman spectra look very similar from day-to-day, slight differences appear and require a new tuning of the Raman coefficients for each day of measurements. Calibration coefficients issued from the RAMSES code can be used in combination with the classic ones. However, though their shape in temperature space is likely to be correct, they may be over- or underestimated, since not all Raman cross-talks are taken into account for their determination. A tool has been designed to display plots of both series of coefficients, so that the shape of the classical coefficients can be adjusted to those found with the RAMSES code. The next step is to tune the gain of the coefficients. This is generally performed by processing the calibration measurements one-by-one, in the same order as they were recorded (see Figure II.9). Using the real-time display, results are matched with the expected number densities. Number densities are used rather than mass fraction or molar fraction, since they provide absolute results for each species, somehow independent from each other. An example of the coefficients display is shown in Figure II.16, where the chart corresponding to the main Raman calibration coefficients is shown. All coefficients can be displayed in the same way in the other pages. There may be an offset between both coefficients but their shape is generally quite similar. Comparable curves of Raman calibration coefficients can be seen in [*Dibble* 1987, *Fuest* 2011].

In order to get more accurate results, only the gains are tuned while processing calibration measurements performed on non-ignited/cold flows. The shapes are tuned afterwards, while processing flame measurements since they provide information on the temperature range 1800 - 2200 K. Laminar premixed methane/air flat flames are very convenient for this purpose since they can be confidently compared to laminar flame calculations.

As described in Figure II.9, methane/air non-reacting mixtures are first measured. This enables to know if there is any offset between the assigned flow rates to the mass flow controllers and the actual reactant flow compositions. It also allows calculating a more accurate equivalence ratio than the theoretical one, which improves the comparison between processed results and those from the one-dimensional laminar flame calculations. The typical procedure is, first, to create a batch file containing information to process the seven premixed methane-air flat flames measurements in a row. Then, the results are displayed together with those from the laminar flame calculations, as illustrated in Figure II.17. Calibration coefficients can be optimized by spotting the right coefficients to modify, tuning them at the proper temperature, and matching both series of results. Laminar premixed $CH_4/O_2/CO_2$ flat flames help to complete this task in a similar way.

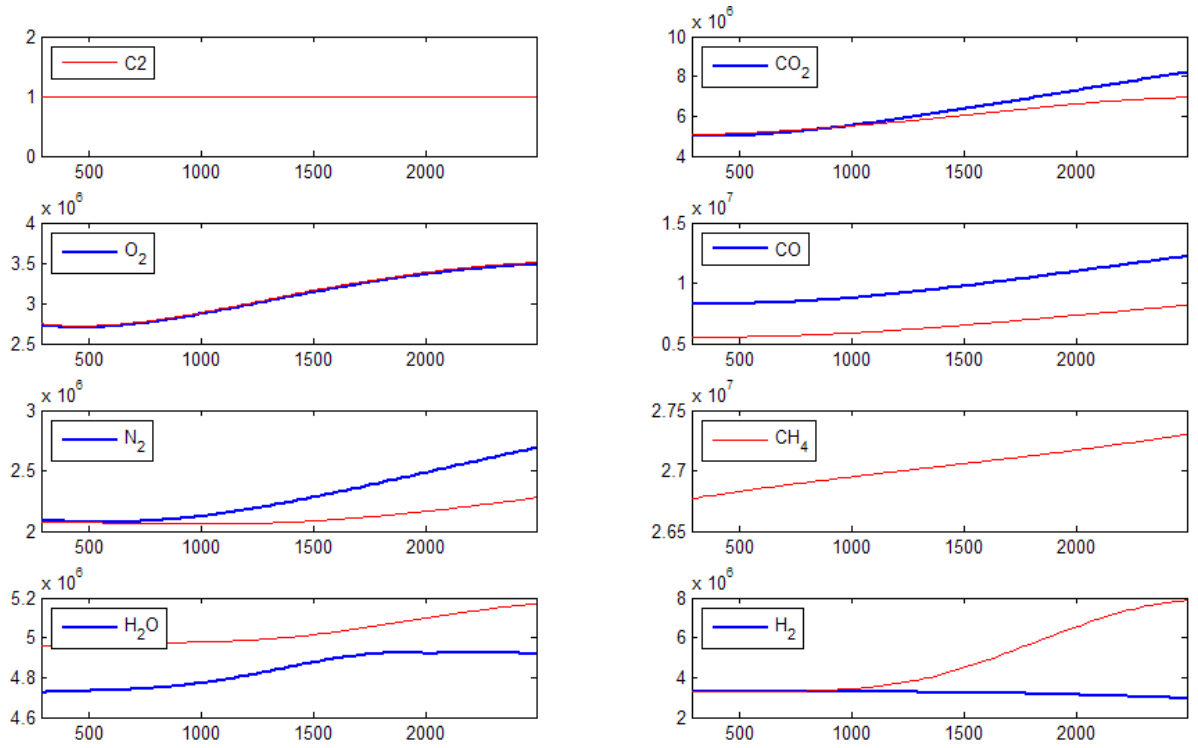

Figure II.16: Example of display of the main Raman calibration coefficients versus temperature (K). The blue solid lines correspond to the coefficients found with the RAMSES code, while the red ones are the classic coefficients that can be tuned.

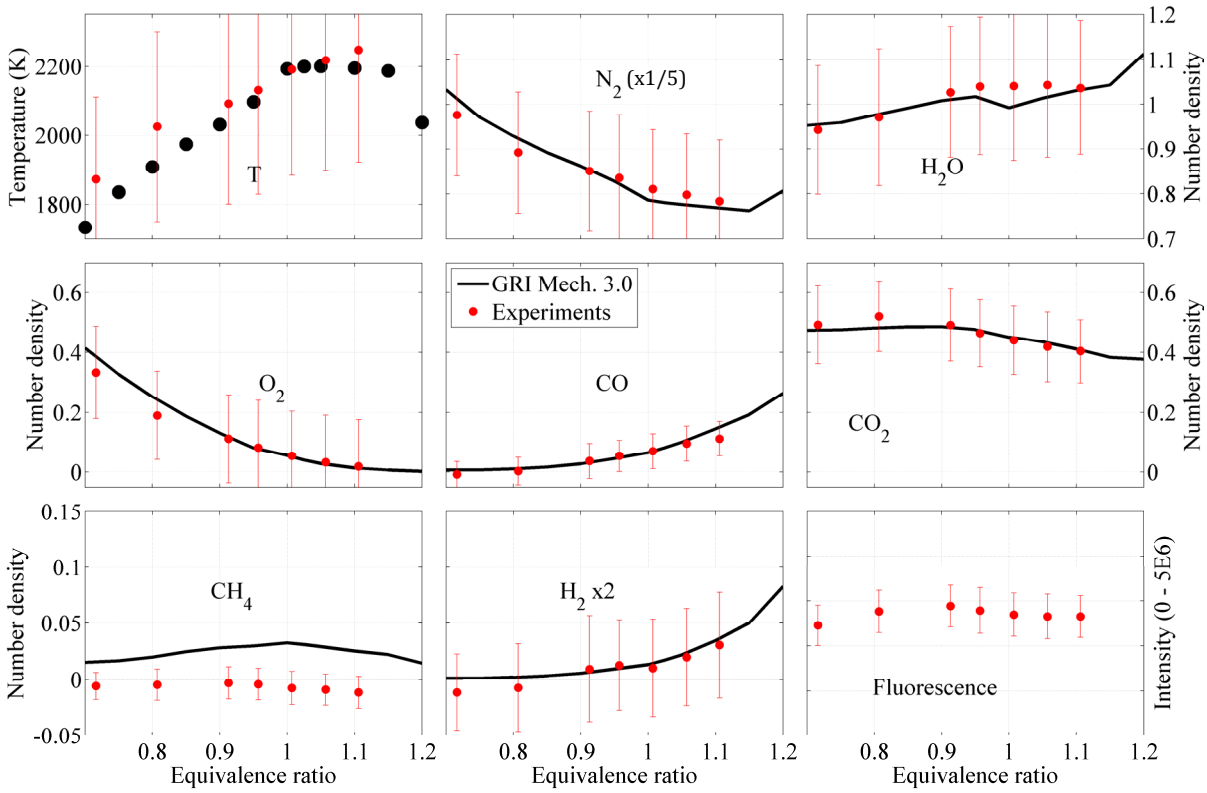

Figure II.17: Example of display of processed results from laminar premixed methane/air flat flames (red dots) and results from laminar flames calculations (black dots/lines). The RMS of the processed results is shown by vertical red lines. Number densities are given in [mol.m^{-3}].

The adjustment of the Raman calibration coefficients in the intermediate range of temperatures is generally performed either by extrapolation, or while processing the main flame measurements. For example, the whole temperature range is covered while radially crossing the flame region of a non-premixed jet flame. It is then possible to spot the cross-talk coefficients that are not properly tuned or to optimize the main Raman coefficients. An incorrect cross-talk coefficient is likely to appear as a local accidental shape in a number density profile across the flame region. It typically means that the coefficient is overestimated under a certain temperature and underestimated above it, or the other way around. Changing the slope of the coefficient around this temperature would make the accidental shape disappear.

5.2.6. Post-processing tools

A series of tools have been developed using Matlab to make the most of the processed results. A filtering tool allows removing outliers from the processed results. The filtering parameters are editable in a GUI and the number of rejected measurements can be monitored in real-time. An option of multi-selection of files enables fast treatments of long series of files.

Another GUI allows assembling processed files into radial profiles using multi-selection of files. Data can be grouped according to three methods:

- **Simple grouping**. The whole set of data is read, sorted out relatively to the mixture fraction and assembled into radial profiles. The purpose is to write *.txt* results files eventually used for scatter plots of radial profiles in mixture fraction space.

- **Conditional statistics**. The whole set of data is read, sorted out relatively to the mixture fraction and divided into consecutive subgroups. All the subgroups contain the same amount of data points, as defined by the "sampling parameter" in the GUI. Means and RMS of fluctuations are then calculated on subgroups, and assembled into radial profiles. The purpose is to write *.txt* results files eventually used in plots of radial profiles of conditional statistics in mixture fraction space. Note that the "sampling parameter" can be used to efficiently smooth the radial profiles.

- **Reynolds statistics**. The whole set of data is read and sorted out relatively to the radial coordinate. Reynolds statistics are then applied to each subgroup of point measurements with identical radial coordinate. A "smoothing distance" can be defined in the GUI. The parameter allows smoothing the radial profiles by including in each calculation the subgroups located within a distance equal to the "smoothing distance". Reynolds statistics are calculated as defined in

Section 2.2.7. The purpose is to write *.txt* results files eventually used for plots of radial profiles of scalars versus radial location. In the present case, Reynolds statistics are more adapted than Favre statistics since on-CCD accumulations are performed to improve the recorded signals and induce averaging effects. Favre statistics are more meaningful with single-shot measurements.

Note that the “smoothing distance”, as the “sampling parameter” should be cautiously used, not to loose information on data, such as peak locations or values, for instance.

6. EXPERIMENTAL SETUP AT NTNU

6.1. Description of the experimental setup

6.1.1. Overview of the experimental setup

Figure II.18 shows a general overview of the experimental setup as used during the experiments. The experimental setup is mainly composed of:

- A frequency-doubled Nd:YAG Continuum Agilite laser system, emitting at 532 nm, 10 Hz and ca**.** 530 mJ/pulse,
- The oxy-fuel combustion chamber standing on a moving structure,
- An Acton Research SP300i spectrometer collecting the Raman signals,
- A Princeton Instruments PI-MAX ICCD camera directly fitted on the spectrometer.

Due to space constraints in the operating room, the laser system is in a separate room, offering the advantage of a better temperature control of the laser system. A narrow tunnel links the two rooms, so that the laser beam can pass through.

In the laser system room, once the laser pulse is emitted from the laser system, it hits two mirrors to pass the tunnel following a horizontal plane. Before reaching the operating room, a polarizer and a 25.4-mm-diameter focusing lens (f = 0.4 m) lay on the laser beam path. The focus is then achieved inside the chamber. The 8-mm original beam is focussed to ca. 65 µm, calculated between the points where the intensity has fallen to $1/e^2$. At both ends of the probe volume imaged onto the entrance slit of the spectrometer, the beam diameter is ca. 69 µm. On the other side of the chamber, a beam dump dissipates the laser energy.

The optical collection system is aligned with a normal direction to the laser beam. It consists of a 100-mm-diameter collection lens (f = 250 mm), a notch filter to separate out the strong Rayleigh signal at 532 nm, a spectrometer and an intensified CCD camera. Raman signals are captured and spectrally decomposed through the system, recorded and sent to the computer where results are displayed as spectra.

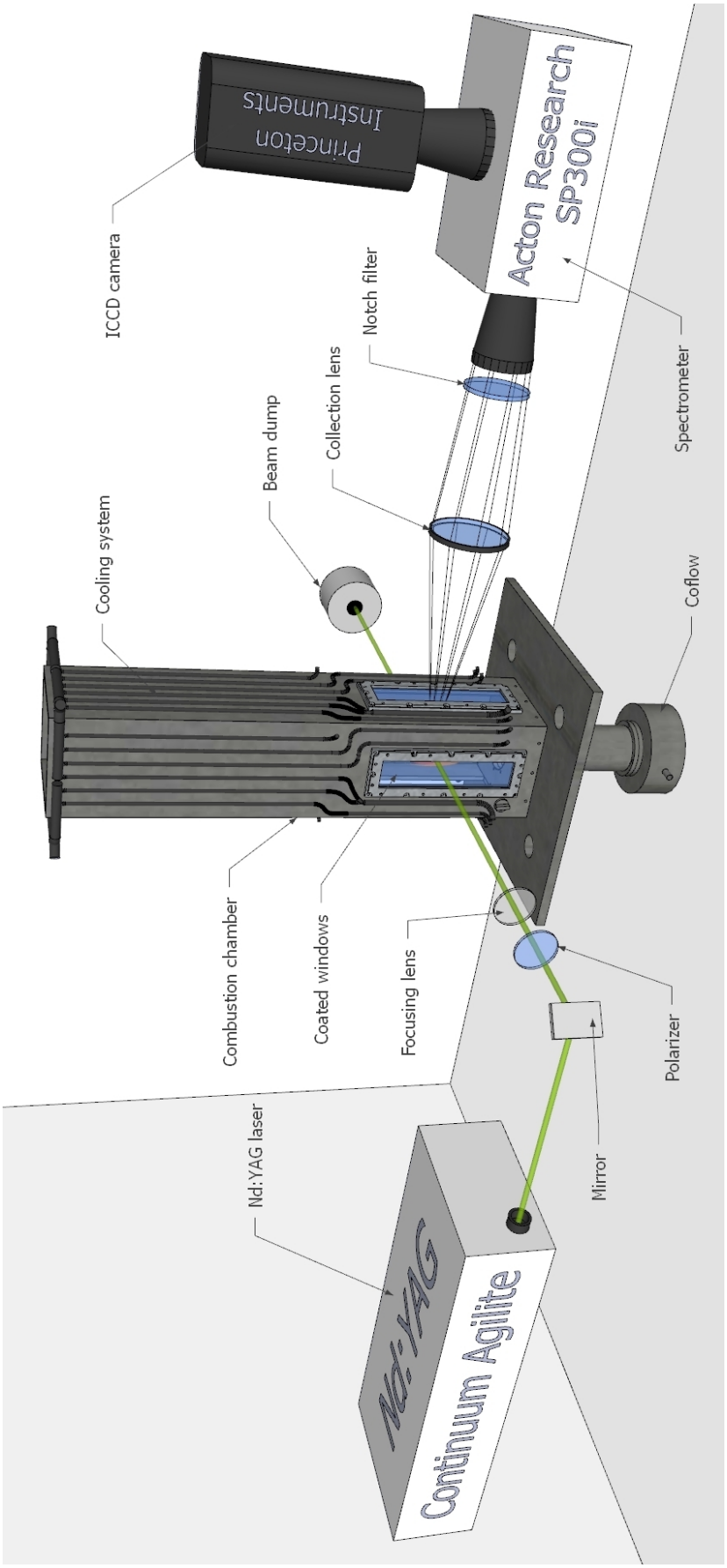

Figure II.18: General overview of the laser Raman scattering experimental setup for the oxy-fuel combustion chamber.

6.1.2. Laser system

The laser system is a Continuum Agilite 569-10 frequency-doubled Nd:YAG. Three pairs of flash lamps (cf. Figure II.19) make it reach ca. 530 mJ/pulse at 532 nm, 10 Hz and with pulse duration of 400 ns. A pulse shaper enables temporal shaping the pulse. The laser system is fully controlled through a laptop computer, whose controls are duplicated in the operation room for more convenience. An overview of the laser spatial profile is shown in Figure II.20. Measurements were made by the manufacturer at 532 nm and 0.75 m from the laser output port. They show great repartition of the laser energy and good circularity.

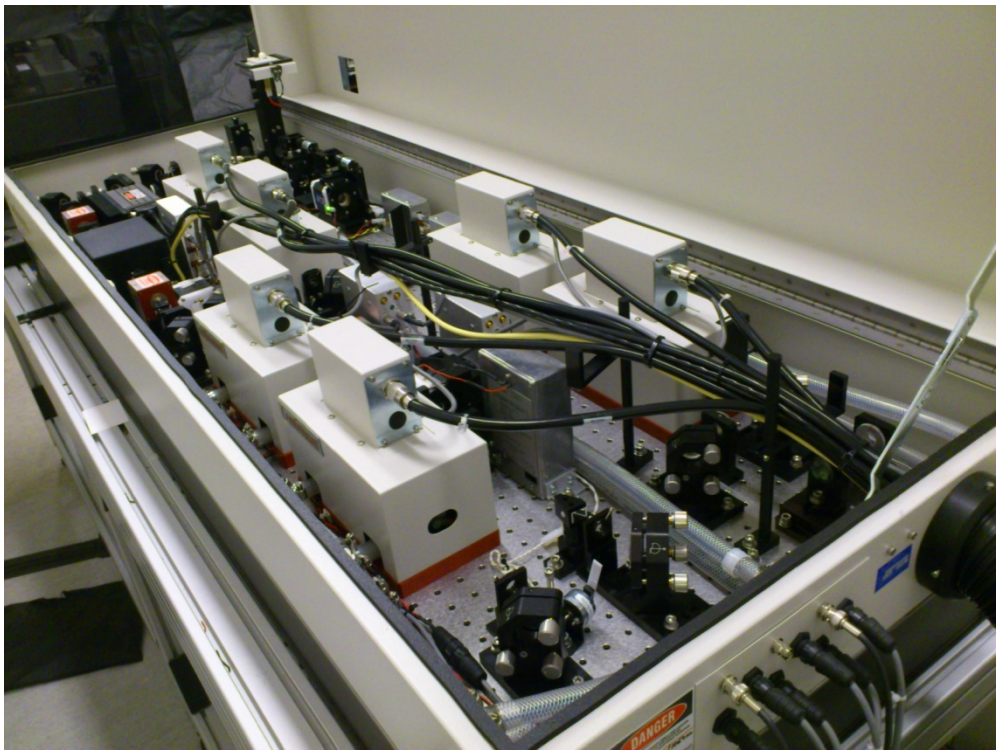

Figure II.19: Continuum Agilite laser system, under the hood.

The laser system was initially optimized by the manufacturer for pulse duration of 200 ns to achieve the highest laser energy output with the best stability. Though resulting Raman signals from the setup were of good quality in open air, the instantaneous laser energy peak was too high to pass through the precision windows from the oxy-fuel combustion chamber. Indeed, first tests using full laser power through the windows lead to one damage on one of the precision windows, as depicted in Figure II.21.

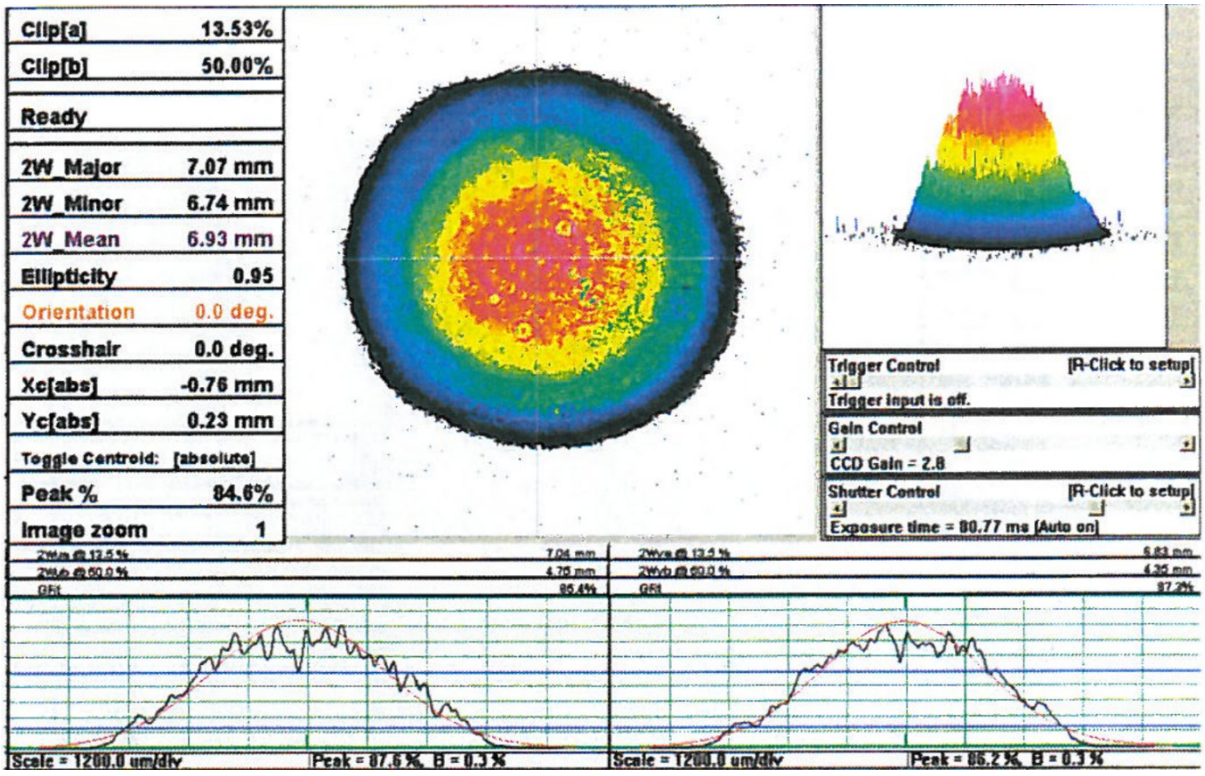

Figure II.20: Overview of the laser spatial profile. [Continuum 2008]

Figure II.21: Damage on precision window due to intense laser beam.

Two changes were made to solve the problem without affecting the Raman signals quality. First the focusing lens, with a focal length of 1000 mm at the time, was replaced by another with a focal length of 400 mm. The purpose was to decrease the laser energy density through the precision windows. Previously, the laser focus was achieved at about 100 mm from both precision windows, so that ca. 90 % of the maximum laser energy density was reached while crossing the window. With a 400-mm

focal length, only ca. 75 % of the maximum laser energy density was achieved at this point. Using an even shorter focal length was not possible due to the significant laser reflections induced by the windows and the space required around the combustion chamber for translation movements.

The second change that was made consisted in doubling the pulse duration. Usually, a complex and non-flexible optical setup, so-called pulse stretcher [*Nguyen* 1996, *Wehr* 2007, *Kutne* 2011], is required to divide the laser beam and delay it through different paths. This also enables to avoid optical breakdowns. Thanks to the temporal pulse shaping functionality of the Continuum Agilite laser system, this can be conveniently achieved without using a pulse stretcher. Within the firmware, a module allows designing the curve of the electrical input into the pulse shaper unit. Using a photodiode monitoring a reflection of the laser beam close to the laser output, the evolution of the pulse temporal shape can be observed on an oscilloscope. The pulse temporal shape can be iteratively built up by tuning the pulse shaper. An example of the pulse temporal shape recorded on oscilloscope is shown in Figure II.22. The temporal shape showed relatively good regularity during each day of measurements, and from day to day.

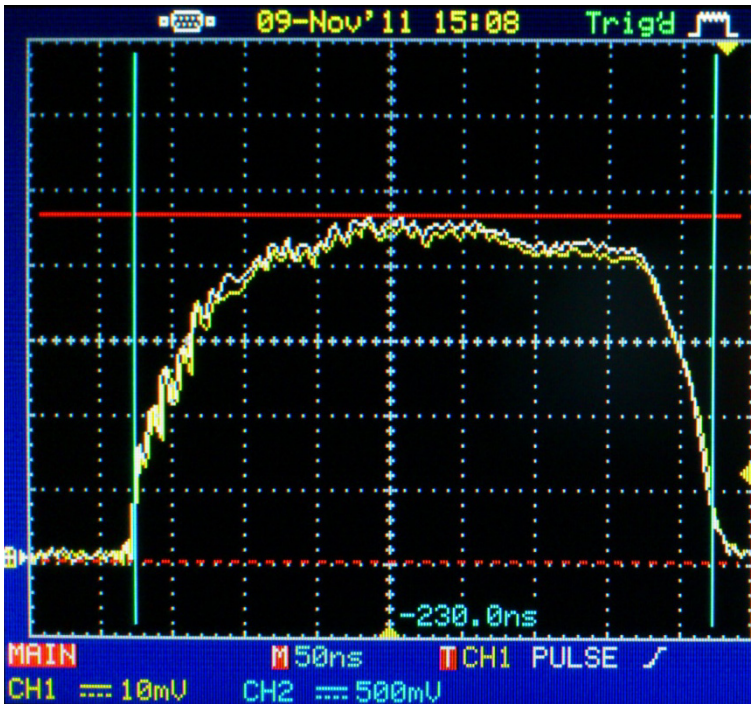

Figure II.22: Pulse temporal shape recorded on oscilloscope. The yellow solid line is the pulse being measured, and the white solid line is a pulse shape stored in the memory of the oscilloscope four weeks before.

Measurements of the energy from the 400-ns long laser pulse were performed on a daily basis. Figure II.23 shows the evolution of the laser output energy recorded over 2000 consecutive pulses. The amplitude of the fluctuations over 2000 pulses, calculated as the ratio of the standard deviation and the mean energy always remains in

the range 0.6 - 0.8 % of the mean laser energy. The laser system is undeniably the component of the setup giving the least uncertainties.

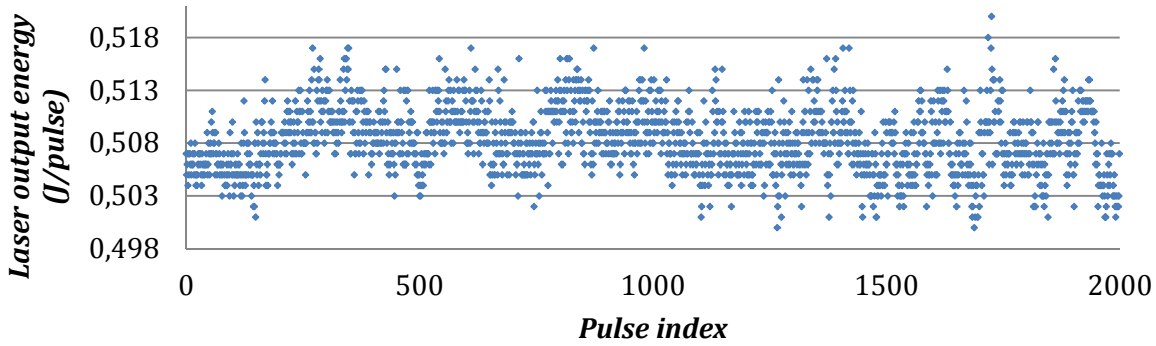

Figure II.23: Scatter plots of the laser output energy over 2000 consecutive pulses, recorded with Coherent Labmax-Top.

6.1.3. Light collection and detection system

The light collection and detection system consists of all elements conveying the signals from the probe volume to the operator's screen. Each of those elements has been selected to give the best available transmittance to keep signals intensity at acceptable levels and their number is reduced to the minimum to lower losses and non-linear optical effects. Some elements are hidden by the protective shield preventing from laser reflection leaks into the collection system.

The first element is a 100-mm-diameter $f/2.5$ plano-convex collection lens with a 250-mm focal length. Since the actual focal length depends on the wavelength of observed signals, the focus and the alignment are performed relatively to the 607-nm band from the nitrogen Raman signal. The large diameter of the lens enables to capture sufficient signal intensity through a fairly wide solid angle. A 160-mm-diameter black tube surrounds the lens to prevent any laser reflection from being carried into the collection system through the collection lens. The tube proves to significantly reduce the noise level in the spectra by attenuating the effects induced by laser reflections.

The second element is a 25-mm holographic notch filter from Kaiser Optical Systems Inc**,** used as a band rejection filter to transmit most wavelengths without alteration and to attenuate most of the Rayleigh signal intensity centred on 532 nm. Its FWHM is ca. 15 nm. This element is located right in front of the spectrometer slit due to its small diameter and its ability to reject potential laser reflections leaking into the collection system. The filter has a strong dependence on the impact angle, which has been optimized for the best attenuation of the Rayleigh signal without altering the Raman signals on the spectra. Rayleigh scattering signals in flames are relatively more intense than in non-reacting flows and tend to spread out of the efficient bandwidth of the notch filter. Thus, branches of the Rayleigh signal appear on spectra on each side on

the attenuated Rayleigh band at 532 nm, though their intensity is not sufficiently high to significantly affect Raman signals.

The third element is an Acton Physics SP300i spectrometer using a Czerny-Turner configuration with aspheric mirrors and a reflective ruled diffraction grating with a density of 300 grooves.mm^{-1}, a blaze wavelength of 300 nm and a dispersion of ca. 11 nm.mm^{-1} at 500 nm. Though, its best efficiency is given for 200 – 500 nm, it can properly capture the whole range of useful wavelengths (from about 500 nm to 700 nm). The grating is centred at 610 nm, very close to the nitrogen band at 607 nm. The spectrometer and the wavelength calibration have been regularly performed using a Hg lamp from Lot-Oriel.

The fourth element is a Princeton Instruments PI-MAX intensified CCD camera. The camera is set up at the top of the spectrometer, at the exit of its optical path. Its CCD chip is an EEV 256x1024F CCD 30, its resolution was 1024 x 256 pixels and the chip is kept at -20 °C during operations to limit the dark noise. The ICCD camera is linked to a Princeton Instruments ST-133 controller, where the laser pulse trigger is received to synchronize the gating with the laser pulse. The intensifier enables signal enhancement of the weak Raman signals at the expense of a significant level of electronic noise added to the recorded spectra. The camera achieves relatively accurate and short temporal gating.

The controller and the spectrometer are linked to the operator's computer where Winspec is used as the data acquisition platform. Winspec enables to control the camera and the spectrometer, to calibrate the spectrometer and to record series of spectra. Output *.SPE* files are typically recorded as three dimensional matrices, with namely, spectral, spatial and temporal dimensions. A series of parameters is also encapsulated into the *.SPE* files. The spectral dimension is taken over 1024 pixels, while the spatial dimension is recorded over 256 pixels. The choice of the optimal parameters for the spectrometer and the camera is described in Section 6.3.2.

6.1.4. Hencken burner

As illustrated in Figure II.24, a Hencken burner is used on the side of the oxy-fuel combustion. The burner achieves flat fields of cold flows or laminar premixed flat flames in quasi-adiabatic conditions. The burner does not actually issue a proper premixed flame, but rather a fine array of non-premixed flamelets from a pattern of adjacent capillary tubes. Flames generally appear as thin flame sheets, a short distance above the burner. Besides fuel and oxidizer, a third inlet is available in the Hencken burner for a shroud flow. Generally consisting of air or nitrogen flow, the shroud accompanies the main flow and prevents it from early mixing with the ambient air. One

of the main assets of the Hencken burner is its ability of generating flows that can be readily predicted with commercial combustion codes.

Figure II.24: Hencken burner.

6.1.5. Gas supply

The layout of the gas supply is illustrated in Figure II.25. A total of seven mass flow controllers are used for the oxy-fuel combustion rig. Details are given in Table II.6. CO_2 flow is divided into two flows: the main one coupled with O_2 in the oxidizer stream, and another coupled with CH_4. N_2 flow has a free end in the operation room since it is mainly used with the Hencken burner. Any of the other gases can also be plugged into the Hencken burner from the valve control panel. No laminar flow elements were available to calibrate the mass flow controllers and the calibration from the suppliers brings uncertainties estimated at 2 % of the set point value.

Table II.6: List of mass flow controllers used with the oxy-fuel combustion rig.

Name	***Gas***	***Range (Nl.min^{-1})***	***Uncertainties (%)***
MFC – 21	CO_2	0 – 250	2
MFC – 30	CO_2	0 – 5	2
MFC – 15	O_2	0 – 80	2
MFC – 1	H_2	0 – 30	2
MFC – 19	CH_4	0 – 70	2
MFC – 3	N_2	0 – 80	2
MFC – 27	Air	0 – 500	2

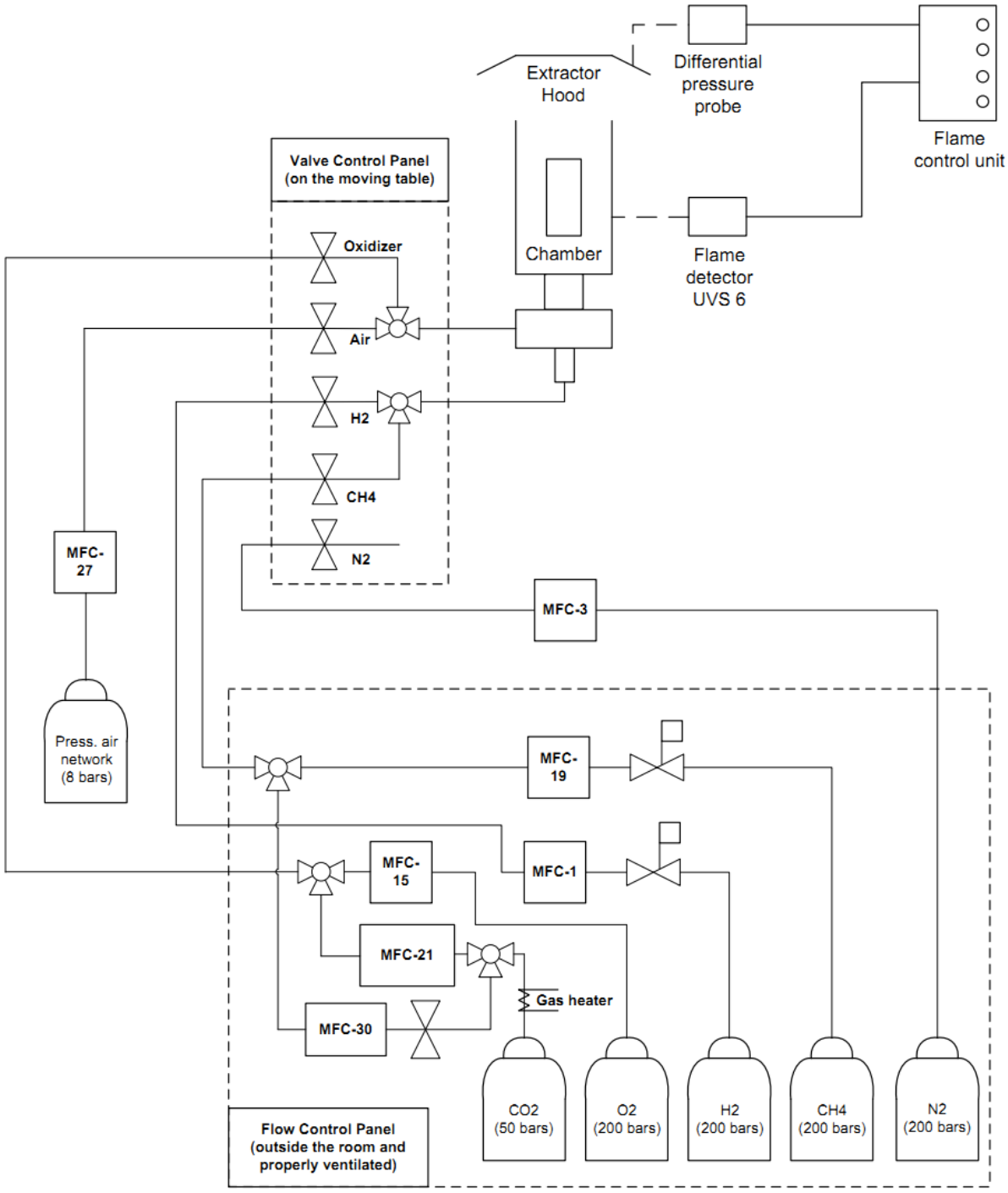

Figure II.25: Layout of the gas supply for the oxy-fuel combustion rig.

6.2. Combustion chamber design

6.2.1. Requirement of a new combustion rig

A previous combustion chamber erected for SINTEF Energy Research had provided great results during the previous campaigns of experiments with oxy-fuel combustion [*Ditaranto* 2011]. This setup was using a 100-mm coflow and 3- to 6-mm central fuel tubes, and provided a power outlet within the range 0 - 25 kW. However, the design of the chamber did not match the optical access requirements to apply LRS measurements. At least three windows are required: two opposed to each other to let the laser beam pass through, and one normal to the laser beam for data collection, as LRS is a non-coherent laser technique [*Eckbreth* 1996]. Consequently, a new chamber was designed to fulfill those requirements. The choice was done to keep the same range of dimensions and to use a similar coflow burner, to make the new results comparable to the previous ones. Measured temperatures, flame lengths and flame stability from previous experimental campaigns provided significant help for designing the new chamber.

Based on experience, considerable improvements from the previous combustion rig were implemented in the design of the new one. The previous chamber was based on a cylinder whose walls were probably too thin to stand high temperature gradients. Consequently, while welding the flat flanges made to withstand the flat optical windows, the high temperature curved the flat surfaces, inducing non-flat areas where windows often broke down while being tightened to the chamber. Additionally, it was not possible to ensure that windows were set parallel to each other to avoid laser energy losses or uncontrolled reflections. Therefore, the new chamber is square-based, with thick walls, to solve the former issues. The cross-section of the chamber is also reduced to lower the amplitude of the potential recirculation at the coflow outlet. However, a certain width was required to avoid having the flame into contact with the walls, which could dramatically affect the measurements.

Another improvement is to use wider and longer windows to offer more flexibility with the optical measurements and a sufficiently large solid angle to perform Laser Doppler Velocimetry, for instance, which might eventually complete the data library on oxy-fuel flames.

Furthermore, as the previous rig showed some instability, such as lift-off, when burning methane with an oxidizer mixture of 70 % CO_2 and 30 % O_2 or below [*Lode* 2009], the new coflow burner enabled burning mixtures of methane and hydrogen to increase the range of stability.

6.2.2. Overview and general design specifications

A CAD drawing shown in Figure II.26 offers an overview of the oxy-fuel combustion chamber. It consists of four rectangular walls, leaning on a robust table. The coflow is screwed to the down side of the table and passes through a squared-hole to access the inside of the chamber. Four frames opposed two-by-two are set up on the wall to hold the optical windows. Four independent cooling systems are set up along the walls. The whole block shown in Figure II.26 is about 1.5 m high.

General design specifications:

- Power outlet: 0 - 25 kW.
- Operating pressure: atmospheric.
- Fuel: CH_4 + H_2.
- Oxidizer mixture: O_2 + CO_2, O_2 molar fraction in oxidizer from 20 to 100 %.
- Burner: 95-mm coflow, with 3.6-mm central fuel tube.
- Combustion chamber height with mounted coflow: 1.5 m.
- Combustion chamber cross-section: 200 x 200 mm.
- Chamber wall thickness: 10 mm.
- Chamber and coflow material: steel/stainless-steel.
- Wall-cooling with water.
- Aperture for windows: 80 x 300 mm.

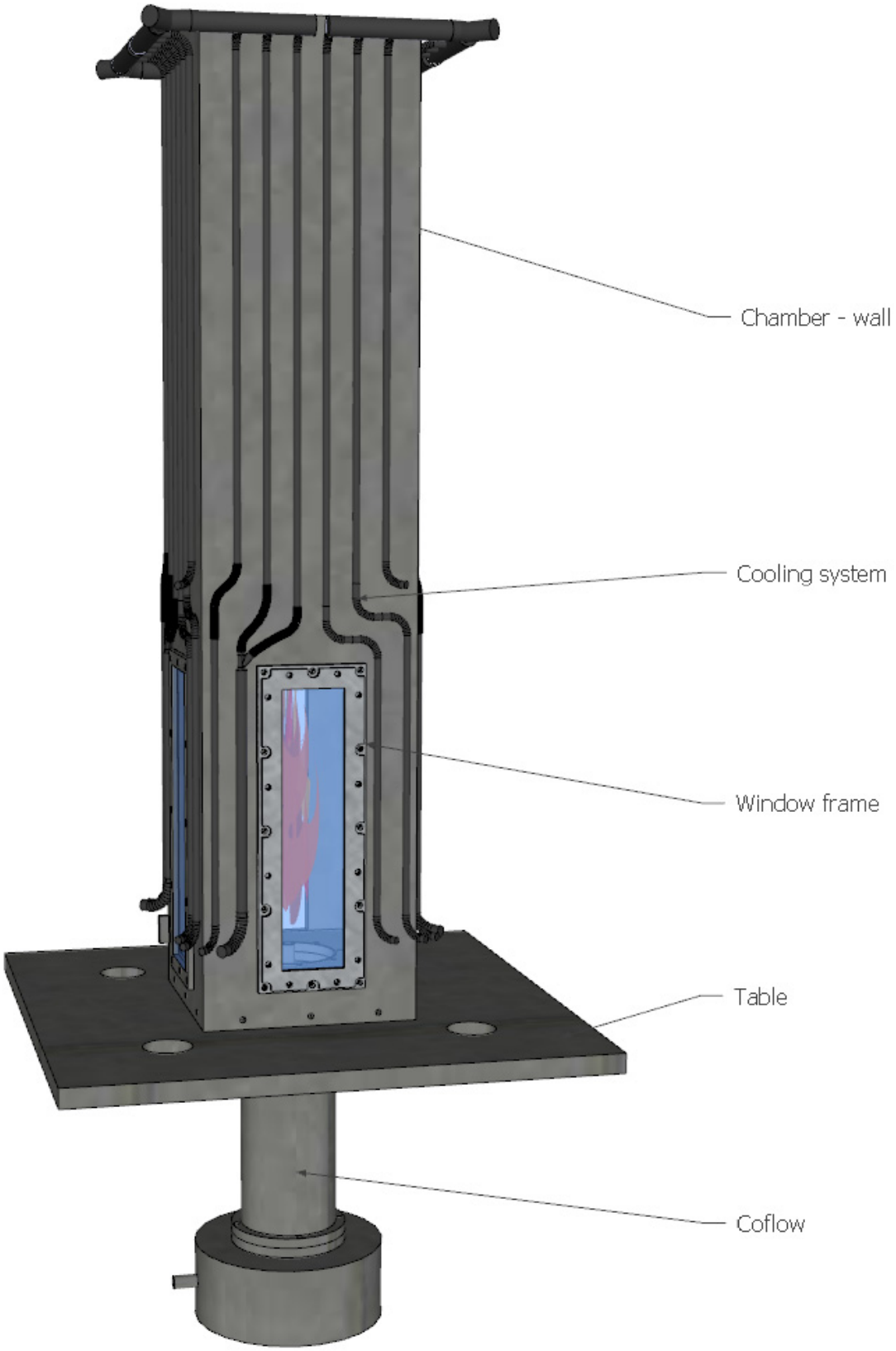

Figure II.26: CAD drawing of the oxy-fuel combustion chamber.

6.2.3. Combustion chamber

The chamber, shown in Figure II.27, is made of stainless steel, and is around 1-m high to contain the longest flames measured in the previous chamber. The wall thickness is 10 mm to prevent from any deformation resulting from temperature changes inside the chamber. The faces inside the stainless steel walls are coated with black body paint of emissivity around 0.95 - 0.98. Besides reducing laser reflections, the paint gives a better thermal inertia to stabilize the temperature of the chamber walls, which is essential for the stability of the flame. On each side, a large opening has been made to fit the precision windows for laser applications. The windows are ca. 300-mm high, 80-mm wide and 5-mm thick. As shown in Figure II.28, their bottom-line corresponds to the coflow outlet, so that they enable to perform measurements over the 300 first millimeters of the flame development, which is the area of interest of this investigation. Even if each side does not require openings as large as those, it has been made to keep the symmetry inside the chamber, to comply with the assumption of the axisymmetric flame.

The walls are screwed all together, to avoid affecting the flatness of the sides by welding at high temperature. This helps fulfill the symmetry assumption of the chamber, and also ensures that the windows lay on a proper flat surface. A circular opening has been made on one of the sides, at the bottom left corner of the window (cf. Figure II.27), large enough to enable a manual propane igniter to go through. This opening should not affect the symmetry, since a stainless steel cork is made to cap it. A series of thermocouples can be also be set up along the central vertical axis of one of the chamber's sides to probe wall temperatures.

As shown in Figure II.28, to limit the recirculations around the coflow, a fitting for the upper part of the coflow allows the down flat part of the chamber to meet the level of the coflow outlet. In addition, the coflow and its fitting are lifted up by a few centimeters, so that the coflow outlet reaches the bottom-line of the precision windows. This enables to capture the flame from the very beginning of its propagation.

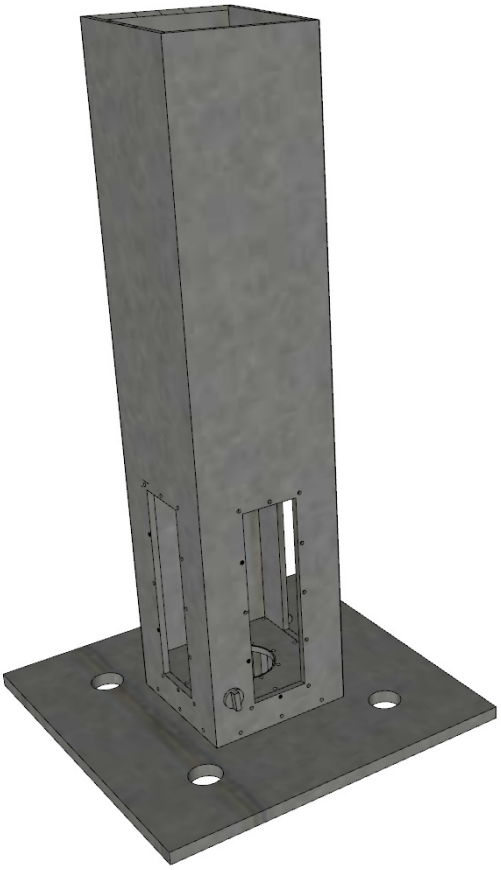

Figure II.27: CAD drawing of combustion chamber alone.

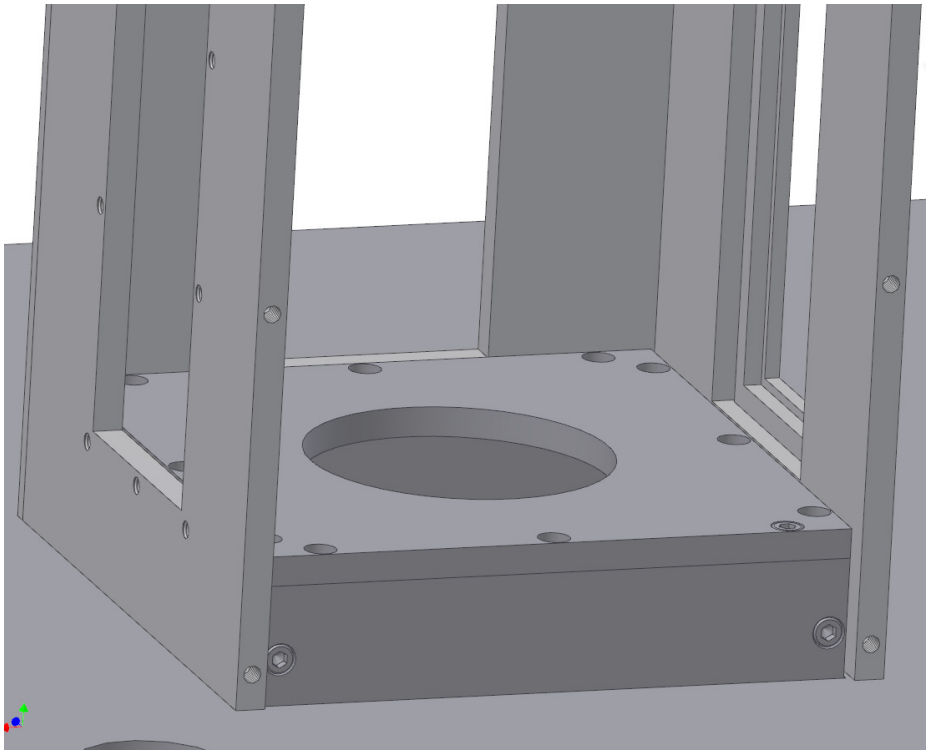

Figure II.28: CAD drawing of the fitting for the coflow upper part, inside the chamber.

6.2.4. Coflow burner

The coflow block, shown in Figure II.29 (left), has a relatively simple geometry. It is 450-mm long and is the essential part of the combustion rig. It consists of the coflow tube, two weld-neck collars, the fuel tube, the plenum, and the fuel flange.

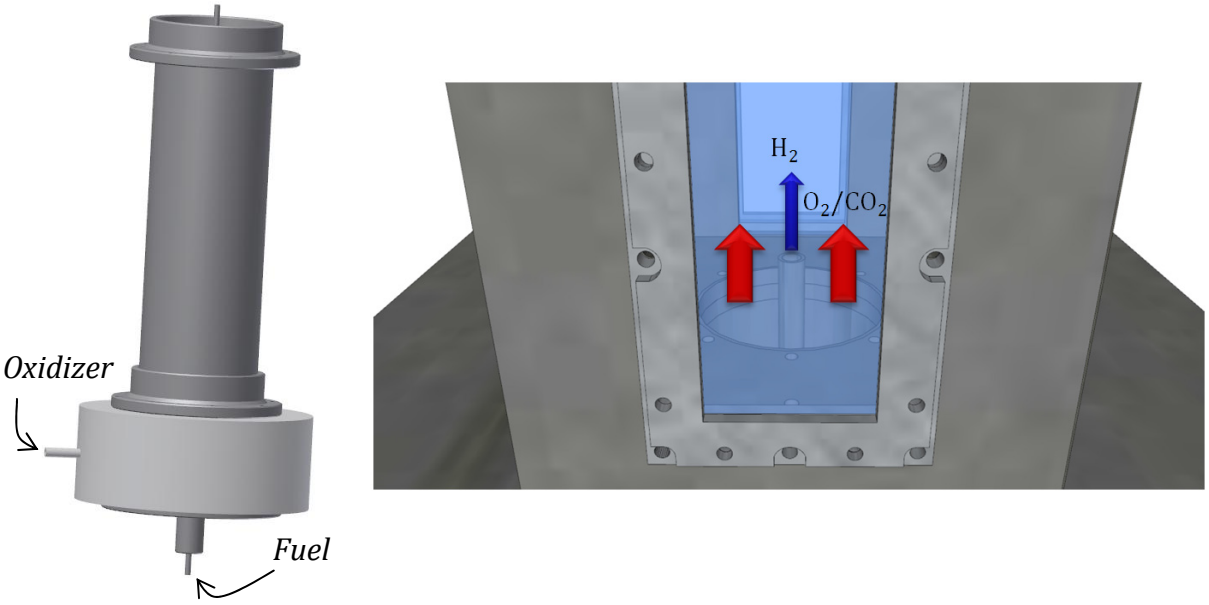

Figure II.29: Left: CAD drawing of the coflow block with 3.6-mm-inside diameter nozzle. Right: CAD drawing of the coflow top inside the oxy-fuel combustion chamber.

The coflow tube is 300-mm long and 95-mm inside diameter. The fuel tube is going all along its centerline. It has been designed with such a length that the flow is fully developed when reaching the coflow outlet. Besides, as shown in Figure II.30, a 80-mm long honeycomb cylinder in aluminium with 3-mm diameter cells is set in the middle of the coflow tube to ensure this condition. Upstream from the honeycomb, a layer of around 100 mm of glass beads is contained between two perforated plates to ensure proper mixing and homogeneous flow.

The seamless fuel nozzle is 3.6-mm inside diameter and 4.6-mm outside diameter. The nozzle has 0.5-mm wall thickness and squared-off end to improve flame stabilization by the small recirculation on the rim. Its length of 550 mm ensures that the flow inside the tube is fully developed at the outlet.

Figure II.29, left-hand side shows also the plenum, where the oxidizer mixture consisting of O_2 and CO_2 has its last step of mixing before entering the coflow tube. The plenum has a diameter of 200 mm and is 80-mm high. This plenum is similar to the one used in the previous combustion rig, which was providing great results. The different items of the coflow are gas tight thanks to the use of large O-rings between every item.

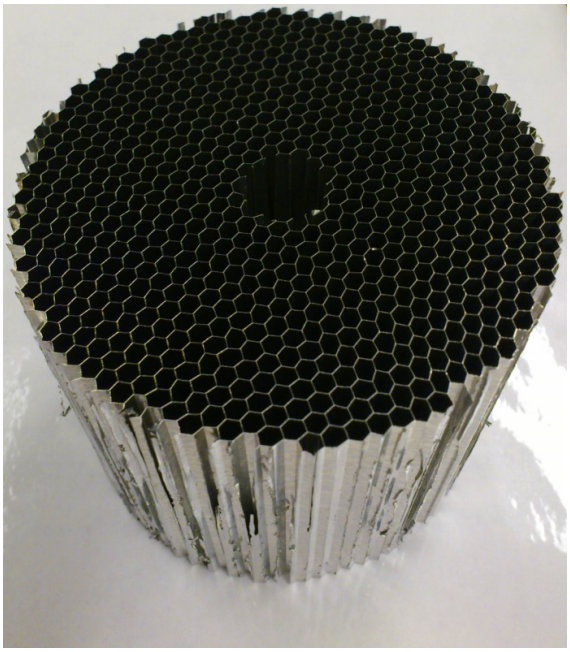

Figure II.30: Honeycomb cylinder.

While designing the coflow, a narrow diameter of the fuel nozzle was chosen to reach relatively high jet Reynolds numbers. The upper flow rate limit of the gas supply is around 150 Nl.min^{-1} per typical gas bottle with the present tubing. Considering this limitation, the 3.6-mm fuel nozzle allows reaching jet Reynolds number up to 10,000 in CO_2-diluted oxy-fuel conditions. The limitation is the CO_2 supply affected by Joule-Thomson effect. A powerful in-line gas heater is required along the CO_2 line to compensate with the significant decrease in temperature.

This relatively simple configuration ensures flame reproducibility, and brings a wide flame stability range if H_2 is used as fuel. It enables to obtain fairly blue and Raman-friendly flames in some conditions. The counterpart is that using H_2 as fuel brings the experimental results further away from typical methane flames, though hydrogen is Raman-active and brings no new atomic species to the mixture.

Simple flame calculations were carried out with Gaseq to determine the adiabatic flame temperatures of $CH_4/O_2/CO_2$ and $H_2/O_2/CO_2$ mixtures, under the same conditions of pressure and reactants temperature. The purpose was to verify that both mixtures are in the same range of flame temperatures, relatively to the oxygen content in the oxidizer. Results are shown in Figure II.31 at stoichiometric conditions. Though $H_2/O_2/CO_2$ mixtures lead to higher flame temperatures, the two different mixtures follow the same trend and are in the same range.

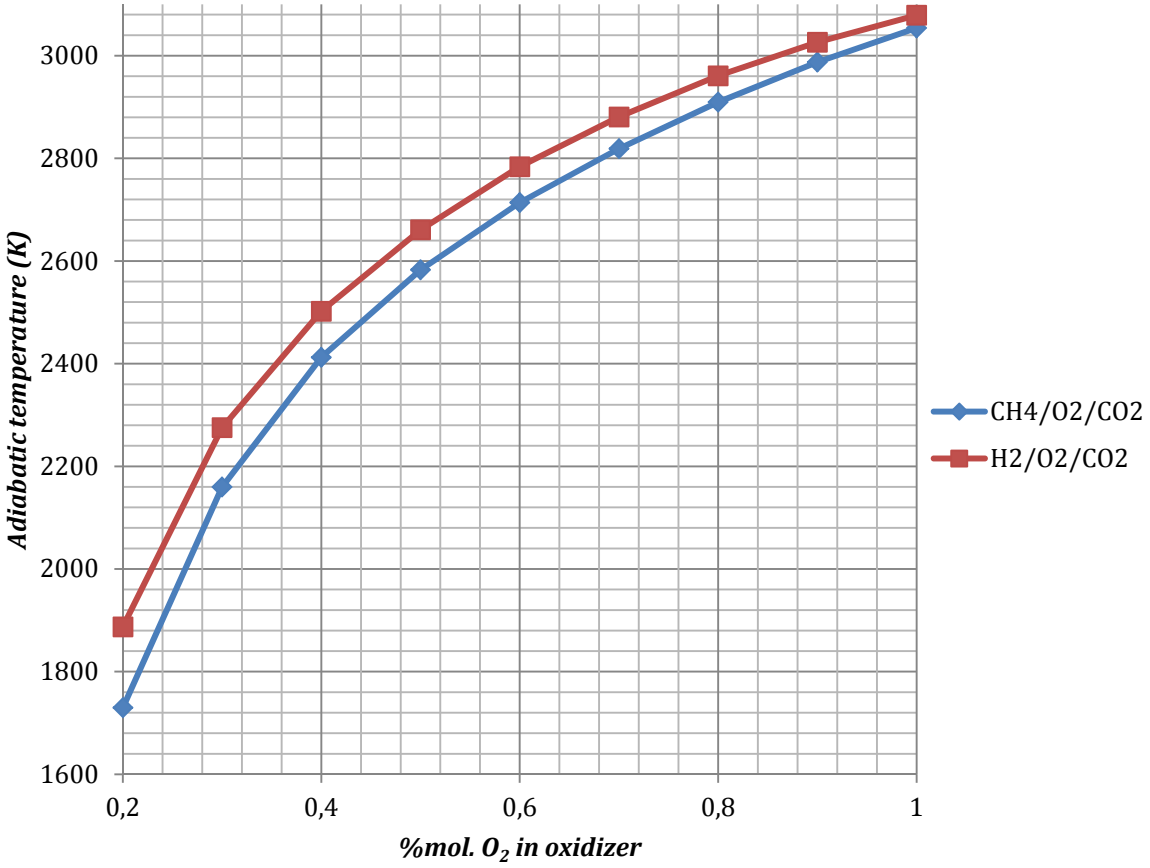

Figure II.31: Results from Gaseq calculations on adiabatic temperature versus oxygen molar fraction in oxidizer for two different mixtures: $CH_4/O_2/CO_2$ and $H_2/O_2/CO_2$.

6.2.5. Windows frames

To enable the oxy-fuel combustion rig to be used with laser-based diagnostics such as LRS, large precision windows are required. Those are 80-mm wide and 5-mm thick. The dimensions of the precision windows provide a large solid angle to collect the scattered light from the probe volume. Made of Fused Silica Corning 7981 of high purity, the precision windows are able to stand very high laser power in normal impact. A special anti-reflection coating optimized for 532-nm lasers allows reducing losses when passing through the interfaces of the windows.

All those requirements made the precision windows pricy. Since, on the previous combustion chamber, the fitting for the precision windows eventually weakened them, a frame has been designed to hold them and ease their manipulation with the new combustion chamber (cf. Figure II.32 and Figure II.33). The frame is made of stainless steel flanges. A fitting is manufactured in one of them to receive the precision window. A rectangular 1-mm-thick carbon sealing is set on both sides of the windows to avoid any steel-glass contact, reduce physical stresses and keep the walls gas-tight. The two flanges can then be assembled together with screws. Once assembled,

the frame does not need to be taken apart, even for cleaning the precision windows. The frame protects the precision window from any risk of breaking or being damaged while mounting it on the wall, or cleaning it. Fine parallelism between the precision windows can be directly adjusted while mounting the frame on the wall, thanks to another 1-mm-thick carbon sealing between the frame and the wall. Since some of the frames have to be regularly taken down from the walls, it also eases the manipulation and storage of the windows.

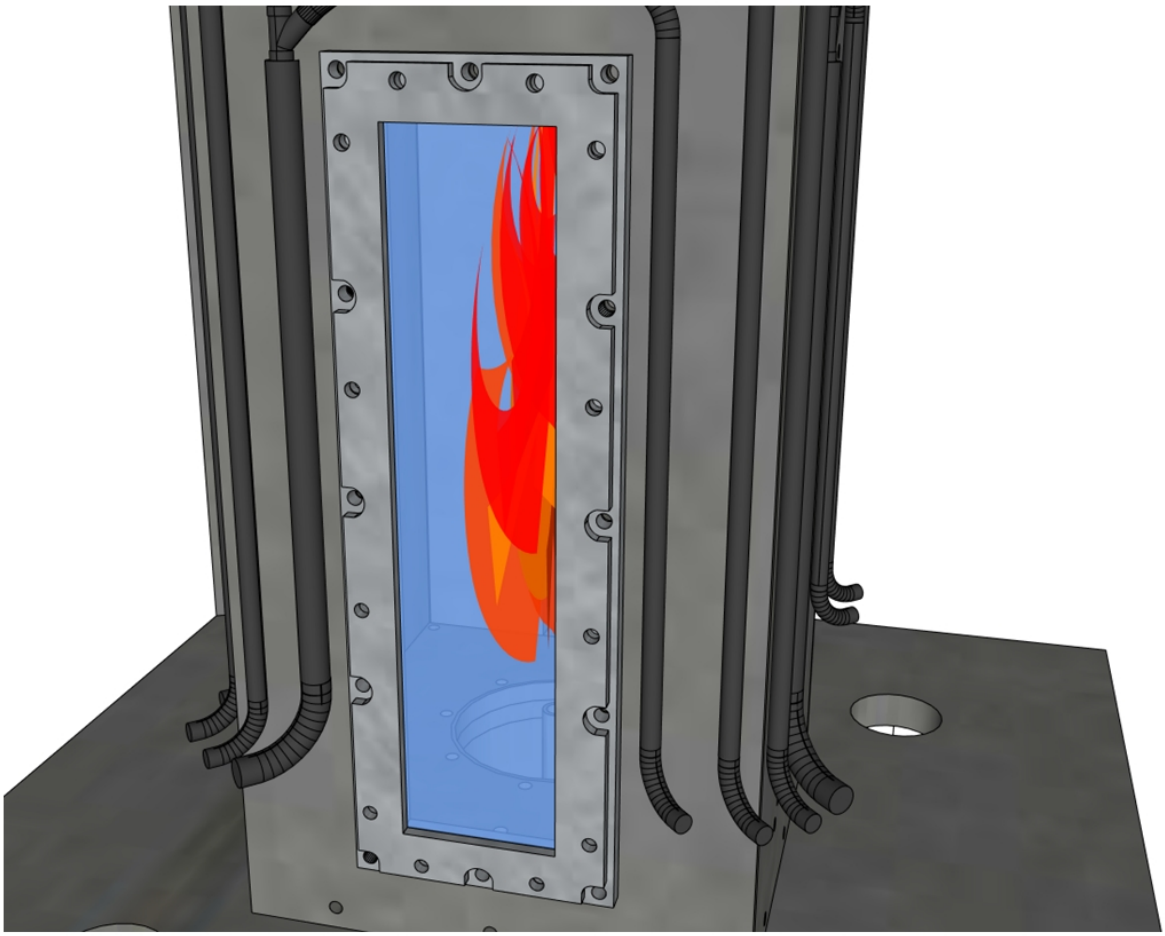

Figure II.32: CAD drawing of the window frames set on the combustion chamber.

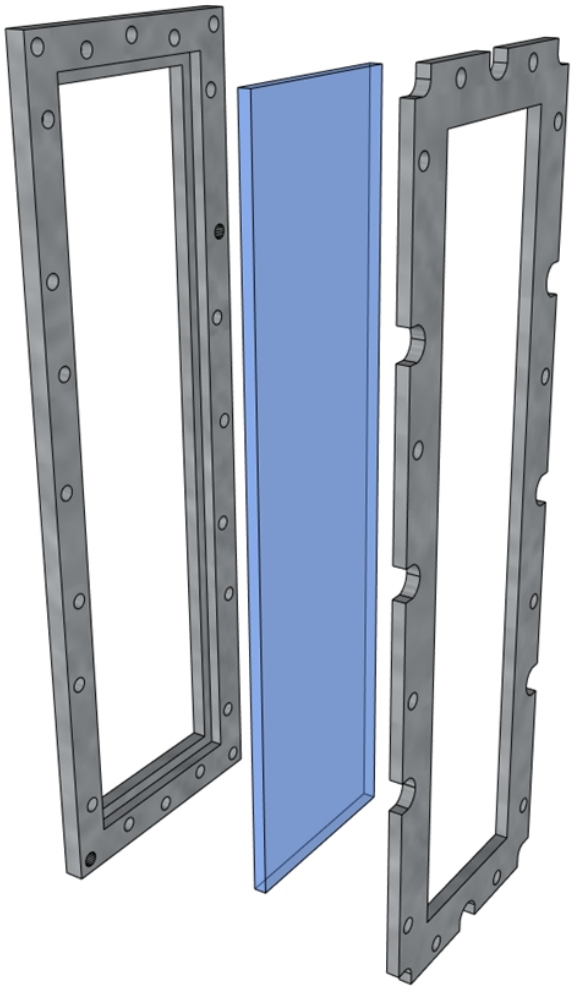

Figure II.33: CAD drawing of the window frames.

6.2.6. Cooling system

Despite a relatively low range of power (0 - 25 kW), a water cooling system is implemented on the combustion chamber. It maintains the wall temperature quite constant, all along the walls, induces more stability for the flame and makes experimental conditions easier to reproduce. The maximum wall temperature is also reduced for a better protection of the chamber material.

Since high cooling efficiency is not targeted, the cooling system design is fairly simple. As shown in Figure II.34, metallic tubes are set along the walls. To simplify the tubing, the cooling along the walls is divided into four independent systems, with one inlet at the top of each wall (Figure II.34). Note that the fittings at the manifolds are easily removable since the four walls should be removable for more flexibility. Then the tubes carry the water downwards the walls, to smooth the potential vertical temperature gradient. Around the windows, some of the tubes merge, solving space constraints. The tubes pass finally through the large circular holes drilled in the main table to join the control valve after merging into one main tube per network. Since high

local temperature gradient could have altered the flatness of the walls, welding the cooling tubes was avoided in favour of simply leaning them along the walls. Metal parts are screwed to the walls to hold firmly the cooling tubes into contact with the walls, as depicted in Figure II.34. Consequently, squared-tubes are used to get large surface into contact with the hot areas. The cooling system efficiency is sufficient for the present rig and given flame power range.

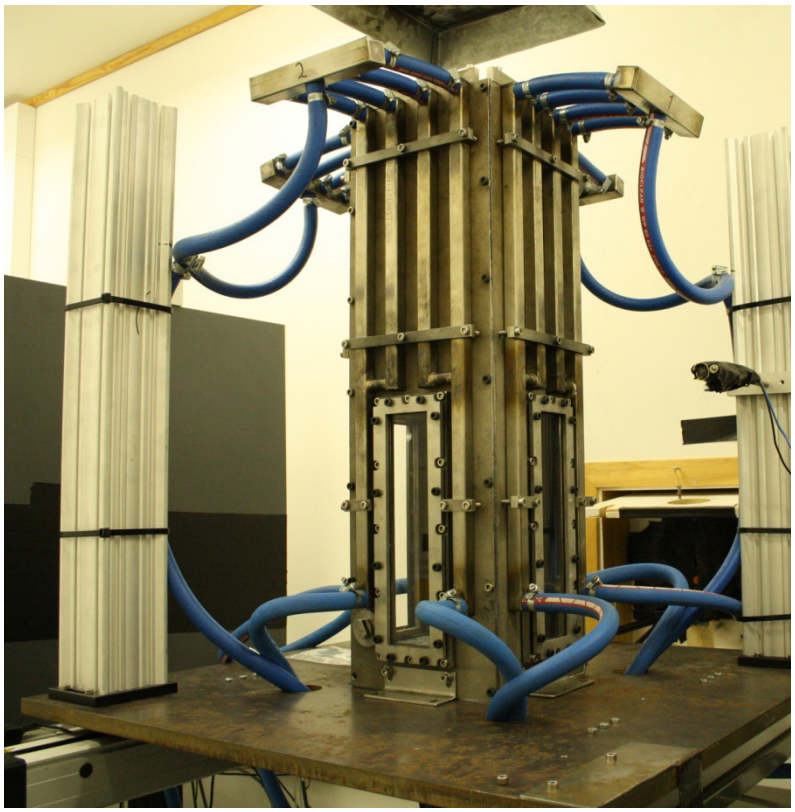

Figure II.34: Cooling system along the wall of the oxy-fuel combustion chamber.

As illustrated in Figure II.35, the inlet tube is plugged to the water tap of the laboratory, where cooling water temperature can be changed from ca. 4 °C to 65 °C. The control panel is set downstream from the four networks and enables to control the different water flow rates. A thermocouple is set upstream from each network to harmonize the cooling of the four units. The water flow rate of each unit can also be visually controlled, and eventually measured, at the outlet of the tubes where the water is evacuated in the sink, as shown in Figure II.35.

Figure II.35: Cooling system control panel, system inlet and system outlet.

6.3. Signal optimization

The following focuses on a series of improvements made to optimize the raw Raman signals recorded in Winspec, as the quality of the processed results is directly correlated to the quality of the raw signals. Those improvements are made at different levels, from the effects induced by the combustion rig to the detection system settings.

6.3.1. Combustion rig

The combustion rig is, by definition, interfering with the recorded signals. The construction of the rig itself or fresh gases temperature and purity might be sources of interferences.

As mentioned in Section 6.1.5, while expanding the gas from the bottles to the setup, gases are affected by the Joule-Thomson effect. Depending on the nature of the gas and its flow rate, the Joule-Thomson effect might have a significant impact on the outlet gas temperature. A powerful electric gas heater is set along the CO_2 gas line, between the bottles and the mass flow controllers, to balance with the induced temperature drop. The control of the CO_2 temperature might have been un-reliable for some experiments, due to fast back pressure changes in the CO_2 bottle compared to the

thermal inertia of the gas heater. This is also the reason why experiments on localized extinction are not carried out with the setup at NTNU, since the coflow temperature has a considerable influence on the localized extinction behaviour.

Gas bottles of industrial quality are systematically used since they are economical and readily available. Quality and purity of the gases are given in Table II.7. Due to their very low levels, impurities do not induce significant interferences. This quality is sufficient with the present LRS setup, since the detection limit at flame temperature is about 1 $\%_{mol}$.

Table II.7: Quality and purity of fresh gases used for the present experiments.

	O_2	H_2	CH_4	N_2
Quality	2.5	2.6	3.5	2.6
Purity (%)	99.5	99.6	99.95	99.6

Due to the detection limit, mixtures of nitrogen and oxygen are used for Raman coefficient calibration, rather than air, which includes about 1 % argon and many trace species. Argon is a single atom, and consequently not Raman active, so that it cannot be quantified by LRS. Another argument not to use air for Raman coefficient calibration was the presence of small particles, such as dusts, from the compressed air network supply of the laboratory. They visually appear across the laser beam as flashes or luminous dots of the same wavelength as the laser, and may be the source of optical breakdowns. Most of the induced light intensity on the ICCD camera is centred at the laser wavelength (532 nm), and is blocked by the notch filter. However, this may impact elsewhere in the spectra. Figure II.36 shows an example of interferences seen on two consecutive Raman spectra recorded using air from the compressed air network. The spectrum at the top displays more interference peaks, such as those emphasized by the red rectangle. Unphysical fluctuations and uncertainties might appear in the processed results if this is not corrected. Critical cases are generally handled by the optical breakdown filter implemented in the pre-processing software (cf. Section 5.2.3).

Reflections can also generate residual signals on spectra, which would alter the results. The combustion chamber is made of stainless steel for most, which might reflect the Rayleigh scattering from the laser beam, or simply the flame luminosity, though the walls are coated with black paint. An example of such reflections was observed with nitrogen-based calibration spectra at ambient temperature. Water and hydrogen radial profiles showed a significant presence on the right-hand side of the spatial profiles, though they were not present in the flow. This was due to a residual reflection entering the spectrometer. A curtain was set up next to the rig, so that the light from the combustion rig can only enter the spectrometer though the collection lens. The residual signal disappeared and signals displayed significantly less interferences.

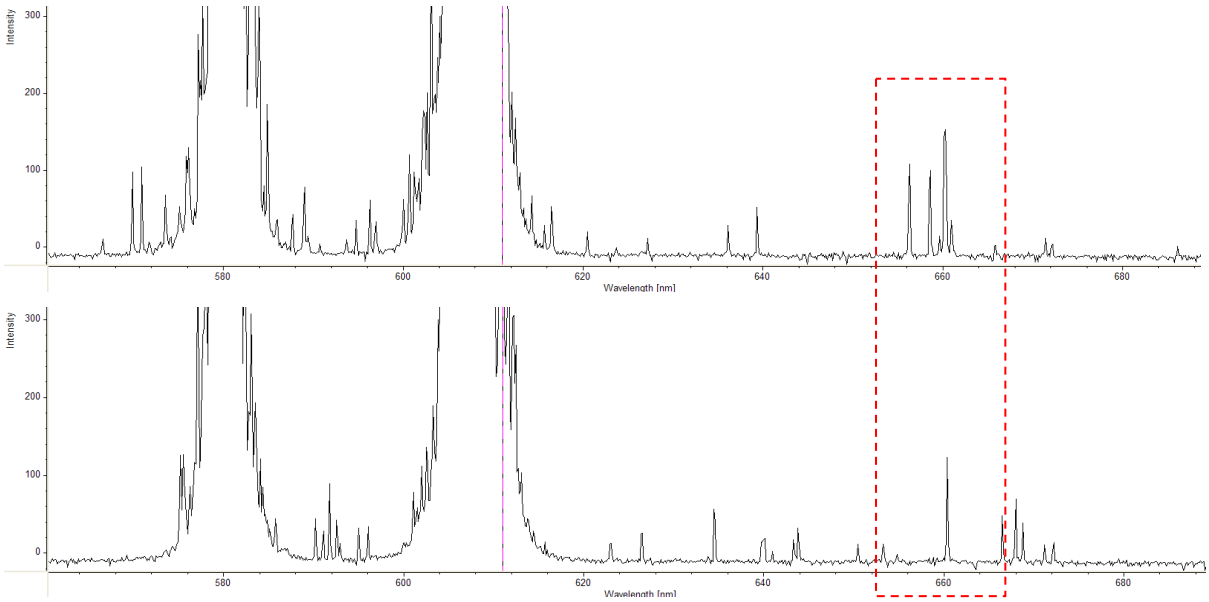

Figure II.36: Close-ups of two consecutive Raman spectra measurements in air.

For measurements performed in the combustion chamber, one precision window had to be crossed by the laser beam about 100 mm before the focal point, leading to laser reflections, slight deviation of the beam, or eventually deformation of the beam spatial profile. However, calibration measurements, mainly using a Hencken burner, have to be performed outside the combustion chamber. Despite the high purity of the precision windows and the anti-reflection coating, effects induced by the window have to be taken into account. The most efficient solution is to remove the first precision window crossed by the laser beam, and to locate the Hencken burner about 100 mm after the laser hits the second precision window, which was identical to the first one. This way, all effects induced by the precision window were directly included in the Raman calibration coefficients. The only remaining difference between both setups was the precision window settled between the probe volume and the collection lens. Nevertheless, only a slight decrease in total signal intensity was observed and could be readily compensated by an adjustment of the correcting ratio of the laser output energy within the data-processing (cf. Section 5.2.5).

6.3.2. Optical setup

Once most of the interferences induced by the combustion rig are cleared up, it becomes possible to optimize the optical setup, and especially the settings from the ICCD camera and the spectrometer.

Concerning the optics, it is necessary to get the best optical adjustment of the collection lens relatively to the combustion rig and the spectrometer slit. The probe volume should be accurately located in the centre of the combustion chamber, while its

image should be focussed on the spectrometer slit. However, the focal distance of the collection lens depends on the wavelength and is not exactly the same on both sides of the lens due to imperfections. Once an optimum setup is found, the position of the laser beam is marked by two irises, ca. 1-m distant from each other, along the laser beam path. This allows re-positioning the laser beam at the exact same location for an optimum signal when needed. The collection lens is also equipped with a vertical step motor enabling fine positioning while controlling the signal on the operator screen. Another important factor to optimize the signal quality is to have a minimum number of optics along the laser path. This avoids laser energy losses, signal deformations or fastidious alignments over time.

Most of the remaining improvements on the optical setup are made on the spectrometer and the ICCD camera. First, a grating for the spectrometer has to be chosen to offer the best response of the system over the whole spectral range of interest. Measurements using a Tungsten halogen spectral lamp LSB021 (S/N LSK 114) from LOT Oriel GmbH & CO KG allows evaluating the spectral response of the collection system. The wings of the spectra appear to be unreliable due to optical effects, so that 50 to 70 pixels on each wing cannot be used (out of 1024 pixels in total). Keeping the requirement of being able to monitor about 200 nm of the spectral axis, the 300-grooves.mm^{-1} grating has been selected. The results of the measurements with the spectral lamp are shown in Figure II.37, together with the theoretical response provided by a dedicated test report edited by Heraeus Noblelight GmbH [*Heraeus* 2006]. The gap around 530 nm is due to notch filter, blocking the Rayleigh scattering signals. With this configuration, the spectral domain of interest (from 560 to 700 nm) seems to be fairly close to the theory. A specific spectral correction is not required here since it is implicitly made in the Raman calibration coefficients. Indeed, each of those is affected to a specific spectral bandwidth, which always suffers the same spectral efficiency from the detection system.

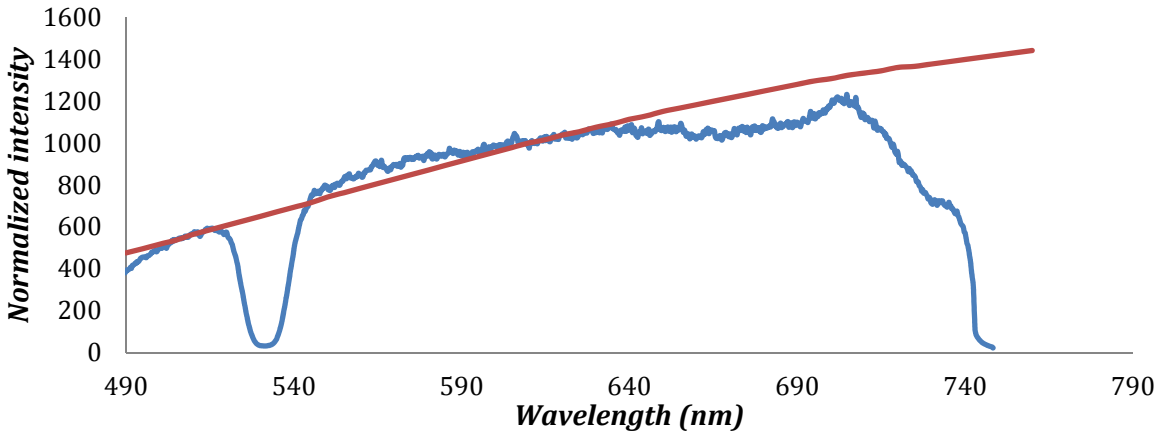

Figure II.37: Averaged measurement of the spectral response to the spectral lamp from Heraeus (blue solid line) and theoretical response (red solid line).

Another parameter concerning the spectrometer is the slit width at the spectrometer inlet. The laser beam diameter at the focus point is very narrow and may be flickering due to changing refractive index of the medium. For example, passing from high concentration of CO_2 to high concentration of H_2 might induce a significant beam steering. Consequently, the slit width should be larger than the laser beam at the focus point in order to capture the scattered signal independently of the beam steering. Besides, if the slit is too wide, undesired light (laser reflections, flame luminosity) enters the spectrometer and induces more noise on the spectra. A wide opening also leads to larger cross-talk between the spectral bandwidths, making the calibration more tedious. If the slit is too narrow, not enough Raman signal is captured. Measurements were performed in laminar premixed $CH_4/O_2/CO_2$ flat flames (50 $\%_{mol}$ O_2, Φ = 0.5) with a varying slit width from 100 to 300 µm, in order to evaluate the impact on the SNR. An averaged flame luminosity measurement was subtracted from each file. Results are shown in Figure II.38 for the CO_2 spectral bandwidth. As the purpose is to have the highest achievable SNR, the measurements seem to indicate that 250 µm would be an optimum slit width. This value is larger than the laser beam diameter of ca. 69 µm in the probe volume (cf. Section 6.1.1), so that the whole beam is captured, and no extra light, from reflections for instance, enters the spectrometer.

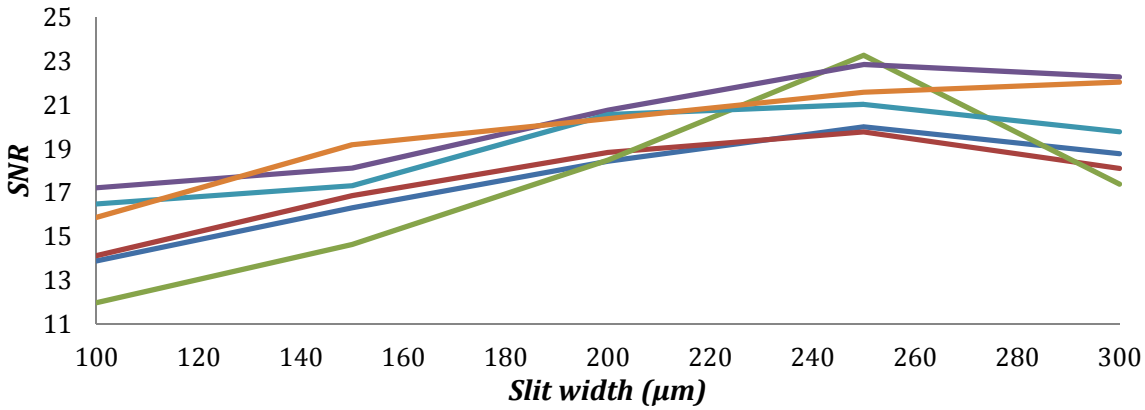

Figure II.38: SNR on CO_2 spectral bandwidth versus spectrometer slit width for a series of measurements in laminar premixed $CH_4/O_2/CO_2$ flat flames (50 $\%_{mol}$ O_2, Φ = 0.5).

Similar SNR evaluations are performed for experimental parameters related to the ICCD camera. In the present configuration of the LRS setup, single-shot measurements are not achievable since the SNR would be excessively weak. An option enables to perform on-CCD accumulations, which means that a certain number of laser pulses can be recorded on each pixel before the information is sent from the pixel to the rest of the system. Besides providing a higher signal, the noise induced by the information transfer is reduced. However, saturation can occur if too many accumulations are made. Measurements were performed in laminar premixed $CH_4/O_2/CO_2$ flat flames (50 $\%_{mol}$ O_2, Φ = 0.5) with a varying number of on-CCD accumulations from 5 to 25 to remain under the saturation limits. An averaged flame luminosity measurement was subtracted from each file. Results are shown in Figure

II.39. As expected, the trend shows that the more on-CCD accumulations, the higher the SNR. Thus, the best achievable SNR would be at the highest number of on-CCD accumulations under the saturation limits, though the laser energy fluctuations and the required time for accumulations have to be taken into consideration.

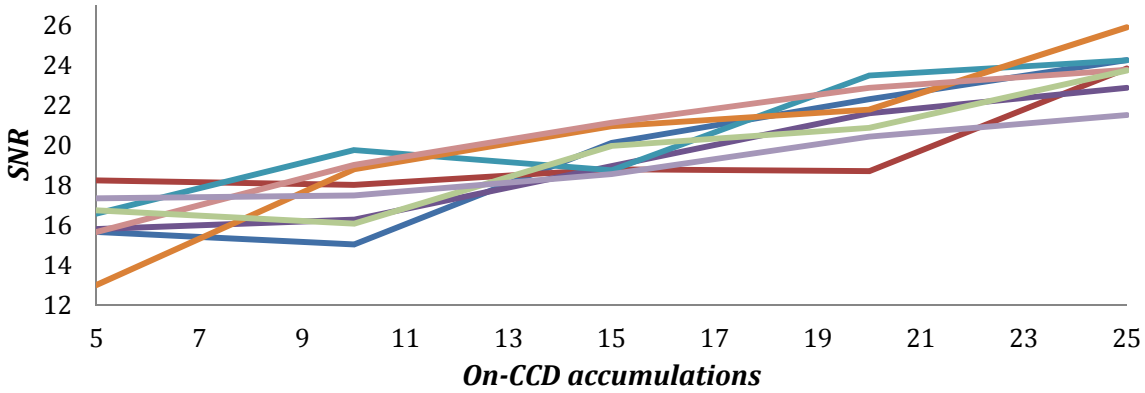

Figure II.39: SNR on CO_2 spectral bandwidth versus number of on-CCD accumulations for a series of measurements in laminar premixed $CH_4/O_2/CO_2$ flat flames (50 $\%_{mol}$ O_2, Φ = 0.5).

The gate width is the time duration used by the ICCD camera to capture the light through the spectrometer, each time after the ICCD camera receives a triggering signal from the laser system announcing a new laser pulse. Raman scattering effects are quasi-instantaneous. Therefore, a gate width slightly longer than the pulse duration (400 ns) is expected to be very adapted. Measurements were performed in laminar premixed $CH_4/O_2/CO_2$ flat flames (48 $\%_{mol}$ O_2, Φ = 0.8) with a varying gate width from 300 to 1300 ns. An averaged flame luminosity measured with similar gate width was subtracted from each file. Results are shown in Figure II.40. Despite high fluctuations, the highest SNR clearly appears for a gate width of 600 ns. First the slope increases quasi-linearly, until the laser pulse is entirely captured, and then starts to decrease as noise from reflections and flame luminosity builds up on the spectra, with no remaining Raman scattering to capture.

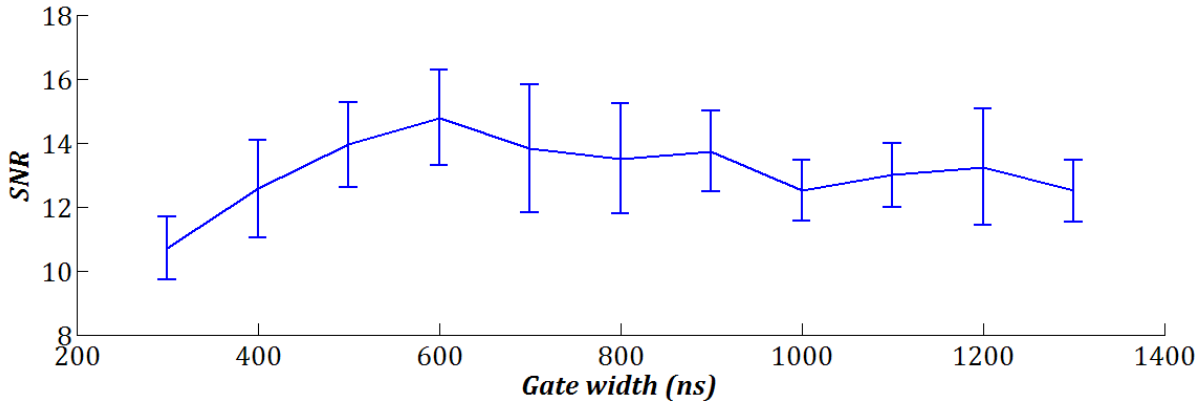

Figure II.40: Averaged SNR on CO_2 spectral bandwidth versus ICCD camera gate width for a series of measurements in laminar premixed $CH_4/O_2/CO_2$ flat flames (48 $\%_{mol}$ O_2, Φ = 0.8). The vertical bars represent the fluctuations of each averaged SNR value.

A proper setting of the gate width is especially important with O_2/CO_2 atmosphere at flame temperature due to CO_2* chemiluminescence (cf. Section 3.2.5). Indeed the chemiluminescence signal intensity accumulates linearly with the gate width. An example can be seen in Figure II.41, where 4 different gate widths were used in laminar premixed $CH_4/O_2/CO_2$/ flat flames (48 $\%_{mol}$ O_2, Φ = 0.8). The spontaneous flame luminosity can be recorded to be used as a background measurement. However, the correction is not fully efficient if the latter reaches high intensity compared to the Raman signals.

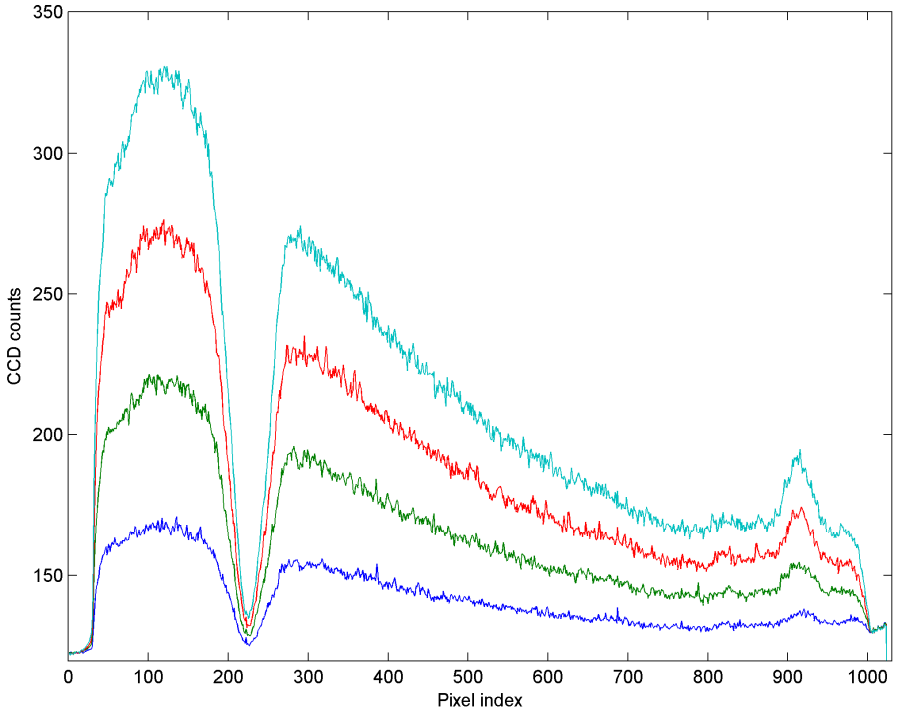

Figure II.41: Averaged spectra of flame luminosity recorded with 4 different gate widths in laminar premixed $CH_4/O_2/CO_2$ flat flames (48 $\%_{mol}$ O_2, Φ = 0.8). Gate widths: 300 ns (dark blue line), 600 ns (green line), 900 ns (red line) and 1200 ns (light blue line).

Another efficient way to improve the SNR is to use on-CCD binning. For the present case, it has only been used for the spatial dimension. It consists in grouping pixels together, by adding up received intensities directly on the chip before sending the results to the controller. For instance, binning 10 pixels together in the spatial dimension would lead to only one result in the controller, which includes electronic noise due to only one transmission, while 10 transmissions would have been necessary without on-CCD binning. Besides, intensities are added up, leading to larger signals and more convenient use of the gain factor offered by the intensifier. Consequently, on-CCD binning enables reaching higher SNR. Great results are found with spatial binning of 10 pixels, though it is at the expense of the spatial resolution that becomes ten times lower, at 0.262 mm.

From this point, the gain of the intensifier is the only remaining parameter inherent to the ICCD camera that rules the intensity of the observed signals. The intensifier enables amplifying signals that would not necessarily be distinguished from the noise. It is an essential device for LRS due to the weakness of Raman signals, though it also represents a great source of electronic noise. To optimize its effect, the gain should be set sufficiently high, so that Raman signals are picked up and amplified, but under a certain limit, not to amplify noise signals. Figure II.42 shows averaged SNR measurements performed in air at ambient temperature. For both oxygen and nitrogen, the SNR peaks for a corresponding intensifier gain of 220 (255 is the maximum).

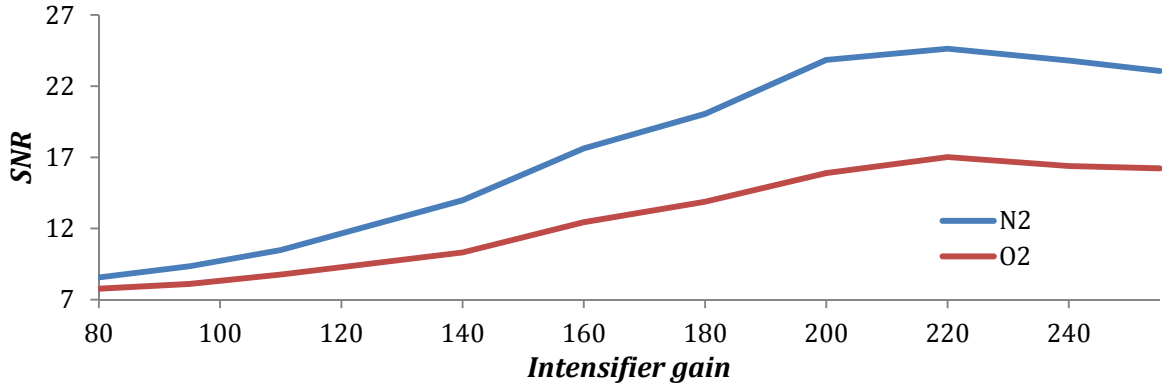

Figure II.42: SNR versus intensifier gain for N_2 and O_2 from a series of measurements of air at ambient temperature.

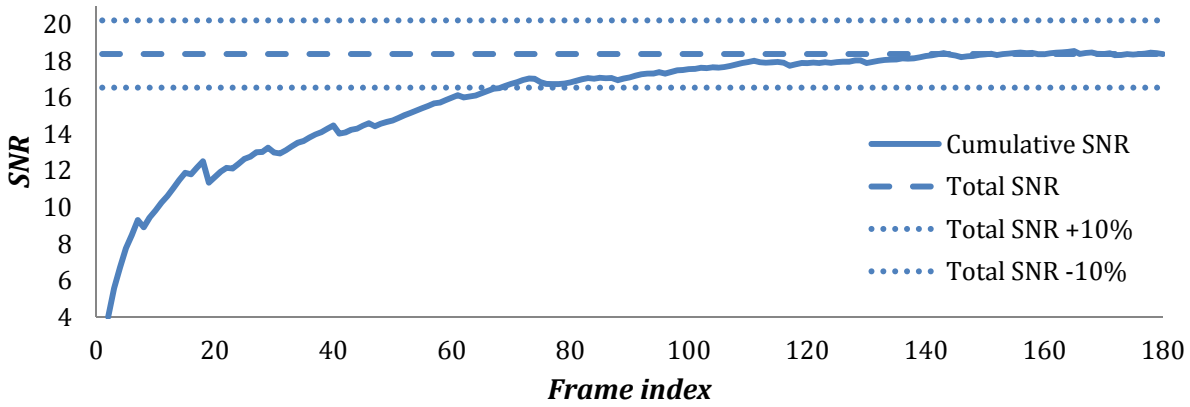

Figure II.43: Cumulative SNR on CO_2 spectral bandwidth versus frame index for a series of measurements in laminar premixed $H_2/O_2/CO_2$ flat flames (40 $\%_{mol}$ O_2, Φ = 0.5).

Once all previous parameters are set, the last significant parameter to set for the ICCD camera is the minimum number of frames to be recorded for each file to get the best achievable accuracy. One way is to consider the cumulative SNR over one series of measurements and to determine from which amount of frames the SNR reaches its maximum at more or less 10 %. Results are shown in Figure II.43, corresponding to laminar premixed $H_2/O_2/CO_2$ flat flames (40 $\%_{mol}$ O_2, Φ = 0.5). Those results are quite representative, though they could be slightly different for other flames, especially for

non-premixed flames. It can be seen that, from about 70 frames, the cumulative SNR is stable and close to its maximum by more or less 10 %. Furthermore, recording more than 100 frames would not bring much more accuracy to the results.

6.3.3. Laser system

Time can be a significant limiting factor to monitor the probe volume, or to efficiently filter cosmic rays and optical breakdowns. 15 on-CCD accumulations is a trade-off between SNR (cf. Section 6.3.2), saturation limits of the CCD camera and recorded time per frame. Considering the laser frequency of 10 Hz, 1.5 seconds are required for each frame to be recorded.

Figure II.44 shows the results of a series of measurements of the laser output energy corresponding to 2000 consecutive pulses, recorded using a Coherent Labmax-Top energy metre, and divided into groups of 15 pulses. Results allowed ensuring that laser fluctuations were below 1 % of the mean laser output energy over the whole series. Consequently, using this mean value instead of systematically measuring the laser output energy for each pulse would not significantly affect the quality of the results. Though laser output energy fluctuations are not significant, the mean value tends to decrease over time during the measurement sessions by around 6 % from the start of the day to its end (ca. 10 hours). The variation of the mean laser output energy is sufficiently slow, so that it can be totally captured by regular energy measurements performed along the day.

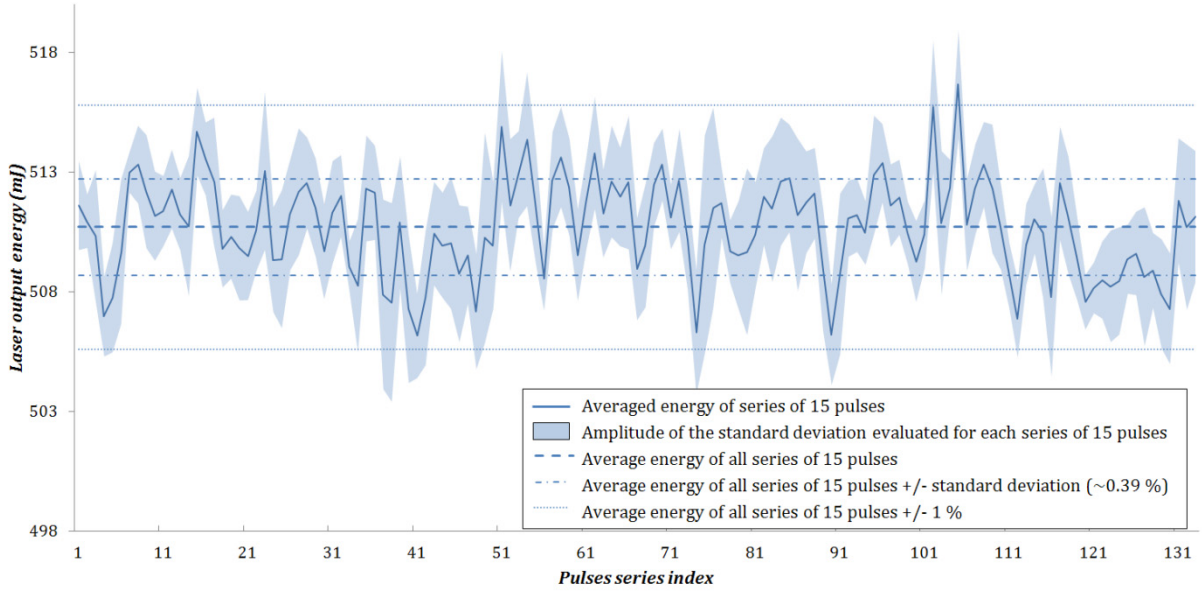

Figure II.44: Laser output energy sampled by 15 pulses, recorded with Coherent Labmax-Top device.

Another parameter to be considered is the influence of the number of recorded frames captured onto the cumulated means of laser output energy. Figure II.45 shows the cumulated mean of the laser output energy over groups of 15 pulses. A minimum of 55 consecutive groups of 15 pulses is sufficient to enter a stable zone where the cumulative mean is within 0.07 % of what it would be after 130 groups of pulses. It means that more than 55 groups would not bring much more accuracy on the determination of the laser energy output energy. This is relatively consistent with the minimum amount of frames to be recorded by the ICCD camera for best accuracy, as illustrated in Figure II.43.

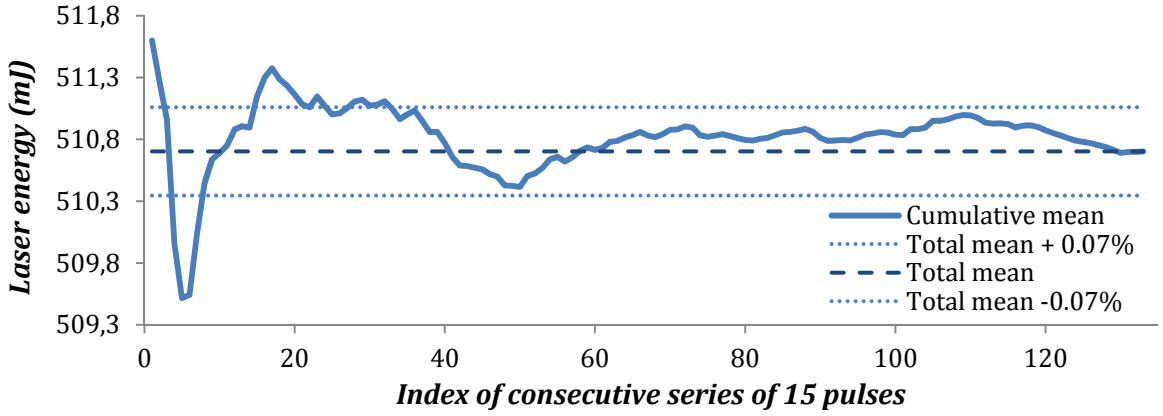

Figure II.45: Cumulative mean laser output energy calculated over groups of 15 pulses.

6.3.4. Flame luminosity

Typical flame luminosity levels seen in H_2/air or CH_4/air flames, excluding sooting flames, are generally not significant compared to the accuracy of the present setup. However, in presence of large concentrations of CO_2 and high temperature, flame luminosity becomes a major component of the spectra, mainly due to CO_2* chemiluminescence. It appears as a broadband signal more intense on the blue side than on the red side, as illustrated by Figure II.41.

Figure II.46 shows an averaged spectrum from a laminar premixed $CH_4/O_2/CO_2$ flat flame (50 $\%_{mol}$ O_2, Φ = 0.9), where a strong broadband luminosity appears. A typical background correction from a dark measurement would not be sufficient, since it does not account for flame luminosity. However, correcting the measurements with an averaged measurement of the flame luminosity, taken in the same conditions without laser, enables to achieve a relatively clear signal. An accurate correction is essential as any remaining signal from broadband luminosity could be interpreted by the data-processing software as higher number densities. This would consequently affect the determination of the temperature as well. The limit of the application of such corrections is that each flame generates its own pattern of flame luminosity. Thus, flame

luminosity measurements should be performed for every single flame measurement, which is considerably time-consuming.

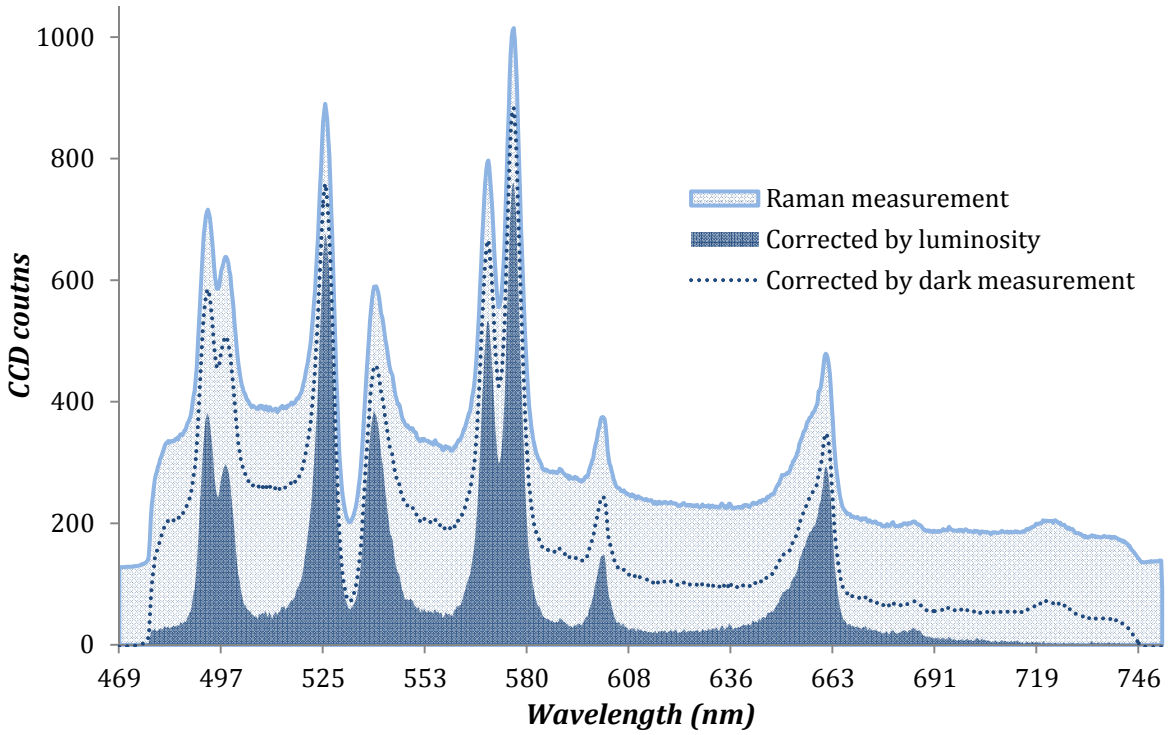

Figure II.46: Averaged spectra displaying flame luminosity from measurements in a laminar premixed $CH_4/O_2/CO_2$ flat flame (50 $\%_{mol}$ O_2, Φ = 0.9).

6.4. Experimental settings

- **Laser system:**

  - Model: Continuum Agilite 569-10
  - Output laser wavelength: 532 nm
  - Averaged laser output energy: 530 J/pulse
  - Pulse duration: 400 ns
  - Frequency: 10 Hz

- **Spectrometer:**

  - Model: Acton Physics SP300i
  - Grating: 300 grooves.mm^{-1}
  - Blaze wavelength: 300 nm
  - Dispersion: 11 nm.mm^{-1} at 500 nm
  - Centring: 610 nm

- **ICCD camera:**

- Model:	Princeton Instruments PI-MAX ICCD camera
- Chip:	EEV 256x1024F CCD 30
- Controller:	Princeton Instruments ST-133
- Gating:	Pulse-timing generator
- Gate delay:	2100 ns
- Gate width:	600 ns
- Intensifier gain (max. 255):	220
- ADC options:	Low noise, 10 kHz
- On-CCD accumulations:	15 laser pulses
- Spatial on-CCD binning:	10 pixels into 1
- Spectral on-CCD binning:	None
- Probe length:	5.502 mm
- Spatial resolution:	0.262 mm

6.5. Level of uncertainties

A thorough uncertainty analysis of the experimental setup was performed by Nicoloso [*Nicoloso* 2010]. The uncertainty analysis is very complex for such system, since many variables play a role on the final results. For most variables, only a rough estimate of the uncertainties can be given. The uncertainty analysis enables to better spot the weaknesses of the setup in order to optimize it, and to set the limits of the experimental investigation. It is also a very convenient way to prioritize the tasks to improve the setup.

Nevertheless, because of the requirements of the rough estimates, levels of uncertainties can end up away from the reality. Another way to estimate the uncertainties is to directly look at the results from measurements with known composition and temperature. The comparison between results from one-dimensional laminar flame calculations and results from experiments (cf. Figure II.17), after refinement of the Raman calibration coefficients, is very suitable for this task. This gives an indication of the uncertainties at flame temperature and in premixed conditions. Those estimates are more realistic, though they do not enable to retrieve the source of the uncertainties. Table II.8 gives representative uncertainties of the setup. They were calculated by comparing fluctuations and averaged results from calibration measurements, both in cold flows and laminar premixed flat flames, to theoretical results and laminar flame calculations. Uncertainties are lower in cold flows, since Raman signals are more intense. They are also expected to be slightly higher in non-premixed flames, since steep scalar gradients appear and no proper calibration can be performed at intermediate temperatures. Both standard deviation and relative uncertainty increase while the molar fraction of the measured species decreases.

Table II.8: Representative uncertainties of the LRS setup.

Scalar	Cold flows		Premixed flames	
	Standard deviation (%)	*Uncertainty (%)*	*Standard deviation (%)*	*Uncertainty (%)*
T	3.5	1.5	12	3
CO_2	4.5	2.5	19	13
O_2	5	2.5	38	22
CO	/	/	33	25
N_2	3	2	11	4
CH_4	3	3	/	/
H_2O	/	/	13	6
H_2	5	2.5	/	/

By propagating the errors, the uncertainties on mixture fraction, F_B, were estimated at ca. 35 - 40 % in jet flames. The main source of uncertainties remains the fluctuations found in spectra. Those are correlated to the standard deviation given in Table II.8. They are quite significant at ambient temperature and especially high in flames. The fluctuations are due to the high level of noise that may be amplified by the intensifier of the ICCD camera. Though they are relatively weak during calibration measurements, they induce errors in the determination of the Raman calibration coefficients, which propagate to the results. Uncertainties can be very high when species are at high temperature and at low number densities, since their Raman signals are weak and close to the noise level.

Compared to other LRS setups of higher maturity, the overall uncertainties are considerably higher, especially at flame temperatures [*Bergmann* 1998, *Barlow* 2009b]. The key to significantly lower the level of uncertainties would be to increase the SNR by using spectral on-CCD binning, increasing the laser output energy, or using a different detection system without intensifier, for instance. Though the level of uncertainties is quite high, it allows using the results for qualitative purposes. The accuracy of the results is sufficient to make comparative analysis between flames of similar compositions, track changes in the flame structure, follow the evolution of combustion products or give flame temperature ranges, for instance.

6.6. Safety considerations

Developments related to safety issues, especially on laser system, gas supply, cooling system, operational procedures and ventilation system, are described in Appendix B.

7. EXPERIMENTAL SETUP AT SANDIA NATIONAL LABORATORIES

7.1. Motivations for an exchange at Sandia

Part of the research program took place at the Combustion Research Facility (CRF) at Sandia National Laboratories (SNL) in Livermore (California, USA). The exchange was performed under the supervision of Dr. Robert Barlow, who is one of the leaders in laser diagnostics applied to combustion, with a very high level of expertise in LRS diagnostics. His laboratory combines different laser techniques, such as LRS, Rayleigh scattering, CO and OH laser-induced fluorescence (LIF), and is known as one of the most accurate LRS setups [*Barlow* 2007, *Barlow* 2009b]. Some of the very first pieces of literature about LRS techniques for combustion were actually from SNL, written for most by Prof. Robert Dibble, Prof. Assaad Masri and Dr. Robert Barlow [*Dibble* 1987, *Masri* 1988, *Dibble* 1990, *Masri* 1992]. He also took part in the development of the latest calibration and data-processing method, so-called Hybrid Method [*Fuest* 2011], as described in Section 5.1.6.

He created in the late 90's the Turbulent Non-premixed Flames (TNF) workshop [TNF 2012], gathering every second year the leading researchers in experimental combustion diagnostics, and in premixed and non-premixed flames calculations. The main purpose of the workshop is to link the two fields, so that they better complete each other. In this view, the flames investigated at the CRF are intended to produce data libraries used to validate combustion models. Among all the configurations he has studied and those available on the TNF website, none deals with oxy-fuel combustion. Therefore the idea was to learn about his methods, while performing measurements in oxy-fuel flames at the CRF to enrich the available experimental data library.

Observing and performing experiments at the CRF brought many ideas and answers that were used afterwards at NTNU to improve the LRS setup, especially for the calibration and data-processing methods. Though a data-processing code had been written using Visual Basic prior to the exchange, a functional and evolutive calibration and data-processing procedure for the setup at NTNU was still missing. The exchange provided an opportunity to write the complete data-processing software suite

described in Section 5.2.5, based on the methods used at the CRF and notably using the Hybrid Method.

At the CRF, the setup enabled measurements in turbulent non-premixed jet flames of CH_4/H_2 mixtures in O_2/CO_2 atmosphere, without confining the flames into a combustion chamber. Results enabled qualifying the typical structure of turbulent CO_2-diluted oxy-fuel non-premixed flames, and eventually comparing it to CH_4/H_2/air flames at equivalent Reynolds number found in the literature. A journal publication summarizing the results can be found in Appendix D.

7.2. Description of the experimental setup

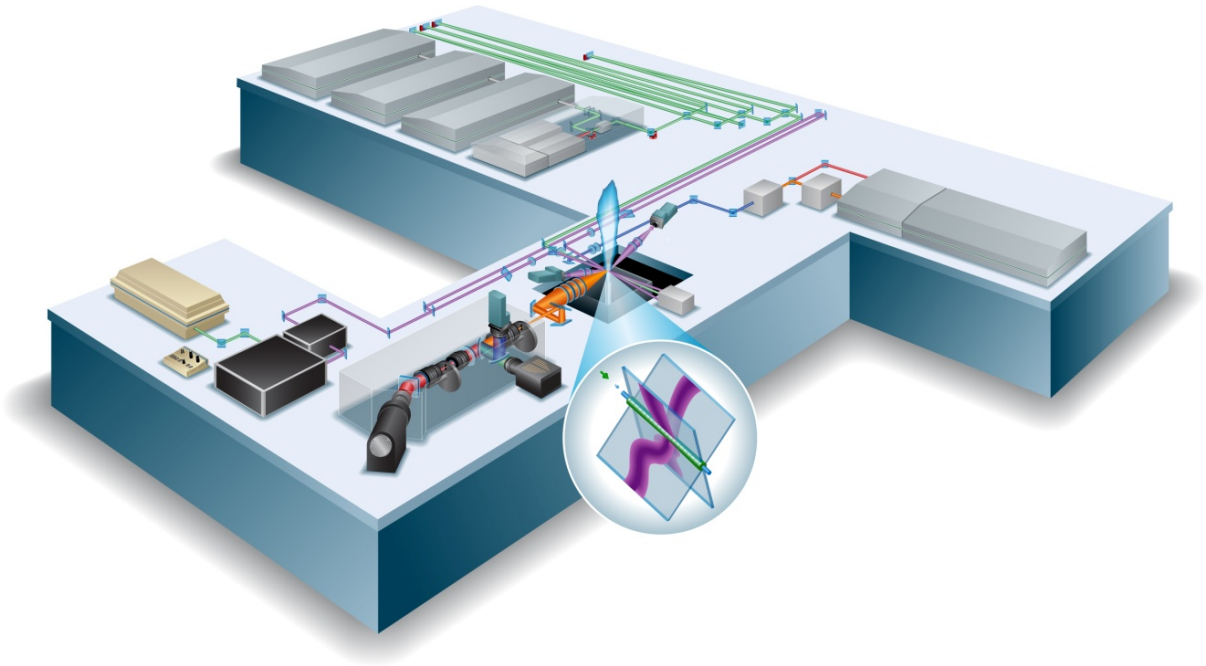

Figure II.47: Overview of the simultaneous line-imaging of spontaneous Raman-Rayleigh scattering, cross-planar OH-LIF, and two-photon LIF of CO experimental setup at SNL. (Figure provided by R. S. Barlow, Sandia National Laboratories)

The facility at the CRF is the state-of-the-art of the combustion optical diagnostics. An overview is shown in Figure II.47. It has been described many times in the literature [*Barlow* 2007, *Barlow* 2009a, *Barlow* 2009b]. It combines line imaging of spontaneous Raman scattering, Rayleigh scattering, cross-planar OH-LIF, and two-photon LIF of CO, in order to obtain single-shot profiles of the temperature and the concentrations of the major hydrocarbon flame species (CO_2, O_2, CO, N_2, CH_4, H_2O and H_2) and OH radicals. The beams from four frequency doubled Nd:YAG lasers at 532 nm are used for Raman and Rayleigh line imaging, yielding a total energy of 1.8 J/pulse in the probe volume, at 10 Hz and with a pulse duration of 400 ns. A pulse stretcher regulated by mirrors mounted on piezoelectric actuators is used to combine and delay

the four laser beams. Simultaneous cross-plane images of OH-LIF are also taken to allow the determination of the local flame orientation and the flame-normal gradient of the reaction progress variable. A custom-made collection system, including rotational shutters, was designed to temporally gate and combine the three CCD cameras recording Raman and Rayleigh scattering signals, and CO-LIF signals, as illustrated in Figure II.48. Details can be found in [*Barlow* 2009b]. The setup allows performing radial profile measurements from the central axis to the pure oxidizer region, using a 6-mm probe, translated by steps of 3 mm taking a minimum of 500 shot measurements at each position. Considering a spatial binning of 5 pixels to optimize the SNR, the final spatial resolution is 0.104 mm.

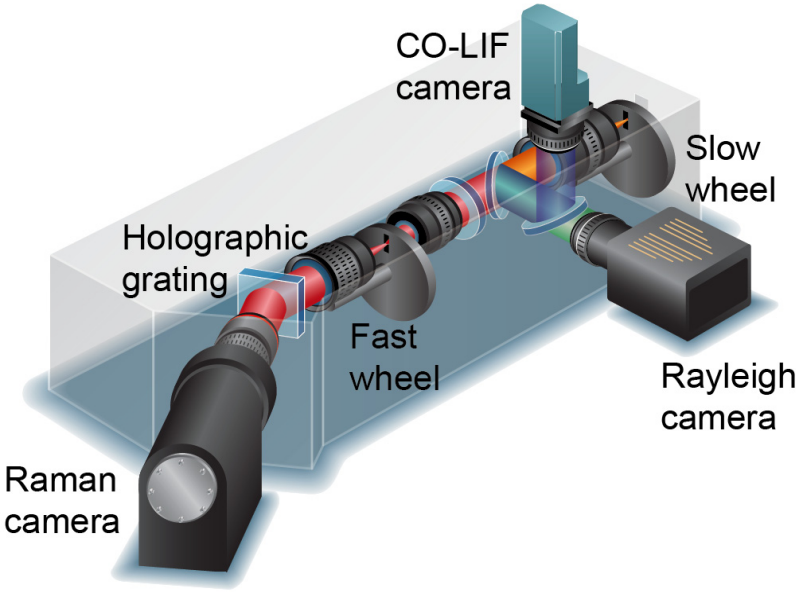

Figure II.48: Main optical components of the light collection and detection system for combined Raman/Rayleigh/CO-LIF line imaging from the setup at SNL. [Barlow 2009b]

The configuration actually used for the experiments performed on oxy-fuel flames was slightly different. In order to avoid any optical breakdown and saturation of the CCD camera with CO_2 signals, only three of the four Nd:YAG lasers were running together through the pulse stretcher, providing a 400-ns pulse of about 1 J/pulse at 10 Hz. Cross-planar OH-LIF and CO-LIF were not used for the experiments, due to the large presence of CO_2, which would have required a new definition of the data-processing routine to give reliable results. Note that, one of the OH planar-LIF cameras was recording images for qualitative analysis. A 1-mm thick window was used as a protective shield in front of the light collection and detection system, due to the high level of radiation emitted by CO_2 within the flames.

As illustrated in Figure II.49, the main burner is a coflow, similar to the one used at NTNU. The coflow inside diameter is 96.5 mm, with a 5-mm inside diameter central nozzle. The oxidizer mixture (O_2/CO_2) is issued by the coflow, while the fuel mixture (H_2/CH_4) flows through the central nozzle. Perforated plates and a honeycomb

are mounted inside the coflow to allow a uniform flow distribution of the oxidizer. The fuel nozzle has 0.5-mm wall thickness and squared-off end to help stabilize the jet flames. Its tip is 40 mm above the coflow and is long enough, so that the flow is considered fully developed and fully mixed when the fuel mixture reaches the nozzle tip. The burner is mounted at the top of a 25 cm x 25 cm square-section wind tunnel from where fresh air flows at 0.5 $m.s^{-1}$ to accompany the flow and to prevent from early mixing with ambient air. This enables to confidently perform measurements in the near-field of the axisymmetric jet flames, from 1 to 20 diameters above the nozzle, without requiring confinement in a combustion chamber.

The calibration and data-processing method used for LRS is the Hybrid Method. Signals are corrected for CCD background, flat field, total Nd:YAG laser energy, interferences from laser induced fluorescence in Raman signals, broadband flame luminosity, beam steering through flames, and bowing effect through Raman optics [*Fuest* 2011]. Data are filtered for sparks and dusts particles altering Rayleigh and Raman signals, although such events are rare, since in-line particle filters are installed along the critical gas lines.

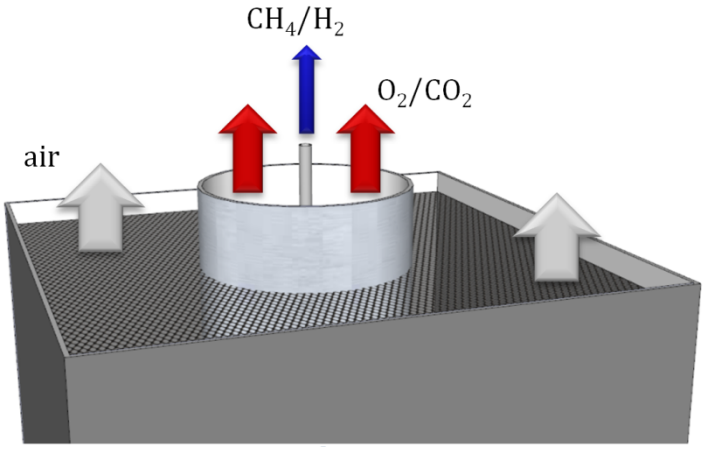

Figure II.49: CAD drawing of the coflow burner used for CO_2-diluted oxy-fuel jet flames measurements at SNL.

7.3. Level of uncertainties

Table II.9 lists the calculated uncertainties at representative conditions for the simultaneous Raman/Rayleigh imaging setup. The numbers are based on uncertainties in calibration flow conditions and repeatability of the measurements. The calibration of the experimental setup relied on cold flows, heated flows, laminar jet diffusion flames, and laminar premixed CH_4/air flat flames measurements, for which compositions are well-known. Estimates are also given for turbulent flames, and are mostly higher than those from the flat flames to account for uncertainties from corrections for interferences from flame luminosity and from laser induced fluorescence, except for CO,

whose relatively high levels in oxy-fuel flames balances with the interferences. Mass flow controllers used for the experiments were calibrated using laminar flow elements and provided uncertainties only within 1 % of the reading. Additional errors may appear due to sharp gradients that cannot be totally captured with the current spatial resolution. The measurement challenges concerning the oxy-fuel jet flames investigated at SNL are discussed in Appendix D (Sections 4.5 - 4.6).

Table II.9: Calculated uncertainties in scalar measurements at flames conditions, corresponding to the simultaneous Raman/Rayleigh imaging setup at SNL.

Scalar	*Standard deviation (%)*	*Uncertainties (flat flames, %)*	*Laminar premixed flat flames*	*Uncertainties (turbulent flames, %)*
T	1.3	2	Φ = 0.97, T = 2185 K	2
N_2	1.1	2	Φ = 0.97, T = 2185 K	3
CO_2	4.5	4	Φ = 0.97, T = 2185 K	6
H_2O	4.1	3	Φ = 0.97, T = 2185 K	6
Φ	3.1	5	Φ = 0.97, T = 2185 K	-
CO	6.7	8	Φ = 1.28, T = 2045 K	8
H_2	9.2	8	Φ = 1.28, T = 2045 K	10

7.4. Main differences with the setup at NTNU

Evidently, the low level of uncertainties represents the main difference between both setups. Years of experience performing LRS at SNL allowed combining the best components to reach the highest accuracy, as listed in the following:

- The **laser output energy** is about twice higher than at NTNU for the same pulse duration. According to Eq. II.1, Raman signals are consequently expected to be twice more intense, reducing the uncertainties. However, the laser output energy has to be recorded for each pulse to correct the measurements due to its fluctuations over time.

- A custom **holographic grating**, optimized for the current LRS configuration, is used instead of a typical spectrometer (cf. details in [*Barlow* 2009b]), enabling achieving a higher efficiency.

- The **Raman camera** (Princeton Instrument VersArray 1300B) is non-intensified, low-noise and its CCD array is cryogenically-cooled to -110 °C (CryoTiger Cooling Unit). Consequently, dark noise and electronic noise are considerably reduced compared to the setup at NTNU.

- **No intensifier** is required in the current setup due to the capabilities of the equipments, which achieve higher overall collection efficiency.

- The **collection system** (cf. Figure II.48) uses two independent rotational shutters to gate the three cameras (cf. details in [*Barlow* 2009b]). The slow chopper wheel (ca. 3,000 rpm and 300 µs FWHM gate) is located at the focus of the collection lens pair, while the fast chopper wheel (ca. 21,000 rpm and 3.9 µs FWHM gate) is dedicated to the Raman camera. At NTNU, the gating of the camera is performed through the intensifier in front of the CCD array. It enables reaching a gating time about six times shorter than at SNL. This is a considerable advantage in presence of luminous flames. However, it is at the expense of a much higher electronic noise, which significantly affects the SNR.

- The temperature is determined iteratively using the **Rayleigh scattering signal** instead of the Raman scattering signals. This brings more confidence and independence in the determination of the temperature, and allows two-dimensional monitoring the laser beam behaviour through the Rayleigh scattering signal (focus, beam diameter, homogeneity, steering).

- Another significant difference is the complete use of the **on-CCD binning**. At NTNU, on-CCD binning is used in the spatial direction to group 10 pixels together and reduce the SNR of the collected signal. At SNL, only 5 pixels are binned in the spatial direction, which leads to a spatial resolution of 0.104 mm (0.262 mm at NTNU). However, on-CCD binning is applied as well in the spectral direction, reducing the CCD array to only a dozen of super-pixels. This greatly improves the SNR and considerably decreases the total volume of data to be treated, at the expense of the spectrally resolved data.

Another great advantage of the setup at SNL is the large capabilities of the gas supply. Higher gas flow rates, and consequently higher jet Reynolds numbers can be achieved due to the layout and flexibility of the setup. Considering the burner configuration, coflow speeds of ca. 1.3 $m.s^{-1}$ for the oxidizer and ca. 120 $m.s^{-1}$ for the fuel, can be reached. This corresponds to a jet Reynolds number of ca. 20,000 (oxidizer composed of 30 $\%_{mol}$ O_2, 70 $\%_{mol}$ CO_2, and fuel composed of 50 $\%_{mol}$ CH_4 and 50 $\%_{mol}$ H_2*)*. 6-pack gas supplies are used for N_2, O_2, H_2 and CH_4. Three liquid CO_2 tanks are combined to a large evaporator to meet the required CO_2 supply. This enables to very efficiently manage the issues related to the Joule-Thomson effects. At NTNU, coflow speeds are limited to ca. 0.3 $m.s^{-1}$ for the oxidizer and ca. 50 $m.s^{-1}$ for the fuel, for similar compositions.

8. PARTICULARITIES OF LRS IN OXY-FUEL FLAMES

In addition to the supplementary degree of freedom offered by the oxygen content in the oxidizer, replacing N_2-dilution with CO_2-dilution brings significant differences between oxy-fuel and regular air-fired flames. Those relatively unexplored flames bring new challenges to LRS diagnostics. The most relevant particularities of LRS in CO_2-diluted oxy-fuel flames that were observed during the present investigation are listed in the following paragraphs.

8.1. Combustion rig

8.1.1. Protection from ambient air

While performing LRS in CO_2-diluted oxy-fuel flames, any mixing with ambient air should be avoided to prevent addition of oxygen and nitrogen to the mixtures through recirculation structures. The most effective solution to such issues is to confine the flame. At NTNU, a combustion chamber is used to protect the oxy-fuel flame from ambient air. The main advantage is the ability to observe the complete development of the flames under oxy-fuel atmosphere and perform measurements relatively far downstream from the fuel nozzle. The main drawback is the presence of windows across the laser path and the optical collection path. Despite their custom anti-reflection coating, windows reduce the collection efficiency and add a new source of non-linear optical effects. Since the SNR is directly linked to the power of the scattered signals, losses should be reduced to the minimum. Another drawback is the wide range of flame temperatures induced by the large oxygen content in the oxidizer. The oxy-fuel chamber has to stand flames up to 3000 K.

At SNL, another strategy has been used by coflowing air around the burner at the same velocity as the oxy-fuel coflow. This allows performing LRS measurements in oxy-fuel conditions without confinement, though those are limited to the near-field of the flames. The mixing with ambient air is delayed by the coflowing air and takes place only from ca. 40 to 60 diameters above the fuel nozzle. In the present case, this brings sufficient room for LRS measurements, since LIF interferences from soot precursors start to be predominant from about the same height. Another advantage of not using a confinement is the opportunity of using higher laser energy. Windows on the laser path are generally close to the flames, so that, besides the thermal load from combustion,

they receive a fairly high laser energy density onto a tiny area. This induces strong energy gradients across the windows, which can lead to breakdowns at a certain limit. The issue happened with the LRS setup at NTNU (cf. Section 6.1.2) and one way to solve the problem without lowering the laser energy has been to extend the laser pulse duration. However, longer pulse duration goes along with longer gate width for the ICCD camera, which may add up uncertainties to the recorded signals through spontaneous flame luminosity and interferences, depending on the type of flames.

Note that this applies especially to non-premixed flames, since, for the laminar premixed flames, the shroud flow available on Hencken burner is sufficient to efficiently protect the flow up to the height of the measurement probe.

8.1.2. CO_2 supply temperature

As detailed previously, CO_2 is very sensitive to Joule-Thomson effects, due its high Joule-Thomson coefficient. The temperature of the CO_2 supply is practically dependent on the flow rate and the pressure in the liquid CO_2 bottle. Due to the high flow rates, replacing readily available air supply by O_2/CO_2 mixtures might be out of reach. CO_2 supply expected at 300 K can drop down to 260 - 270 K when high CO_2 flow rates in the range 100 - 130 $Nl.min^{-1}$ are required, due to the Joule-Thomson effects.

At NTNU, two in-line gas heaters are located on the CO_2 gas line, onto the first expansion stage and downstream from the second one to help compensate for Joule-Thomson effects. However, the inertia of the gas heating system does allow fast response to varying CO_2 temperatures due to change of pressure in the liquid CO_2 bottle. The system has to be carefully monitored to reduce the amplitude of the CO_2 temperature variations. At SNL, larger liquid CO_2 tanks are used along with a large evaporator, two in-line gas heaters and long supply lines across the laboratory (cf. Section 7.2) to vanish out Joule-Thomson effects. Though those effects apply to any gas, other gases used in the present project do not have high Joule-Thomson coefficients and are supplied at lower flow rates. The length of the gas supply tubes surrounded by ambient air is generally sufficient to guarantee a supply at ambient temperature.

The temperature of CO_2 supply is particularly important for calibration when conditions have to be absolutely stable and well known, and for non-premixed jet flames, since the oxidizer temperature greatly influences the flame stability.

8.2. CO_2-diluted oxy-fuel flame properties

8.2.1. CO_2 physical properties

Carbon dioxide has a much higher heat capacity than nitrogen or water steam. Its specific heat capacity at constant pressure at 1000 K is about twice higher than for nitrogen for the same molar quantity (59.2 versus 32.7 $J.mol^{-1}.K^{-1}$). This leads to lower flame temperatures than for air-fired flames for the same oxygen content in the oxidizer. Higher heat capacity also goes along with higher quenching effects, which greatly affects the flame stability domain in some cases.

Carbon dioxide has a slightly higher refractive index than air (1.00048 versus 1.00028). This may cause some steering of the laser beam when it passes through the unsteady interface between air and the O_2/CO_2 coflow. The issue is not that critical, since, for instance, similar situations are successfully faced with pure methane, which has nearly the same refractive index as CO_2. The induced beam steering has not been severe with the oxidizer mixtures used for the present investigation. Those effects have been accounted for automatically by the hybrid Raman/Rayleigh processing method used at SNL. At NTNU, the averaging effect of the on-CCD accumulations has not let any severe steering appear in the results, and thus, measurements have not required any supplementary correction.

Carbon dioxide has a higher density than nitrogen and than any other of the main flame species of the present experiments. Compared to hydrogen, CO_2 has a molar mass 24 times higher. The density difference leads to some difficulties for the calculations of the mass fractions, especially within the flame zone. For instance, a small error in the determination of the CO_2 number density could propagate into a large discrepancy in mixture fraction space through the mass fraction calculations (cf. Section 6.5). The effect is especially seen with pure hydrogen as fuel, due to the high difference of density at the interface fuel/oxidizer.

Due to its fairly high heat capacity, carbon dioxide tends to radiate a significant part of the heat absorbed in flames to the surroundings. Combined to water vapour, the radiative heat transfer is enhanced and helps reaching a uniform temperature distribution across the flames. To some extent, heat radiated from the flames may also damage the laboratory equipment. At NTNU, the chamber confining the flames receives a high thermal load, giving the need of a dedicated cooling system to maintain the walls of the chamber at acceptable temperatures. The precision windows can also absorb a significant part of the thermal load, which helps protecting the components of the Raman collection system. At SNL, aluminium foil has been set up on critical equipments to reflect the radiated thermal load. The collection system has been shielded by a 1-mm thick window of infrared absorbing filter glass (Schott KG2). Adding windows across the

optical collection path may generate significant signal intensity losses (up to ~15 %) in the overall efficiency of the collection system though their transmittance is generally optimized for the visible range. Note also that flames can potentially re-absorb the radiations from the chamber or those reflected by the aluminium foil, though the impact is not believed to be significant on the investigated near-field of the present flames.

8.2.2. Wide range of flame temperatures

One particularity from CO_2-diluted oxy-fuel flames is the wide range of flame temperatures that can be reached by varying the oxygen content in the oxidizer. In the investigated transitional non-premixed H_2 – O_2/CO_2 jet flames, flame temperatures are scattered between 1500 and 3000 K. Since the calibration is not performed on a daily basis for temperatures between 300 and 1800 K, and for temperatures above 2200 K, those large variations of temperatures are generally accompanied of significant uncertainties. If such flames were already well known, they would be of great use as calibration flames to refine the Raman calibration coefficients.

8.2.3. Radical pool

Another drawback is that, at high temperatures, the radical pool may represent a non-negligible part of the mixtures and cannot be any more ignored in the LRS resolution algorithm (cf. Section 3.4.2). Above 2500 K, O, H and OH radicals, which cannot be detected by LRS, can reach up to 2 - 3 $\%_{mol}$ in the reaction zone. This systematic error was reported in [*Linow* 2002] in oxy-fuel flames without CO_2-dilution. They underlined the very large measurement uncertainties above 2500 K from common LIF techniques for O, H and OH, so that they cannot accurately supplement Raman signals. Instead, they attempted to solve the issue by implementing in the LRS data-processing radical concentrations resulting from flame calculations. Their results were still limited by the lack of proper calibration at high temperatures and the accuracy of the calculations. Based on the experience of the present investigation, results from calculations of concentrations of radicals greatly depend on the type of reaction mechanism and the models used. Consequently, results from flame calculations are not implemented in the LRS data-processing and the flames whose radical pool is no longer negligible (typically above 2500 K) are only qualitatively studied.

8.3. Spectral properties

8.3.1. Raman signals distribution and the enhanced detection of CO

The two Raman bands for CO_2 can reach very high intensities relatively to other species from hydrocarbon flames. This is due to their high Raman cross-section (cf. Table II.1) and the Raman scattering linearity with the number density. Consequently, CO_2 tends to dramatically affect surrounding species on the Raman spectra, especially oxygen appearing on its red-side. At high temperatures, the O_2 Raman peak and one of the CO_2 Raman peaks actually converge to about the same location on the spectra, leading to an unclear distinction between both signals. This brings especially high uncertainties in the results for O_2 concentrations at intermediate to high temperatures, where O_2 is only present at low concentrations and no proper calibration can be achieved. In addition, reciprocal cross-talks between CO_2 and O_2 are the most sensitive coefficients to beam steering effects.

Another main drawback of replacing nitrogen with carbon dioxide is the significant Raman rotational bands of H_2 appearing on the blue-side of the CO_2 Raman peaks [*Hoskins* 1977, *Sharma* 1980, *Warren* 1980, *Kojima* 2004]**.** They also appear in the down part of Figure II.6, on the blue side of the spectra dedicated to hydrogen. Those are especially considerable when H_2 is present in large quantities and at intermediate to high temperatures. Figure II.50 shows an averaged spectrum recorded in the flame zone of a non-premixed H_2 – O_2/CO_2 jet flame compared to an averaged spectrum recorded in one air-fired flame of similar conditions. Since the two flames have about the same flame temperature of ca. 2000 K, and the same range of H_2 number density at the location where spectra have been recorded, the Raman peaks induced by H_2 is expected to be quite similar. The Raman rotational bands of hydrogen ("Rot. H_2" in Figure II.50) form a regular pattern of alternated intensities along the spectra, with most visible peaks from 540 to 600 nm. In NP-H_2-air (cf. B in Figure II.50), no CO_2 is present and peaks of significant intensity appear in the Raman spectral bandwidth of CO_2, as well as in the one of O_2. Their intensity is comparable to the CO_2 Raman peaks seen in NP-H_2-OF-2 (cf. Figure II.50, A), as the visible peaks in the CO_2 bandwidth are made of the addition of peaks from both CO_2 and rotational H_2. Though the cross-talks from hydrogen are accounted for in the Raman calibration coefficients and refined with NP-H_2-air up to 2000 K, they keep bringing non-negligible uncertainties as they tend to greatly vary over time and with the temperature.

Compared to air-fired conditions, an important advantage is the absence of nitrogen in the burning mixtures. Nitrogen has a relatively high Raman cross section and is present in large concentration in air-fired flames, inducing a significantly high Raman band on spectra. The Raman band of N_2 interferes with the one of CO, whose maximum is located only a few nanometres away on its blue side (cf. Figure II.50). In

some cases, the cross-talk from N_2 onto CO is in the same range of intensity as the CO Raman band itself, leading to a poor accuracy in CO quantification. State-of-the-art LRS setups for air-fired conditions generally combine LRS with a CO-LIF detection system to reduce the uncertainties on CO concentration [*Meier* 2000, *Barlow* 2007, *Barlow* 2009b]. With oxy-fuel flames, the CO Raman band is relatively well isolated from large Raman cross-talks. In addition, CO levels are potentially higher in those flames than in air-fired flames (cf. Section 3.4.1), which greatly improves the SNR for the Raman band of CO. Consequently, in oxy-fuel conditions, CO can be relatively well quantified using LRS rather than CO-LIF.

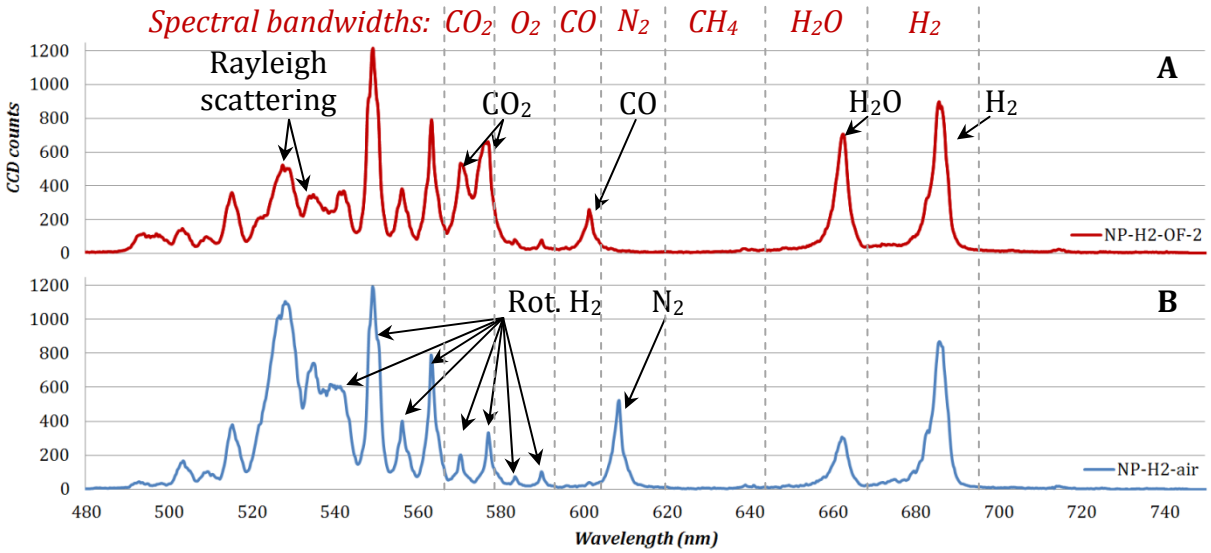

Figure II.50: Averaged spectra recorded in the flame zone of non-premixed jet flames. A: NP-H_2-OF-2; B: NP-H_2-air; cf. Section 9.5 for flame conditions.

8.3.2. Spontaneous flame luminosity

As detailed in Section 3.2.5, CO_2* chemiluminescence reaches significant levels in CO_2-diluted oxy-fuel flames. Results from [*Ditaranto* 2011] showed that spontaneous broadband luminosity in the visible region considerably increases with the oxygen fraction in the oxidizer, from 30 to 50 % O_2 (cf. Figure I.15). Due to the high content of CO_2 in the hot products, it is assumed that most of the spontaneous flame luminosity comes from CO_2* chemiluminescence. Figure II.51 shows averaged spectra from luminosity recorded in various flames investigated in the present project. No treatment is applied on spectra to correct for the optical path transfer function. Therefore, similarly to Figure II.37, the spectral response on the blue side is slightly amplified, while the response on the red side is under-estimated. Signals are chopped off at both ends of the spectra due to the response of the grating and other optics from the optical collection system. As seen previously, the narrow gap at 532 nm is due to the presence of the notch filter on the optical collection path.

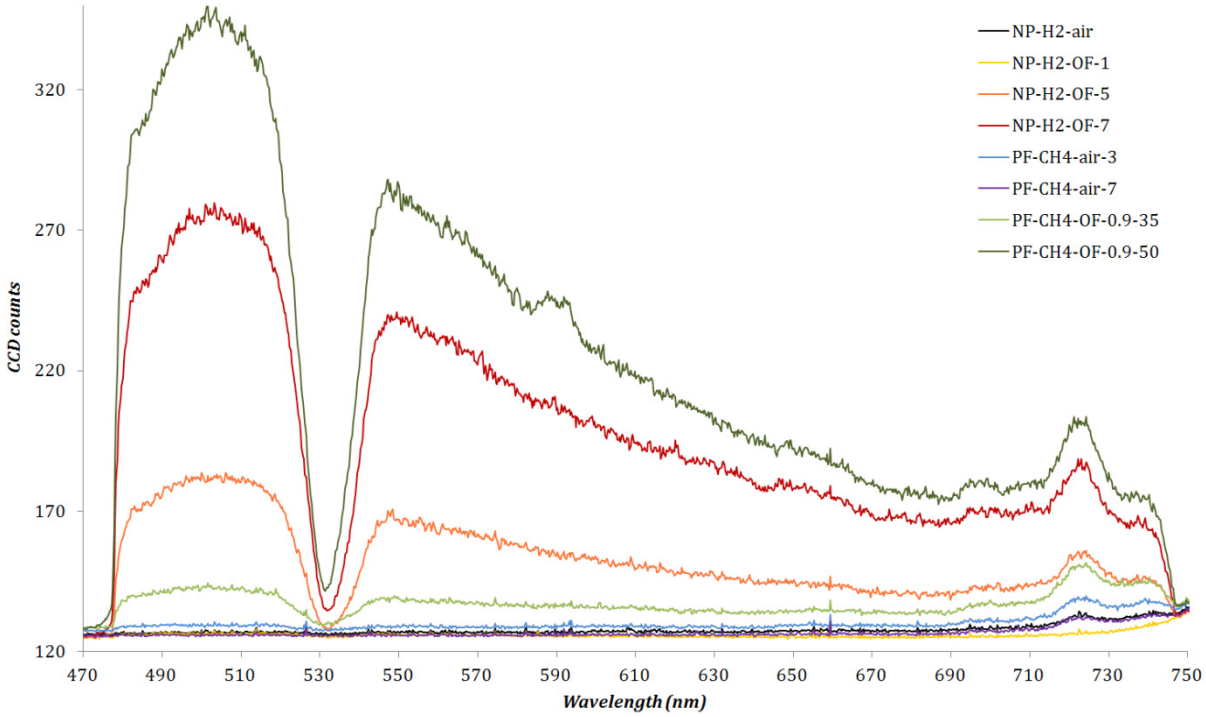

Figure II.51: Averaged flame luminosity recorded from various flames used in the present project; cf. Section 9 for flame conditions.

It can be observed that air-fired flames do not emit significant levels of luminosity. Only a weak band can be recorded around 710 – 740 nm for those flames, though this is out of the spectral bandwidth of interest for LRS measurements. This spectral band originates from the emission band of highly vibrationally excited water, which is the main combustion product in this case. It actually ranges from 600 to 900 nm, giving a red colour to the flame [*Gaydon* 1974, *Schefer* 2009].

Spontaneous flame luminosity emitted by CO_2-diluted oxy-fuel flames varies over a large span. The flame region of NP-H_2-OF-1, with 15 $\%_{mol}$ O_2 in the oxidizer, emits so low spontaneous luminosity that it can barely be distinguished from the background level of the ICCD detector. Conversely, NP-H_2-OF-5 and NP-H_2-OF-7, with 50 and 70 $\%_{mol}$ O_2 in the oxidizer respectively, displays very high levels of spontaneous flame luminosity, increasing with the oxygen content in the oxidizer. PF-CH_4-OF-0.9-35 and PF-CH_4-OF-0.9-50, with respectively 35 and 50 $\%_{mol}$ O_2 in the oxidizer display a similar trend.

In CO_2-diluted oxy-fuel flames, as the oxygen content in the oxidizer increases, the broadband signal dominated by CO_2* chemiluminescence becomes more and more significant. The broadband signal accounts for the blue colour of these flames. The intensity of the spectral band around 710 – 740 nm also seems to increase with the oxygen content in the oxidizer. The growing contribution from this band explains the rather white colour of the flames at high oxygen contents in the oxidizer, as the whole visible range receives contributions from the two modes of luminosity.

CO_2* chemiluminescence is induced by the overall chemical reaction described in Eq. II.9 and is represented by $h\upsilon$. The chemiluminescence intensity directly depends on the number density of CO and O species [*Samaniego* 1995, *Ditaranto* 2011]. Consequently, the phenomenon is, on the one hand, amplified by a higher presence of CO_2 and higher temperatures, and on the other hand, promoted by larger concentration of O_2 and higher temperatures. Therefore, CO_2* chemiluminescence should pass by a maximum while varying the O_2 content in the oxidizer, though it has not been observed in the present experiments up to 70 $\%_{mol}$ O_2 in the oxidizer for hydrogen non-premixed flames and up to 55 $\%_{mol}$ O_2 for laminar premixed flat flames.

$$CO + O \rightarrow CO_2 + h\upsilon \qquad \textit{Eq. II.9}$$

The intensity of the phenomenon has only a weak dependency to temperature [*Slack* 1985, *Samaniego* 1995, *Ditaranto* 2011]. Though high temperatures are required to observe the phenomenon, the intensity of CO_2* chemiluminescence is much more dependent to the O_2 content in the oxidizer, within the range of flames tested in this investigation. Figure II.52 shows averaged spontaneous flame luminosity spectra recorded from three laminar premixed $CH_4/O_2/CO_2$ flat flames with the same adiabatic temperature (ca. 2475 K). The overall intensity of the luminosity clearly increases with the oxygen content in the oxidizer, by only varying the oxidizer composition by a few percents. This is a striking result in this case, since both the concentration of CO_2 and the equivalence ratio are reduced. Thus, despite a potentially least production of CO molecules, the intensity of CO_2* chemiluminescence is controlled by the availability of O radicals rather than CO, at least in the conditions used for the present experiments. This is consistent with the flame calculations performed for each flame, giving increasing number density of O radicals with the oxygen content in the oxidizer.

Note that the peak visible at ca. 590 nm is believed to be induced by overheated particles from the Hencken burner, as the high-temperature flames with the highest contents of oxygen have probably been intermittently attached to the burner. The peak has never showed up using the coflow burner, even at high oxygen contents in the oxidizer.

The spontaneous broadband signals require the luminosity correction detailed in Section 6.3.4. Statistics noise, whose level increases with the overall spontaneous flame luminosity, can also be seen in Figure II.51 and Figure II.52. This noise brings a higher level of uncertainties of high oxygen contents in the oxidizer, since it cannot be totally corrected. The down side of this type of correction remains the time required to record the spontaneous flame luminosity spectra. A minimum of 70 frames have to be recorded before each LRS measurement to perform an acceptable correction. This corresponds to about 2 minutes for each location of the probe volume. Since Raman calibration coefficients tend to significantly vary within hours in the present configuration, this brings a considerable handicap for LRS measurements in oxy-fuel flames. The delay

between flame luminosity measurements and actual Raman measurements is only acceptable because of the averaging effect of the 15 on-CCD accumulations. Such sequential correction would not be applicable if single-shot measurements were applied in turbulent flames, for instance, due to the scalar fluctuations.

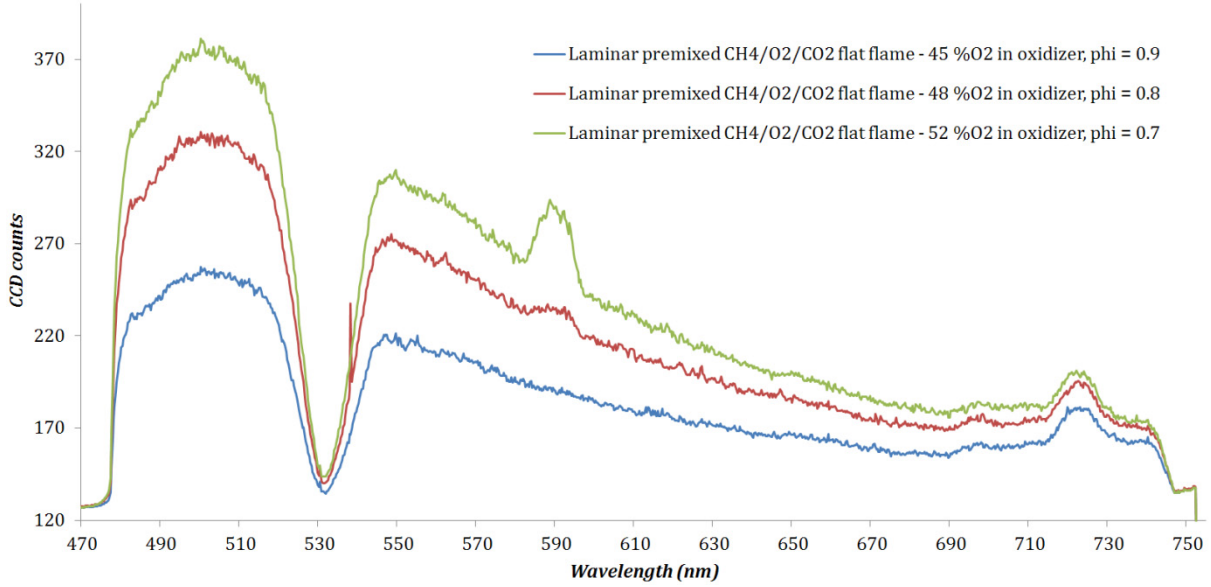

Figure II.52: Averaged spontaneous flame luminosity spectra recorded from three laminar premixed $CH_4/O_2/CO_2$ flat flames with the same adiabatic temperature.

SUMMARY OF PART II

A complete description is given of the experimental methods designed to investigate the structure of CO_2-diluted oxy-fuel flames, with a focus on the application of the combustion diagnostics method, the design of the experimental setup at NTNU and the description of the experimental setup at Sandia National Laboratories (SNL).

Laser Raman scattering diagnostics

- Laser Raman scattering enables to perform measurements of the local temperature and main gas species concentrations within reacting or non-reacting mixtures.

- The background on LRS diagnostics is given, with an overview of the different calibration and data-processing methods, their advantages and drawbacks.

- The Hybrid Method has been applied for calibration and data-processing in the present investigation. Its application is detailed and the corresponding calibration measurements routine is described. The resolution of Raman spectra through this method is based on an iterative algorithm linking to local temperature and total number density through the ideal gas law.

- A dedicated software suite has been developed for the present investigation to apply the Hybrid Method to the Raman measurements. The suite enables to prepare the recorded spectra for data-processing, determine the temperature-dependent Raman calibration coefficients and to process and post-process the data. Most items of the software suite have a graphical interface, are evolutive and can be used in any other LRS setup.

Experimental setup at NTNU

- A complete water-cooled combustion rig has been designed to achieve non-premixed oxy-fuel jet flames, stand relatively high flame temperatures and enable a variety a laser diagnostics.

- The experimental setup mainly consists in the oxy-fuel combustion chamber, a 2-axis moving table, a frequency-doubled 532-nm Nd:YAG Continuum Agilite laser system, an Acton Research SP300i spectrometer, a Princeton Instruments PI-MAX ICCD camera and optics.

- Due to the low intensity of Raman scattering signals, an exhaustive work has been performed on signal optimization. The main improvements achieved on each of the main items of the experimental setup are detailed.

- The work on signal optimization justifies the selection of the experimental settings used during the main measurement campaign.

- Though the final uncertainties are significant despite the work on signal optimization, the system provides respectable response enabling parametric studies of quality with non-premixed jet flames.

- Safety has been systematically considered during the whole design of the experimental setup and the resulting inputs to the setup have been reported.

Experimental setup at Sandia National Laboratories

- A 6-month exchange at Sandia National Laboratories enabled to achieve Raman/Rayleigh measurements of great quality in more complex flame conditions than at NTNU.

- The main differences between the experimental setups from SNL and NTNU are highlighted and justify the higher output quality of the LRS setup at SNL.

Particularities of LRS in oxy-fuel flames

Despite the absence of nitrogen, which simplifies the data-processing algorithms by accounting for only six species, replacing air with O_2/CO_2 mixtures makes LRS measurements relatively more challenging than in air atmosphere. The most relevant issues are reported.

- The design of the experimental setup should prevent the flame from mixing with ambient air, which may limit the performance of the LRS measurements.

- Supplying CO_2 at high flow rates can greatly affect its outlet temperature through the Joule-Thomson effects, leading to potentially unstable flame conditions.

- CO_2 physical properties are radically different from those of nitrogen. The higher heat capacity addresses challenging issues regarding the flame stability. The higher refractive index may cause beam steering at the fuel/oxidizer interface. The higher mass density might induce higher levels of uncertainties, especially when CO_2 is a minor species of a mixture dominated by hydrogen. Due to radiative properties of CO_2 and H_2O, oxy-fuel flames radiate a significant thermal load to the surroundings equipments, which may need to be shielded.

- The high range of flame temperatures reached by varying the oxygen content in the oxidizer is not fully covered by the typical calibration procedures.

- The radical pool becomes significant in the burning mixture and cannot be ignored at the considerably high temperatures induced by high oxygen contents in the oxidizer.

- CO_2 displays two intense Raman bands with 532-nm laser. One of them overlaps the one of O_2, and leads to a serious level of uncertainties in the determination of O_2 number density at intermediate and high temperatures.

- Some of the intense Raman rotational bands of H_2 overlap with CO_2 and O_2 and also lead to high levels of uncertainties at intermediate and high temperatures.

- The spontaneous flame luminosity from oxy-fuel flames, mainly consisting of an intense broadband signal originating from CO_2* chemiluminescence and the emission band of highly vibrationally excited water, is very dependent on the oxygen content in the oxidizer. It is a great matter of concern for LRS and requires a dedicated correction procedure.

References

[*Barlow* 2007] *Laser diagnostics and their interplay with computations to understand turbulent combustion*, Barlow, R.S. Proceedings of the Combustion Institute, 2007. 31: p. 49-75.

[*Barlow* 2009a] *Piloted jet flames of CH_4/H_2/air: Experiments on localized extinction in the near field at high Reynolds numbers*, Barlow, R.S., Ozarovsky H.C., Karpetis A.N., and Lindstedt R.P. Combustion and Flame, 2009a. 156(11): p. 2117-2128.

[*Barlow* 2009b] *Application of Raman/Rayleigh/LIF diagnostics in turbulent stratified flames*, Barlow, R.S., Wang G.H., Anselmo P., Sweeney M.S., and Hochgreb S. Proceedings of the Combustion Institute, 2009b. 32: p. 945-953.

[*Bergmann* 1998] *Application of spontaneous Raman and Rayleigh scattering and 2D LIF for the characterization of a turbulent $CH_4/H_2/N_2$ jet diffusion flame*, Bergmann, V., Meier W., Wolff D., and Stricker W. Applied Physics B: Lasers and Optics, 1998. 66(4): p. 489-502.

[*Chigier* 1991] *Combustion Measurements*, Chigier, N.A. 1991: Hemisphere Pub. Corporation.

[*Continuum* 2008] *Service Report Continuum Agilite - Agilite 569-10 QA-Report*, Continuum, A. 2008: December 12th, 2008.

[*Dibble* 1987] *The Spontaneous Raman-Scattering Technique Applied to Nonpremixed Flames of Methane*, Dibble, R.W., Masri A.R., and Bilger R.W. Combustion and Flame, 1987. 67(3): p. 189-206.

[*Dibble* 1990] *An Improved Method of Data Aquisition and Reduction for Laser Raman-Rayleigh and Fluorescence Scattering from Multispecies*, Dibble, R.W., Starner S.H., Masri A.R., and Barlow R.S. Applied Physics B-Photophysics and Laser Chemistry, 1990. 51(1): p. 39-43.

[*Ditaranto* 2011] *Radiative heat flux characteristics of methane flames in oxy-fuel atmospheres*, Ditaranto, M. and Oppelt T. Experimental Thermal and Fluid Science, 2011. 35(7): p. 1343-1350.

[*Eckbreth* 1996] *Laser Diagnostics for Combustion Temperature and Species*, Eckbreth, A.C. 1996: Gordon and Breach Publishers.

[*Fuest* 2011] *A Hybrid Method for Data Evaluation in 1-D Raman Spectroscopy*, Fuest, F., Barlow R.S., Geyer D., Seffrin F., and Dreizler A. Proceedings of the Combustion Institute, 2011. 33(1): p. 815-822.

[*Gaydon* 1974] *The spectroscopy of flames*. Gaydon, A.G. 1974, Chapman and Hall.

[*Geyer* 2005] *1D-Raman/Rayleigh Experiments in a Turbulent Opposed-Jet*, Geyer, D. 2005, Tu Darmstadt, VDI-Verlag, Düsseldorf, Germany. p. ISBN 3-18-353306-5.

[*Heraeus* 2006] *Test Report #18331*, Heraeus. 2006, Heraeus Noblelight GmbH: March 31st, 2006.

[*Hoskins* 1977] *Pure rotational Raman spectroscopy: A dry-lab experiment*, Hoskins, L.C. Journal of Chemical Education, 1977. 54(10): p. 642.

[*Kojima* 2004] *Measurement and simulation of spontaneous Raman scattering in high-pressure fuel-rich H_2–air flames*, Kojima, J. and Quang-Viet N. Measurement Science and Technology, 2004. 15(3): p. 565.

[*Kutne* 2011] *Experimental Analysis of the Combustion Behaviour of Oxyfuel Flames in a Gas Turbine Model Combustor*, Kutne, P., Kapadia B.K., Meier W., and Aigner M. Proceedings of the Combustion Institute, 2011. 33(2): p. 3383-3390.

[*Linow* 2002] *Measurement of temperature and concentration in oxy-fuel flames by Raman/Rayleigh spectroscopy*, Linow, S., Dreizler A., Janicka J., and Hassel E.P. Measurement Science & Technology, 2002. 13(12): p. 1952-1961.

[*Lode* 2009] *Master Thesis*, Lode, B. 2009, NTNU, Trondheim (Norway).

[*Masri* 1988] *Turbulent Nonpremixed Flames of Methane near Extinction - Mean Structure from Raman Measurements*, Masri, A.R., Bilger R.W., and Dibble R.W. Combustion and Flame, 1988. 71(3): p. 245-266.

[*Masri* 1992] *Chemical Kinetic Effects in Nonpremixed Flames of H_2/CO_2 Fuel*, Masri, A.R., Dibble R.W., and Barlow R.S. Combustion and Flame, 1992. 91(3-4): p. 285-309.

[*Meier* 2000] *Raman/Rayleigh/LIF measurements in a turbulent $CH_4/H_2/N_2$ jet diffusion flame: Experimental techniques and turbulence-chemistry interaction*, Meier, W., Barlow R.S., Chen Y.L., and Chen J.Y. Combustion and Flame, 2000. 123(3): p. 326-343.

[*Nguyen* 1996] *Raman-LIF measurements of temperature, major species, OH, and NO in a methane-air Bunsen flame*, Nguyen, Q.V., Dibble R.W., Carter C.D., Fiechtner G.J., and Barlow R.S. Combustion and Flame, 1996. 105(4): p. 499-510.

[*Nicoloso* 2010] *Final Project Report: Investigation of oxy-fuel flame structure by laser diagnostics*, Nicoloso, J. 2010, NTNU, Trondheim (Norway).

[*Nooren* 2000] *Raman-Rayleigh-LIF measurements of temperature and species concentrations in the Delft piloted turbulent jet diffusion flame*, Nooren, P.A., Versluis M., van der Meer T.H., Barlow R.S., and Frank J.H. Applied Physics B-Lasers and Optics, 2000. 71(1): p. 95-111.

[*Reaction-Design* 2008] *CHEMKIN-PRO*, Reaction-Design. 2008: San Diego, 2008.

[*Rondeau* 2011] *Final Project Report: Investigation of oxy-fuel flame structure by laser diagnostics*, Rondeau, D. 2011, NTNU, Trondheim (Norway).

[*Samaniego* 1995] *CO_2* Chemiluminescence in Premixed Flames*, Samaniego, J.M., Egolfopoulos F.N., and Bowman C.T. Combustion Science and Technology, 1995. 109: p. pp. 183-203.

[*Schefer* 2009] *Visible emission of hydrogen flames*, Schefer, R.W., Kulatilaka W.D., Patterson B.D., and Settersten T.B. Combustion and Flame, 2009. 156(6): p. 1234-1241.

[*Sharma* 1980] *Raman Measurements of Hydrogen in the Pressure Range 0.2-630 Kbar at Room-Temperature*, Sharma, S.K., Mao H.K., and Bell P.M. Physical Review Letters, 1980. 44(13): p. 886-888.

[*Singh* 2002] *C. V. Raman and the discovery of the Raman effect*, Singh, R. Physics in Perspective, 2002. 4(4): p. 399-420.

[*Slack* 1985] *High temperature rate coefficient measurements of CO + O chemi-luminescence*, Slack, M. and Grillo A. Combustion and Flame, 1985. 59(2): p. 189-196.

[*Smith* 1999] *http://www.me.berkeley.edu/gri_mech/*, Smith, G.P., Golden D.M., Frenklach M., Moriarty N.W., Eiteneer B., Goldenberg M., Bowman C.T., Hanson R.K., Song S., Gardiner W.C., Lissianski V.V., and Qin Z. 1999.

[*TNF* 2012] *TNF Workshop web site, Sandia National Laboratories, 2012.* TNF. www.ca.sandia.gov/TNF.

[*Warren* 1980] *The Infrared-Spectrum of Matrix-Isolated Hydrogen and Deuterium*, Warren, J.A., Smith G.R., and Guillory W.A. Journal of Chemical Physics, 1980. 72(9): p. 4901-4908.

[*Wehr* 2007] *Single-pulse 1D laser Raman scattering applied in a gas turbine model combustor at elevated pressure*, Wehr, L., Meier W., Kutne P., and Hassa C. Proceedings of the Combustion Institute, 2007. 31: p. 3099-3106.

PART III

RESULTS AND DISCUSSION

INTRODUCTION OF PART III

Results from experimental measurements of the flames described in Section 4 are reported in details in Part III. Flames have been investigated through parametric studies, whose boundaries have been set as follows:

- Laminar premixed flat flames (using a Hencken burner):
  - CH_4/air with equivalence ratio, Φ, varying from 0.7 to 1.15,
  - $CH_4/O_2/CO_2$ with Φ from 0.5 to 0.9 and from 35 to 55 $\%_{mol}$ O_2 in the oxidizer,
  - $H_2/O_2/CO_2$ with Φ from 0.5 to 0.9 and from 15 to 40 $\%_{mol}$ O_2 in the oxidizer.

- Transitional non-premixed jet flames (using a coflow burner):
  - H_2 – air with Re_f = 1600 and coflow speed of 0.23 $m.s^{-1}$,
  - H_2 – O_2/CO_2 with Re_f = 1600, coflow speed of 0.22 $m.s^{-1}$ and from 15 to 70 $\%_{mol}$ O_2 in the oxidizer.

- Turbulent non-premixed jet flames (using a coflow burner):
  - H_2/CH_4 – O_2/CO_2 with 32 $\%_{mol}$ O_2 in the oxidizer, Re_f = 15,000, and from 37 to 55 $\%_{mol}$ H_2 in the fuel,
  - H_2/CH_4 – O_2/CO_2 with 32 $\%_{mol}$ O_2 in the oxidizer, varying Re_f from 12,000 to 18,000 and 55 $\%_{mol}$ H_2 in the fuel.

For the laminar premixed oxy-fuel flames and the transitional non-premixed oxy-fuel flames, results in similar air-fired conditions are systematically reported to highlight the main differences in the flame structure. For the transitional non-premixed oxy-fuel flames, measurements are reported in non-reacting mixtures as well, to emphasize the flame structure features induced by the flame/vortex interactions and the chemical processes.

Laminar flame calculations using Chemkin-Pro [*Reaction-Design* 2008] have been performed in each case to support the analysis and highlight the main features of the flame structures and the chemical processes.

All experimental results described in Part III have been performed using the LRS setup at NTNU (cf. Section 6), except for the turbulent CH_4/H_2 - O_2/CO_2 non-premixed jet flames, which have been performed at Sandia National Laboratories (SNL)

(cf. Section 7). Supplementary non-commented results for the transitional non-premixed oxy-fuel flame can be found in Appendix C. A complementary analysis of the experimental results of the turbulent CH_4/H_2 - O_2/CO_2 non-premixed jet flames can be found in Appendix D, in the form of a journal publication.

In this part, the flame conditions are first detailed for all investigated flames and settings are provided for the laminar flame calculations performed to support the results analysis. Then, a complete description and discussion of the ensemble of results is given, with a special focus on general observations, flame structure and products of combustion.

9. FLAME CONDITIONS

The following tables show the flame conditions of all the flames reported in details within this PhD work. Flames have been investigated at atmospheric pressure. Reactants have been systematically used at ambient temperature, at ca. 294 K.

9.1. Laminar CH_4/air premixed flat flames

Table III.1: Laminar CH_4/air premixed flat flames conditions using a Hencken burner.

			Flow rates ($Nl.min^{-1}$)		
Name	**Equivalence ratio**	**T_{Ad} (K)**	**CH_4**	**Air**	**N_2 (shroud)**
PF-CH_4-air-1	0.70	1734	2.1	28.5	32.0
PF-CH_4-air-2	0.80	1908	2.4	28.5	32.0
PF-CH_4-air-3	0.90	2031	2.7	28.5	32.0
PF-CH_4-air-4	0.95	2098	2.8	28.5	32.0
PF-CH_4-air-5	1.00	2194	3.0	28.5	32.0
PF-CH_4-air-6	1.05	2201	3.1	28.5	32.0
PF-CH_4-air-7	1.10	2196	3.3	28.5	32.0

9.2. Laminar $CH_4/O_2/CO_2$ premixed flat flames

Table III.2: Laminar $CH_4/O_2/CO_2$ premixed flat flames conditions using a Hencken burner.

				Flow rates ($Nl.min^{-1}$)			
Name	**Φ**	**T_{Ad} (K)**	**$\%_{mol}$ O_2 in oxidizer**	**CH_4**	**O_2**	**CO_2**	**N_2 (shroud)**
PF-CH_4-OF-0.9-35	0.90	2248	35	4.2	9.4	17.4	32.0
PF-CH_4-OF-0.9-40	0.90	2366	40	4.7	10.5	15.8	32.0
PF-CH_4-OF-0.9-45	0.90	2466	45	5.2	11.6	14.2	32.0
PF-CH_4-OF-0.9-50	0.90	2552	50	5.7	12.6	12.6	32.0
PF-CH_4-OF-0.7-35	0.70	2036	35	3.4	9.7	17.9	32.0
PF-CH_4-OF-0.7-40	0.70	2188	40	3.8	10.9	16.3	32.0
PF-CH_4-OF-0.7-45	0.70	2317	45	4.2	12.0	14.7	32.0
PF-CH_4-OF-0.7-50	0.70	2418	50	4.6	13.2	13.2	32.0
PF-CH_4-OF-0.5-35	0.50	1689	35	2.5	9.0	18.5	32.0
PF-CH_4-OF-0.5-40	0.50	1818	40	2.8	11.3	16.9	32.0
PF-CH_4-OF-0.5-45	0.50	1973	45	3.1	12.5	15.3	32.0
PF-CH_4-OF-0.5-50	0.50	2110	50	3.4	13.8	13.8	32.0
PF-CH_4-OF-0.5-55	0.50	2235	55	3.7	15.0	12.3	32.0

9.3. Laminar $H_2/O_2/CO_2$ premixed flat flames

Table III.3: Laminar $H_2/O_2/CO_2$ premixed flat flames conditions using a Hencken burner.

				Flow rates ($Nl.min^{-1}$)			
Name	**Φ**	**T_{Ad} (K)**	**%$_{mol}$ O_2 in oxidizer**	**H_2**	**O_2**	**CO_2**	**N_2 (shroud)**
PF-H_2-OF-0.9-15	0.90	1491	15	14.9	8.3	46.8	32.0
PF-H_2-OF-0.9-20	0.90	1791	20	18.5	10.3	41.2	32.0
PF-H_2-OF-0.9-25	0.90	2039	25	21.7	12.1	36.2	32.0
PF-H_2-OF-0.9-30	0.90	2222	30	24.6	13.6	31.8	32.0
PF-H_2-OF-0.9-35	0.90	2356	35	27.1	15.0	27.9	32.0
PF-H_2-OF-0.9-40	0.90	2463	40	29.3	16.3	24.4	32.0
PF-H_2-OF-0.7-20	0.70	1541	20	15.3	10.9	43.7	32.0
PF-H_2-OF-0.7-25	0.70	1789	25	18.2	12.9	38.9	32.0
PF-H_2-OF-0.7-30	0.70	2001	30	20.7	14.8	34.5	32.0
PF-H_2-OF-0.7-35	0.70	2176	35	23.0	16.4	30.5	32.0
PF-H_2-OF-0.7-40	0.70	2315	40	25.2	17.9	26.9	32.0
PF-H_2-OF-0.5-25	0.50	1452	25	14.0	14.0	42.0	32.0
PF-H_2-OF-0.5-30	0.50	1648	30	16.2	16.1	37.7	32.0
PF-H_2-OF-0.5-35	0.50	1831	35	18.2	18.1	33.7	32.0
PF-H_2-OF-0.5-40	0.50	1995	40	20.0	20.0	30.0	32.0
PF-H_2-OF-0.5-45	0.50	2142	45	21.7	21.7	26.5	32.0

9.4. Transitional H_2 - O_2/CO_2 non-premixed jet flames

Table III.4: Transitional H_2 - O_2/CO_2 non-premixed jet flames conditions using a coflow burner.

Name	**%$_{mol}$ O_2 in oxidizer**	**Re_f**	**Jet speed ($m.s^{-1}$)**	**Coflow speed ($m.s^{-1}$)**	**T_{ad} (K)**	**$F_{B\text{-}st}$**
NP-H_2-OF-1	15	1600	47.0	0.22	1580	0.0142
NP-H_2-OF-2	22	1600	47.0	0.22	1984	0.0210
NP-H_2-OF-3	30	1600	47.0	0.22	2277	0.0291
NP-H_2-OF-4	40	1600	47.0	0.22	2514	0.0396
NP-H_2-OF-5	50	1600	47.0	0.22	2691	0.0505
NP-H_2-OF-6	60	1600	47.0	0.22	2839	0.0618
NP-H_2-OF-7	70	1600	47.0	0.22	3288	0.0736

9.5. Transitional H_2 - air non-premixed jet flames

Table III.5: Transitional H_2 - air non-premixed jet flames conditions using a coflow burner.

Name	Re_f	Jet speed ($m.s^{-1}$)	Coflow speed ($m.s^{-1}$)	T_{ad} (K)	$F_{B\text{-}st}$
NP-H_2-air	1600	47.0	0.23	2001	0.0284

9.6. Turbulent H_2/CH_4 - O_2/CO_2 non-premixed jet flames (at SNL)

Table III.6: Turbulent H_2/CH_4 - O_2/CO_2 non-premixed jet flames conditions using a coflow burner.

Name	$\%_{mol}$ O_2 in oxidizer	$\%_{mol}$ H_2 in fuel	Re_f	Jet speed ($m.s^{-1}$)	Coflow speed ($m.s^{-1}$)	T_{ad} (K)	$F_{B\text{-}st}$
A-1	32	55	15,000	98.2	0.778	2250	0.0535
A-2	32	45	15,000	84.4	0.755	2243	0.0553
A-3	32	37	15,000	75.8	0.739	2236	0.0565
B-1	32	55	12,000	78.6	0.622	2250	0.0535
B-2	32	55	15,000	98.2	0.778	2250	0.0535
B-3	32	55	18,000	117.8	0.933	2250	0.0535

9.7. Flame calculations settings

- CFD software: Chemkin-Pro [*Reaction-Design* 2008]
- Models:
  - "Premixed-stabilized burner" for laminar premixed flat flames
  - "Opposed-jets flow burner" for non-premixed jet flames
- Kinetic mechanisms:
  - GRI-Mech 3.0 [*Smith* 1999] in presence of CH_4
  - Davis mechanism [*Davis* 2005] for flames involving only H_2 as fuel
- Transport regimes:
  - Full multi-component with thermal diffusion/Soret effect
  - Equal diffusivities
- Heat losses: Radiation transfer to surrounding ambient air
- Strain rate: Calculated for opposed-jet flows with formula defined in [*Cheng* 2006]

Flame compositions are similar to those achieved with the LRS setup. Flame calculations were performed to get reference cases, either for calibration or to highlight physical phenomena happening in the flame structure or chemistry. For non-premixed flames, calculations were systematically performed using two different transport regimes. The full multi-component transport regime (FMCT) combined with thermal diffusion (Soret effect) is the most accurate, since each species is characterized by its own molecular diffusion properties and the Soret effect is used to account for molecular transport induced by temperature gradients. The equal diffusivities transport regime (EDT) simplifies the transport equations by considering all diffusivities equal to the thermal diffusivity. EDT is especially adapted to turbulent flows, where the mixing is rather controlled by turbulent mixing rates than by diffusion.

The GRI-Mech 3.0 was selected due to its wide use for natural gas combustion in air atmosphere. The mechanism includes a large number of chemical reactions (325), involving 53 species, making it an adapted candidate to tackle oxy-methane combustion. Nevertheless, when dealing with non-premixed oxy-fuel jet flames using hydrogen as fuel, Chemkin-Pro calculations using the GRI-Mech 3.0 did not converge for strain rates higher than 15 s^{-1}. Since higher strain rates were aimed for those flames [*Barlow* 2000], the Davis mechanism was used instead and provided acceptable results for strain rates up to 200 s^{-1}. The Davis mechanism counts 41 chemical reactions involving 14 species, and was developed and tested for H_2-CO combustion [*Davis* 2005, *Weydahl* 2011]. It is an interesting mechanism for CO_2-diluted oxy-hydrogen flames since all required elements are present in the reactions and computer-time is low with the reduced number of reactions compared to the GRI-Mech 3.0. Supplementary mechanisms, such as those from Yetter, Jones-Lindstedt, Westbrook-Dryer [*Westbrook* 1981, *Jones* 1988, *Yetter* 1991, *Andersen* 2009, *Weydahl* 2011], could have also been of interest for comparison with the experimental results. However, the focus of the present investigation was set on carrying out experiments rather than testing kinetic mechanisms.

10. LAMINAR PREMIXED OXY-FUEL FLAT FLAMES

10.1. Introduction

Laminar premixed CO_2-diluted oxy-fuel flat flames are still relatively un-explored, though they enable to isolate the impact of oxy-fuel conditions on the chemical processes. The quasi-adiabatic conditions associated to the Hencken burner allows comparing the flames directly with laminar flame calculations, whose main settings are described in Section 9.7. LRS measurements have been performed in the post-flame region at 25 mm above the Hencken burner, giving a composition of the flame products directly comparable to the results of the laminar flame calculations. This enables to emphasize the relative importance of the different reactions in the composition of the combustion products.

Besides being performed for calibration purpose, laminar premixed CH_4/air flat flames are also used as reference cases to highlight the main particularities of CO_2-diluted oxy-fuel conditions. Three cases are described in the following paragraphs: reference case with air, laminar premixed $CH_4/O_2/CO_2$ flat flames and laminar premixed $H_2/O_2/CO_2$ flat flames. Each case is also compared to its corresponding laminar flames calculations. For each case, the results analysis starts with general observations and is followed by a discussion about the products of combustion at equilibrium and the flame structure.

10.2. Reference case: laminar premixed CH_4/air flat flames

10.2.1. General observations

Laminar premixed CH_4-air flat flames (cf. typical flame in Figure III.1) are well understood and have well-known compositions and temperatures. As seen in Figure III.1, the probe volume is located above the flat flames, and under the zone where ambient air starts to mix with combustion products. Only a low red luminosity is visible on the photograph, which is typical from flames generating water and having negligible CO_2* chemiluminescence. Since the red luminosity appears away from the Raman bandwidth of interest on the spectra (cf. Section 8.3.2), no correction for flame luminosity is required for those flames. Besides, no soot is generated within the

conditions described in Table III.1. Those observations make laminar premixed CH_4-air flat flames good candidates for confident LRS calibration at flame temperatures, and reference cases for the present investigation.

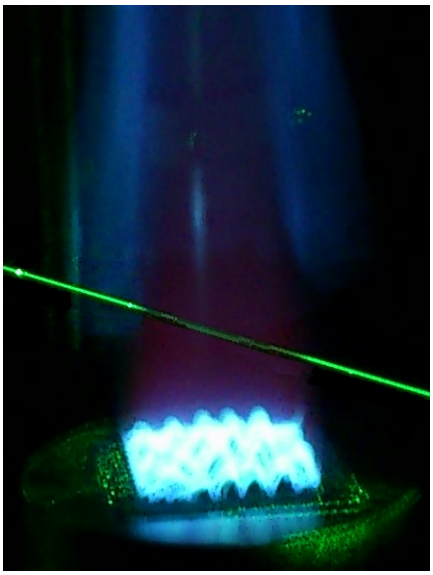

Figure III.1: Photograph of laminar premixed CH_4-air flat flame (PF-CH_4-air-3).

10.2.2. Equilibrium - products of combustion

As described in Section 5.2.2, since those flames are part of the calibration routine, results from data-processing are refined to fit the results from one-dimensional laminar flame calculations using the GRI-Mech 3.0. Figure III.2 shows an example of averaged experimental results from laminar premixed CH_4/air flat flames compared to the results from corresponding laminar flame calculations. Equivalence ratios are adjusted relatively to the non-reacting mixtures previously measured (cf. Figure II.9). Results are given for the temperature, and molar fractions of the main flame species. The species of interest are the major products of fuel-lean combustion: O_2, H_2O, CO_2 and N_2, and the major products from fuel-rich combustion: H_2O, CO_2, CO, H_2, N_2 and CH_4. Results from CH_4 molar fraction are not shown in Figure III.2, since no CH_4 Raman band appeared on recorded spectra, meaning that no CH_4 was present in the burning mixture, within the detection limits of the LRS setup. Despite a slight contribution from CH_4 indicated by the laminar flame calculations, the difference in molar fraction for other species should not be significant and remain within the uncertainties of the experimental results.

The amplitude of the vertical bars in Figure III.2 represents the root mean square (RMS) of the fluctuations in the processed experimental results. The flames are supposedly flat fields and relatively stable. Besides, performing 15 on-CCD accumulations averages any field fluctuations. Consequently, most of the fluctuations

come from the detection system itself and from amplifying effects from cross-talk coefficients. For instance, a small variation of CO_2 number density could lead to a large variation in O_2 number density through the cross-talk coefficients during data-processing. The vertical bars are thus quite representative of the accuracy of the LRS setup and account for the level of uncertainties displayed in Section 6.5.

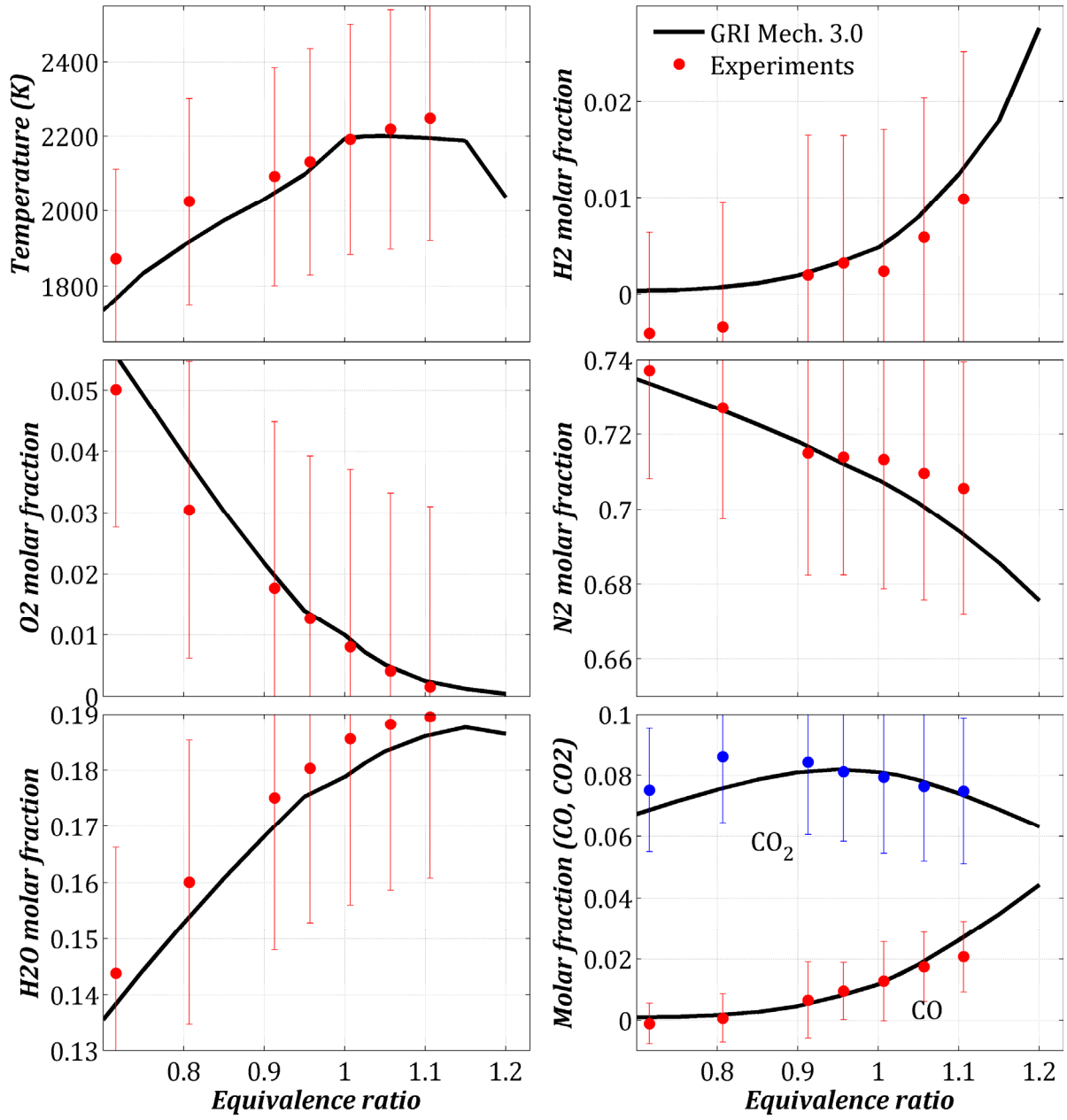

Figure III.2: Averaged experimental results from laminar premixed CH_4/air flat flames over 70 frames, compared to results from laminar flame calculations. Vertical bars indicate the RMS of the fluctuations in the processed results.

Averaged scalars are relatively consistent with the trends displayed by the results from laminar calculations. They display some discrepancy at low equivalence ratios, probably amplified by a locally fail cross-talk, which over-corrects H_2 number

density and whose effects are propagated to other species. The LRS detection of H_2 at flame temperatures is known to be complex, which can be seen through the level of uncertainties for H_2 in other LRS setups [*Bergmann* 1998, *Barlow* 2009].

Temperature peaks beyond stoichiometric conditions, at ca. Φ = 1.05. This can be detailed using an analogy with a description of propane-air flame calculations described in [*Turns* 2000]. The peak temperature is due to both heat combustion and heat capacity of the products declining for equivalence ratio superior to 1. From Φ = 1 to Φ = 1.05, the heat capacity decreases more rapidly than the heat combustion, while it is the other way around beyond Φ = 1.05. The decrease in heat capacity rather comes from the decrease in number of product moles formed per mole of fuel burned than by the decrease in mean specific heat.

CO, H_2 and H_2O display an increasing molar fraction with the equivalence ratio, due to the increasing presence of C and H atoms from more abundant CH_4 in the reactants. The slope for CO and H_2 molar fraction increases, while the slope for H_2O decreases, as the number density of O_2 molecules is reduced by the growing equivalence ratio. CO_2 molar fraction is also affected by the lack of O_2 molecules at high equivalence ratios. It starts to decrease around stoichiometric conditions, where its oxidation cannot be completed and CO molecules are rather produced with the increasing number of C atoms brought by the increasing amount of CH_4 in the reactants. N_2 molar fraction decreases as the air-to-fuel ratio varies with the equivalence ratio. The simultaneous presence of O_2, H_2 and CO at stoichiometric conditions is a result of dissociation. The three species would be zero if the assumption of complete combustion was fulfilled.

10.2.3. Flame structure

An insight into the flame structure of the laminar premixed methane-air flat flames is also of interest. Figure III.3 shows the axial profiles of the main species molar fractions from the laminar flame calculations corresponding to PF-CH_4-air-5, whose equivalence ratio is equal to 1. Figure III.4 shows the corresponding results for O, H and OH radicals, and the temperature. The unburned gas mixture flows from the left to the right of the figures. N_2 molar fraction profile is not completely straight, which indicates that N_2 is not totally inert. No significant dissociation of N_2 happens at this range of temperature, due to its strong triple covalent bond, but N_2 rather takes part in reaction of NO_x formation. NO_x are not shown, since their molar fraction is at least an order of magnitude lower than for other displayed radicals, and NO_x is beyond the scope of the present investigation.

The flame region is readily identified by the sharp gradients in profiles of molar fractions and temperature. It can be clearly seen how CH_4 and O_2 are consumed and lead to formation of main products H_2O, CO_2, CO and H_2. Molar fractions of minor products

(O, H and OH) also locally peak in the flame region and slowly decrease in the post-flame region. CO molar fraction rises up to the point where no more C atoms from CH_4 are available and reactions leading to O, H and OH radicals start to be significant. From this point, CO is rather oxidized into CO_2 through the CO burnout reaction given in Eq. I.16, also known as CO burnout reaction.

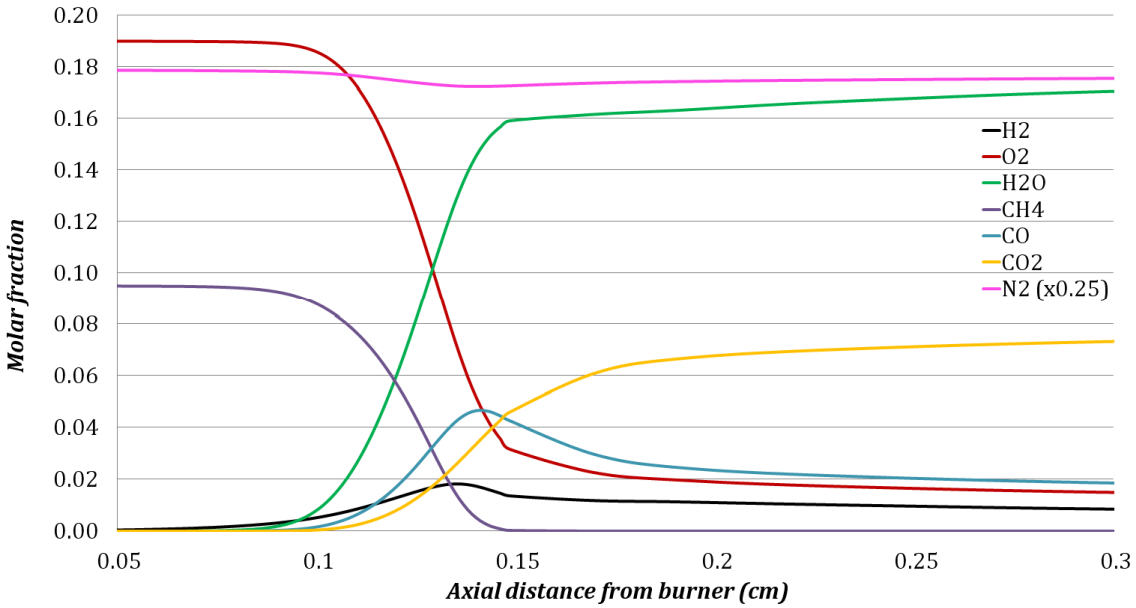

Figure III.3: Axial profiles of the main species molar fractions from one-dimensional laminar flame calculations corresponding to PF-CH_4-air-5 (Φ = 1) using GRI-Mech 3.0.

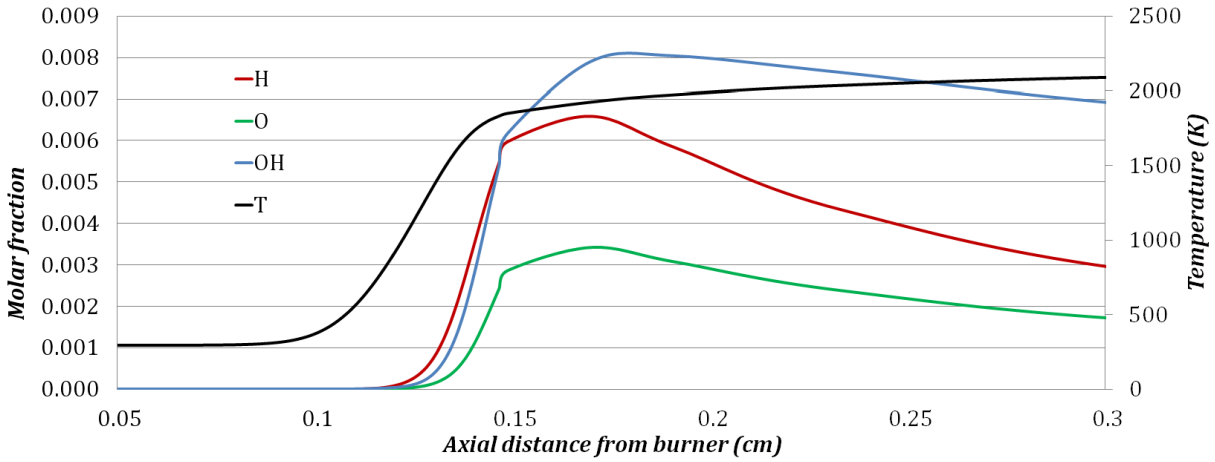

Figure III.4: Axial profiles of the radicals species molar fractions and temperature from one-dimensional laminar flame calculations corresponding to PF-CH_4-air-5 (Φ = 1) using GRI-Mech 3.0.

It is interesting to note that CO molar fraction is locally larger than CO_2 molar fraction at stoichiometric conditions. This happens only from an equivalence ratio beyond 0.95 and is promoted by dissociation reactions that tend to be more pronounced at higher temperatures (cf. Section 2.2.9), within the zone of equivalence ratio where temperature peaks (cf. Figure III.2). The dissociation reaction given in Eq.

I.17 tends to minimize the changes due to increased temperatures by shifting towards the right side, rather producing CO and O_2. The final balance of this reaction also helps understand why O_2 remains present in the products at stoichiometric conditions.

In the post-flame region, the presence of CO, H_2 and other radicals tends to slowly decrease as CO_2 and H_2O keep being formed. For richer mixtures, the lack of available O atoms prevents CO from being oxidized into CO_2 in the post-flame region. Molar fractions of H, O and OH radicals tend to increase with the equivalence ratio up to stoichiometric conditions. Then the molar fractions of O and OH radicals decrease due to the lack of available O atoms while the molar fraction of H radical keeps increasing.

10.3. Laminar premixed $CH_4/O_2/CO_2$ flat flames

10.3.1. General observations

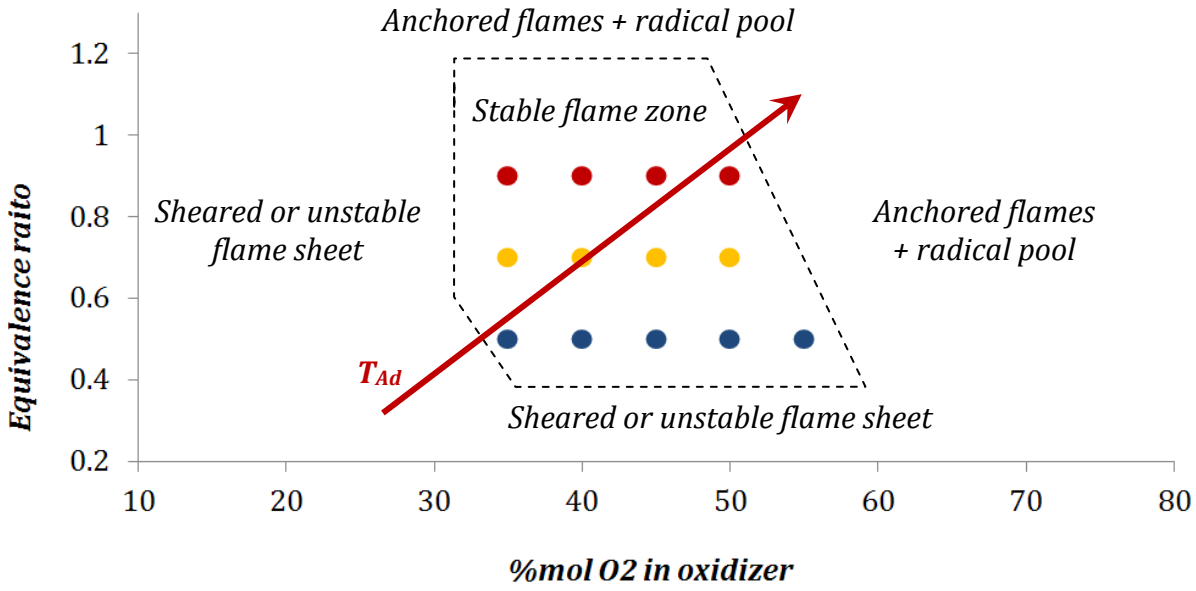

Figure III.5: Stability domain of the laminar premixed $CH_4/O_2/CO_2$ flat flames with the Hencken burner used in the conditions given in Table III.2. Investigated flames are represented by the coloured dots and the stability domain is delimited by the black dotted lines.

Within the range of flow rates used with the Hencken burner (cf. Table III.2), the range of stable flames is limited in terms of equivalence ratio and oxygen content in the oxidizer. Figure III.5 gives a schematic view of the stability domain and the coordinates of the investigated laminar premixed $CH_4/O_2/CO_2$ flat flames within this domain (coloured dots). If the molar fraction of oxygen in the oxidizer is not sufficiently high, the flame sheet shifts downstream and eventually becomes sheared or unstable, so that no LRS measurements can be reliably performed. This limit is also a convergence criterion for the one-dimensional laminar flame calculations. If the molar fraction of

oxygen in the oxidizer is too high, the flame sheet is anchored to the Hencken burner. The high flame temperature associated to the high oxygen content in the oxidizer may damage the burner. This also brings to the equation a conductive heat transfer from the flame to the burner, which cannot be accurately accounted for in the one-dimensional laminar flame calculations. Similar limits are reached with the equivalence ratio. If the latter is too low, the flame becomes unstable, while the flame is anchored if it is too high. Another limit associated to high equivalence ratios or high oxygen contents in the oxidizer is the significant local concentration of radicals (cf. Section 8.2.3) that cannot be detected with LRS techniques and is not accounted for in the calibration procedure.

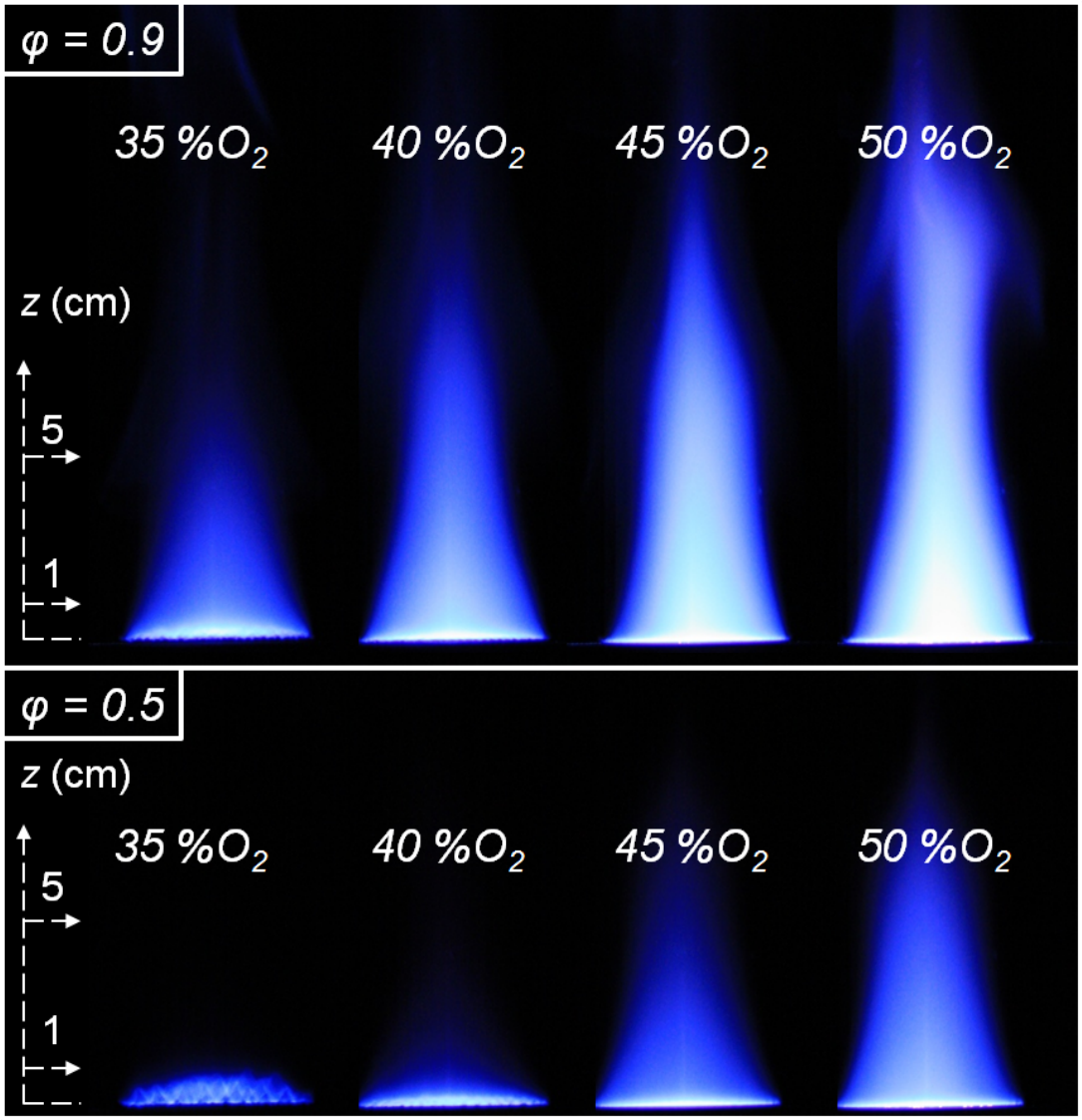

Figure III.6: Photographs taken from the laminar premixed $CH_4/O_2/CO_2$ flat flames for $\Phi = 0.9$ and $\Phi = 0.5$. ISO: 1600. Exposure time: 1/100 s.

Figure III.6 shows photographs taken from the laminar premixed $CH_4/O_2/CO_2$ flat flames with $\Phi = 0.9$ and $\Phi = 0.5$. Camera settings were the same for all photographs. While similar flames in air atmosphere rather display a red colour, the dominant colour

in those flames is blue, indicating that the flame luminosity is dominated by CO_2* chemiluminescence (cf. Section 8.3.2). It can be seen that the length of the visible plume increases with the oxygen content in the oxidizer, leading to a more and more intense flame luminosity at the location of the probe volume (z = 25 mm). Those observations are valid for both flame series at Φ = 0.9 and Φ = 0.5. The intensity of the visible flame luminosity significantly increases with the equivalence ratio, as it can be seen from the two series of flames. This is related to the dependency of CO_2* chemiluminescence to CO and O concentrations, whose presence is potentially higher while getting closer to stoichiometric conditions (cf. Section 8.3.2).

10.3.2. Equilibrium - products of combustion

Figure III.7 shows the averaged experimental results from laminar $CH_4/O_2/CO_2$ flat flames and the corresponding results from one-dimensional laminar flame calculations using GRI-Mech 3.0. Results for the main species and the temperature are given for three different equivalence ratios, as detailed in Table III.2. Laminar flame calculations for Φ = 0.7 were not performed. Experimental results for CH_4 and H_2 are not shown since they did not appear in the recorded Raman spectra, or were under the detection limits of the LRS setup. Though CH_4 molar fraction was almost zero at these equivalence ratios, results from flame calculations for H_2 are shown as they display a non-negligible molar fraction.

The overall experimental results seem to follow the trends given by the laminar flame calculations. They also seem consistent when comparing the trends for the three different equivalence ratios. The match between calculations and experimental results is poorer at Φ = 0.9. The flame luminosity is more intense (cf. Figure III.6) at this equivalence ratio and thus, giving away more interferences which cannot be completely corrected. This could explain the misalignment between the dots, and especially the behaviour of the results for the flame at Φ = 0.9 and with 50 $\%_{mol}$ O_2 in the oxidizer (PF-CH_4-OF-0.9-50), which show more discrepancy. O_2 molar fraction at Φ = 0.9 seems to be the most affected. The trend of the experimental results for CO_2 looks also slightly off, though the offset most likely comes from the interdependence of the results while calculating the molar fractions. CO_2 number density (not shown here) actually shows better agreement with the laminar flame calculations, so that the offset cannot be induced by CO_2, but rather by the combination of small offsets from O_2, H_2O and CO.

Results from the laminar flame calculations for O, H and OH radicals shown in Figure III.8 can help understand the underlying phenomena inducing the equilibrium composition of the combustion products. First, it should be noted that temperature increases with both the oxygen content in the oxidizer and the equivalence ratio. For a given oxygen content in the oxidizer, temperature and H_2O, H_2, CO, OH, O and H molar fractions increase as the mixture gets richer, while O_2 molar fraction decreases. The

trends are quite comparable to laminar premixed CH_4/air flat flames. The large increase in temperature with higher oxygen contents in the oxidizer is rather linked to the decreasing content of CO_2 in the oxidizer. Due to its fairly large heat capacity, CO_2 significantly absorbs heat from combustion and mitigates the flame temperature. N_2 has a somewhat lower influence in air-fired flames, as its heat capacity is lower.

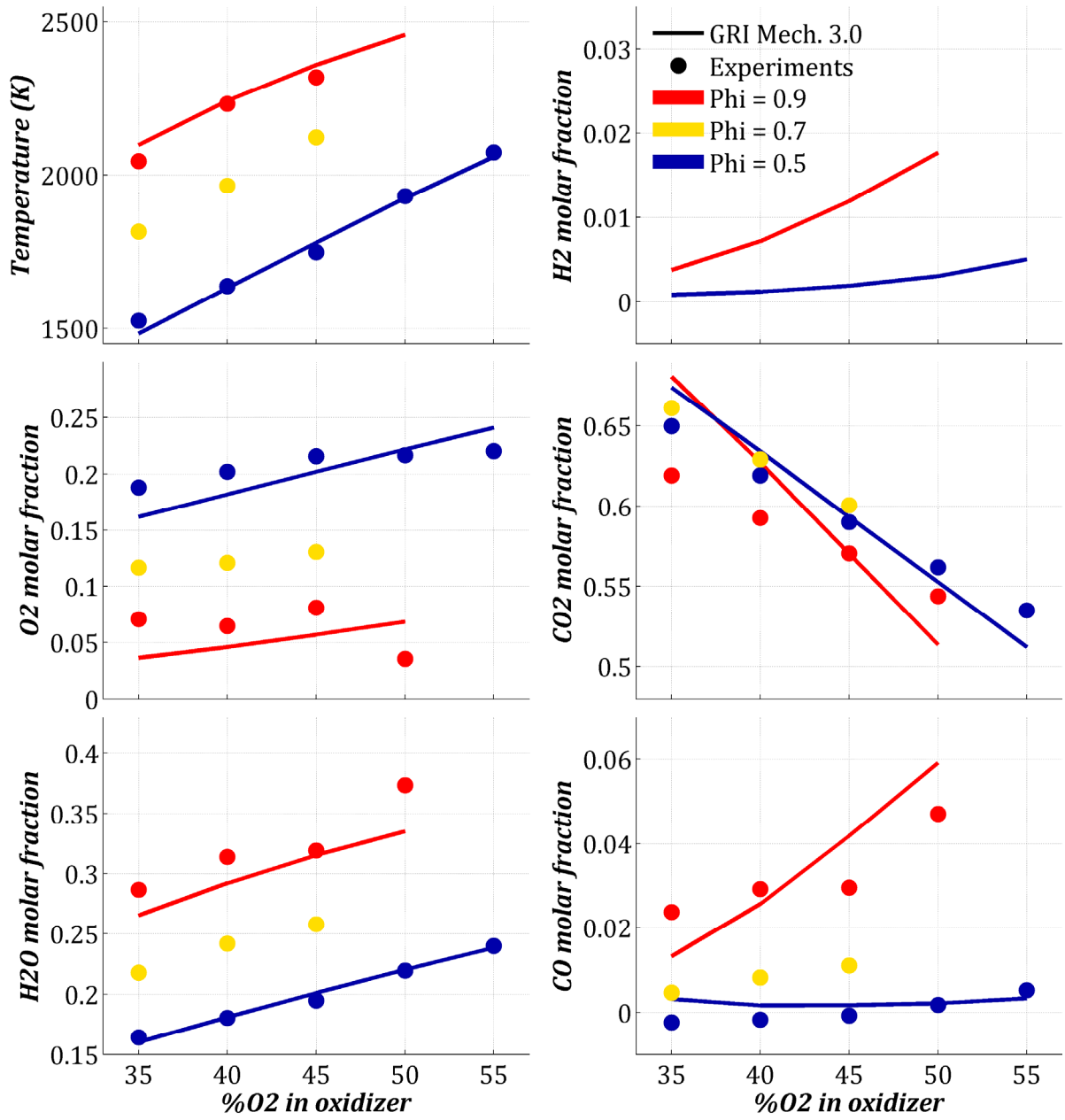

Figure III.7: Averaged experimental results from laminar premixed $CH_4/O_2/CO_2$ flat flames compared to corresponding results from one-dimensional laminar flame calculations using GRI-Mech 3.0.

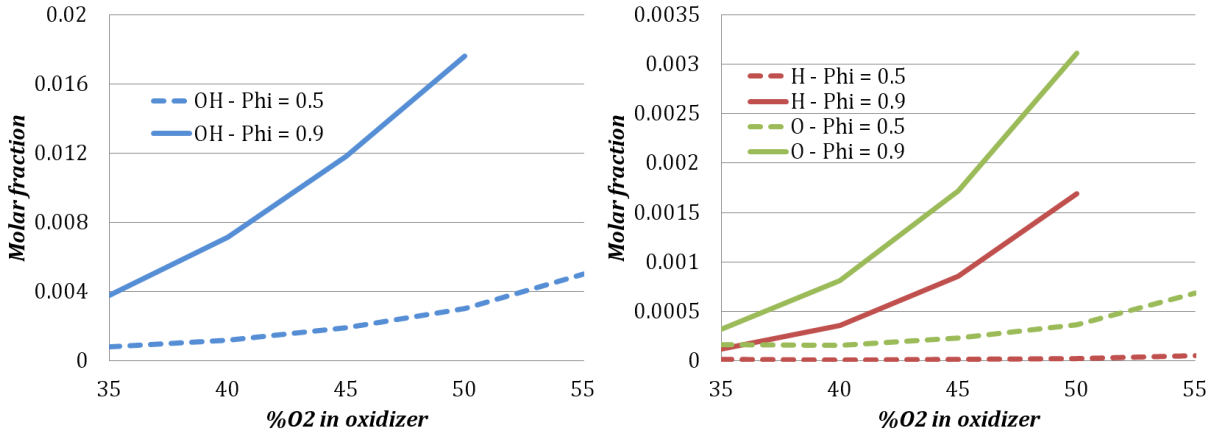

Figure III.8: Results from one-dimensional laminar flame calculations for O, H and OH radicals, using GRI-Mech 3.0.

The evolution of CO_2 is more complex as the species is, at the same time, a diluent, a combustion product and participates to the reaction. Within these conditions, the CO_2 molar fraction always ends up higher in the combustion products than in the unburned mixture of reactants. The relative part of CO_2 originating from the oxidation of CH_4 increases with the O_2 content in the oxidizer. However, according to the laminar flame calculations, the slope of CO_2 molar fraction, as a function of oxygen content in the oxidizer, is lower at Φ = 0.9 than at Φ = 0.5. This means that the net production of CO_2 is least at Φ = 0.9, and that CO is rather formed, up to reaching a considerable molar fraction for a mixture under stoichiometric conditions.

As it can be seen with the evolution of minor species as a function of the oxygen content in the oxidizer, dissociation is much greater at Φ = 0.9. Molar fractions of the radicals are several times larger than in comparable laminar premixed CH_4/air flat flames. Dissociation is responsible for a reduction in temperature: CO_2 is dissociated into CO and O radical through the reaction given in Eq. I.17. The effects can also be seen in the slope of H_2O molar fraction at Φ = 0.9. Its slope decreases with the oxygen content in the oxidizer, while those of OH and H radicals increases, as the degree of dissociation of H_2O into OH and H radicals increases. The slope of temperature is consequently seen to decrease within these conditions. Besides, the reverse direction of the CO burnout reaction (cf. Eq. I.16) contribute to the conversion of CO_2 into CO and OH, at high oxygen contents in the oxidizer and Φ = 0.9, since H radicals are more available (cf. Section 3.4). The result is interesting since the CO_2 participates to a larger degree in the reaction as its content is decreased in favour of O_2. Therefore, this trend should attain a maximum before reaching 100 $\%_{mol}$ O_2 in the oxidizer, though flames could not be tested up to these conditions.

10.3.3. Flame structure

Figure III.9 shows the axial profiles of the main species molar fractions from the laminar flame calculations corresponding to PF-CH_4-OF-0.9-45 (Φ = 0.9, 45 $\%_{mol}$ O_2 in oxidizer). Figure III.10 shows the corresponding results for O, H and OH radicals, and the temperature. Compared with the laminar premixed CH_4/air flames, two main observations can be done. First, as written previously, CO_2 is not only a diluent, since its increasing molar fraction across the flame profile attests of its positive net production. Second, radical species display molar fractions several times higher than in laminar premixed CH_4/air flames. Other species do not display radically different profiles.

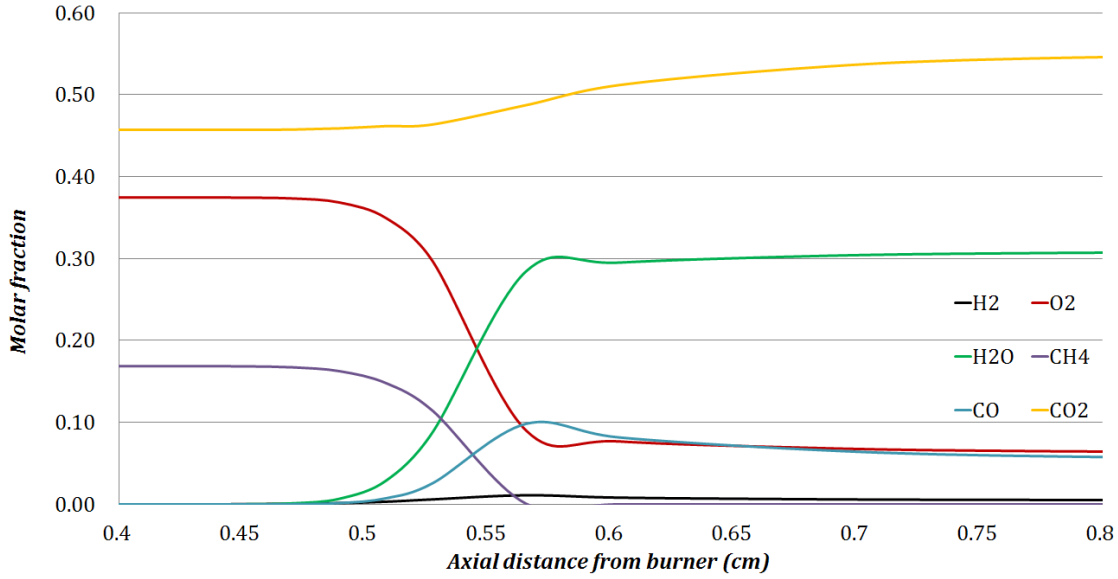

Figure III.9: Axial profiles of the main species molar fractions from one-dimensional laminar flame calculations corresponding to PF-CH_4-OF-0.9-45 (Φ = 0.9, 45 $\%_{mol}$ O_2 in oxidizer) using GRI-Mech 3.0.

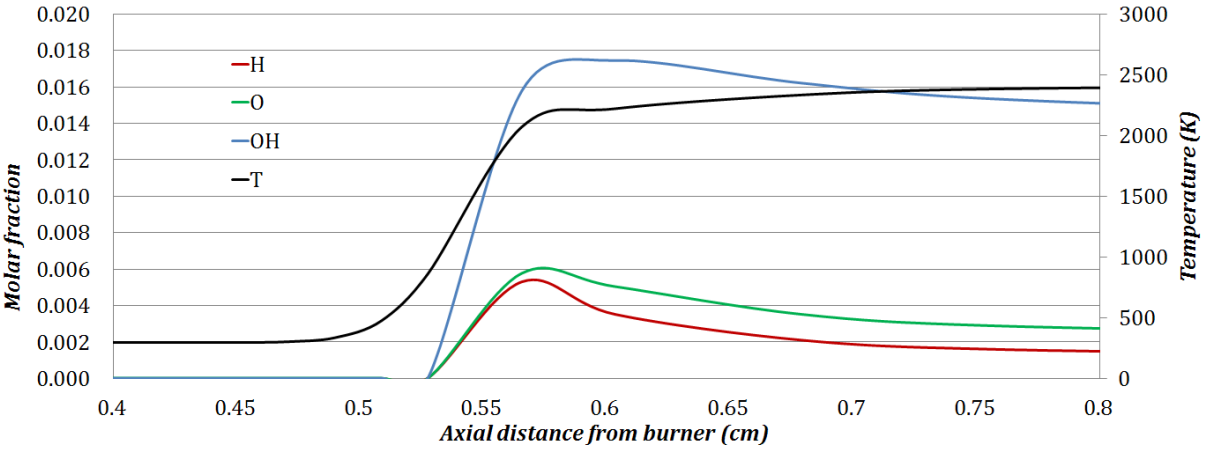

Figure III.10: Axial profiles of the radical species molar fractions from one-dimensional laminar flame calculations corresponding to PF-CH_4-OF-0.9-45 (Φ = 0.9, 45 $\%_{mol}$ O_2 in oxidizer) using GRI-Mech 3.0.

Regarding the evolution of the flame structure by varying the equivalence ratio, the flame thickness is the most affected. Considering two points where temperature is at 10 and 90 %, respectively, of the total temperature rise, with 45 $\%_{mol}$ O_2 in the oxidizer, flames at Φ = 0.5 appear 8 times thicker than at Φ = 0.9 (cf. Table III.7). Using similar geometry, flow rates and reaction mechanism, results from one-dimensional flame calculations for PF-CH_4-air-3 give a flame thickness 50 % thicker than PF-CH_4-OF-0.9-45. The flame thickness scales as shown in Eq. III.1 (found in [*McAllister* 2011]) and an increase in flame temperature will increase both the thermal diffusivity, α, and the laminar flame speed, S_L. Laminar flame speed generally peaks near stoichiometric conditions and decreases in leaner or richer mixtures, leading to a minimum flame thickness near stoichiometric conditions [*McAllister* 2011]. Considering CO_2-dilution, previous researches showed that high CO_2-dilution reduces laminar flame speeds, while high O_2 content in the oxidizer increases it (cf. Section 3.3.1), compared to laminar flame speeds found in laminar premixed CH_4/air flat flames. As shown in Table III.7, oxy-fuel conditions induce wider amplitude variations of flame thickness than those met in air-fired conditions.

$$\delta \approx \frac{\alpha}{S_L} \qquad \textit{Eq. III.1}$$

Table III.7: Flame thickness from one-dimensional laminar flame calculations for a sample of investigated flames, using GRI-Mech 3.0.

Flame	***PF-CH_4-air-3***	***PF-CH_4-OF***			
		-0.5-35	***-0.5-45***	***-0.9-35***	***-0.9-45***
Flame thickness (mm)	0.9	5.3	4.8	1.0	0.6

10.4. Laminar premixed $H_2/O_2/CO_2$ flat flames

10.4.1. General observations

Besides providing an insight into CO_2-diluted oxy-hydrogen flames, those flames are especially of interest to investigate the participation of CO_2 in the combustion reactions. CO_2 is expected to contribute to the reverse rate of the CO burnout reaction (cf. Section 3.4.1). This could be readily identified by the presence of CO in the flame products, since CO_2 is the only source of C atoms within these conditions. Consequently, the comparison with laminar premixed $CH_4/O_2/CO_2$ flat flames and with laminar premixed CH_4/air flat flames can highlight the chemical processes specific to oxy-fuel conditions.

Within the range of flow rates used with Hencken burner (cf. Table III.3), the domain of stable flames shown in Figure III.11 meets similar restrictions as those for laminar premixed $CH_4/O_2/CO_2$ flat flames (cf. Section 10.3.1). Sufficiently high equivalence ratios lead to anchored flames and non-negligible radical pool, while too low equivalence ratios result in sheared or unstable flame sheets. Similarly, sufficiently high oxygen contents in the oxidizer lead to anchored flames and significant radical pool, while too low oxygen contents in the oxidizer result in sheared or unstable flame sheets.

Compared to laminar premixed $CH_4/O_2/CO_2$ flat flames, the stability domain is shifted towards lower oxygen contents in the oxidizer for the same equivalence ratios. In addition, the range of adiabatic temperatures is even wider than for laminar premixed $CH_4/O_2/CO_2$ flat flames, starting with temperatures as low as 1452 K, as shown in Table III.3. This comes from the lower auto-ignition temperature and the higher molecular diffusivity of hydrogen, which allows self-sustaining flames at relatively low temperatures and wide flammability limits.

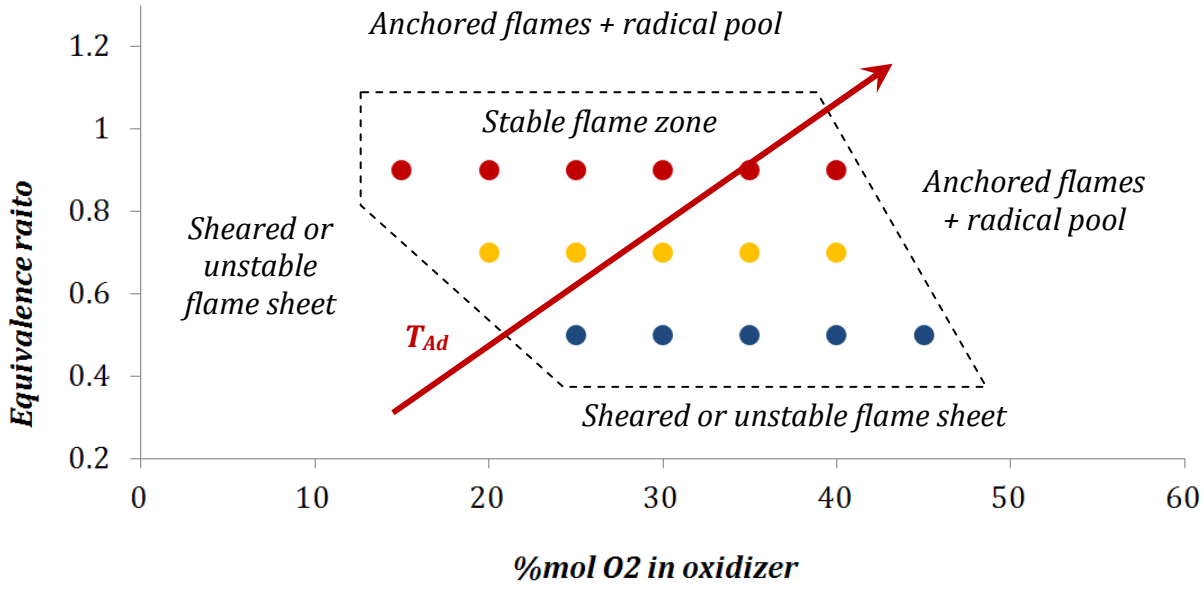

Figure III.11: Stability domain of the laminar premixed $H_2/O_2/CO_2$ flat flames with the Hencken burner used in the conditions given in Table III.3. Investigated flames are represented by the coloured dots and the stability domain is delimited by the black dotted lines.

Figure III.12 shows a sample of photographs from laminar premixed $H_2/O_2/CO_2$ flat flames. Their overall visible luminosity is not as strong as with laminar premixed $CH_4/O_2/CO_2$ flat flames. At low equivalence ratios and low oxygen contents in the oxidizer, the flame sheet has a blue/white colour, while the plume is hardly visible. As the equivalence ratio and the oxygen content in the oxidizer increase, the flame sheet turns to intense white and the plume is dominated by a slight purple/red spontaneous emission, linked to the high presence of hot water in the flame products (cf. Section 8.3.2). This is confirmed by the wide spectral band around 710 – 740 nm on recorded

Raman spectra (cf. Figure II.51). For richer mixtures and higher oxygen contents in the oxidizer, the plume is dominated by a light blue colour originating from CO_2* chemiluminescence, enhanced by higher presence of CO and O radicals (cf. Section 8.3.2). Within these conditions, the plume length also gets longer, as observed in laminar premixed $CH_4/O_2/CO_2$ flat flames.

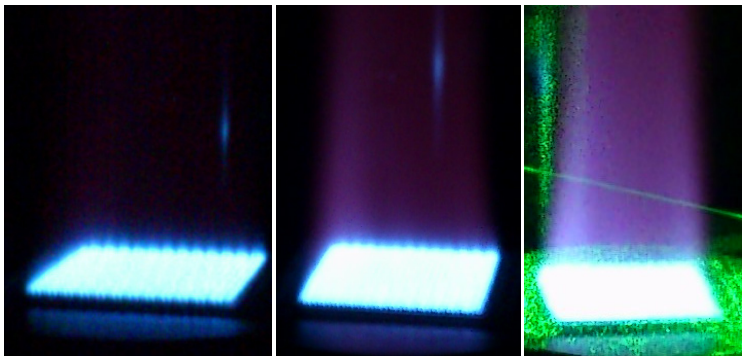

Figure III.12: Sample of photographs from laminar premixed $H_2/O_2/CO_2$ flat flames. From left to right: PF-H_2-OF-0.5-35, PF-H_2-OF-0.5-40 and PF-H_2-OF-0.5-45.

10.4.2. Equilibrium - products of combustion

Figure III.13 shows the averaged experimental results from laminar premixed $H_2/O_2/CO_2$ flat flames and the corresponding results from one-dimensional laminar flame calculations using GRI-Mech 3.0 and Davis mechanism. Results for the main species, OH radicals and the temperature are given for three different equivalence ratios, as detailed in Table III.3. Experimental results for H_2 molar fraction are not shown since they do not appear in the measurements, or are under the detection limits of the LRS setup, as no corresponding Raman peaks shows up on spectra.

The averaged experimental results and the one-dimensional laminar flame calculations from both mechanisms display some discrepancy. This can mainly be explained by the differences observed for CO molar fraction. CO profiles calculated using the Davis mechanism seem to indicate that the flame calculations have converged before the oxidation of CO into CO_2 in the post-flame region has reached its full equilibrium in the flame products. CO molar fraction appears then too high, especially at low oxygen contents in the oxidizer. This also highlights the difficulty for the mechanism to accurately predict CO molar fraction from laminar premixed $H_2/O_2/CO_2$ flat flames, as both mechanisms predict different trends for CO, and the corresponding experimental results do not agree. This can especially be seen for the flames at Φ = 0.9 and at high oxygen contents in the oxidizer, despite the uncertainties from the experimental results. The over-prediction of CO_2 dissociation into CO leads to higher total number densities, and consequently, to lower temperatures in the results from the laminar flame calculations than in the experimental results.

Similarly to the results from laminar premixed $CH_4/O_2/CO_2$ flat flames, experimental results show more discrepancy at Φ = 0.9, most likely due to the high interferences from spontaneous flame luminosity that could not be properly corrected. This can especially be seen for O_2 molar fraction. Most observations on the evolution of the temperature and molar fractions of flame species with the equivalence ratio and the oxygen content in the oxidizer are comparable to those made for premixed $CH_4/O_2/CO_2$ flat flames in Section 10.3.1.

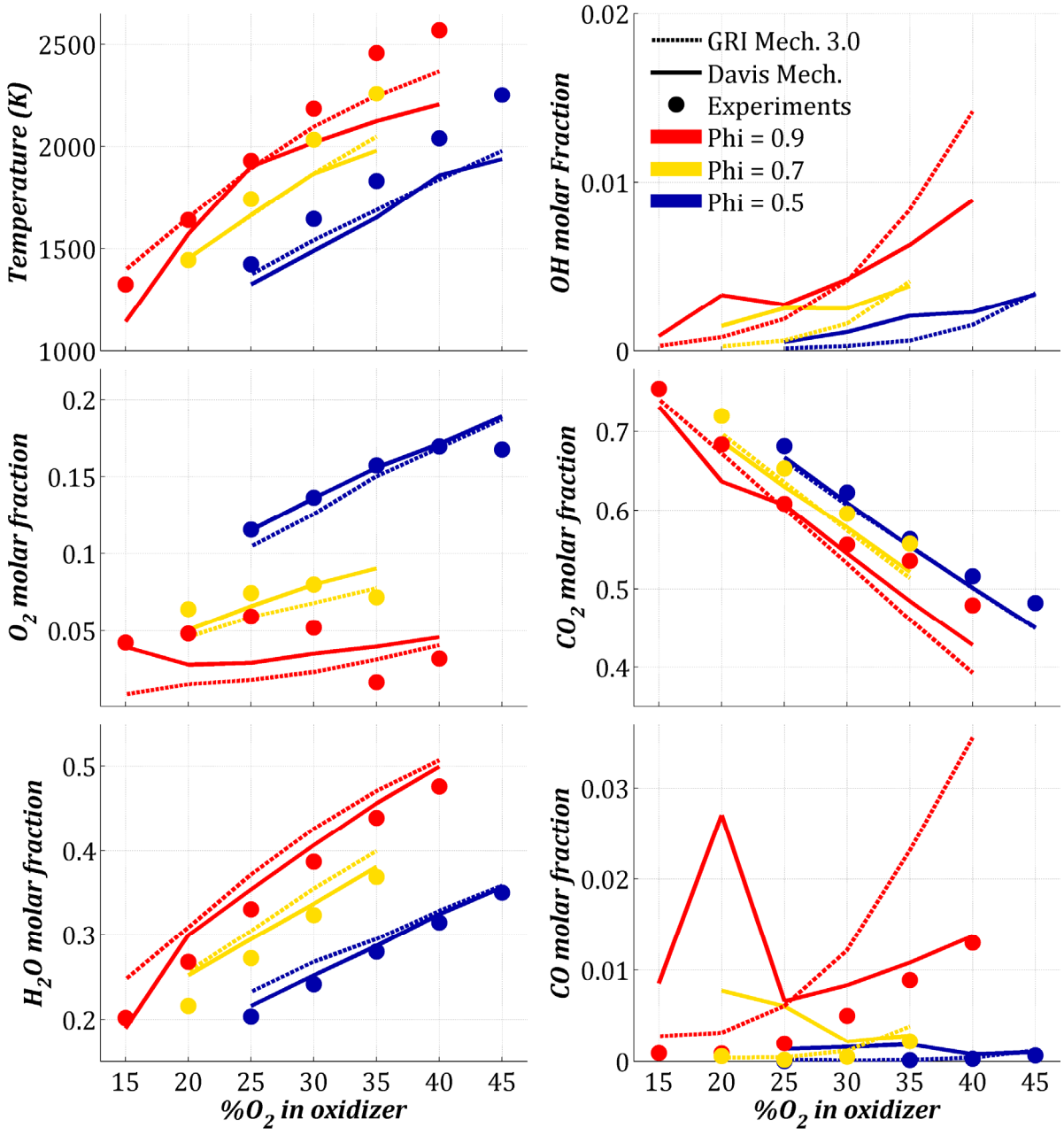

Figure III.13: Averaged experimental results from laminar premixed $H_2/O_2/CO_2$ flat flames compared to corresponding results from one-dimensional laminar flame calculations using GRI-Mech 3.0 and Davis mechanism.

Results for the molar fractions of H and O radicals from the laminar flame calculations are shown in Figure III.14. Once again, discontinuities can be seen from the results using Davis mechanism at low oxygen contents in the oxidizer, indicating an early convergence of the flame calculations before radicals reach full equilibrium in the post-flame region. This can be explained by the reduced number of reactions to 28 in Davis mechanism, while GRI-Mech 3.0 counts 325 reactions. Though GRI-Mech 3.0 only displays results for the same number of species as the Davis mechanism in these conditions (11 species), a higher number of reactions seem to participate in the global combustion reaction. This results in finer and more consistent results for minor species. Nevertheless, results for CO molar fraction using GRI-Mech 3.0 appear over-predicted at high oxygen contents in the oxidizer compared to the experimental results.

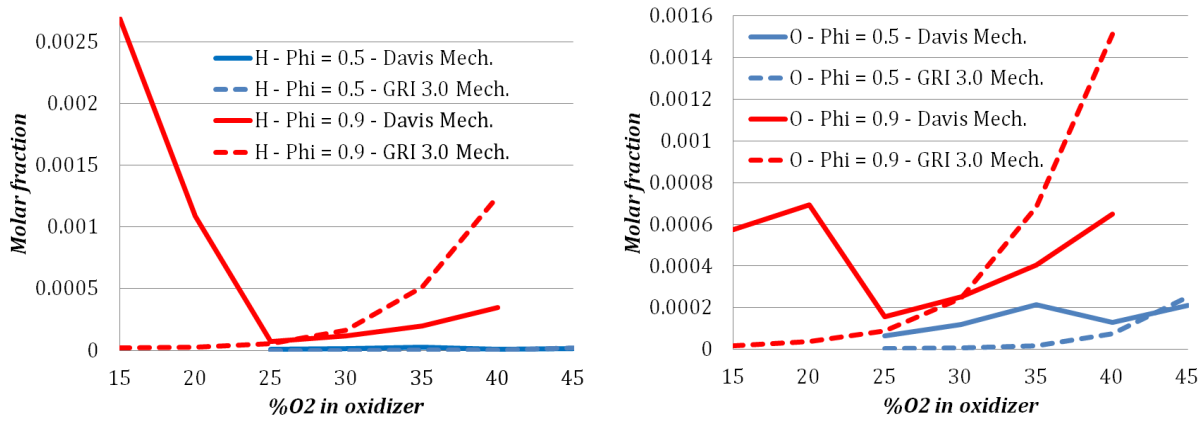

Figure III.14: Results from one-dimensional laminar flame calculations for H and O radicals, using Davis mechanism and GRI-Mech 3.0 for two different equivalence ratios.

10.4.3. Flame structure

Figure III.15 shows the axial profiles of the main species molar fractions from the laminar flame calculations corresponding to PF-H_2-OF-0.9-25 (Φ = 0.9, 25 $\%_{mol}$ O_2 in oxidizer) using GRI-Mech 3.0. Figure III.16 shows the corresponding results for OH, H and O radicals, and the temperature. Corresponding profiles calculated using Davis mechanism (not shown here) display very comparable trends. The main difference is the axial location of the flame region, which significantly varies from one mechanism to another. Using Davis mechanism leads to flames regions generally closer to the burner than using GRI-Mech 3.0. This tendency is the opposite for low equivalence ratios and low oxygen contents in the oxidizer.

Most profiles have similar trends to those observed in laminar premixed $CH_4/O_2/CO_2$ flat flames, considering H_2 as fuel instead of CH_4. A major difference with the latter profiles and those from laminar premixed CH_4/air flat flames is the broadened molar fraction profile of H_2 due its large diffusion coefficient and its heat conductivity. This leads to low values at the onset of the flame region and to a maximum in the O_2

profile at the same location. This is consistent with the observations made in results of flame calculations from laminar premixed H_2/air flames found in [*Warnatz* 2000]. This explanation also applies for the local maximum seen for CO_2.

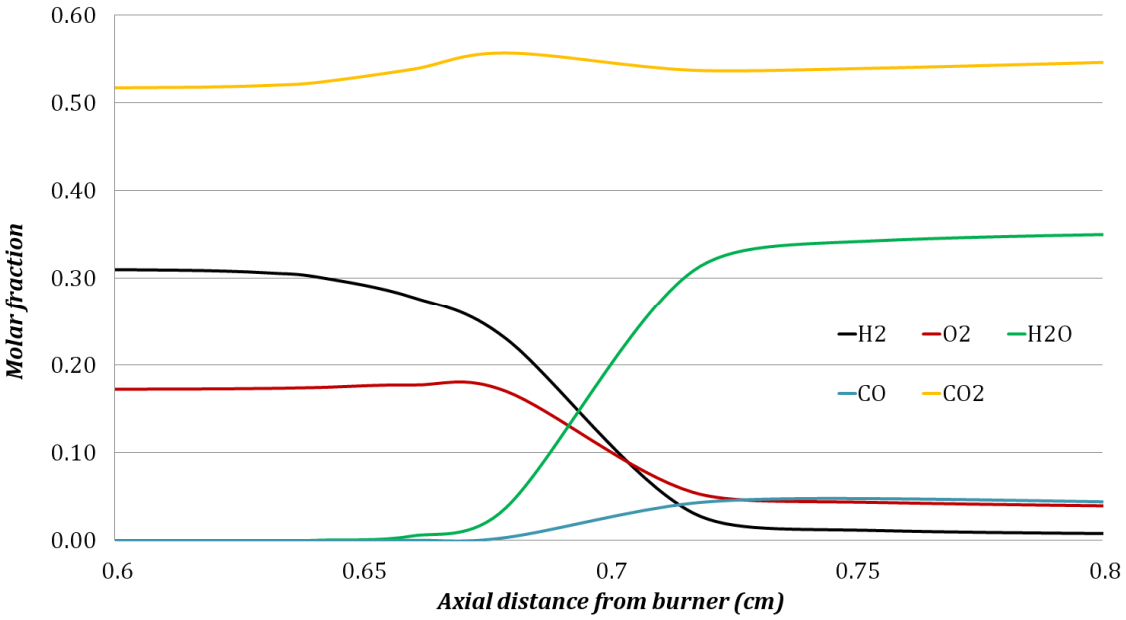

Figure III.15: Axial profiles of molar fractions of the main species from one-dimensional laminar flame calculations corresponding to PF-H_2-OF-0.9-25 (Φ = 0.9, 25 %$_{mol}$ O_2 in oxidizer) using GRI-Mech 3.0.

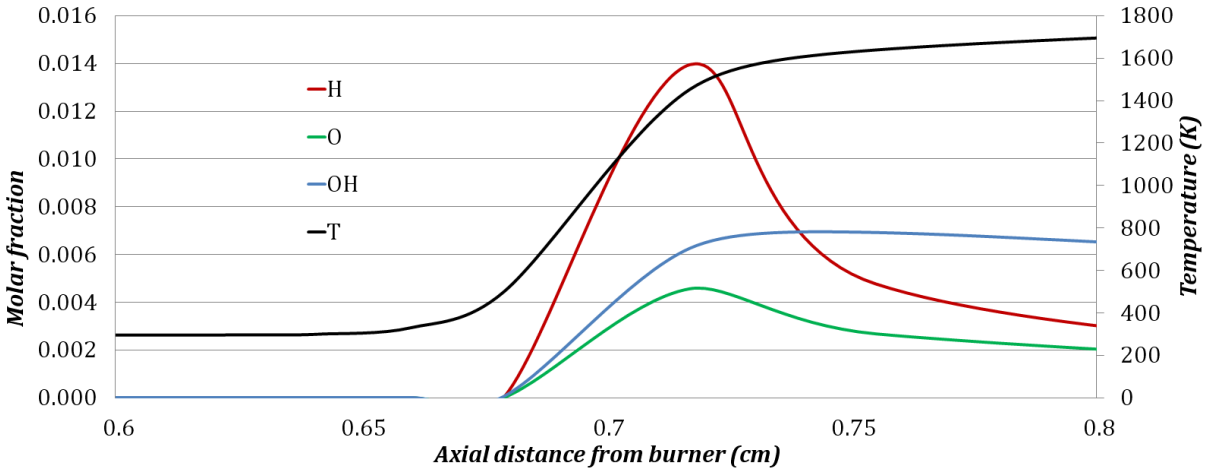

Figure III.16: Axial profiles of the temperature and molar fractions of OH, H and O radicals from one-dimensional laminar flame calculations corresponding to PF-H_2-OF-0.9-25 (Φ = 0.9, 25 %$_{mol}$ O_2 in oxidizer) using GRI-Mech 3.0.

Another major difference with profiles from laminar premixed $CH_4/O_2/CO_2$ flat flames is the molar fraction of H radicals that dominates O and OH radicals. This has also been observed for fuel-rich laminar premixed CH_4/air flames, when no more oxygen atoms are available after the flame region. The phenomenon has also been

observed in results of flame calculations from laminar premixed H_2/air flames found in [*Warnatz* 2000] and is characteristic from flames using hydrogen. The molar fraction of OH radicals tends to dominate in the flame region at higher oxygen contents in the oxidizer. Farther downstream, in the post-flame region, the molar fraction of OH radicals dominates in all the investigated laminar premixed $H_2/O_2/CO_2$ flat flames.

Though it passes by a local maximum, CO_2 molar fraction globally increases. However, CO_2 cannot have a positive net production since it is the only species with C atoms within the reactants and CO shows up in the flame region. Therefore, the net production of CO_2 is actually negative. At Φ = 0.5, CO_2 molar fraction slowly increases, without passing by a local maximum, since the molar fraction profile of H_2 is not as broadened as at Φ = 0.5, due to lower temperatures, and consequently, lower diffusion effects.

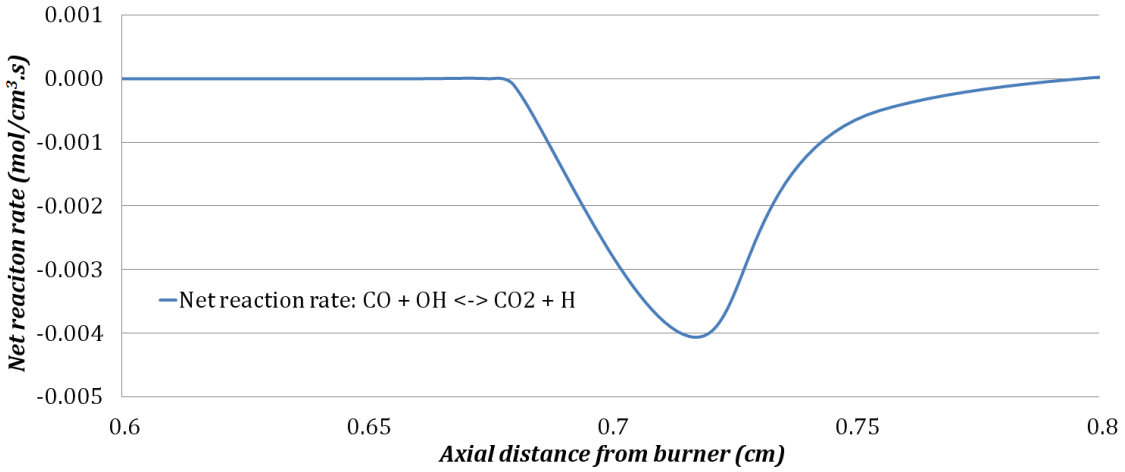

Figure III.17: Axial profile of the net reaction rate of the CO burnout reaction from one-dimensional laminar flame calculations corresponding to PF-H_2-OF-0.9-25 (Φ = 0.9, 25 $\%_{mol}$ O_2 in oxidizer) using GRI-Mech 3.0.

Figure III.17 shows the results from laminar flame calculations using GRI-Mech 3.0 for the net reaction rate of the CO burnout reaction (cf. Eq. I.16). In terms of magnitude, this reaction is the main one involving both CO and CO_2 and is about one or two orders of magnitude greater than the net reaction rate of the dissociation reaction given in Eq. I.17. The ranges of net reaction rate are about the same using both reaction mechanisms. The net reaction rate is zero in the preheat zone and becomes negative once the temperature is sufficiently high to trigger the reverse rate of the CO burnout reaction in the flame region, forming CO. This is well correlated with the sudden presence of CO in the flame region. The reaction is promoted by the relatively high presence of H radicals in the flame region. The negative peak of the net reaction rate is actually correlated with the maximum molar fraction of H radicals in the flame region. From this point, the relative importance of the reaction decreases, along with the molar fraction of H radicals. Within the post-flame region, the net reaction rate reaches a

positive peak about an order of magnitude lower in absolute value than the negative peak from the flame region. This is consistent with the partial oxidation of CO into CO_2 in this region.

The amplitude of the negative peak of the net reaction rate increases with both the equivalence ratio and the oxygen content in the oxidizer. This shows that the reaction is rather controlled by the availability of H radicals, which is enhanced by both high oxygen contents in the oxidizer inducing high temperatures, and the use of hydrogen as fuel. It is interesting to note that, despite CO_2 is one of the two reactants of the reverse reaction, higher presence of CO_2 leads to lower amplitudes of the negative net reaction rate in this case.

Table III.8 shows examples of flame thicknesses from one-dimensional laminar flame calculations using GRI-Mech 3.0, for a sample of investigated flames. Results from calculations using Davis mechanism generally give substantially thicker flames. Unlike the flame thicknesses displayed in Table III.7, the influence of the equivalence ratio for one given oxygen content in the oxidizer is quite low. This is due to the flame speeds found in hydrogen flames, which are several times higher than for CH_4-based laminar flames (cf. Figure I.17 and [*Liu* 2003]). This provides an extensively greater stability to the flames. The influence of the oxygen content appears much larger, since a change of 15 $\%_{mol}$ O_2 in the oxidizer doubles the flame thickness for the sample of flames used in Table III.8.

Table III.8: Flame thicknesses from one-dimensional laminar flame calculations using GRI-Mech 3.0 for a sample of investigated flames.

Flame	***PF-H_2-OF***			
	-0.5-25	***-0.5-40***	***-0.9-25***	***-0.9-40***
Flame thickness (mm)	1.3	0.6	1.3	0.7

11. NON-PREMIXED OXY-FUEL JET FLAMES

11.1. Introduction

Non-premixed oxy-fuel jet flames are complex and have been relatively unexplored, due to most reasons detailed in Section 8. The significant level of soot particulates prevents from performing LRS in non-premixed CO_2-diluted methane jet flames. Hydrogen-dilution of the fuel enables to reduce laser-induced fluorescence signals from soot precursors to an acceptable level on Raman spectra. Replacing methane by pure hydrogen also enables to perform LRS in favourable conditions and brings comparable flames to the investigation.

The present chapter first deals with a non-premixed transitional hydrogen – air flame, which is used as a reference case for comparison with similar jet flames in oxy-fuel atmosphere. Then, the experimental results are detailed and discussed for the transitional non-premixed H_2 - O_2/CO_2 jet flames and the turbulent non-premixed H_2/CH_4 – O_2/CO_2 jet flames.

11.2. Reference case: transitional non-premixed H_2 – air jet flame

11.2.1. General observations

A transitional non-premixed H_2 – air jet flame is used as a reference case for the study of non-premixed oxy-fuel jet flames, since the flame is Raman-friendly and its chemistry and flame structure are relatively well known. Its jet Reynolds number and its coflow speed are similar to those used for the transitional non-premixed H_2 - O_2/CO_2 jet flames. Its Raman characteristics also enable to refine the Raman calibration coefficients for a few Raman cross-talks, such as those induced by the Raman rotational bands of hydrogen at flame temperature (cf. Section 8.3.1).

Figure III.18 shows a photograph of NP-H_2-air. Despite the longer exposure time compared to Figure III.6 (1/30 s versus 1/100 s), the contrast appears very weak. The flame luminosity exhibits a very low intensity, dominated by a red/purple colour, characteristic of hot water at flame temperatures (cf. Section 8.3.2). The flame luminosity does not reach sufficiently high levels to add up any significant uncertainties.

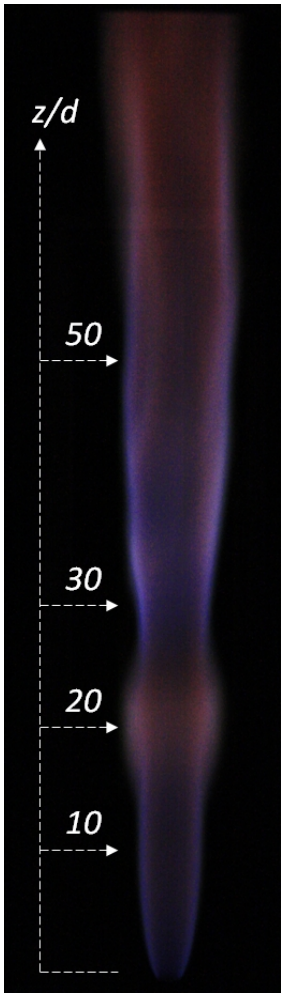

Figure III.18: Photograph of a transitional non-premixed H_2 – air jet flame (NP-H_2-air). ISO: 1600. Exposure time: 1/30 s.

It can also be seen that, in the near field, the jet flame develops with a laminar structure. Farther downstream, evidences of an instability are revealed by a spherical shape followed by a bottleneck pattern (at about z/d = 20 in Figure III.18). Due to its blurry appearance, the instability seems to intermittently oscillate more or less around the same axial location. Instabilities in transitional non-premixed jet flames have been widely investigated, as detailed in Section 2.3.2. This instability corresponds to the breakpoint between the laminar region upstream and the turbulent region downstream.

The main parameter influencing the onset of the breakpoint is the jet exit Reynolds number, Re_f. The phenomenon tends to happen especially for Re_f from ca. 1350 to 2000, which is characteristic from the transitional regime of pipe flows. The instabilities induced by the shear stress in the velocity gradient near the wall can only be dampened by viscous forces until the breakpoint. The onset of the breakpoint is expected to decrease with Re_f, as the pipe flow generates larger and more intense instabilities at the pipe outlet, until the flow is totally controlled by turbulent mixing rates.

The phenomenon happens in both reacting and non-reacting mixtures, though it is delayed in flames, as the combustion reaction laminarises the flow in the near-field (cf. Section 2.3.2). All non-premixed hydrogen jet flames from the present investigations display relatively similar instabilities since they are defined by $Re_f = 1600$.

11.2.2. Non-reacting jets

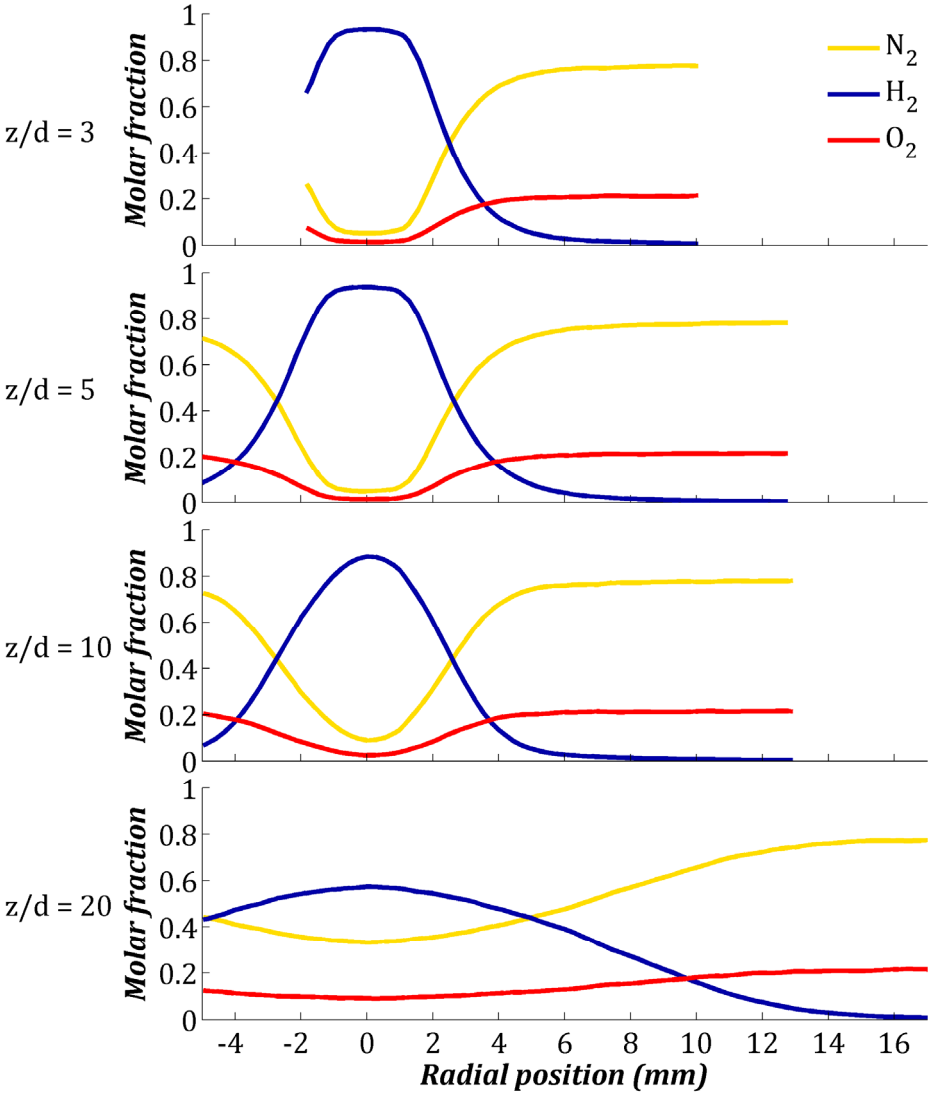

Figure III.19: Reynolds-averaged radial profiles of H_2, N_2 and O_2 molar fractions from non-premixed non-reacting jet flow of H_2 – air with $Re_f = 1600$, at four different heights above the fuel nozzle.

Figure III.19 shows the Reynolds-averaged experimental results from radial profiles of H_2, N_2 and O_2 molar fractions from non-premixed non-reacting jet flow of H_2 – air, at four different heights above the fuel nozzle. The inner hydrogen jet first develops as a laminar jet, gently mixing with the oxidizer through the shear layer (cf. Section 2.3.2.2). The mixing region is initially relatively broad due to the high diffusivity

of hydrogen, and does not seem to expand within the ten first diameters above the fuel nozzle.

The onset on the breakpoint marking transition between laminar and turbulent flows occurs between 10 and 20 diameters above the fuel nozzle. Beyond this point, the inner jet is dominated by turbulent mixing rates rather than diffusion rates. Turbulent mixing rates tend to flatten the radial profiles of scalars by considerably increasing axial and radial mixing. During the overall development of the non-premixed jet, the axi-symmetry is conserved, at least for the averaged scalars.

Results show that oxygen and nitrogen are present at low molar fractions in the inner jet, at least from three diameters above the fuel nozzle. This is verified on the recorded spectra and is not induced by Raman cross-talks effects from hydrogen. The molar fraction of oxygen and nitrogen resulting from the early mixing does not significantly vary between 3 and 5 diameters above the nozzle.

11.2.3. Flames

11.2.3.1. Radial profiles of scalar measurements

Figure III.20 shows the Reynolds-averaged radial profiles of the molar fraction of the main species and the temperature from NP-H_2-air, measured by LRS at different heights above the fuel nozzle. The profiles are not perfect, especially at 20 and 30 diameters above the fuel nozzle, due to the different Raman cross-talks at intermediate and flame temperatures, which are not fully calibrated. At high temperatures, the molar fraction of oxygen appears slightly over-corrected due to the cross-talk from hydrogen.

The inner jet of hydrogen develops as a laminar diffusion jet, up to reaching the onset of the breakpoint between 20 and 30 diameters above the nozzle, from where the flow is expected to be fully dominated by the turbulent mixing rates. The onset of the transition of flow regime occurs more downstream than in the non-reacting case. The phenomenon is well-known and was widely observed in similar flow configurations (cf. Section 2.3.2). Due to the combustion reactions, temperatures are locally higher and the kinematic viscosity increases, inducing local laminarisation effects in the outer layer of the hydrogen jet. The higher kinematic viscosity helps dampening the micro-turbulent structures initiated at the nozzle exit up to the onset of the breakpoint, where the turbulent structures cannot be handled anymore and the turbulent mixing rates prevail. Beyond the breakpoint, the combustion takes place in the central jet, as seen by the mixing of reactants and products, and the higher temperatures.

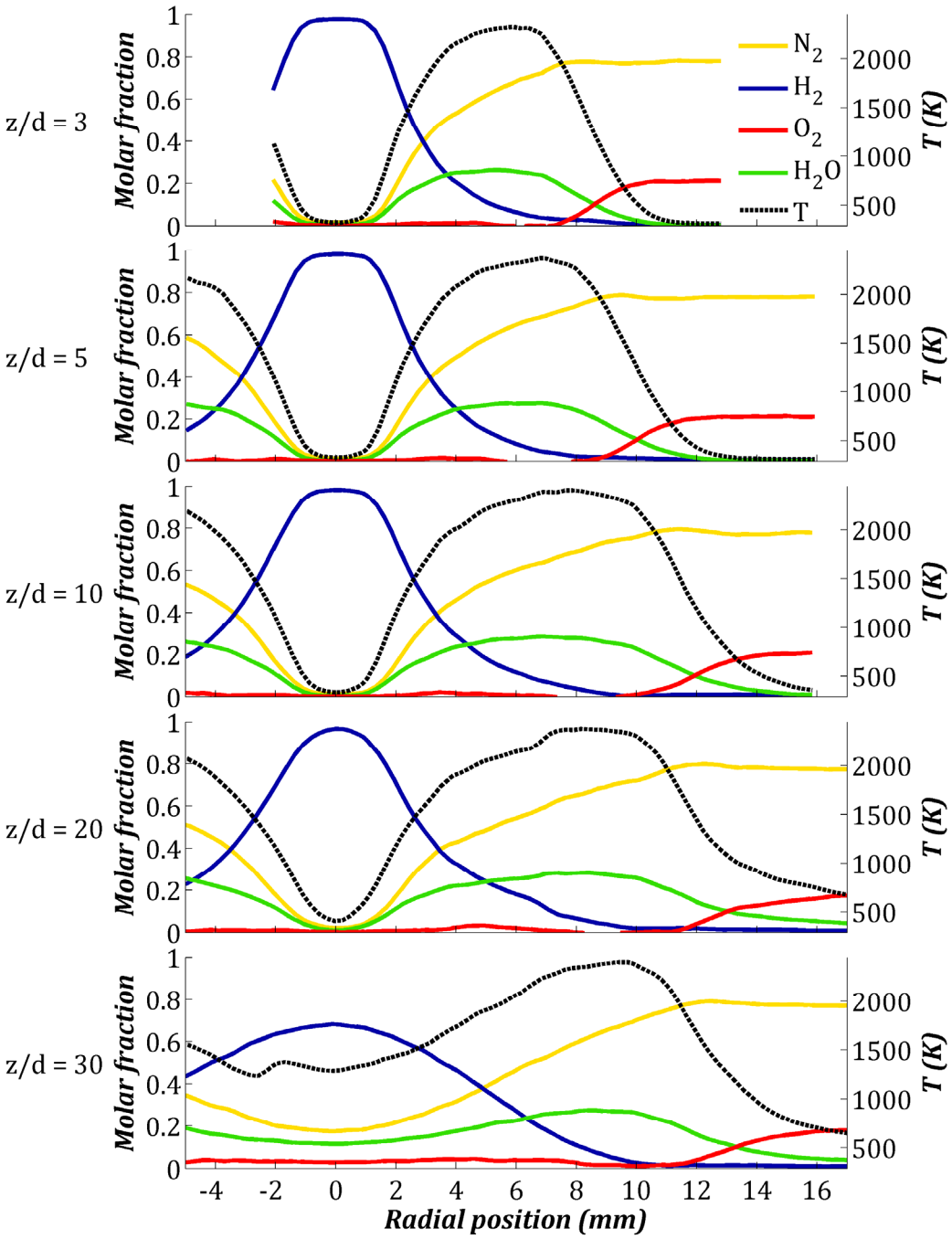

Figure III.20: Reynolds-averaged radial profiles of H_2, N_2, O_2 and H_2O molar fractions and temperatures from non-premixed jet flames of H_2 – air with Re_f = 1600, measured by LRS at different heights above the fuel nozzle.

The inner jet of hydrogen gently broadens with the axial distance in the laminar part. The broadening is slightly amplified compared to the non-reacting case, due to the high diffusivity of hydrogen increasing with the temperature. Oxygen is consumed at the outer border of the flame region while nitrogen dilutes the reaction. Unlike in the non-reacting case, nitrogen does not penetrate the inner jet until the breakpoint, as a consequence of the combustion reaction.

The temperature peak of the flame region is relatively constant along the investigated axial distances. As seen with the temperature profiles, the reaction zone broadens radially with the axial distance, as expected from the expansion of laminar diffusion flames in the near-field. A broadening of the temperature profile towards the inner core marks the regime transition, as the turbulent mixing rates prevail on diffusion in the central jet. Another striking feature of the temperature profile is the sudden expansion of the intermediate temperatures towards the oxidizer side at z/d = 20. The latter effect seems to be correlated to a non-zero molar fraction of H_2O near the oxidizer side from z/d = 20. Considering that only averaged results are shown, these two observations are likely to indicate a radial entrainment of the flames products away from the central axis induced by the growing turbulent structures surrounding the outer flame region. The phenomenon appears in Figure III.18 as a blurry pink circular shape at z/d = 20, suggesting that hot water is intermittently pulled away from the reaction zone.

11.2.3.2. Scalar measurements in mixture fraction space

Figure III.21 and Figure III.22 show the scatter plots of temperatures and the molar fractions from the main species in mixture fraction space from NP-H_2-air, measured by LRS at different heights above the fuel nozzle. The results from the corresponding laminar non-premixed flame calculations are also shown for comparison. Calculations have been performed with Chemkin-Pro using the opposed-jets burner and the Davis mechanism (cf. Section 9.7). Two transport regimes were used for the laminar flame calculations: equal diffusivities transport regime (EDT) and the full multi-component transport regime (FMCT). EDT assumes all molecular diffusivities equal to each other and equal to the thermal diffusivity. FMCT assumes that each species has its own molecular diffusivity, and take into account the thermal diffusivity. Using both regimes allows underlining the relative importance of differential diffusion in the results, which could be of interest in hydrogen flames (cf. Section 2.2.10). Though calculations have been performed for different strain rates, a, results are only shown for a = 200 s^{-1}. The flame structure in the near-field is expected to better match a moderate-to-high strain rate (cf. Section 9.7) and reliable results from calculations could not be achieved at higher strain rates in these conditions. In addition, the match between experimental data and calculations is relatively acceptable. The displayed results from laminar calculations are systematically the same for all axial positions.

Scatter plots expressed in mixture fraction space are relatively narrow between the region of pure oxidizer (F_B = 0) and the stoichiometric mixture fraction, F_{Bst}. Beyond F_{Bst}, they display a considerable discrepancy due to the propagation of errors related to the calculations of the mixture fraction in presence of Raman cross-talks at intermediate and high temperatures (cf. Section 6.5). Note that, due to the averaging effects of the 15 on-CCD accumulations from the LRS measurements (cf. Section 5.2.6), the effects of

turbulent fluctuations should not appear. Despite the discrepancy, scatter plots display a trend similar to the laminar flame calculations.

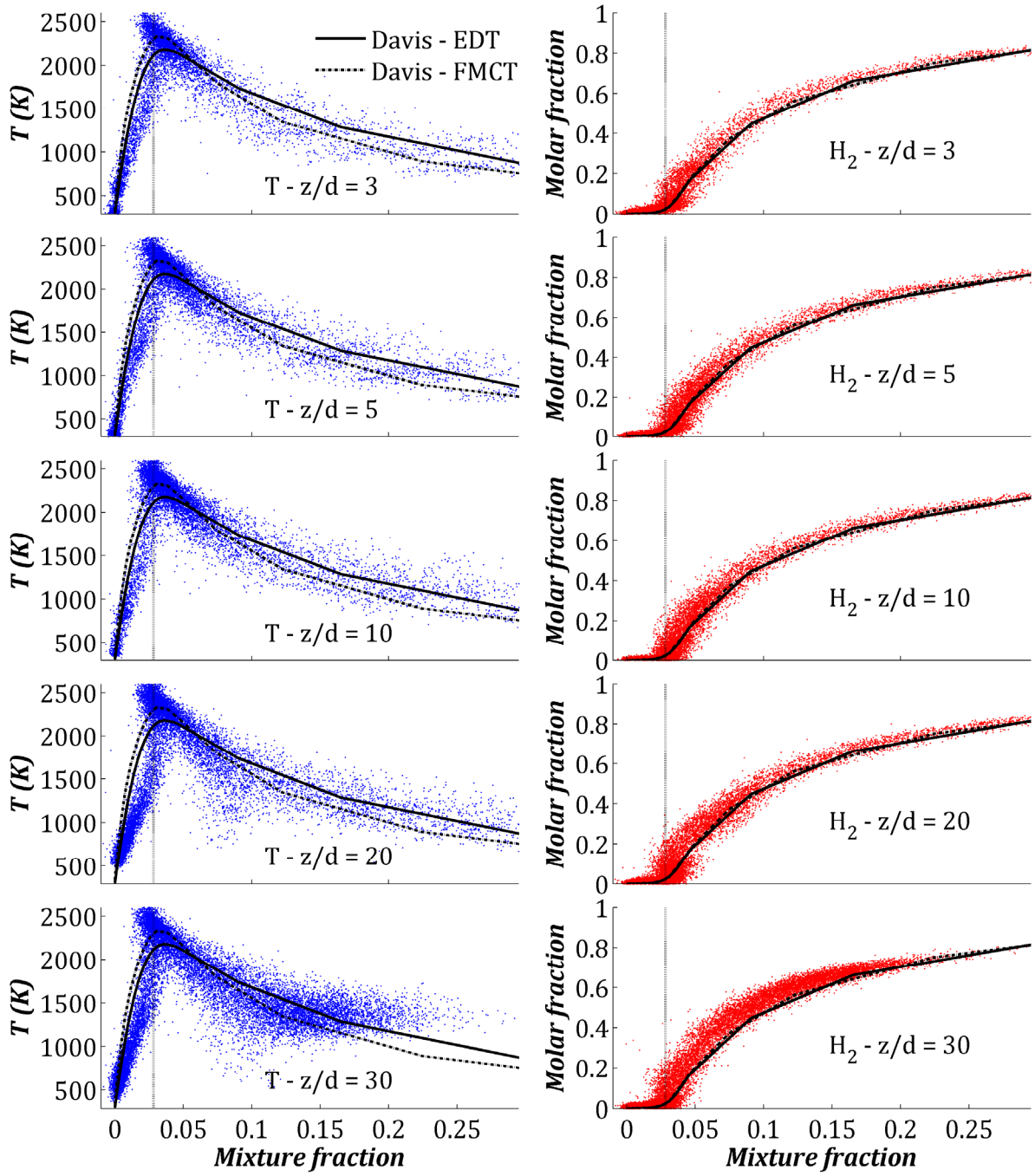

Figure III.21: Scatter plots of temperatures and H_2 molar fractions in mixture fraction space from NP-H_2-air, measured by LRS at different heights above the fuel nozzle. Results from corresponding laminar non-premixed flame calculations are shown for EDT regime (solid lines) and FMCT regime (dashed lines). The stoichiometric mixture fraction is indicated by a vertical dashed line.

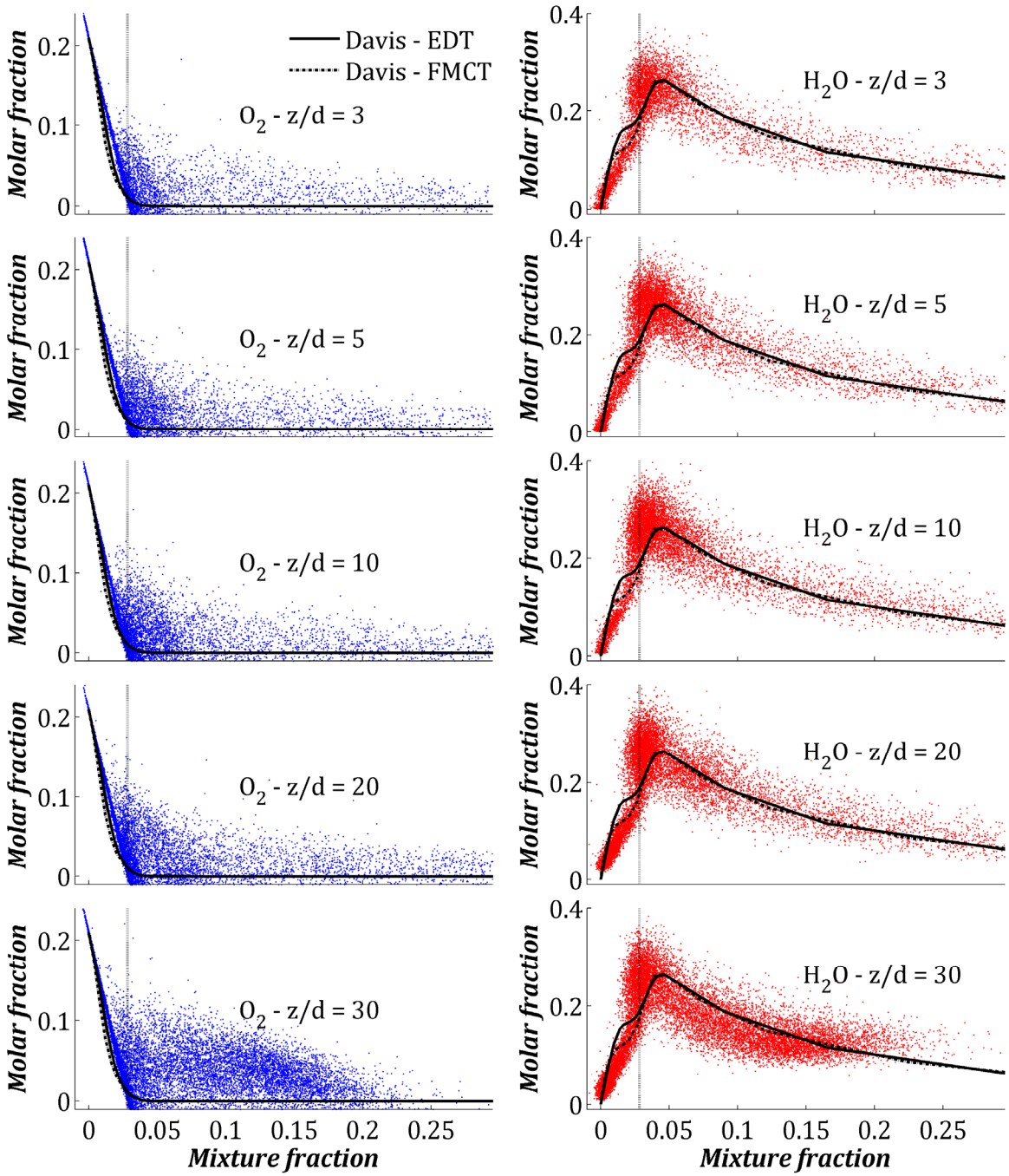

Figure III.22: Scatter plots of O_2 and H_2O molar fractions in mixture fraction space from NP-H_2-air, measured by LRS at different heights above the fuel nozzle. Corresponding results from laminar non-premixed flame calculations are shown for EDT regime (solid lines) and FMCT regime (dashed lines). The stoichiometric mixture fraction is indicated by a vertical dashed line.

A moderate departure can be seen for the temperature and H_2O molar fraction on the lean-side of the stoichiometric mixture fraction. This can be explained both by the uncertainties on mixture fraction calculations and by the over-estimated oxygen molar fraction in this region. In addition, the extrapolation of the Raman calibration coefficients to high temperatures is not perfect and may contribute to the locally higher temperature measurements on the lean-side of the stoichiometric mixture fraction.

Scatter plots in mixture fraction space do not differ much from one axial distance to another in the laminar development of the jet. If there should be any difference, it cannot be clearly seen due to the discrepancy. At 30 diameters above the nozzle (cf. Figure III.21 and Figure III.22), the fuel-rich region close to stoichiometric mixture fraction is much more populated than for other axial locations. This is a consequence of the intense mixing induced by turbulence beyond the onset of the regime transition.

Results from laminar flame calculations for both transport regimes are very similar. The main differences are the higher temperatures observed with FMCT near stoichiometric mixture fraction and the lower temperatures in the fuel-rich region. This is characteristic of the high diffusivity of hydrogen and the Soret diffusion effects (thermal diffusion) enabling a better supply of hydrogen molecules towards the reaction zone [*Yang* 2010].

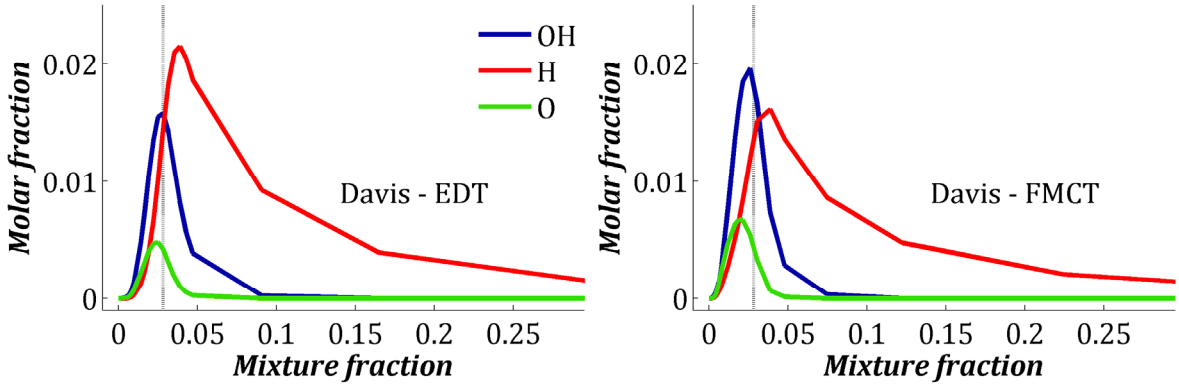

Figure III.23: Molar fraction profiles of OH, H and O radicals from laminar non-premixed flame calculations corresponding to NP-H_2-air composition for EDT regime (left) and FMCT regime (right). The stoichiometric mixture fraction is indicated by a vertical dashed line.

Figure III.23 shows the molar fractions profiles of OH, H and O radicals in mixture fraction space, from the laminar flame calculations. For both transport regimes, OH and H radicals reach a significantly high molar fraction within the flame zone, which can induce a systematic error in LRS measurements performed in the flame region. For both transport regimes, molar fractions of OH and O radicals peak in the fuel-lean side, whereas the molar fraction of H radicals peaks in the fuel-rich side. The molar fractions of OH and O radicals display peaks of higher amplitude with FMCT regime than with EDT regime, while the effect is the opposite for the molar fraction of H radicals. The trend might be due to the temperature shift towards the fuel-lean side with FMCT regime, enhancing the dissociation reactions involving H_2O on the fuel-lean side. A deeper look at the reaction mechanisms would be necessary to further comment the figure, though this is beyond the scope of the present investigation.

11.3. Transitional non-premixed H_2 - O_2/CO_2 jet flames

11.3.1. General observations

Transitional non-premixed H_2 - O_2/CO_2 jet flames display many features of interest for the present investigation. Due to the absence of hydrocarbons in the fuel, soot particles are not formed. This prevents from interferences induced by hydrocarbon fluorescence on Raman spectra. Besides, these flames generally display a great stability, which enables to vary the oxygen content in the oxidizer over a wide range of conditions (cf. Table III.4) while keeping acceptable Raman signals. These oxy-fuel flames are also ideal to study the participation of CO_2 into the combustion reaction by monitoring the production of CO. Since CO_2 is the only supplier of C atoms in the reaction, CO can only originate from CO_2.

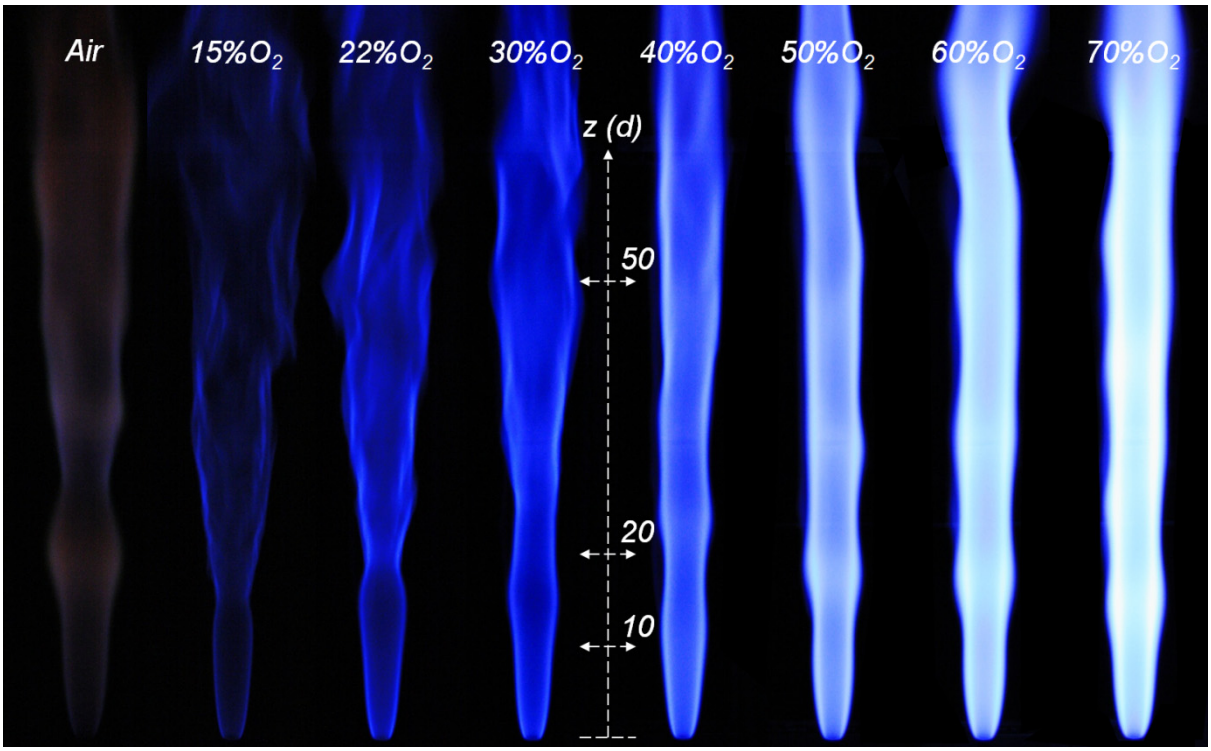

Figure III.24: Photographs of the transitional non-premixed H_2 - O_2/CO_2 jet flames with Re_f = 1600. The transitional non-premixed H_2 - air jet flame (Re_f = 1600) is added for comparison. ISO: 1600. Exposure time: 1/100 s.

Two major issues make the LRS measurements in those flames relatively challenging: the cross-talk effects induced by H_2 (cf. Section 8.3.1) and the overall spontaneous flame luminosity (cf. Section 8.3.2). The overall spontaneous flame luminosity increases with the oxygen content in the oxidizer, as it can be observed in Figure III.24. The dominating colour is blue, due to CO_2* chemiluminescence, going from dark blue at low oxygen contents in the oxidizer, to intensively bright blue/white, saturating the whole visible range. Measurements from the spontaneous flame

luminosity have systematically been performed for all reported axial and radial locations, to be subtracted from the LRS measurements. The correction proves to be reasonably efficient, though at high oxygen contents in the oxidizer, the spontaneous flame luminosity is accompanied by statistic noise of high amplitude associated to the interferences. The threshold, in the case of transitional non-premixed H_2 - O_2/CO_2 jet flames, corresponds to about 40 $\%_{mol}$ oxygen in the oxidizer, which is also the threshold where the radical pool becomes non-negligible for LRS measurements (cf. Section 8.2.3).

As seen in Figure III.24, non-premixed H_2 - O_2/CO_2 jet flames exhibit a laminar structure on the near-field, followed by a tri-dimensional instability with, either a bottleneck, or a blurry spherical shape. Either way, the instability somewhat marks the transition between laminar and turbulent flows and is the consequence. The distinction between both flow regimes clearly appears for all the flames. The phenomenon is detailed in Sections 2.3.2 and has also been evidenced for NP-H2-air in Section 11.2.

The transitional non-premixed H_2 - O_2/CO_2 jet flames can be separated into two categories relatively to their transition pattern. From 15 to 30 $\%_{mol}$ oxygen in the oxidizer, the near-field displays a very regular and symmetrical pattern of an inverted cone, up to the onset of the transition. Downstream, the flame looks brushy and fully dominated by turbulent mixing. The near-field is very stable and the onset of the regime transition does not oscillate.

From 40 to 70 $\%_{mol}$ oxygen in the oxidizer, the pattern is slightly different, starting in the near-field with a more diffuse and more curved flame region outbound, and a weak radial expansion beyond a few diameters above the nozzle. Farther downstream, instabilities appear as wavy patterns, regularly located along the central axis. The flame radial expansion is rather limited compared to flames with lower oxygen content in the oxidizer. Unlike in flames at low oxygen contents in the oxidizer, the instabilities greatly fluctuate radially and axially, though they oscillate more or less around the same axial locations. Photographs of these flames taken at another moment would give slightly different locations of the instabilities. These oscillations induce the blurry appearance of the instabilities on photographs, due to the averaging effects of the exposure time. The pattern is very similar to the one observed for NP-H_2-air.

Both patterns are characteristic of transitional regimes and have been widely investigated (cf. Section 2.3.2). In both cases, the transition is induced by a Kelvin-Helmholtz instability. The longitudinal instability pattern follows both axisymmetric and helical modes, depending on the flame [*Mungal* 1991].

The onset of the breakpoint between laminar and turbulent flows clearly shifts downstream with increasing oxygen contents in the oxidizer from 15 to 30 $\%_{mol}$. Within this range, the adiabatic temperature increases from 1580 to 2277 K, inducing higher

kinematic viscosity enabling to dampen small turbulent structures along a longer axial distance before the regime transition.

From 40 to 70 $\%_{mol}$ oxygen in the oxidizer, the exact onset of the breakpoint seems unclear due to its oscillations. Induced by the high flame temperature, the large kinematic viscosity in the flame region achieves more effective suppression of the development of turbulent structures. The radial expansion downstream is also clearly reduced on the photographs compared to lower oxygen contents in the oxidizer. This observation illustrates the laminarisation effects reported from oxy-fuel jet flames with increasing oxygen contents in the oxidizer, as mentioned in Section 3.3.2.

11.3.2. Non-reacting jets

Figure III.25 and Figure III.26 show the Reynolds-averaged radial profiles of species molar fraction from non-reacting NP-H_2-OF-1 and NP-H_2-OF-4, respectively, at different axial locations. Similar profiles have been recorded from NP-H_2-OF-2 and NP-H_2-OF-3 and fit in line with the displayed sets of results, so they are not shown here. For both Figure III.25 and Figure III.26, the profiles are relatively axisymmetric, except at 5 diameters above the nozzle. The asymmetric pattern at this axial location is seen for all non-reacting mixtures based on O_2/CO_2 oxidizer, and not for those based on air or for the flames. It might come from a localized instability due to an imperfection of the fuel nozzle, which would appear in limited conditions. Another slightly asymmetric profile can be seen at 10 diameters above the nozzle for NP-H_2-OF-1, most likely from the same origin.

The level of penetration of CO_2 into the inner fuel jet at z/d = 3 is more significant in NP-H_2-OF-1 than in NP-H_2-OF-4. Comparable level of penetration of N_2 has been seen in non-reacting NP-H_2-air (cf. Figure III.19). The entrainment of oxidizer into the inner fuel jet is especially linked to the higher CO_2 content in the oxidizer and the induced higher momentum of the oxidizer at constant coflow velocity. The momentum of the fuel stream remains the same for all investigated non-premixed transitional jet flames.

Looking at both Figure III.25 and Figure III.26, the degree of mixing and the sudden radial expansion of the mixing zone indicate that the onset of the breakpoint between laminar and turbulent regimes is most likely located upstream from z/d = 10. In addition, the mixing region seems to shrink at z/d = 5 for both mixtures. Consequently, compared to non-reacting NP-H_2-air, which has similar jet Reynolds number and coflow speed, the onset of the breakpoint is located more upstream. The shift is due to the difference of density between air and O_2/CO_2 mixtures, inducing different momentum ratios between fuel and oxidizer, and to the difference of kinematic viscosity, greater for air than for any of the present O_2/CO_2 mixtures. Table

III.9 lists the fluid properties of interest at ambient temperature. Higher oxidizer momentum increases the intensity of the turbulent structures developing from the base of the jet. In addition, lower kinematic viscosity enables the turbulent structures to dominate the jet flow over a shorter distance. This also explains why the degree of mixing looks greater at z/d = 10 in NP-H_2-OF-1 than in NP-H_2-OF-4 and in NP-H_2-air.

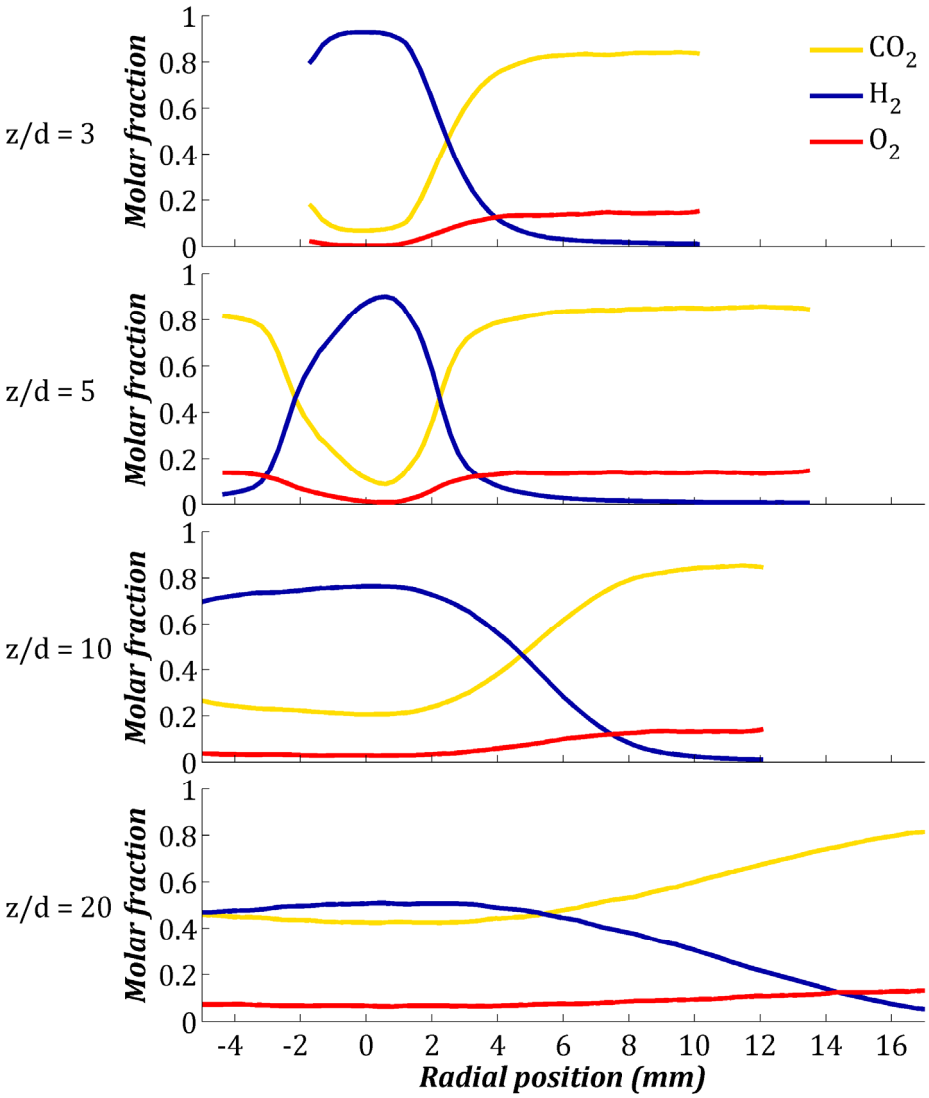

Figure III.25: Reynolds-averaged radial profiles of CO_2, H_2 and O_2 molar fractions from non-reacting NP-H_2-OF-1, measured by LRS at different heights above the fuel nozzle.

Table III.9: Fluid properties of different oxidizer mixtures at 294 K and atmospheric pressure (Gaseq).

Oxidizer mixture	***NP-H_2***			
	-air	***-OF-1***	***-OF-4***	***-OF-7***
Density (kg.m^{-3})	1.20	1.75	1.63	1.48
Kinematic viscosity (m^2.s^{-1})	1.53E-5	8.76E-6	1.02E-5	1.23E-5

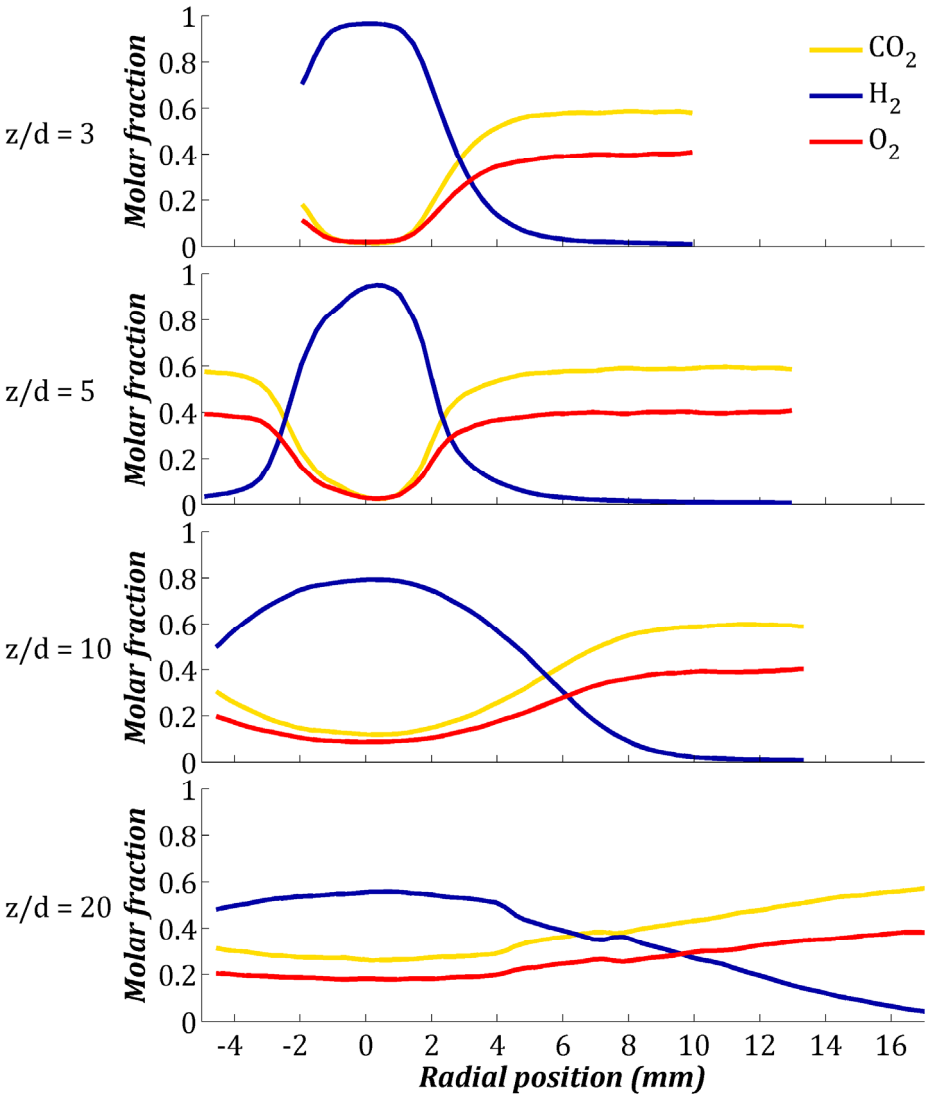

Figure III.26: Reynolds-averaged radial profiles of CO_2, H_2 and O_2 molar fractions from non-reacting NP-H_2-OF-4, measured by LRS at different heights above the fuel nozzle.

11.3.3. Flames

11.3.3.1. Radial profiles of scalar measurements

Figure III.27 and Figure III.28 show the Reynolds-averaged radial profiles of scalars from NP-H_2-OF-1 and NP-H_2-OF-4 flames at different axial locations. Similar profiles have been recorded from NP-H_2-OF-2 and NP-H_2-OF-3 (cf. Appendix C) and fit in line with the displayed sets of results.

Results for CO_2 and O_2 are considerably affected by the Raman cross-talks from the Raman rotational bands of H_2 at intermediate and high temperatures. For example, oxygen molar fraction appears non-zero at the location of the maximum flame temperature, whereas it should be zero according to the absence of actual oxygen band

on Raman peak on spectra. The error propagates to the temperature, which may consequently display an accidental shape.

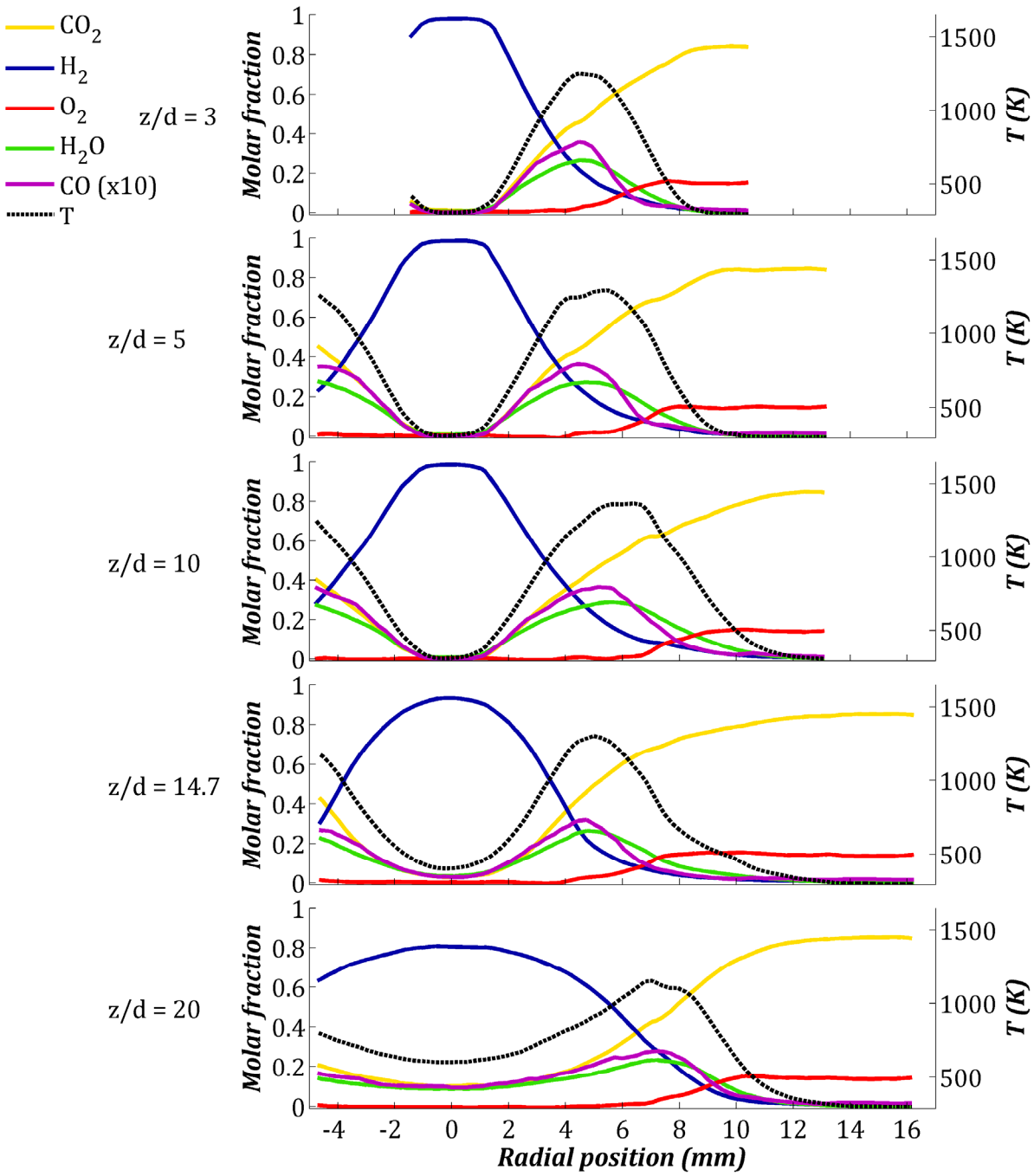

Figure III.27: Reynolds-averaged radial profiles of molar fractions of the main species and temperatures from NP-H_2-OF-1, measured by LRS at different heights above the fuel nozzle.

In the near-field of both displayed sets of results, the flame region broadens with the axial distance up to the transition breakpoint, as observed in similar air-fired conditions (cf. Section 11.2.3). For NP-H_2-OF-1, a radial profile has been measured at the centre of the bottleneck pattern visible in Figure III.24, at z/d = 14.7. The flame region appears to shrink at this axial location, while the inner jet keeps expanding as a laminar

diffusion jet. A similar shrinking pattern has been observed in non-reacting flows on the molar fraction profile of hydrogen, though it is located more upstream (cf. Figure III.25 and Figure III.26, z/d = 5).

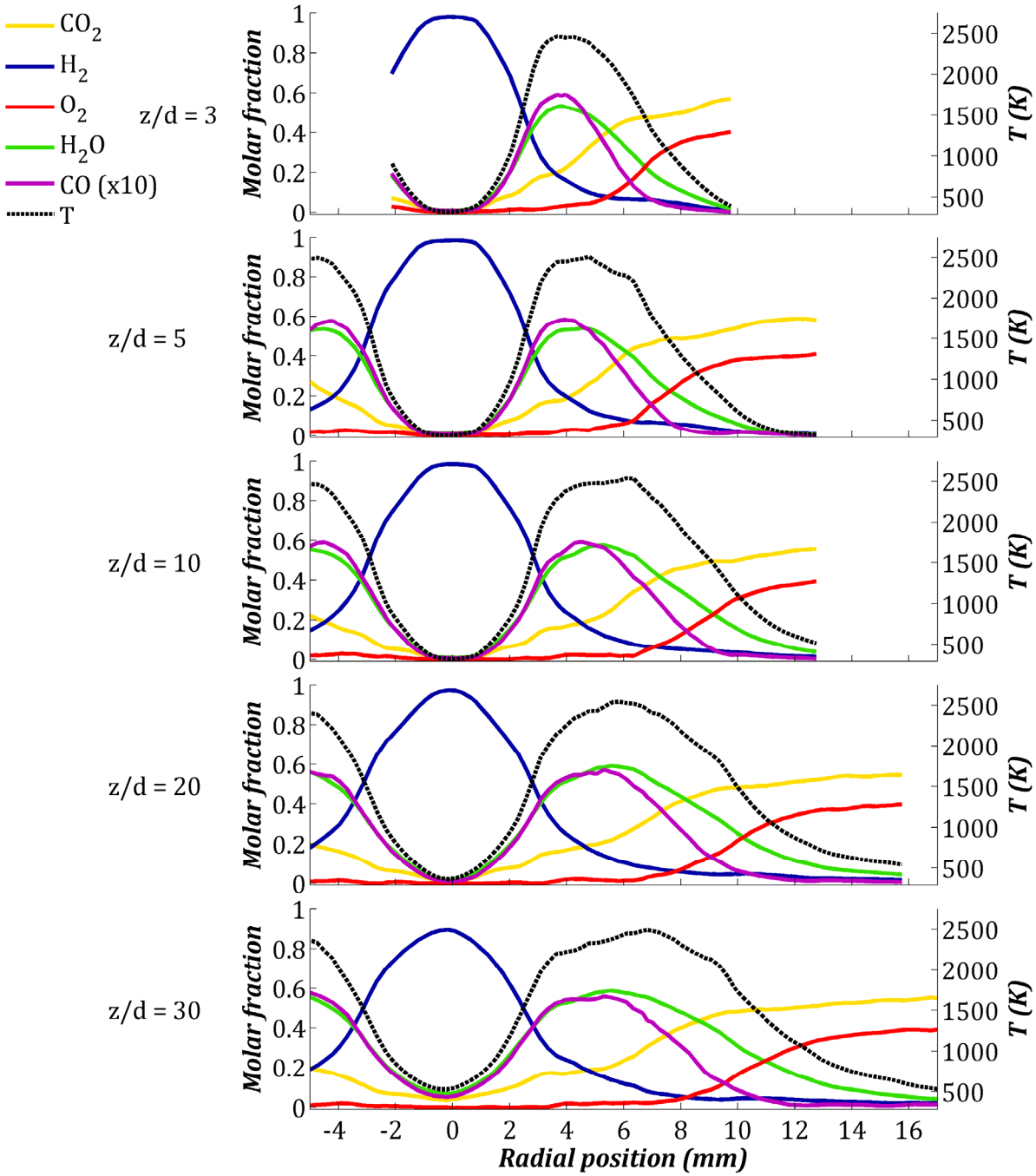

Figure III.28: Reynolds-averaged radial profiles of molar fractions of the main species and temperatures from NP-H_2-OF-4, measured by LRS at different heights above the fuel nozzle.

The shrinking of the flame region is observed within the 30 first diameters above the nozzle for flames NP-H_2-OF-1, -2 and -3. Its axial location increases with the oxygen content in the oxidizer, due to induced laminarisation effects of the increasing flame temperature. For the flames with larger oxygen contents in the oxidizer, the flame

region continuously broadens along the 30 first diameters, though the expansion is more pronounced within the 10 first diameters above the nozzle than beyond. For those flames, the onset of the flow regime transition is not clear and the visible instabilities seem to indicate a helical mode (cf. Sections 2.3.2 and 11.3.1). According to the blurry circular shape seen in Figure III.24 at ca. z/d = 15 for NP-H_2-OF-4, -5, -6 and -7, if radial profiles were measured at this axial location, they would probably display evidences of flame products being pulled away from the flame region outbound, as described above for NP-H_2-air flames (cf. Section 11.2.3.1).

The flame temperature greatly varies from one oxidizer mixture to another. For NP-H_2-OF-1 and NP-H_2-OF-4, the flame temperatures vary over an amplitude of ca. 1000 K, only by changing the oxygen content in the oxidizer from 15 to 40 $\%_{mol}$. The high flame temperatures reached with higher oxygen contents in the oxidizer also contribute to the level of uncertainties on the determination of CO_2, O_2 number densities and the temperature, due to the lack of appropriate calibration measurements in this range of temperatures. The higher level of uncertainties is one of the reasons why investigated flames with higher oxygen contents in the oxidizer are not fully detailed here.

Due to the variations of flame temperature, the inner hydrogen jet displays a different shape for both sets of displayed results. In the near-field of NP-H_2-OF-1, the radial expansion of the hydrogen jet first shapes as in the non-reacting case with a linear diffusion pattern (cf. Figure III.25 and Figure III.26). Farther away from the central axis, the molar fraction profile of H_2 considerably curves, since the combustion reaction consumes H_2 molecules and the degree of molecular diffusion of hydrogen increases with the temperature. In the near-field of NP-H_2-OF-4, there is no linear diffusion pattern and the radial expansion of the hydrogen jet directly starts with a curved diffusion pattern, due to the very high temperatures. The reduced content of CO_2 in the oxidizer species also eases the radial molecular diffusion of hydrogen.

Figure III.29 shows the Reynolds-averaged radial profiles of temperatures for the investigated transitional non-premixed jet flames. Since fuel composition, jet Reynolds number and coflow speed are the same for all flames, the figure enables to observe the shape of the flame region as a function of the oxidizer composition only. The results for the transitional non-premixed H_2 – O_2/CO_2 jet flames with 50 to 70 $\%_{mol}$ O_2 in the oxidizer are simply shown to provide an insight, despite their high uncertainties.

The flame region considerably broadens with the oxygen content in the oxidizer, mainly due to the increased kinematic viscosity of the oxidizer mixture, cumulated to higher flames temperatures. In addition, the flammability limits of the burning mixture also increase due to the reduced amount of CO_2 in the oxidizer, enabling the combustion reaction to occur for a wider range of mixtures. The air-fired case displays a broader flame region than for flames with low oxygen contents in the

oxidizer and in the same range as flames with high oxygen contents in the oxidizer. This observation somewhat correlates with the calculated kinematic viscosities for H_2/air and $H_2/O_2/CO_2$ flames shown in Figure I.19. The large scale radial fluctuations of the flame front through axisymmetric and helical modes may also induce part of the broadening of the flame region in the averaged results.

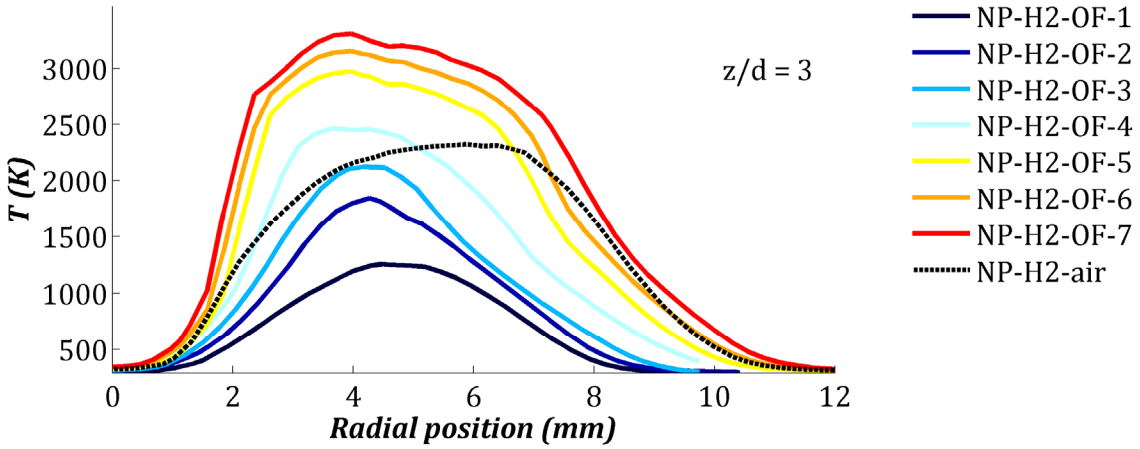

Figure III.29: Reynolds-averaged radial profiles of the temperature from the transitional non-premixed jet flames, measured by LRS at 3 diameters above the fuel nozzle.

The shape of the flame region greatly differs from one flame to another. While for NP-H_2-OF-1, the shape appears very regular and quasi-Gaussian, the maximum temperature shows a tendency to shift towards the central axis as the oxygen content increases in the oxidizer. This can still be seen at high oxygen content in the oxidizer, despite the high level of uncertainties. The phenomenon can be explained by the enhanced molecular diffusion of hydrogen towards the flame region, which is promoted by the reduced content of CO_2 in the oxidizer and improves the fuel supply to the flame region. The phenomenon is correlated with the shape of the profile of molar fraction from hydrogen described above. The wider flammability limits as the oxygen content increases in the oxidizer also plays a role of importance in the shift towards the central axis. Consequently, the molar fractions of the flame products, H_2O and CO also display a shift of their maximum towards the fuel-rich side, as the oxygen content increases in the oxidizer. Note also that CO appears in the fuel-rich side as far as CO_2 penetrates the inner jet of hydrogen.

The shift of maximum temperature is also related to the flame stability [*Yamashita* 1992, *Takeno* 1994]. As the viscous layer, represented by the maximum temperature, moves into the shear layer of the jet velocity distribution, its ability to suppress the turbulent fluctuations becomes more effective. For NP-H_2-air, the viscous layer is located outside the shear layer, leading to the observed oscillations of the transitional instabilities. For the laminar non-premixed oxy-fuel flames, the shift of maximum temperature towards the central axis helps superimposing the viscous layer

to the shear layer, maximizing the effects of the viscosity over the turbulent fluctuations, leading to laminar flames. The phenomenon might contribute to the threshold of the pattern change of the flame structure observed at ca. 40 $\%_{mol}$ O_2 in the oxidizer.

11.3.3.2. Scalar measurements in mixture fraction space

Figure III.30 shows the scatter plots of temperatures and the molar fractions from the main species in mixture fraction space from NP-H_2-OF-1, measured by LRS at three diameters above the fuel nozzle. Results from the corresponding laminar non-premixed flame calculations are also shown for comparison. Calculations have been performed with Chemkin-Pro using the opposed-jets burner and the Davis mechanism for both equal diffusivities transport regime and the full multi-component transport regime, at a = 200 s^{-1}, and according to the oxidizer compositions given in Table III.4.

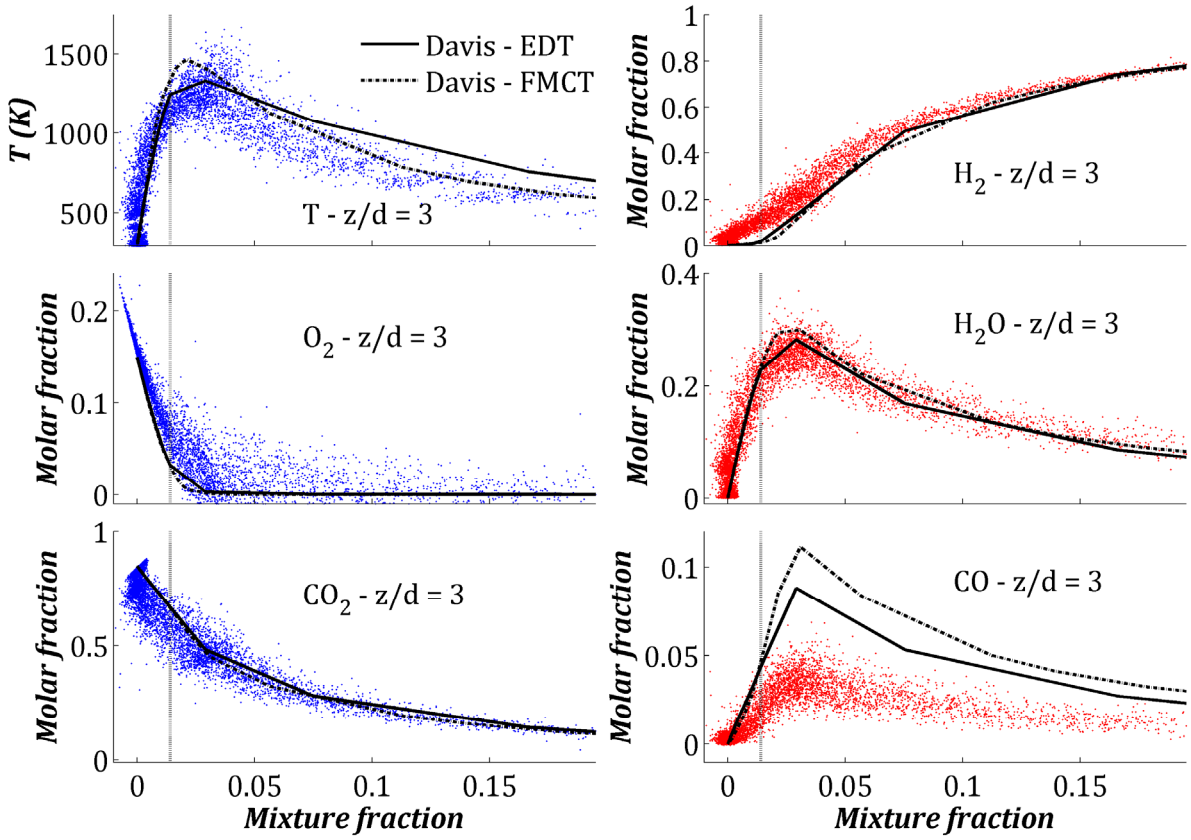

Figure III.30: Scatter plots of the temperature and the molar fractions from the main species in mixture fraction space from NP-H_2-OF-1, measured by LRS at z/d = 3. Corresponding results from laminar non-premixed flame calculations are shown for EDT regime (solid lines) and FMCT regime (dashed lines). The stoichiometric mixture fraction is indicated by a vertical dashed line.

The evolution of the scatter plots with the axial distance does not bring more information than already detailed in Section 11.3.3.1, and therefore, the corresponding plots are only shown in Appendix C. Due to the averaging effects of the 15 on-CCD

accumulations performed during the measurements, the large discrepancy of the scatter plots mainly originates from interferences and uncertainties from the cross-talks evaluation. Therefore, it cannot be related to fluctuations induced by turbulence. A non-negligible level of uncertainties is also associated to the calculations of the mixture fraction (cf. Section 6.5). It should also be noted that the averaging effects of the on-CCD accumulations considerably reduce the resolution in mixture fraction space. All those factors justify that the present experimental investigation only focused on the near-field of transitional flames, rather than on the turbulent part of the flame located farther downstream.

Despite the large discrepancy, the experimental results follow the same general trend as the results from the laminar flame calculations. An exception appears for CO molar fraction, for which the calculations appear at least twice higher than the experimental results. Despite the level of uncertainties linked to the determination of CO molar fraction from LRS, (cf. Section 6.5), the Davis mechanism seems to over-predict the rate of reactions involving CO_2.

The temperature appears higher for the calculations than for the experimental results. The difference can be correlated to the potentially over-estimated molar fractions of O_2 and H_2 in the experimental results near stoichiometric conditions. Those are due to erroneous extrapolations of the Raman calibration coefficients at intermediate and high temperatures. In this case, the LRS resolution algorithm locally sees a total number density higher than it really is, and balances it with a lower temperature than the actual one through the ideal gas law (cf. Section 5.2.5). Though these effects are generally limited in terms of amplitude, they are likely to account for most of the observed differences.

The maximum flame temperature is greater for the laminar flame calculations using FMCT regime than for those using EDT regime, as seen with similar flames in air atmosphere (cf. Section 11.2.3.2). The phenomenon is due to a better supply of atomic and molecular hydrogen to the reaction zone due to the diffusion properties of hydrogen. Correspondingly, temperatures are lower in the fuel-rich side as the maximum temperature is shifted to the fuel-lean side with FMCT. The induced higher temperature is likely to be responsible for the over-prediction of CO molar fraction with FMCT than with EDT, since high temperatures promote the dissociation of CO_2 (cf. Section 2.2.9).

Similar observations can be made for the whole series of transitional non-premixed H_2 – O_2/CO_2 jet flames. Corresponding figures can be found in Appendix C.

Figure III.31 and Figure III.32 show the conditional means of the temperature and the molar fractions from the main species in mixture fraction space from NP-H_2-OF-1 and NP-H_2-OF-4. For both figures, the top plot shows the experimental results

measured by LRS at z/d = 3, while the two other plots display the results from laminar flames calculations using FMCT regime at a = 200 s^{-1}. Only the results from laminar flame calculations using FMCT regime are displayed, since the regime accounts for diffusion phenomena, and thus, is expected to be more realistic in the near field of hydrogen flames (cf. Section 2.2.10).

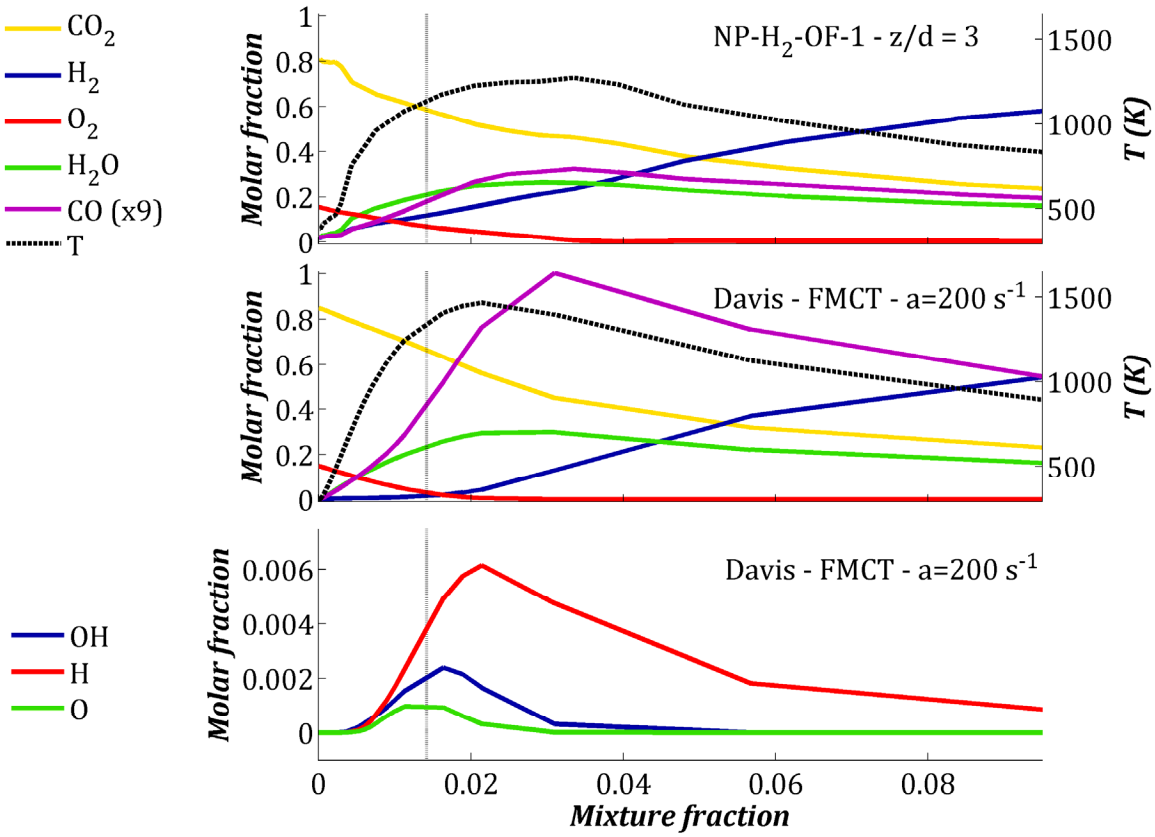

Figure III.31: Conditional means of the temperature and the molar fractions from the main species in mixture fraction space from NP-H_2-OF-1, measured by LRS at z/d = 3. Corresponding results from laminar non-premixed flame calculations are shown for FMCT regime at a = 200 s^{-1}. The stoichiometric mixture fraction is indicated by a vertical dashed line.

Despite the large difference for the molar fraction profiles of CO, trends from calculations and experimental results seem to agree relatively well. The maximum temperature close to stoichiometric mixture fraction is slightly shifted towards the fuel-rich side compared to the laminar flames calculations, probably due to the over-estimated molar fractions of O_2 and H_2 in the flame region, as detailed above.

The molar fractions of OH, H and H radicals account for a significant proportion of the mixture in the flame region at high oxygen contents in the oxidizer, due to high temperatures promoting dissociation reactions. Both CO_2 and H_2O are affected by the dissociation reactions at high temperatures, leading to the maximum molar fractions of OH and CO in the flame region, higher for NP-H_2-OF-4 than for NP-H_2-OF-1.

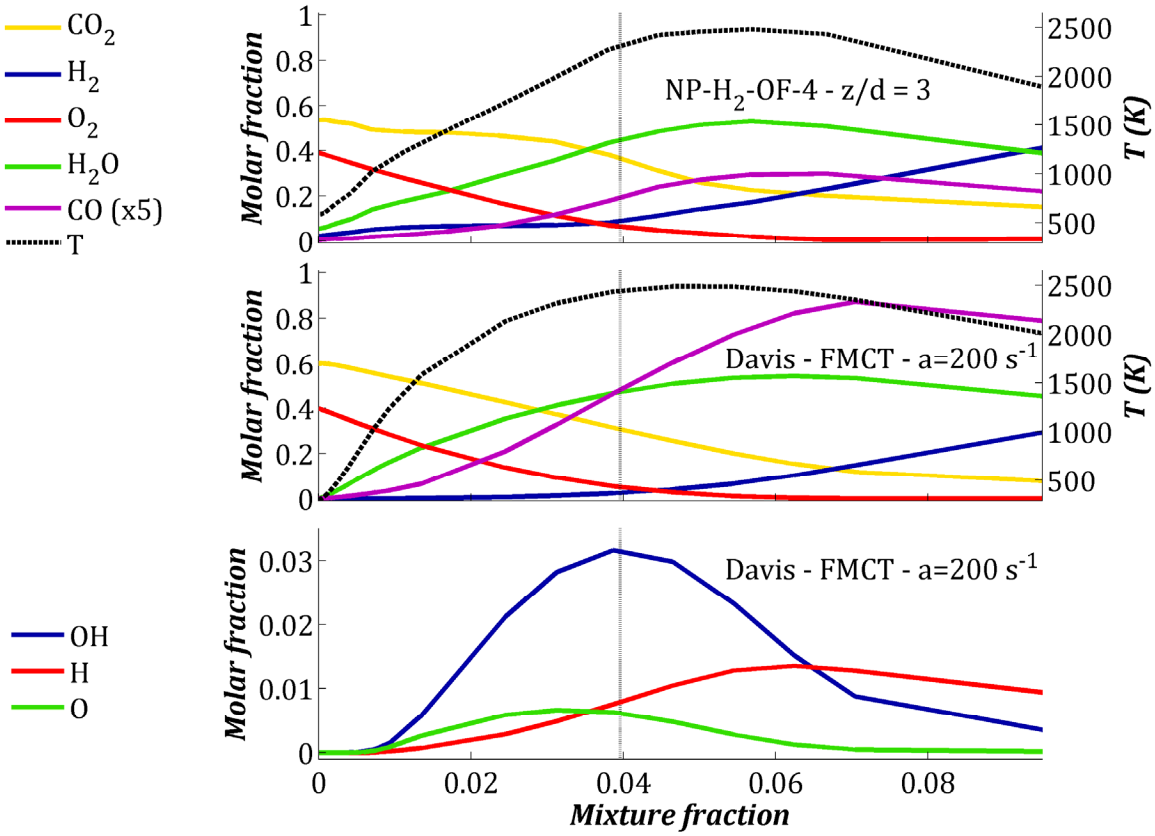

Figure III.32: Conditional means of the temperature and the molar fractions from the main species in mixture fraction space from NP-H_2-OF-4, measured by LRS at z/d = 3. Corresponding results from laminar non-premixed flame calculations are shown for FMCT regime at a = 200 s^{-1}. The stoichiometric mixture fraction is indicated by a vertical dashed line.

Figure III.33 shows the conditional means of the temperature and H_2O and CO molar fractions in mixture fraction space for the transitional non-premixed hydrogen jet flames, from both laminar flame calculations and experimental results. Molar fractions profiles from other species would not significantly bring more information. Experimental results from NP-H_2-OF-5, -6 and -7 are not sufficiently accurate to be meaningful in mixture fraction space, and thus, are not displayed here. Figure III.33 provides another view on the results in mixture fraction, enabling to compare the evolution of the profiles with the oxygen content in the oxidizer.

For both calculations and experimental results, peaks shift towards the fuel-rich side as the oxygen content in the oxidizer increases. As given in Table III.4, the stoichiometric mixture fraction shifts towards the fuel-rich side, since the degree of CO_2–dilution of the oxidizer decreases. Therefore, the relative influence of the quenching effects from CO_2 decreases with its content in the oxidizer, enhancing the combustion rates and broadening the flammability limits of the mixture. Consequently, the maxima in molar fraction profiles are shifted towards the fuel-rich side and the flame region appears wider, covering a larger range of mixtures. This can be seen in both radial profiles and mixture fraction space.

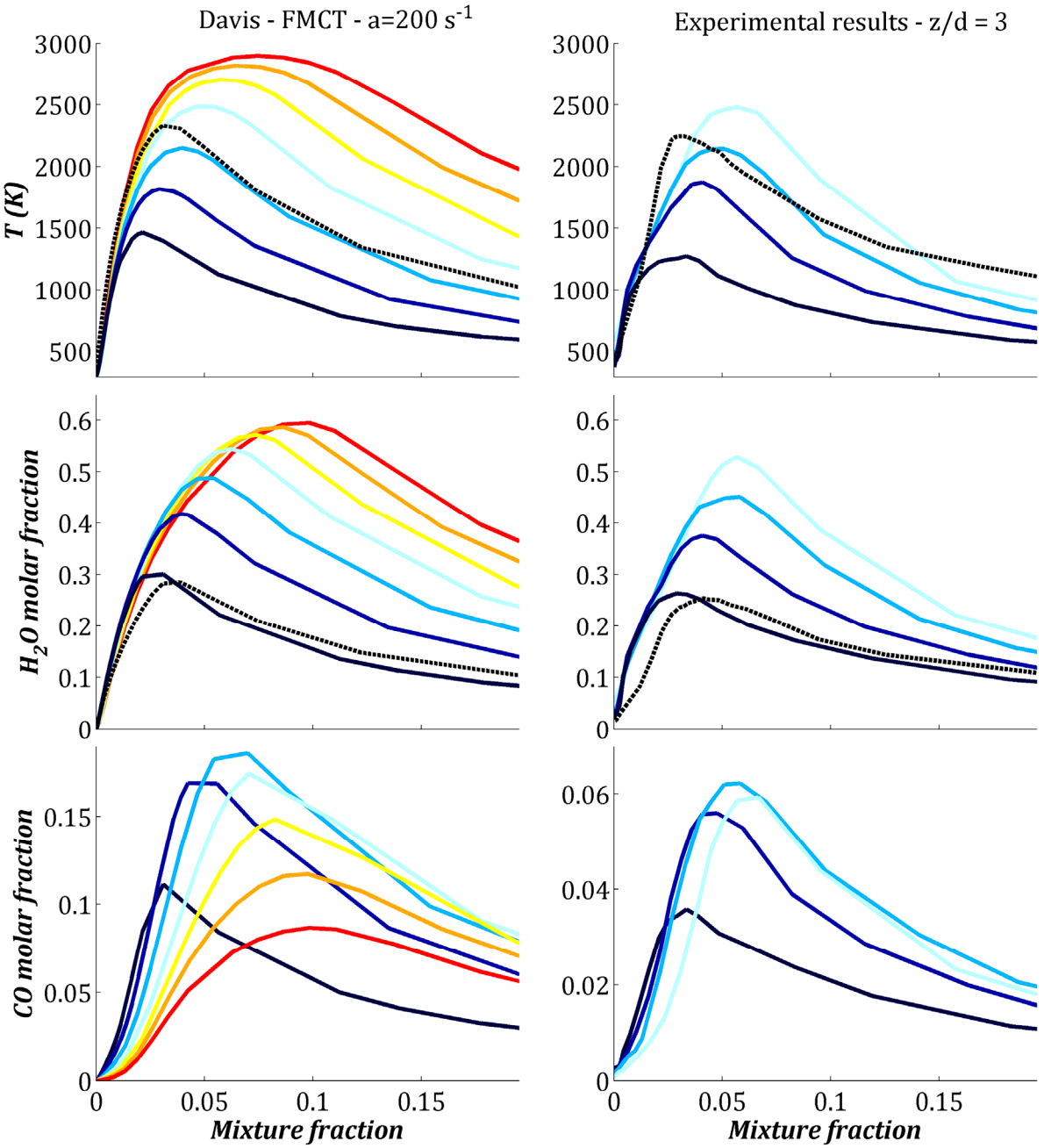

Figure III.33: Conditional means of the temperature and H_2O and CO molar fractions in mixture fraction space from the transitional non-premixed hydrogen jet flames. Left: results from laminar non-premixed flame calculations using FMCT regime at a = 200 s^{-1}. Right: experimental LRS measurements at z/d = 3. The legend from Figure III.29 applies.

The molar fraction of H_2O greatly varies from one flame to another, and actually doubles from 15 to 40 $\%_{mol}$ O_2 in the oxidizer. This variation in molar fraction is amplified by the reduced amount of CO_2 as diluent in the mixture. Compared to NP-H_2-air, the net production rate of water is higher for H_2 – O_2/CO_2 jet flames and keeps increasing with the oxygen content in the oxidizer within the investigated conditions.

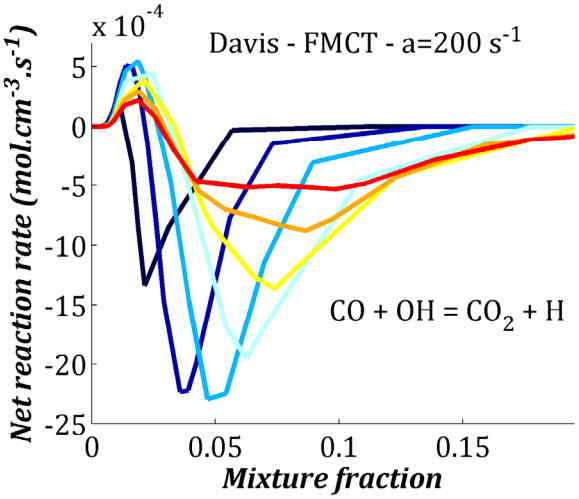

Figure III.34: Net reaction rate of the CO burnout reaction (cf. Eq. I.16) for the transitional non-premixed H_2 – O_2/CO_2 jet flames, from the laminar flame non-premixed flame calculations using FMCT regime at a = 200 s^{-1}. The legend from Figure III.29 applies.

Profiles of CO molar fraction reach a maximum at 30 $\%_{mol}$ O_2 in the oxidizer. This observation is seen for both experimental results and laminar flame calculations at the same locus in mixture fraction space. Nevertheless, the maximum from the experimental results is about three times lower than for the laminar flame calculations. CO is found to mainly originate from the reverse rate of the CO burnout reaction (cf. Eq. I.16). Its absolute net reaction rate is shown in Figure III.34, resulting from the laminar flame calculations using the Davis mechanism. The negative peak of the net reaction is systematically correlated to the maximum molar fraction of CO for each flame, and reaches its maximum amplitude for 30 $\%_{mol}$ O_2 in the oxidizer as well. A relatively weak peak of positive net reaction rate appears in the fuel-lean side, indicating that part of CO is converted into CO_2 in this region.

The net reaction rate of the CO burnout reaction is to be compared to the other reactions involving both CO and CO_2. Their net reaction rate, shown in Figure III.35 in logarithmic scale, is positive for the three chemical processes. In other words, they tend to produce CO_2, rather than CO in this case. However, their net reaction rate is at least two orders of magnitude lower than the CO burnout reaction and peaks in the same lean side of the stoichiometric mixture fraction, similarly to the positive peak of the CO burnout reaction.

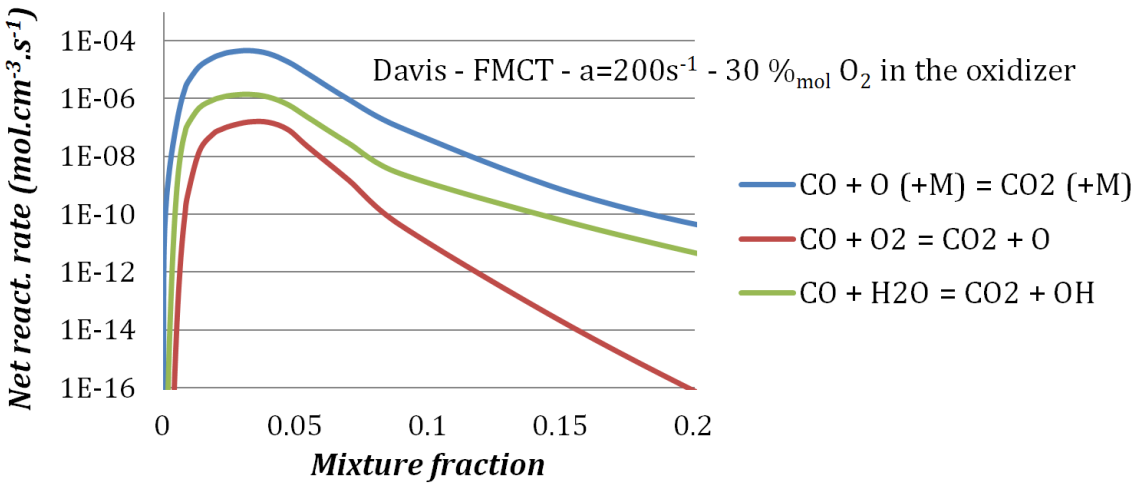

Figure III.35: Net reaction rate (logarithmic scale) of chemical processes involving both CO and CO_2, except CO burnout reaction for NP-H_2-OF-30, from the laminar flame non-premixed flame calculations using FMCT regime at a = 200 s^{-1}.

11.4. Turbulent non-premixed CH_4/H_2 – O_2/CO_2 jet flames (at SNL)

11.4.1. Introduction

LRS measurements in non-premixed CH_4 – O_2/CO_2 jet flames in a coflow burner cannot be performed due to the high level of soot (cf. Section 4.2), so that hydrogen-dilution of the fuel has to be considered. Turbulent non-premixed CH_4/H_2 – O_2/CO_2 jet flames with hydrogen dilution as low as 37 $\%_{mol}$ in the fuel could be investigated using the simultaneous line imaging of Raman/Rayleigh scattering at SNL (cf. Section 7). The oxidizer is composed of 32 $\%_{mol}$ O_2 in the oxidizer and the flames have been generated using a coflow burner. Despite the challenging level of soot in the flames, the accuracy of the LRS setup has enabled to achieve results of great quality for the main species concentrations and the temperature (cf. Section 7.3). Two series of three flames have been performed: one with varying the jet Reynolds number from 12,000 to 18,000, and another with varying the hydrogen dilution in fuel from 37 to 55 $\%_{mol}$. Flames conditions are given in Table III.6.

A detailed investigation of those flames has been published as a journal article and can be found in Appendix D. The publication deals with the evolution of the flame structure in the near-field of turbulent oxy-fuel flames, as a function of the jet Reynolds number and the hydrogen dilution in the fuel. The measurement limits and some particularities of LRS in CO_2-diluted oxy-fuel flames are reported. The low level of uncertainties enables to detail observations on the degree of localized extinction, the influence of differential diffusion, the high levels of CO in the flame products, the shift from stoichiometry of the maximum flame temperature. The experimental results are

also supported by results from laminar flame calculations to highlight the different physical phenomena occurring in the flames.

This investigation is not repeated within this section. Instead, another view is given to the experimental results, in line with the study of the flames performed at NTNU. Details on the experimental setup and levels of uncertainties can be found in Section 7.

11.4.1.1. General observations

Figure III.36 shows photographs from A-series and B-series flames with identical camera settings to allow more reliable comparison. Note that flame A-3 is present in both flame series. For both flame series, the overall flame structure appears quite similar, following a turbulent pattern, with the outbound of the flame region sheared by turbulent structures (cf. Section 2.3.2). Though all flames seem in a fully burning state, their degree of localized extinction significantly varies within the first diameters above the nozzle (cf. Appendix D, Figure 2).

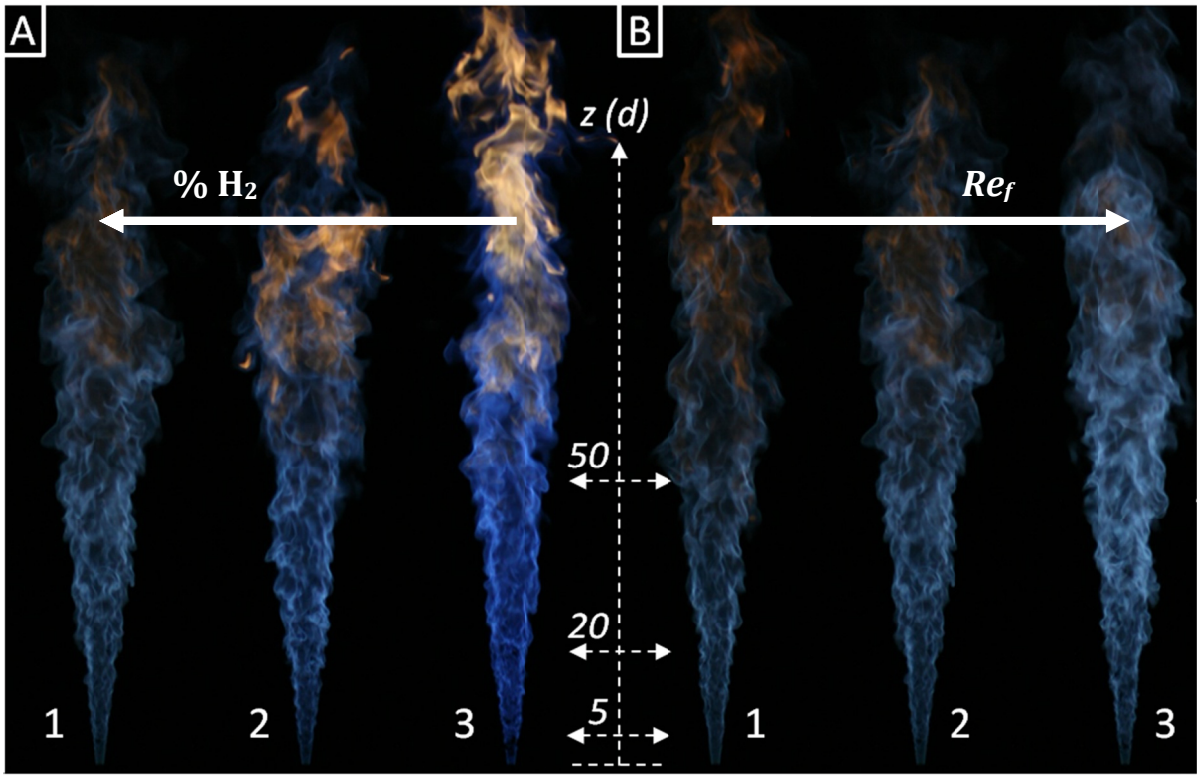

Figure III.36: Photographs of A-series flames (left) and B-series flames (right). Exposure time: 1/2500 s. ISO: 1600.

The level of soot clearly increases at the flame tip with lower hydrogen contents in the fuel (A-series) or with lower jet Reynolds numbers (B-series). This is partly due to lower speeds at the jet exit for a similar jet Reynolds number and the correspondingly longer residence time for soot formation (cf. Section 2.2.11). In addition, for the A-series, the concentration of hydrocarbon species increases. In both flames series, the presence of soot precursors increases with the axial distance, inducing increased LIF signals from the C_2 Swan bands. Measurements have not been performed beyond 20 diameters above the fuel nozzle, since the LIF signals could not be sufficiently well corrected.

11.4.1.2. Radial profiles of scalar measurements

Figure III.37 shows the Reynolds-averaged radial profiles of the temperature and the molar fractions of the main species from turbulent non-premixed CH_4/H_2 – O_2/CO_2 jet flame B-1, measured using the simultaneous line imaging of Raman/Rayleigh scattering at SNL. Characteristics of flame B-1 can be found in Table III.6. Among the flames investigated at SNL, flame B-1 is the least affected by localized extinction and is relatively close to a fully burnt state (cf. Appendix D, Section 4.1). Consequently, flame B-1 is the most adapted for a comparison with the flames investigated at NTNU.

Flame B-1 is characterized by a moderate jet Reynolds number Re_f = 12,000, and its flame structure naturally exhibits the typical features of turbulent flames (cf. Section 2.3.2). The flame structure also displays similarities with transitional non-premixed H_2 – O_2/CO_2 jet flames at high oxygen contents, since the flame region expands away from the central axis and no shrinking of the flame region is observed. The radial expansion of the flame region appears much more pronounced than for the transitional non-premixed jet flames. Unlike the latter flames, the molar fraction profiles of hydrogen also show a relatively rapid radial expansion of the inner fuel jet.

These differences can be explained by the combination of higher turbulence intensity, higher mass density of the fuel mixture (cf. Table III.10) and lower kinematic viscosity of the reaction mixture (cf. Section 3.3.2). The turbulent structures initiated at the nozzle outlet have considerably higher intensities than in transitional flames. Considering the lower kinematic viscosities in the viscous layer, the turbulent structures cannot be dampened downstream to the same extent. In addition, compared to NP-H_2-OF-3, whose oxidizer composition is quite similar, the flame temperature is much lower. This potentially reduces the local kinematic viscosity and, consequently, the dampening effects of the coflowing oxidizer over the velocity fluctuations at the outbound of the flame region. The higher mass density of the fuel mixture, combined to higher jet speed leads to a higher momentum in the inner fuel jet, which amplifies the amplitude of the turbulent structures initiated at the fuel nozzle outlet. Therefore, the

inner fuel jet significantly expands radially, before breaking down with a relatively shorter axial distance than for similar transitional flames.

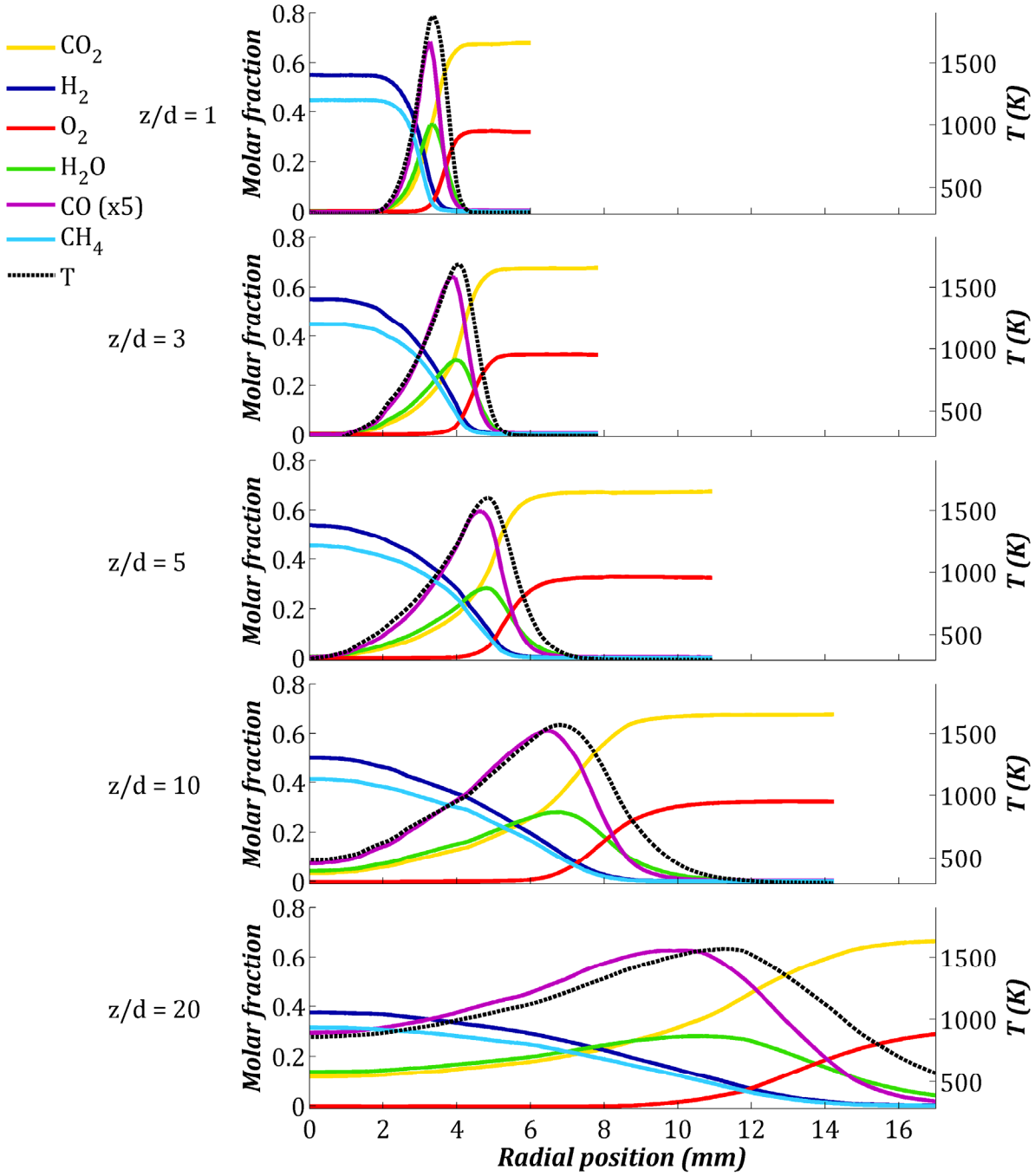

Figure III.37: Reynolds-averaged radial profiles of the temperatures and the molar fractions of the main species from turbulent non-premixed CH_4/H_2 – O_2/CO_2 jet flame B-1, measured using the simultaneous line imaging of Raman/Rayleigh scattering setup at SNL.

Despite the slight variations of kinematic viscosity and mass density from 37 to 55 $\%_{mol}$ H_2 in the fuel stream (cf. Table III.10), the expansion of both the inner fuel jet and the flame region remains quite similar for both A-series and B-series (not shown here).

Table III.10: Fluid properties of different fuel mixtures at 294 K and atmospheric pressure (Gaseq).

Fuel mixture	***CH_4 / H_2 ($\%_{mol}$)***			
	0 / 100	***63 / 37***	***55 / 45***	***45 / 55***
Density ($kg.m^{-3}$)	0.0836	0.4498	0.4033	0.3452
Kinematic viscosity ($m^2.s^{-1}$)	1.06E-4	2.53E-5	2.82E-5	3.28E-5

11.4.1.3. Scalar measurements in mixture fraction space

Figure III.38 shows the scatter plots of the temperature and the molar fractions from the main species in mixture fraction space from flame B-1, measured at three diameters above the fuel nozzle. Corresponding results from laminar non-premixed flame calculations are shown for the EDT regime and the FMCT regime. The flame calculations have been performed using the non-premixed opposed-jets burner from Chemkin-Pro and the GRI-Mech 3.0 with a strain rate a = 800 s^{-1}.

The discrepancy of the scatter plots is greatly reduced compared to the experimental results from the LRS setup at NTNU. In this case, the discrepancy is rather induced by the turbulent fluctuations than by the level of uncertainties (cf. Section 7.3). In addition, the simultaneous line imaging of Raman/Rayleigh scattering setup at SNL enables single-shot measurements and achieves higher spatial resolution than at NTNU, which enables to better capture the flame structure.

The difference between the results from both transport regimes is significantly pronounced in those flames. Similarly to the transitional flames detailed above, FMCT regime accounts for differential diffusion effects and leads to higher maximum temperatures, due to a better hydrogen supply to the flame region. Consequently, CO molar fraction is higher than with the assumption of equal diffusivities, since dissociation reactions have locally higher rates due to the higher temperatures. The effects can also be seen on the molar fraction profile of CO_2, especially at the location of the peak of CO molar fraction. The maximum temperature is also slightly shifted from stoichiometric mixture fraction towards to the fuel-rich side, as a consequence of reduced heat release in the presence of product dissociation. Details on the phenomenon can be found in Appendix D. Differential diffusion effects are also seen on H_2 and CH_4 profiles: for both regimes, H_2 keeps diffusing through the flame region, whereas CH_4 is preferentially burned at richer mixture fraction with the FMCT regime. Consequently, the local content of H_2O appears higher in the flame region with the FMCT regime, due to the higher local ratio of hydrogen in the fuel compared to CH_4. The balancing effect appears in the molar fraction profile of CO_2. The variations in the molar fraction profiles of H_2O, CO_2 and CO from EDT regime to FMCT regime are also consistent with the potential composition of the combustion products from methane flames burning at richer conditions.

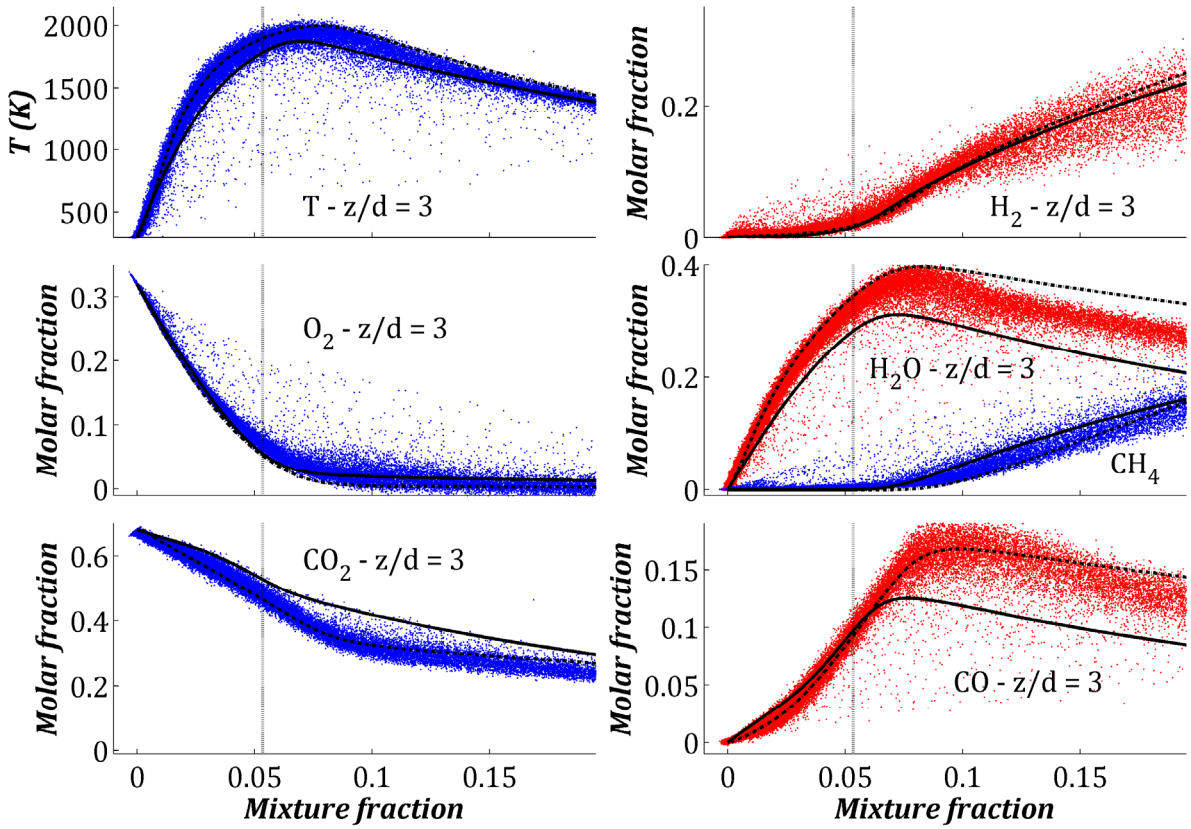

Figure III.38: Scatter plots of the temperature and the molar fractions of the main species in mixture fraction space from flame B-1, measured at z/d = 3 using the simultaneous line imaging of Raman/Rayleigh scattering setup at SNL. Corresponding results from laminar non-premixed flame calculations are shown for EDT regime (solid lines) and FMCT regime (dashed lines) at a = 800 s^{-1}. The stoichiometric mixture fraction is indicated by a vertical dashed line.

At three diameters above the fuel nozzle, the scatter plots seem to rather agree with the FMCT regime, though the results are mitigated between both regimes for H_2O and CH_4 for example. Despite the high turbulent mixing rates, which generally dominate the molecular transport at high Reynolds numbers, differential diffusion effects cannot be ignored in the near-field of these flames. Farther downstream, a departure of the profiles from the FMCT regime towards the EDT regime is observed (cf. Appendix D, Figure 7). The phenomenon is correlated to the broadening of the flame region due to the increasing turbulent mixing rates. Since differential diffusion acts on a micro-scale level, its relative contribution becomes least when the flame region expands, until the turbulent mixing rates fully dominate the molecular transport.

Figure III.39 shows the conditional means of the temperature and the molar fractions of the major flame species in mixture fraction space, around the flame region. Results are shown for both experiments and laminar flame calculations using FMCT regime. Results from the laminar flame calculations for the molar fractions of OH, H and O radicals are also shown. Experimental results and flame calculations agree relatively well, though a slight difference can be observed for H_2O molar fraction and the temperature, which are slightly inferior to the flame calculations.

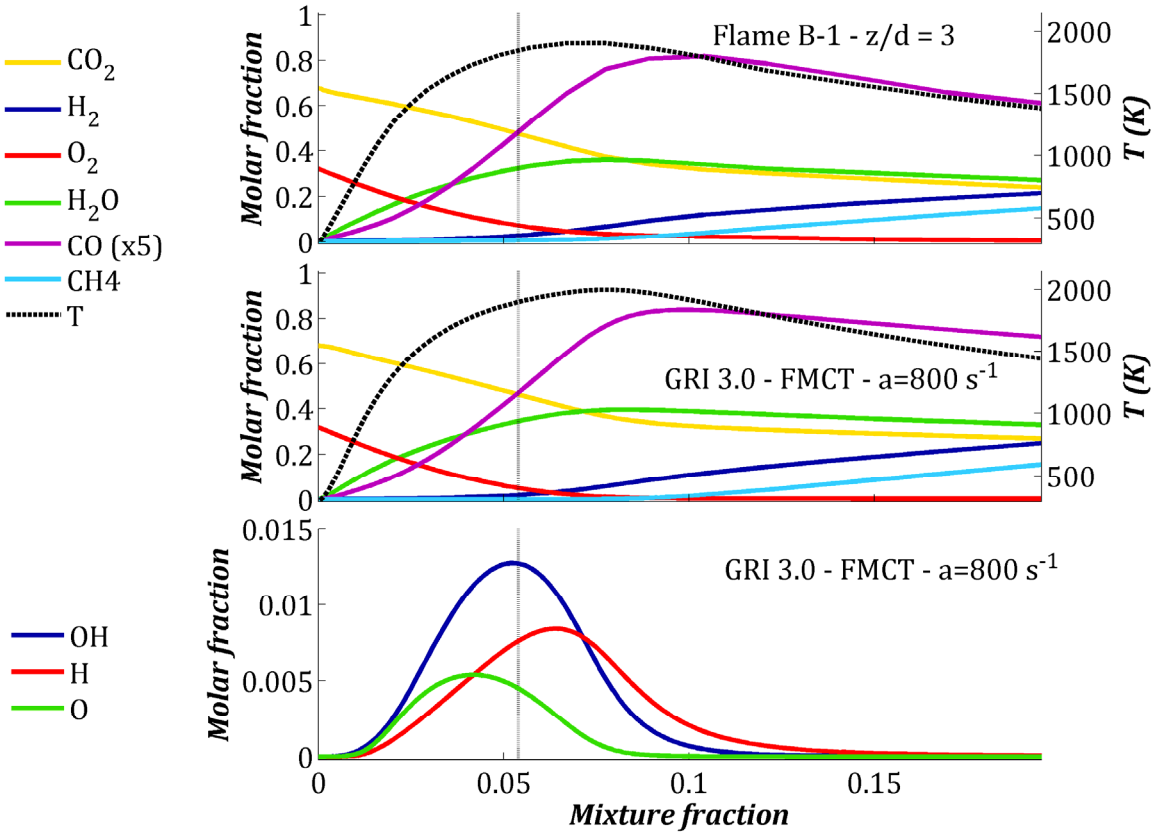

Figure III.39: Conditional means of the temperature and the molar fractions of the main species in mixture fraction space from flame B-1, measured at z/d = 3 using the simultaneous line imaging of Raman/Rayleigh scattering setup at SNL. Corresponding results from laminar non-premixed flame calculations are shown for the FMCT regime at a = 800 s^{-1}. The stoichiometric mixture fraction is indicated by a vertical dashed line.

Due to the overall agreement between laminar flame calculations and experimental results, one can assume the consistence of the calculated molar fractions. The profiles of molar fractions of OH, H and O radicals are quite comparable to those calculated by NP-H_2-OF-4 (cf. Figure III.32), though their amplitude is about half. The difference of amplitude is partly due to the lower flame temperatures. In addition, the overall amplitude of the molar fraction profiles of radicals increases with the hydrogen content in the fuel for these flames, though the adiabatic temperature remains within the same range.

CO molar fraction reaches a relatively high maximum for non-premixed methane jet flames. As detailed in Section 3.4.1, CO_2 is not inert but rather takes part in the chemical reactions. The reverse reaction of the CO burnout reaction (cf. Eq. I.16) is promoted by high CO_2-dilution levels, high temperatures and high amounts of available H radicals in the flame region (cf. Section 3.4.1). The higher amount of available H radicals justifies the slightly higher maximum molar fraction of CO with 55 $\%_{mol}$ H_2 than with 37 $\%_{mol}$ H_2 in the fuel (not shown here). These results are consistent with the laminar flame calculations.

SUMMARY OF PART III

This chapter focuses on results and discussion from LRS measurements performed in various flame configurations in order to isolate the typical features from oxy-fuel conditions. For each case, a parametric study has been carried out to highlight the changes in the flame structure and the chemical processes. The oxy-fuel flame configurations are as follows:

- Laminar premixed $CH_4/O_2/CO_2$ flat flames,
- Laminar premixed $H_2/O_2/CO_2$ flat flames,
- Transitional non-premixed H_2 – O_2/CO_2 jet flames,
- Turbulent non-premixed H_2/CH_4 – O_2/CO_2 jet flames.

In most cases, similar air-fired flames have also been measured with LRS for comparison. All experimental results are supported with corresponding laminar flame calculations using GRI-Mech 3.0 and Davis kinetic mechanisms.

Consistency between flame calculations and experimental results

- Though they display a significant discrepancy due to the uncertainties from the LRS setup, the experimental results generally show relatively good agreement with the laminar flame calculations. This agreement gives more consistency for using the laminar flame calculations to support the result analysis.

- An exception remains for the CO levels that are not totally well reproduced with the Davis mechanism and over-predicted with the GRI-Mech 3.0 in laminar premixed $H_2/O_2/CO_2$ flat flames.

- In non-premixed H_2 – O_2/CO_2 jet flames, predictions of local CO levels are found significantly higher than the experimental results, with both GRI-Mech 3.0 and Davis mechanism.

- In laminar premixed $CH_4/O_2/CO_2$ flat flames and non-premixed H_2/CH_4 – O_2/CO_2 jet flames, the levels of CO calculated using the GRI-Mech 3.0 agree well with the experimental results. This underlines that the GRI-Mech 3.0 is the most appropriate for methane flames.

- Due to the large difference of density between CO_2 and H_2, effects of differential diffusion are significant in the flame structure and cannot be ignored in the laminar flame calculations.

Spontaneous flame luminosity and radical pool

- The intensity of the spontaneous flame luminosity from all the investigated oxy-fuel flames gradually increases with the oxygen content in the oxidizer. This is mostly due to CO_2* chemiluminescence, which is promoted by the presence of CO and O radicals, and thus, by the high flame temperatures.

- According to the results from laminar flame calculations, the radical pool takes a larger share of the reacting mixture in the flame region of the laminar premixed oxy-fuel flat flames than in the corresponding air-fired flames. The contribution of the radical pool in the post-flame region increases with both the oxygen content in the oxidizer and the equivalence ratio.

- Growing levels of spontaneous flame luminosity and radical pool in oxy-fuel flames induce higher uncertainties in the calibration and signal-processing phases of LRS measurements.

Flame structure

- For both types of laminar premixed oxy-fuel flat flames, the flame thickness decreases while the oxygen content in the oxidizer increases, due to increasing kinetic rates.

- In non-premixed jet flames, the kinematic viscosity of the reacting mixture increases with the oxygen content in the oxidizer through temperature, leading to increased laminarisation effects. The main evidence is the shift downstream of the breakpoint between laminar and turbulent patterns observed in transitional non-premixed jet flames at low oxygen contents in the oxidizer. The influence of the kinematic viscosity of the oxidizer is also revealed by the non-reacting flows: using air leads to an onset of the breakpoint farther downstream than using O_2/CO_2 mixtures, which have lower kinematic viscosities than air at ambient temperature.

- In transitional non-premixed jet flames, increasing oxygen content in the oxidizer widens the flammability limits of the mixtures and broadens the flame region, as seen on radial profiles of temperature.

- In transitional non-premixed jet flames, the maximum flame temperature shifts towards the fuel-rich region while the oxygen content in the oxidizer increases. This shift also makes the viscous layer overlap the shear layer, which maximizes the stability of the flames. The phenomenon operates a stronger degree of laminarisation of the near-field as the oxygen content increase sin the oxidizer. This contributes to the significant change of the flame pattern observed at ca. 30 $\%_{mol}$ O_2 in the oxidizer.

- Unlike in turbulent non-premixed H_2/CH_4 – O_2/CO_2 jet flames, the inner fuel jet of the transitional non-premixed H_2 jet flames does not seem to expand radially in the laminar region. However, the flame region radially expands away from the central axis in both cases, though the expansion is more pronounced for the turbulent oxy-fuel flames. The differences can be explained by a combination of the higher density of the fuel jet inducing a higher momentum, the higher intensity of turbulence and the lower kinematic viscosity of the reacting mixture due to the addition of CH_4.

Evolution of CO levels in oxy-fuel flames

- Results from both experiments and flame calculations showed that local CO levels are generally higher in CO_2-diluted oxy-fuel flames than in air-fired conditions.

- As evidenced with oxy-hydrogen flames, the higher CO levels are primarily induced by the significant participation of CO_2 in the reverse rate of the CO burnout reaction. This trend (cf. Eq. I.16) is promoted by high CO_2-dilution levels, high temperatures and high amounts of available H radicals in the flame region.

- A summary of the observations made on the evolution of CO molar fraction profiles from the investigated oxy-fuel flames is presented in Table III.11.

- CO levels are however different farther downstream from the measured locations, since the oxidation of CO into CO_2 greatly depends on the residence time.

Table III.11: Summary of the observations made on the evolution of CO molar fraction profiles from the investigated oxy-fuel flames. Note that the observations are made within the limits of the flames conditions given in Section 9.

Evolution of the molar fraction of CO	***Increasing parameters:***		
	Φ	***O_2 content in oxidizer***	***H_2 content in fuel***
Laminar premixed $CH_4/O_2/CO_2$ flat flames	↗	↗	-
Laminar premixed $H_2/O_2/CO_2$ flat flames	↗	↗	-
Transitional non-premixed H_2 - O_2/CO_2 flames	-	Max. at 30 $\%_{mol}$ O_2	-
Turbulent non-premixed CH_4/H_2 - O_2/CO_2 flames	-	-	↗

References

[*Andersen* 2009] *Global Combustion Mechanisms for Use in CFD Modeling under Oxy-Fuel Conditions*, Andersen, J., Rasmussen C.L., Giselsson T., and Glarborg P. Energy & Fuels, 2009. 23: p. 1379-1389.

[*Barlow* 2000] *Experiments on the scalar structure of turbulent $CO/H_2/N_2$ jet flames*, Barlow, R.S., Fiechtner G.J., Carter C.D., and Chen J.Y. Combustion and Flame, 2000. 120(4): p. 549-569.

[*Barlow* 2009] *Application of Raman/Rayleigh/LIF diagnostics in turbulent stratified flames*, Barlow, R.S., Wang G.H., Anselmo P., Sweeney M.S., and Hochgreb S. Proceedings of the Combustion Institute, 2009. 32: p. 945-953.

[*Bergmann* 1998] *Application of spontaneous Raman and Rayleigh scattering and 2D LIF for the characterization of a turbulent $CH_4/H_2/N_2$ jet diffusion flame*, Bergmann, V., Meier W., Wolff D., and Stricker W. Applied Physics B: Lasers and Optics, 1998. 66(4): p. 489-502.

[*Cheng* 2006] *Lean and ultralean stretched propane–air counterflow flames*, Cheng, Z., Pitz R.W., and Wehrmeyer J.A. Combustion and Flame, 2006. 145(4): p. 647-662.

[*Davis* 2005] *An optimized kinetic model of H_2/CO combustion*, Davis, S.G., Joshi A.V., Wang H., and Egolfopoulos F. Proceedings of the Combustion Institute, 2005. 30(1): p. 1283-1292.

[*Jones* 1988] *Global reaction schemes for hydrocarbon combustion*, Jones, W.P. and Lindstedt R.P. Combustion and Flame, 1988. 73(3): p. 233-249.

[*Liu* 2003] *The chemical effect of CO_2 replacement of N_2 in air on the burning velocity of CH_4 and H_2 premixed flames*, Liu, F., Guo H., and Smallwood G.J. Combustion and Flame, 2003. 133(4): p. 495-497.

[*McAllister* 2011] *Fundamentals of Combustion Processes*. McAllister, S., Chen J.Y., and Fernandez-Pello A.C. 2011, Springer Science+Business Media, LLC 2011.

[*Mungal* 1991] *The Visible Structure of Turbulent Jet Diffusion Flames - Large-Scale Organization and Flame Tip Oscillation*, Mungal, M.G., Karasso P.S., and Lozano A. Combustion Science and Technology, 1991. 76(4-6): p. 165-185.

[*Reaction-Design* 2008] *CHEMKIN-PRO*, Reaction-Design. 2008: San Diego, 2008.

[*Smith* 1999] *http://www.me.berkeley.edu/gri_mech/*, Smith, G.P., Golden D.M., Frenklach M., Moriarty N.W., Eiteneer B., Goldenberg M., Bowman C.T., Hanson R.K., Song S., Gardiner W.C., Lissianski V.V., and Qin Z. 1999.

[*Takeno* 1994] *Transition and structure of jet diffusion flames*, Takeno, T. Symposium (International) on Combustion, 1994. 25(1): p. 1061-1073.

[*Turns* 2000] *An Introduction to Combustion: Concepts and Applications*. Turns, S.R. Second edition ed., ed. M.s. McGraw-Hill Education, 2000 - 676 pp. 2000.

[*Warnatz* 2000] *Combustion*. Warnatz, J., Maas U., and Dibble R.W. Springer. Vol. 3rd Edition. 2000.

[*Westbrook* 1981] *Simplified Reaction Mechanisms for the Oxidation of Hydrocarbon Fuels in Flames*, Westbrook, C.K. and Dryer F.L. Combustion Science and Technology, 1981. 27(1-2): p. 31-43.

[*Weydahl* 2011] *Assessment of existing H_2/O_2 chemical reaction mechanisms at reheat gas turbine conditions*, Weydahl, T., Poyyapakkam M., Seljeskog M., and Haugen N.E.L. International Journal of Hydrogen Energy, 2011. 36(18): p. 12025-12034.

[*Yamashita* 1992] *Characteristics of turbulent fluctuations in jet diffusion flames*, Yamashita, H., Kushida G., and Takeno T. Symposium (International) on Combustion, 1992. 24(1): p. 311-316.

[*Yang* 2010] *A mechanistic study of Soret diffusion in hydrogen–air flames*, Yang, F., Law C.K., Sung C.J., and Zhang H.Q. Combustion and Flame, 2010. 157(1): p. 192-200.

[*Yetter* 1991] *A Comprehensive Reaction Mechanism For Carbon Monoxide/Hydrogen/ Oxygen Kinetics*, Yetter, R.A., Dryer F.L., and Rabitz H. Combustion Science and Technology, 1991. 79(1-3): p. 97-128.

CONCLUDING REMARKS

The present experimental investigation of oxy-fuel flame structure using laser Raman scattering (LRS) diagnostics evidenced the main features specific to oxy-fuel flames compared to air-fired flames. The focus was especially set on chemical kinetic processes, participation of CO_2 in the reactions and turbulence/chemistry interactions. These features could be isolated and discussed by studying different flame configurations: laminar premixed $CH_4/O_2/CO_2$ flat flames, laminar premixed $H_2/O_2/CO_2$ flat flames, transitional non-premixed H_2 – O_2/CO_2 jet flames and turbulent non-premixed H_2/CH_4 – O_2/CO_2 jet flames. The main challenges while performing LRS in oxy-fuel flames were also discussed and justify the estimates of uncertainties from the reported LRS measurements.

Local CO levels were found significantly higher than in comparable air-fired flames. However, the bulk of CO molecules may potentially still be oxidized into CO_2 farther downstream, depending on the residence time. To limit the CO levels in the flue gas, the design of oxy-fuel burners should take this factor into account, so that chemical processes are not quenched too early and prolong the residence time.

Experimental results and laminar flame calculations agreed reasonably well. However, CO levels from the calculations using the Davis mechanism appeared over-predicted and not totally well-behaved. The mechanism may not be the most adapted to CO_2-diluted oxy-fuel flames, though predictions of temperature and other flame species appeared in the same range as the experimental results. The calculations using GRI-Mech 3.0 displayed good agreement with experimental results while CH_4 was present in the fuel in the fuel mixture. However, with pure H_2 as fuel, CO levels appeared over-predicted as well. In addition, effects of differential diffusion were highlighted, especially for the influence on maximum flame temperatures and local CO levels. Differential diffusion effects should be taken into account in the near-field of transitional and turbulent flames for more accurate predictions.

Strong laminarisation effects in the near-field of oxy-fuel flames were evidenced while increasing the oxygen content in the oxidizer. Those effects originate from the higher temperatures, higher kinematic viscosities and wider flammability limits. The increased oxygen content in the oxidizer is also correlated to improved flame stability through the shift of maximum flame temperature towards the inner fuel jet in non-premixed jet flames. The shift operates a better overlap between viscous layer and

shear layer to more effectively dampen the development of turbulent structures responsible for the transition to turbulent regime. Increased oxygen contents in the oxidizer were also seen to increase the laminar flame speeds, contributing to increased flame stability in premixed flames. Being able to tune and improve the flame stability by adjusting the oxygen content in the oxidizer could be of high interest in industrial applications, when different fuels are operated with the same burner, for instance.

Overall levels of spontaneous flame luminosity can considerably limit the application of LRS measurement in CO_2-diluted oxy-fuel flames and should be thoroughly considered when high oxygen contents in the oxidizer are targeted.

Enhanced heat radiation from CO_2-diluted oxy-fuel flames greatly contributes to improved heat transfer across the flame and to the surroundings. Higher heat radiation to the surrounding is especially of interest for boilers. In gas turbines using flue gas as working fluid, more uniform temperature distribution within the CO_2-enriched flue gas might be of interest.

CO_2-diluted oxy-fuel combustion firing natural gas presents many advantages for industrial applications in the CCS context and constitutes a research field where many aspects still have to be investigated. In order to further develop this research field by validating or testing combustion models and kinetic mechanisms, most experimental results used to support the present PhD work are available upon request.

FURTHER WORK

Improvements of the laser Raman scattering setup at NTNU

Mainly based on the experience at Sandia National Laboratories, whose Raman laser setup is one of the most advanced in the field of combustion, the LRS setup at NTNU could be considerably improved by the following means:

- Replacement of spectrometer by a custom holographic grating.
- Adaptation of a cryogenic cooling unit for the ICCD camera to reduce dark noise from CCD array.
- Coflowing air around the oxidizer in order to avoid windows across the laser path and induced reflections or laser energy losses.
- On-CCD spectral binning to improve SNR, though it is at the expense of the spectral resolution.
- If scattered signals have sufficiently high intensities, the intensifier from the ICCD camera should be avoided, due to its relatively high electronic noise.
- If the SNR is sufficiently high, single-shot measurements should be achieved to avoid averaging effects from on-CCD accumulations.
- Measurements can be achieved using a polarizer set in front of the spectrometer. Theoretically, the recorded spectra would only include background noise, LIF from the C_2 Swan band system and spontaneous flame luminosity signals, while Raman signals would be rejected by the polarizer. If those measurements are withdrawn from Raman measurements achieved without polarizer, it should be ideally possible to perform LRS measurements at higher soot levels. Nevertheless, this is only applicable if the flame is laminar or if on-CCD accumulations are achieved, since information from turbulent fluctuations would not be captured.
- Radical concentrations estimated from laminar flame calculations could be implemented in the Raman resolution algorithm. This correction could reduce the uncertainties when the radical pool is known to take a significant share of the reacting mixtures. Nevertheless, it remains challenging to apply it in non-premixed flames.

Further analysis from present results

- The participation of CO_2 in chemical processes might be enhanced by the H_2-addition in the fuel, due to H radicals promoting the reverse rate of the CO burnout reaction. This effect could be investigated from the present sets of results.
- In the transitional non-premixed H_2 – O_2/CO_2 jet flames, the flame structure pattern experiences changes while increasing the oxygen content in the oxidizer above ca. 40 $\%_{vol}$. The responsible flame/vortex interaction should be further investigated.
- A substantial amount of the intense heat radiation from oxy-fuel flames is potentially re-absorbed by the flames, which might result in a shift of maximum temperature towards the lean side. A deeper look into this should be taken, though the level of uncertainties might be too high in the present results.

Further work in the field of oxy-fuel combustion

- The data-library built up from the present experimental investigation is available to test and validate combustion models or kinetic mechanisms dedicated to oxy-fuel combustion.
- The present data-library would be greatly enriched if measurements of the velocity field were performed. This could also benefit to the understanding of the change of flame structure pattern mentioned above in transitional jet flames.
- Similar experimental investigations could be performed in different flame configurations, such as with higher pressure or more complex burners.

PART IV

APPENDICES

A. DATA PRE-PROCESSING ALGORITHMS

Based on Rondeau's internship report [1].

A.1. Overview

The main functions of the pre-processing software are described in Section 5.2.3. The present appendix focuses on the algorithms used for data filtering of optical-breakdowns and cosmic rays, and the way they were implemented in the software.

An overview of the GUI is shown in Figure A.1, and its main components are listed in Table A.1. Data from the raw *.SPE* files are stored into a matrix, *S(p,s,t)*, which contains Raman signal intensity corresponding to each pixel (*p)* on the spectral axis, at various spatial (*s)* and temporal (*t)* locations.

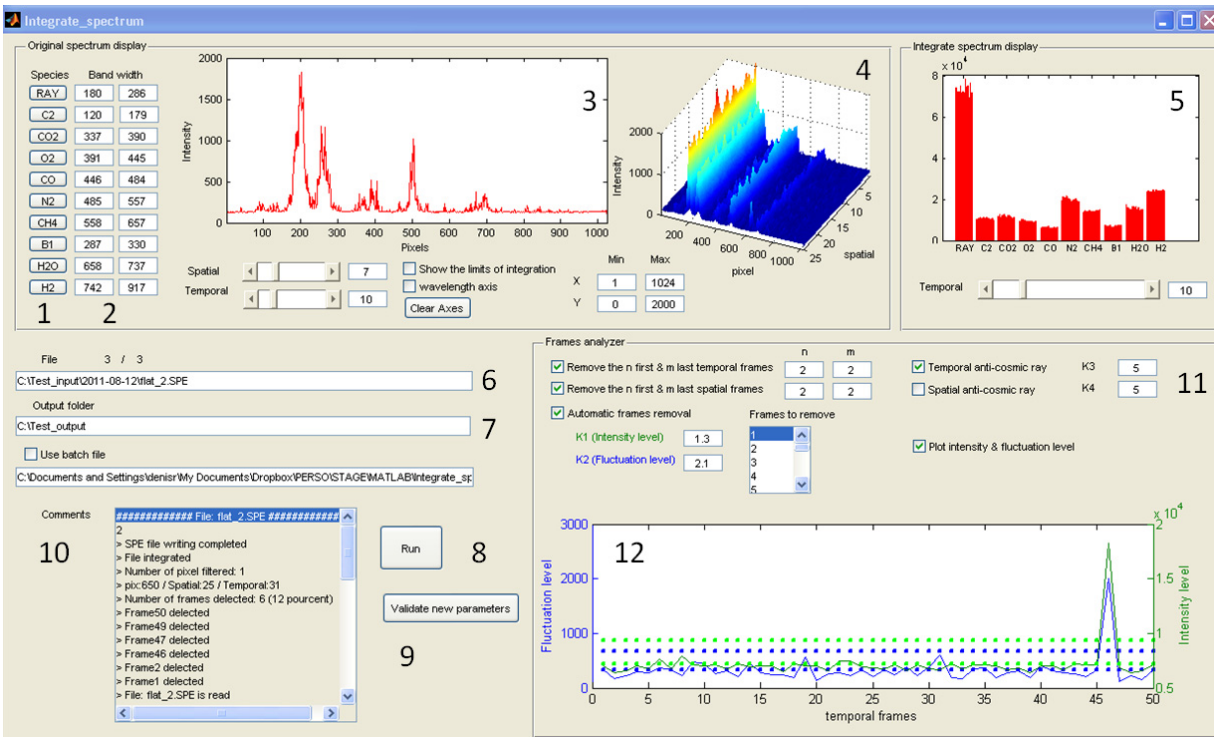

Figure A.1: Overview of the GUI of the pre-processing software. [1]

Table A.1: List of the main components of the GUI. [1]

Index	Description
1	Display species spectral bandwidth on graph
2	Limits of species spectral bandwidths
3	Raw Raman spectrum display
4	3D raw Raman spectra display
5	Integrated Raman spectrum display
6	Raw file directory
7	Output directory
8	Run button
9	New parameters validation
10	Comments/Status box
11	Filtering parameters
12	Fluctuations and intensity levels display

A.2. Optical breakdown detection

High-power laser systems are of interest when dealing with LRS, as Raman signal intensities are linear with the laser energy. However, energy levels in the probe volume can be so high in a very short period of time that they may lead to plasma emission when tiny particles (dust for instance) cross the laser beam. The consequent optical-breakdown can result in the instantaneous saturation of the ICCD camera, which appears in the probe volume as sparks or flashes. Though the events are very short in time, the saturation on the ICCD chip can be generally seen for a longer time. Besides, since on-CCD accumulations are made for improving the signal, an optical breakdown event can be diluted in one frame and only appear as a slightly increased overall signal. Such events should be detected and deleted since they might lead to erroneous results.

In the present configuration, fresh gases were fairly clean, and the laser pulse duration was about 400 ns, so that optical breakdowns were not likely to happen often. However, it may happen more often that particles of the same range of size as the laser wavelength pass by the laser probe and lead to Mie scattering. This would appear as short flashes at 532 nm that temporarily saturates the ICCD camera, though in a much less critical way than with optical breakdowns. The purpose is here to develop an algorithm that is able to detect both of those events and acts by deleting the frame of interest, as well as the following frame, in case of residual effects.

There are two ways to detect a flash event within the spectra: one is based on the integrated signal intensity and the second one on the integrated signal fluctuations. Both of them tend to increase during this event.

A.2.1. Intensity level (IL)

$$IL(t) = \sum_{s=1}^{s_{final}} \sum_{p=287}^{330} S(p,s,t) \qquad \textit{Eq. A.1}$$

Condition:

$$IL(t) > K_1 * mean\left[\sum_{t=1}^{t_{final}} IL(t)\right] \qquad \textit{Eq. A.2}$$

Action:

$$\begin{matrix} IL(t) => removed \\ IL(t+1) => removed \end{matrix} \qquad \textit{Eq. A.3}$$

The signal is only observed in the spectral bandwidth *B1* (pixels: 287-330), where no Raman scattering is present. The matrix *S(p,s,t)*, containing the raw Raman signals, is spatially and spectrally integrated over the bandwidth *B1*. Optical breakdown events are detected when the intensity level is higher than the mean of the integrated value $IL(t)$ weighted by a coefficient K_1. When a cosmic ray or flash event is detected, the corresponding temporal frame and the following one are deleted.

A.2.2. Fluctuation level (FL)

$$FL(t) = \sum_{s=1}^{s_{final}} \sum_{p=287}^{330} abs\big(S(p+1,s,t) - S(p,s,t)\big) \qquad \textit{Eq. A.4}$$

Condition:

$$FL(t) > K_2 * mean\left[\sum_{t=1}^{t_{final}} FL(t)\right] \qquad \textit{Eq. A.5}$$

Action:

$$\begin{matrix} FL(t) => removed \\ FL(t+1) => removed \end{matrix} \qquad \textit{Eq. A.6}$$

The signal is once again taken from the spectral bandwidth *B1* (287 - 330). Before being summed over the spatial dimension, the absolute value of the difference between the signals at pixel p+1 and p is integrated over the spectral bandwidth *B1*. The difference with the mean of the matrix $FL(t)$ weighted by a coefficient K_2, also allows detecting optical breakdowns. When a cosmic ray or flash event is detected, the corresponding temporal frame and the following one are deleted.

A.2.3. Determination of the coefficients K_1 and K_2

Figure A.2 gives an example of flash detection with laminar methane-air premixed flat flame measurements. A peak in the fluctuation and intensity levels is detected in the temporal frame #41 (cf. Figure A.2, C). Note that a higher averaged signal intensity is clearly visible in the spectrum display (cf. Figure A.2, A-B), appearing as a noise over the whole spectral range.

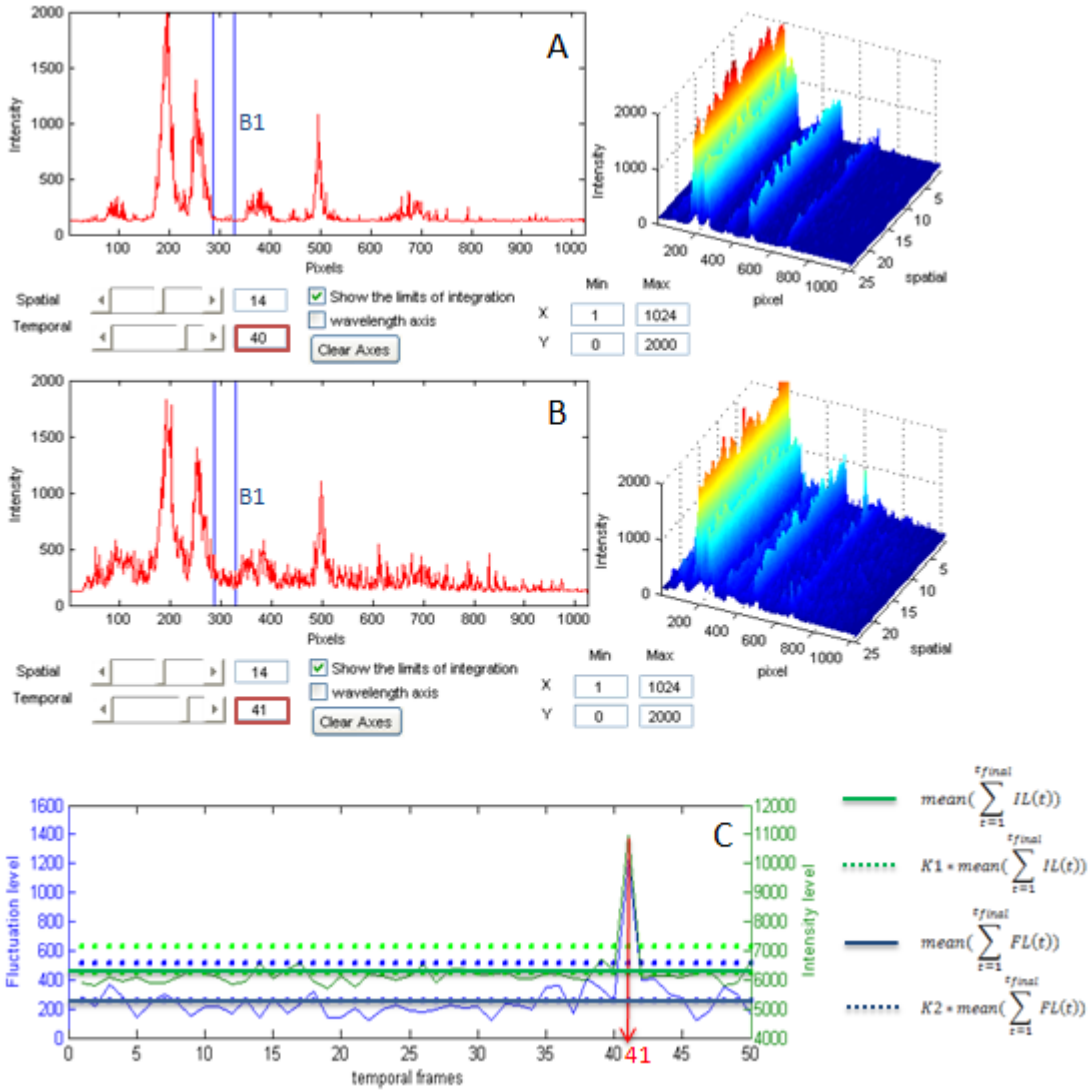

Figure A.2: Raman spectrum display without flash (A), Raman spectrum display with flash (B), fluctuation and intensity levels display (C). [1]

K_1 and K_2 validity ranges were determined by investigating the variation of the number of detected frames over 50 raw files. Various types of spectra were included within the raw files (dark, air, flat flames and jet flames). As shown in Figure A.3, the validity range for coefficients K_1 and K_2 is reached when the number of detected frames is constant. Thus, according to the present results, the validity range is 1.2 - 1.5 for K_1, and 2.0 - 2.6 for K_2. For instance, values of K_1 inferior to 1.2 would be too sensitive and

frames without optical breakdowns would be detected. Above 1.5, frames containing optical breakdowns may not be detected.

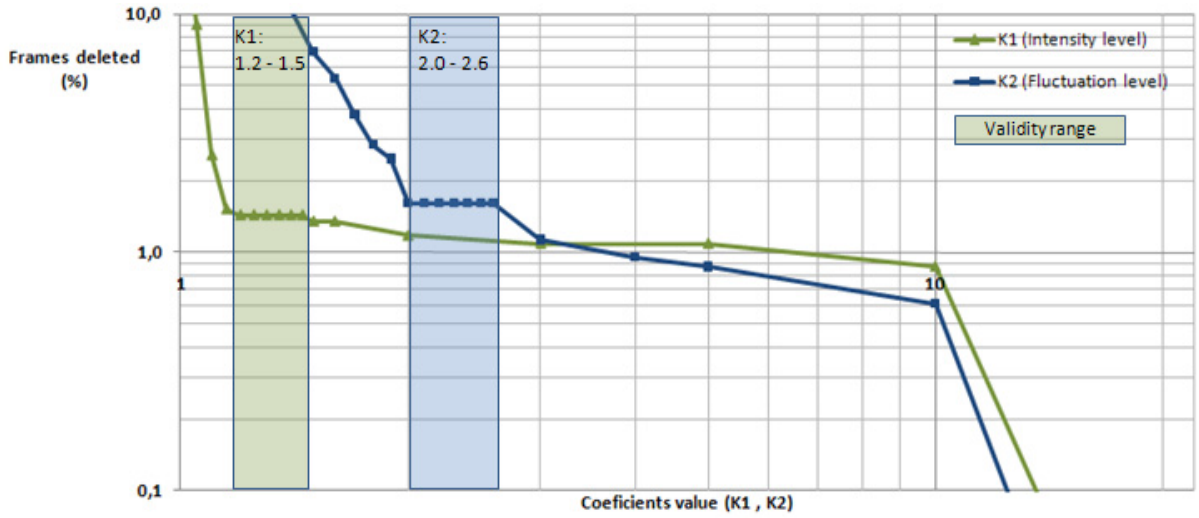

Figure A.3: Validity range for K_1 and K_2. [1]

Note that the level of detection with these two methods is similar. That means that one could be sufficient for flash detection. To ensure proper filtering of frames containing optical breakdowns, both have been used, especially since the required computer-time for filtering is very low. The final values used for the present project are K_1 = 1.3, and K_2 = 2.1.

A.3. Cosmic ray detection

High sensitivity and low noise of ICCD sensors make them ideal for capturing the particularly weak Raman scattering signals. However, they also have a significant sensitivity to cosmic ray events. Historically thought to be electromagnetic radiations, those actually result from subatomic particles originating from outer space, and producing secondary particles as they penetrate the Earth's atmosphere. Despite their small size, they convey significant energy due to their high speed. Relatively to an ICCD chip, cosmic ray events could be pictured as a single photon that is powerful enough to trigger the gain of the intensifier and to appear as a very localized and intense peak on resulting spectra. They tend not to happen often, and rarely twice in one spectrum.

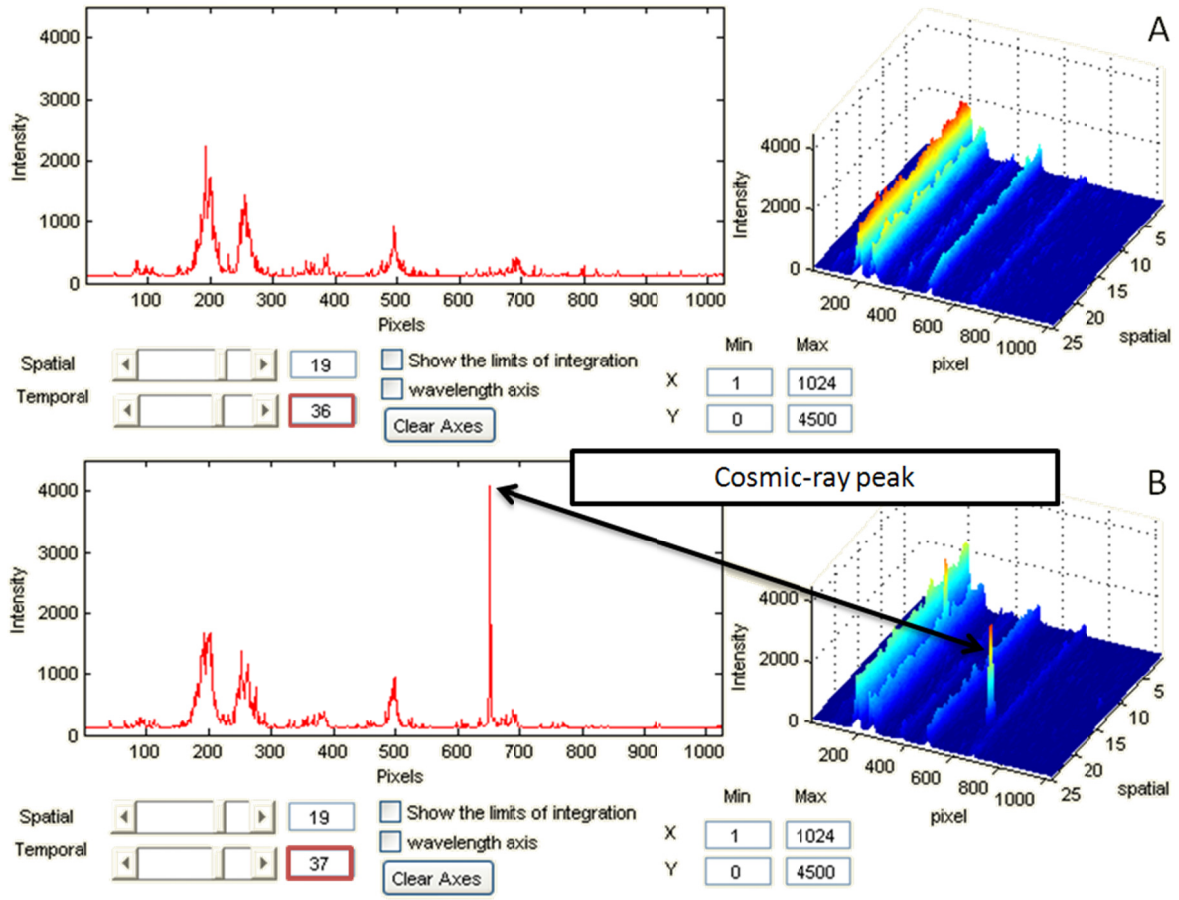

Figure A.4: Cosmic ray detection. Raman spectrum without cosmic ray (A), Raman spectrum with a cosmic ray (B). [1]

Figure A.4 shows an example of cosmic ray event. Cosmic ray events are typically single-pixel events, as it is the case in the frame #37 here. If not detected, they may lead to erroneous results during data-processing. Cosmic ray events contaminating Raman spectra have been properly removed by a peak filtering. Winspec offers a similar filtering option, but it was preferred to keep full control on data filtering. The algorithm for detection works as follows:

Condition #1:

$$S(p,s,t) > K_3 . \sum_{i=-2}^{2} [S(p,s,t-2) + S(p,s,t-1) + S(p,s,t+1) + S(p,s,t+2)]/\,20 \qquad \textit{Eq. A.7}$$

Condition #2:

$$S(p,s,t) > 200 \qquad \textit{Eq. A.8}$$

Action:

$$S(p,s,t) = [S(p,s,t-2) + S(p,s,t-1) + S(p,s,t+1) + S(p,s,t+2)]/4 \quad \text{Eq. A.9}$$

The detection of cosmic rays consists in comparing each pixel with the average of the five pixels of the two previously and following temporal frames, as illustrated in Figure A.5, weighted by a coefficient K_3. The second condition removes the detection of peak only due to the CCD noise at the top of the background level. The value of each pixel has to be more than 200. When a cosmic ray event is detected, the affected pixel intensity is replaced by the mean of the two previous and following temporal frames.

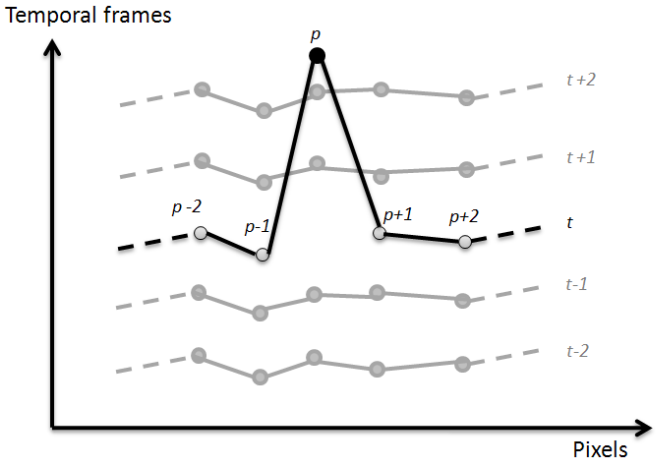

Figure A.5: Temporal cosmic ray detection scheme. [1]

A.4. Conclusions

Both algorithms proved to be efficient over a wide variety of raw spectra files. The multi-selection of files allows fast processing of long list of files. The average of frames removed because of optical breakdowns or flashes detection is about 5 % of the total number of frames for each raw spectra file. The amount of corrected pixels due to cosmic ray detection is about 2 pixels for 50 frames.

As a result of the fast running time and the rare failures of the pre-processing algorithm, a future improvement could be to implement the code into the data-processing software to simplify the whole processing of the raw spectra files.

Reference

1. Rondeau, D., *Final Project Report: Investigation of oxy-fuel flame structure by laser diagnostics*. 2011, NTNU, Trondheim (Norway).

B. SAFETY CONSIDERATIONS

The present appendix exclusively focuses on the experimental setup at NTNU. Safety issues were systematically considered while designing and performing experiments. Within this project, risks can be divided into different origins: laser system, gas supply, cooling system, operational procedures and ventilation system.

B.1. Laser system

Laser systems are highly energized equipments that might lead to great dangers if misused. First, thanks to a course on laser safety attended at the very beginning of the project and different experiences in similar laboratories, the evaluation of the risks could be confidently performed and the main dangers were eluded. Second, practice and/or visit at other laboratories using laser systems helped to manage the risk using experience from others.

The laser system used here is a Continuum Agilite, categorized as a class IV laser in terms of safety hazards. It emits 532-nm laser pulses up to ca. 560 mJ/pulse, which is a considerable energy delivered on a very short time, typically 200 or 400 ns. Protective goggles filtering a short bandwidth centred on 532 nm are systematically worn when the laser is in use, and provide an efficient eyes protection against Rayleigh scattering and laser reflections.

The laser system was delivered shortly before the beginning the project, which enabled to get knowledge and advice directly from the designer of the system. A start-up and shut-down procedure was delivered with the system for the best use. Besides, training for alignment and maintenance was provided to keep the laser system in the best operating conditions.

As the laser beam passes through optics, reflections appear and have to be spotted and dumped to avoid any risk. Any change of the optics or re-alignment requires a new check for reflections. The laser path is also mostly covered to protect the operators from reflections.

The laser system is located in the room adjacent to the operating room due to the layout of the laboratory. A short tunnel enables to let the laser beam pass from one room to another. The operating system can be controlled from both rooms.

To avoid adding an excessive number of optics on the laser path, which would reduce the laser output energy in the probe volume, the beam divides the operating room into two. One part, close to the entrance door, contains all operating controls, whereas one part cannot be accessed during laser operations due to the laser beam across the way. No operating tools are set on this part of the laboratory to avoid any crossing. Furthermore, for safety reasons, a laser beam blocker was designed to physically block the laser beam before it passes the tunnel. If the operator requires passing from one part to another, a protective stripe/chain needs to be unfastened. This energizes a solenoid motor in the laser system room which lifts up a laser dump across the beam. Details of the design can be seen in Figure B.1:.

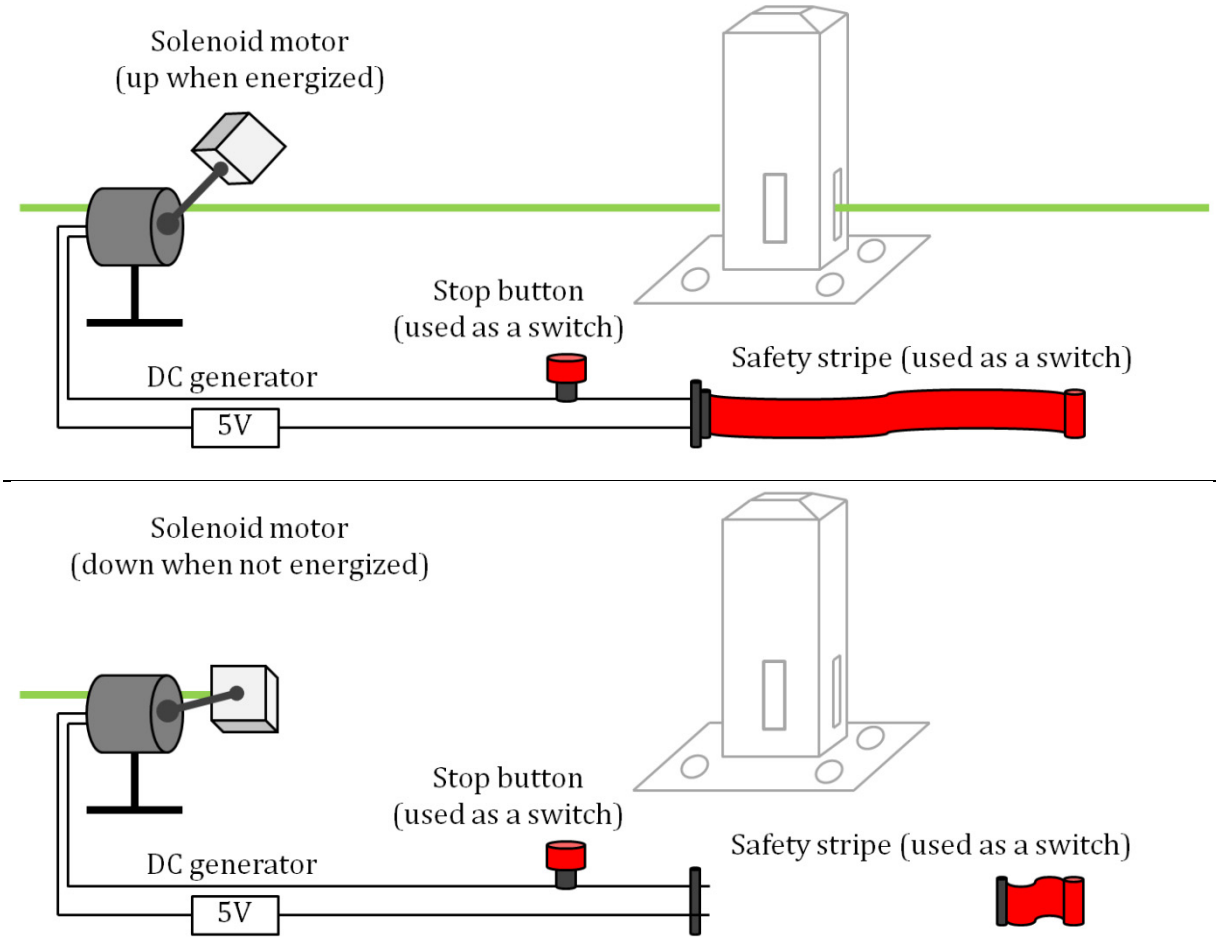

Figure B.1: Laser beam blocking system.

B.2. Gas supply

The layout of the gas supply is illustrated in Figure 3.25. For safety reasons, the laser laboratory is inside closed rooms and gas bottles cannot be stored inside any of them. The storage place is adjacent to the operating room. A ventilation system is right at the top of the bottles, in case of leaks. For the operating conditions of the present project, as many as 8 bottles are required in the storage place. A safety drawing of the tubing, including mass flow controllers and valves, is displayed next to the storage place (cf. Figure 3.25). The tubing is mainly made of stainless steel process pipe and Teflon flexible hoses. Leak tests are regularly performed.

Two solenoid valves are located upstream from the hydrogen and methane mass flow controllers and are controlled by a safety system. Those would open only if the ventilation in the operating room is at sufficient level. A stop-button is located in the operating room, next to the operator desk, to shut-off the two solenoid valves in case of troubles during operations.

B.3. Cooling system

Due to the high flame temperatures that can be reached with oxy-fuel conditions (up to ca. 3000 K for the present project), the combustion chamber requires a cooling system to keep its wall at an acceptable temperature. A water-based cooling system was chosen to simplify the design. Details can be found in Section 6.2.6**.**

Leak tests were performed at full tap water pressure (6 - 8 bars) and inlet- and outlet-valves closed. A main shut-off valve is accessible from the operator desk in case of massive leak. The water flow rate is kept high to prevent long residence time in the tubing that might lead to steam production and a potential local pressure build-up. The design of the tubing allows regulating the water flow rate for each of the four walls. Feedback can be given by observing the water flow rate at the four tubing outlets, or by controlling to water temperature at the four outlets.

B.4. Operational procedures

Specific operational procedures have been written and are displayed in the laboratory. They can also be found in the handbook gathering most of the documentation about safety in the laboratory. The operational procedures consist in three different parts: start-up, running and shut-down procedures.

The start-up procedure especially focuses on the handling of the gas supply, notably, opening the bottles in a certain order, performing leak tests, and igniting a mixture. Ignition of methane or hydrogen can only happen if the ventilation is set at a sufficient level, due to the safety system controlling the solenoid valves on the fuel lines. A propane igniter is used to ignite the mixtures. Besides, indications are given about setting warning signs on the entrance door and outside the laboratory.

The running procedure includes indications on emergency or temporary shut-down of the setup. In case of a major incident, a few steps are described to evacuate the room rapidly and limit the propagation of any danger. Actually, the operation room is designed in such a way that the operator can control each hazardous source from the desk, which is located right in front of the main exit door.

The shut-down procedure includes all the required steps to handle hazardous equipments and free the laboratory from any danger. Additionally, a check list of the most important items from the procedure is displayed on the exit door for a last safety check before leaving the lab.

Each of the safety documents present in the safety handbook of the laboratory must have been read, understood and approved by any operator before being entitled to perform experiments.

B.5. Ventilation system

The ventilation system, located above the combustion chamber, is essential for ensuring safe operational conditions in a closed laboratory. Thus, a proper evaluation of the ventilation system was performed before starting the experiments. The vacuum power of the ventilation should be sufficient to prevent from any danger for the operator, while it should not affect the measured flame/flow structure.

B.5.1. Enhancement through laboratory design

First, a large opaque PVC shield is set up between the operator desk and the combustion rig. Besides shielding the operator desk lights to improve the Raman signal quality, it physically protects the operator from steam/hot water leaks. It also prevents most flow from propagating towards the operator and enhances the ventilation of the domain around the combustion rig. A CO_2 meter is located on the operator desk to monitor the CO_2 level next to the operator in real-time. Note that cold CO_2 can be critical in this situation since CO_2 is heavier than air and tends to rapidly accumulate at the floor level, instead of being entrained in the ventilation system. However, no hazardous levels were ever reached by the detector during measurements.

B.5.2. Flammability limits in the ventilation duct

In presence of flames, high temperatures of the flue gas and buoyancy enhance the vacuum effect induced by the ventilation system. However, in case of cold flows, as those performed daily during the calibration measurements, the risk of diffusion of noxious or flammable mixtures remains uncertain. Thus, the efficiency of the ventilation system needs to be assessed to determine which conditions are safe to operate with.

The first step consists in evaluating the flammability limits of the gas mixture flowing in the ventilation duct, while running it at the usual level, to avoid propagating a hazard through the ventilation. An average volumetric flow rate of 6700 $sl.min^{-1}$ was measured at the ventilation inlet using a thermal anemometer. The total volumetric flow rate is assumed to include the whole quantity of gas released for measurement purposes and the ambient air. This enables to calculate the minimum and maximum flow rate of flammable gas in air to reach the lower explosion limit (LEL) and the upper explosion limit (UEL), in the ventilation duct. Results are shown in Table B.1:. A case with only ca. 75 % of the average level of the ventilation system (5000 $sl.min^{-1}$) is also taken into account, for safety. In any case, results show that under a flow rate of 200 $sl.min^{-1}$ of flammable gas, flammability limits are not reached in the ventilation system. Since the flow rate of flammable gases targeted for calibration measurements ranges from 5 to 20 $sl.min^{-1}$, flammable gases are sufficiently diluted by the ambient air and no safety issues are encountered in the ventilation system while performing calibration measurements.

Table B.1: Flammability limits for H_2 and CH_4 based on flow entering the ventilation system.

	LEL		***UEL***	
Flammable gas	***H_2***	***CH_4***	***H_2***	***CH_4***
Limits	4 $\%_{vol}$ in air	4.4 $\%_{vol}$ in air	75 $\%_{vol}$ in air	17 $\%_{vol}$ in air
Average ventilation level	268 $sl.min^{-1}$	295 $sl.min^{-1}$	5025 $sl.min^{-1}$	1139 $sl.min^{-1}$
75 % of the average ventilation level	200 $sl.min^{-1}$	220 $sl.min^{-1}$	3750 $sl.min^{-1}$	850 $sl.min^{-1}$

B.5.3. Flammability limits in the operation room

During calibration measurements, a flat field of perfectly mixed gas species is required for finer results. This involves using a Hencken burner instead of the coflow burner present in the combustion chamber. Since the Hencken burner has to be set aside from the combustion chamber, a distance of ca. 750 mm has to remain between the Hencken burner and the ventilation system because of the combustion chamber. Thus, the next step consists in evaluating the dispersion of flammable gases around the

gas output and in verifying that no flammable mixtures builds up away from the testing zone.

Two-dimensional simulations using Fluent were performed by Rondeau during his internship [1]. The model is detailed in Figure B.2, and the results are shown in Figure B.3 and Figure B.4. Note that, in fact, gases flow upwards toward the ventilation at the top, but the model is rotated for convenience. The flow rates correspond to those used for the calibration measurements: 30 $sl.min^{-1}$ N_2 and 10 $sl.min^{-1}$ H_2 or CH_4 in the central part, and 40 $sl.min^{-1}$ air in the shroud, to protect from early recirculation in ambient air. All gases are and remain at 300 K. The domain is sufficiently large to include the recirculations that might entrain the flammable gases radially.

Results from Figure B.3 and Figure B.4 show that recirculations tend to spread the flow of flammable gases radially, with a more significant radial distance for H_2 (maximum ca. 180 mm on each side). The radial distance is anyway limited and the dilution in air sufficiently efficient, so that no flammable zone builds up away from the burner. Besides, the flow is diluted with nitrogen to lower the risks. The highly air-diluted mixtures are then slowly directed toward the ventilation system.

Another interesting feature is the role played by the air shroud that prevents the main flow from early recirculation with ambient air. This most likely helps pushing away the main flow toward the ventilation system, without slowing it down too early.

Consequently, measurements can be safely performed, even with cold flows, such as during the calibration measurements. No dispersion of flammable gases, or building up of flammable zone seems to occur away from the burner. Operators and electrical devices would not be exposed if located at least 50 - 100 cm away from the burner.

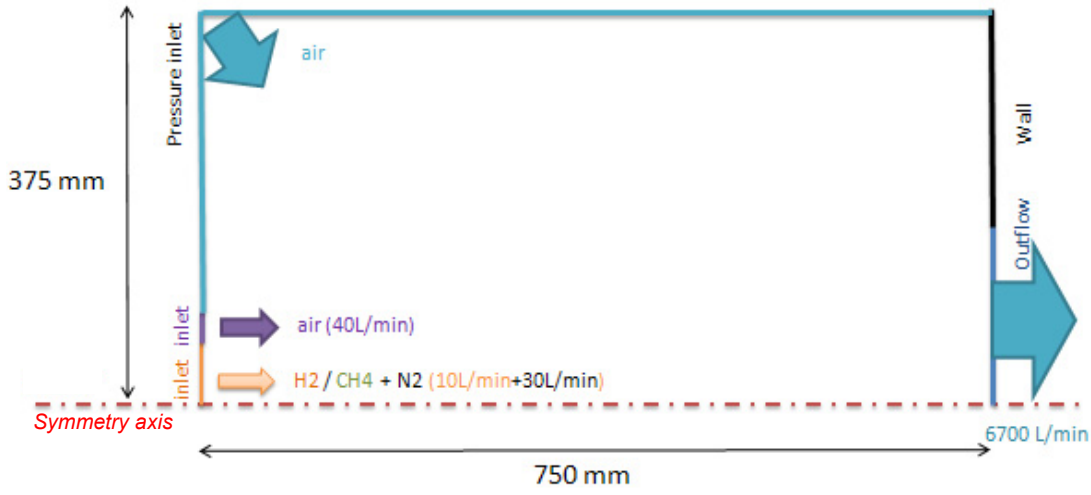

Figure B.2: Model used for the Fluent simulation of the interaction between gas flow and ventilation system with a Hencken burner configuration. [1]

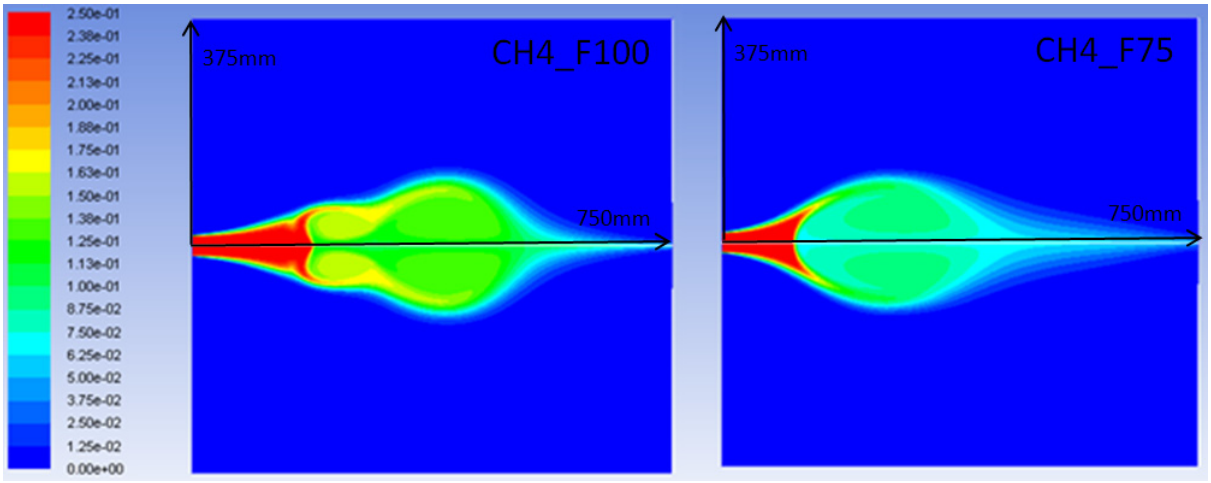

Figure B.3: Molar fraction of CH_4 resulting from simulations using Fluent and the Hencken burner configuration, with 30 sl.min^{-1} N_2 and 10 sl.min^{-1} CH_4 in the centre part, and 40 sl.min^{-1} air in the shroud. Left: using 100 % of the average ventilation level. Right: using 75 % of the average ventilation level. [1]

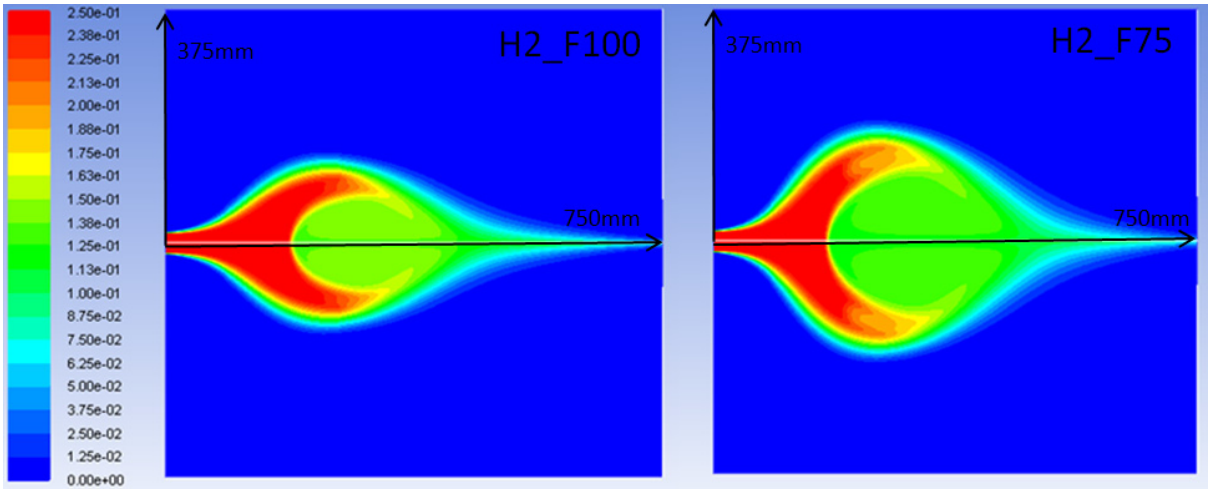

Figure B.4: Molar fraction of H_2 resulting from simulations using Fluent and the Hencken burner configuration, with 30 sl.min^{-1} N_2 and 10 sl.min^{-1} H_2 in the centre part, and 40 sl.min^{-1} air in the shroud. Left: using 100 % of the average ventilation level. Right: using 75 % of the average ventilation level. [1]

Reference

1. Rondeau, D., *Final Project Report: Investigation of oxy-fuel flame structure by laser diagnostics*. 2011, NTNU, Trondheim (Norway).

C. EXPERIMENTAL RESULTS FROM TRANSITIONAL NON-PREMIXED H_2 – O_2/CO_2 JET FLAMES

The present appendix provides the experimental results from the transitional non-premixed H_2 – O_2/CO_2 jet flames, whose flame conditions are given in Table III.4. Experimental conditions are described in Section 6 and summarized in Section 6.4. The most relevant observations are detailed in Section 11.3. The experimental results for NP-H_2-OF-5, 6 and 7 are only presented here to give an insight at the flame structure, since the level of uncertainties is relatively high (cf. Section 6.5).

The experimental results are first displayed as Reynolds-averaged radial profiles of scalars, and then, as scatter plots in mixture fraction space.

C.1. Reynolds-averaged scalar profiles

C.1.1. NP-H_2-OF-1

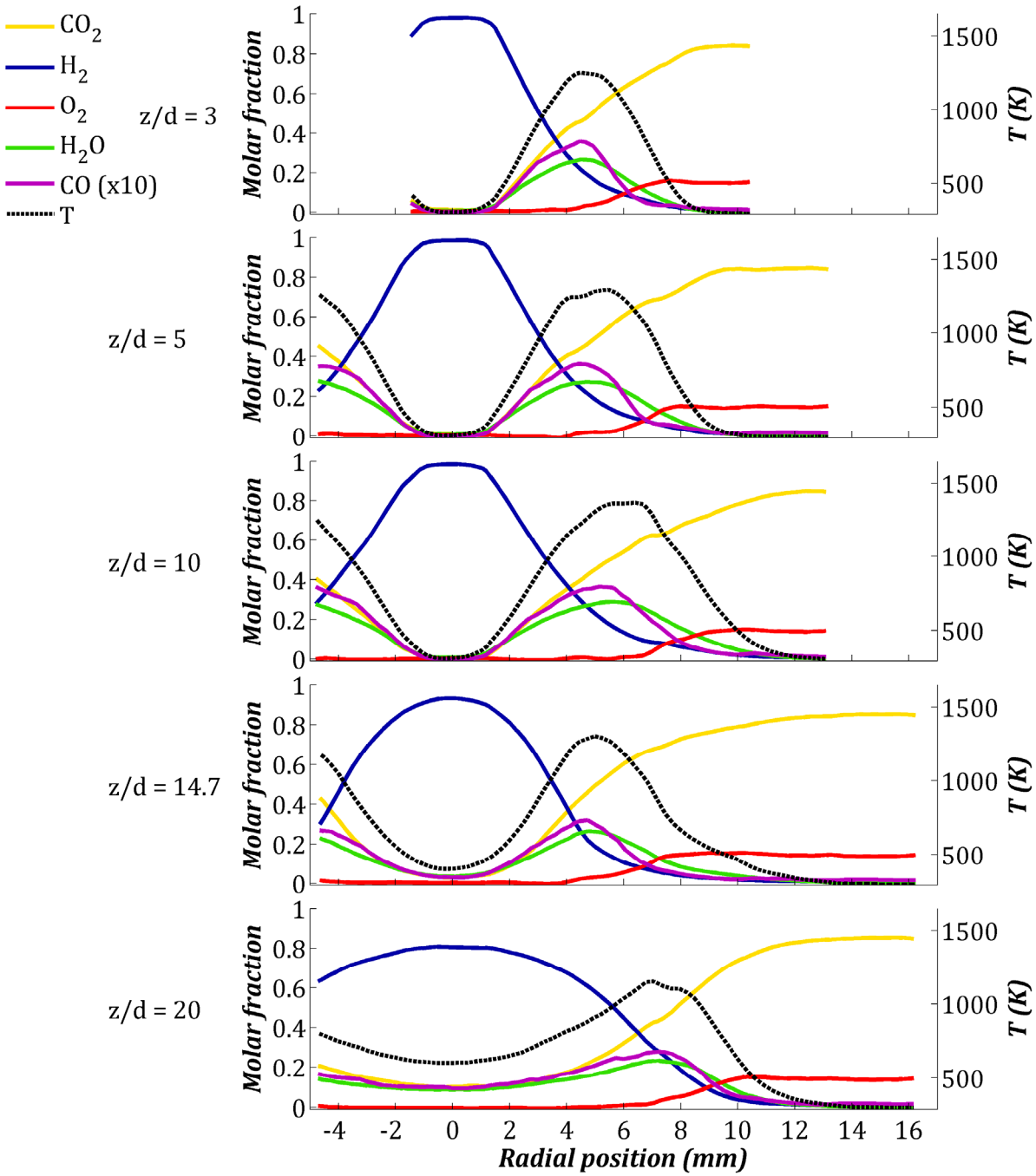

Figure C.1: Reynolds-averaged radial profiles of molar fractions of the main species and temperatures from NP-H_2-OF-1, measured by LRS at different heights above the fuel nozzle.

C.1.2. NP-H_2-OF-2

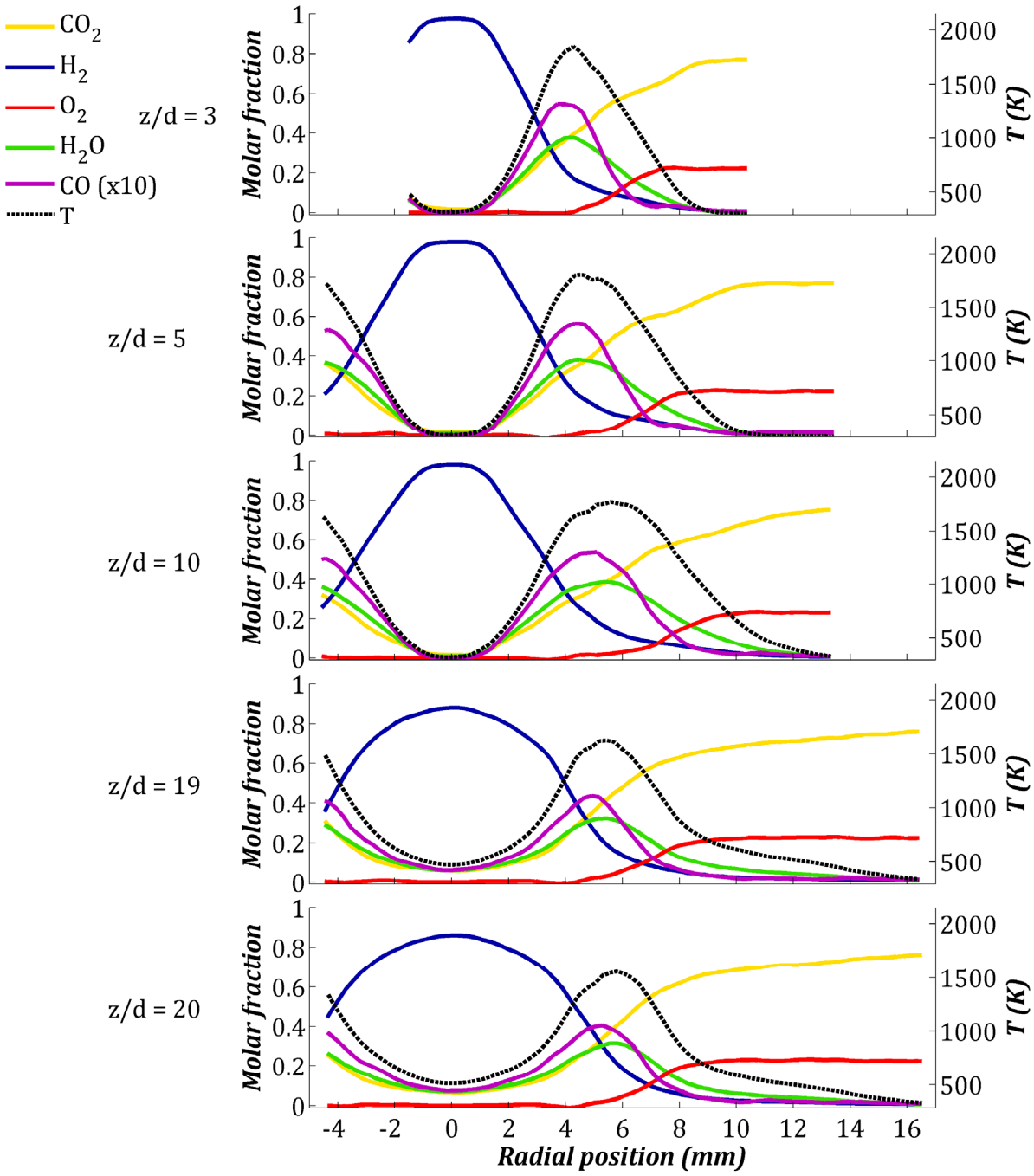

Figure C.2: Reynolds-averaged radial profiles of molar fractions of the main species and temperatures from NP-H_2-OF-2, measured by LRS at different heights above the fuel nozzle.

C.1.3. NP-H_2-OF-3

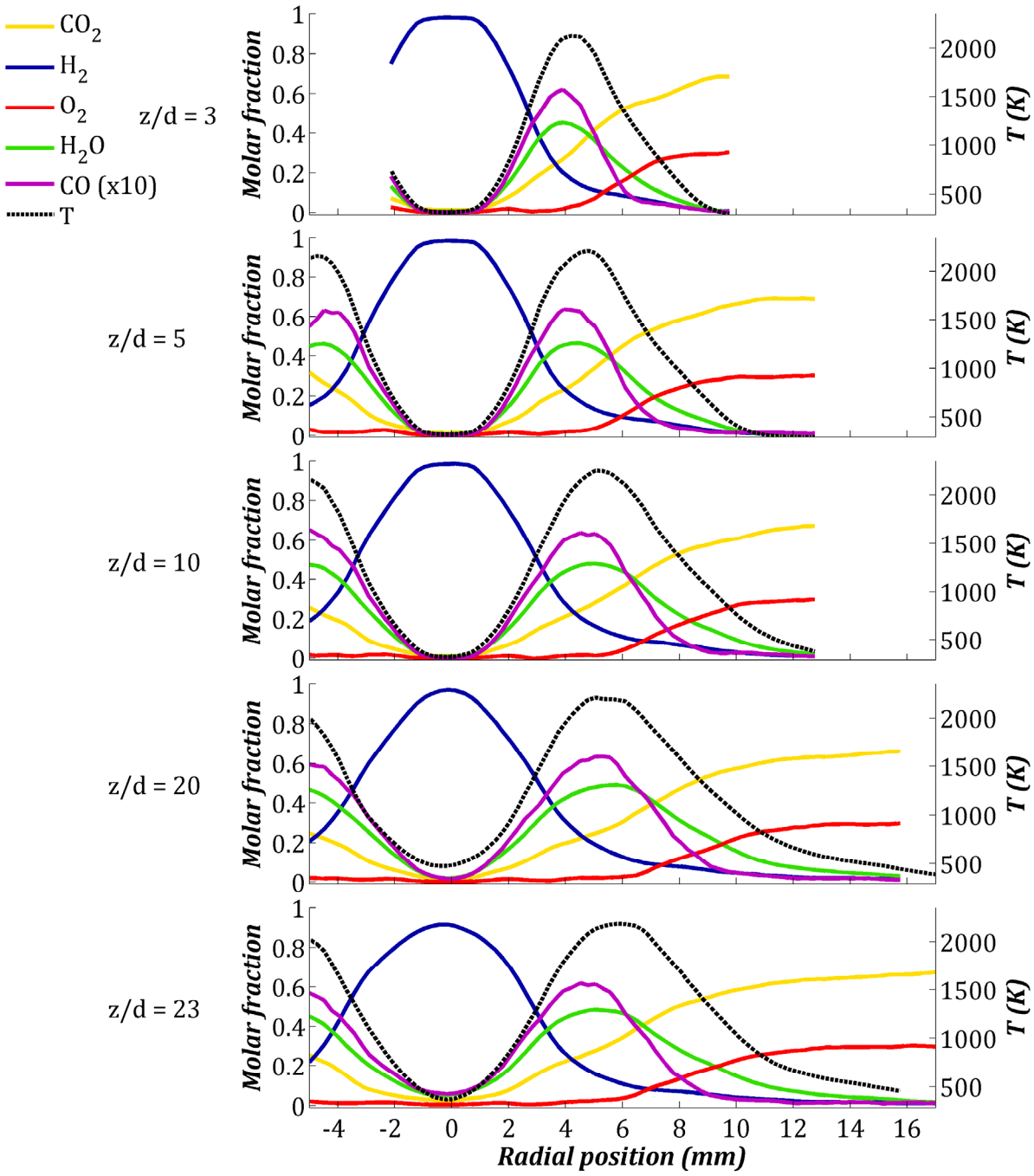

Figure C.3: Reynolds-averaged radial profiles of molar fractions of the main species and temperatures from NP-H_2-OF-3, measured by LRS at different heights above the fuel nozzle.

C.1.4. NP-H_2-OF-4

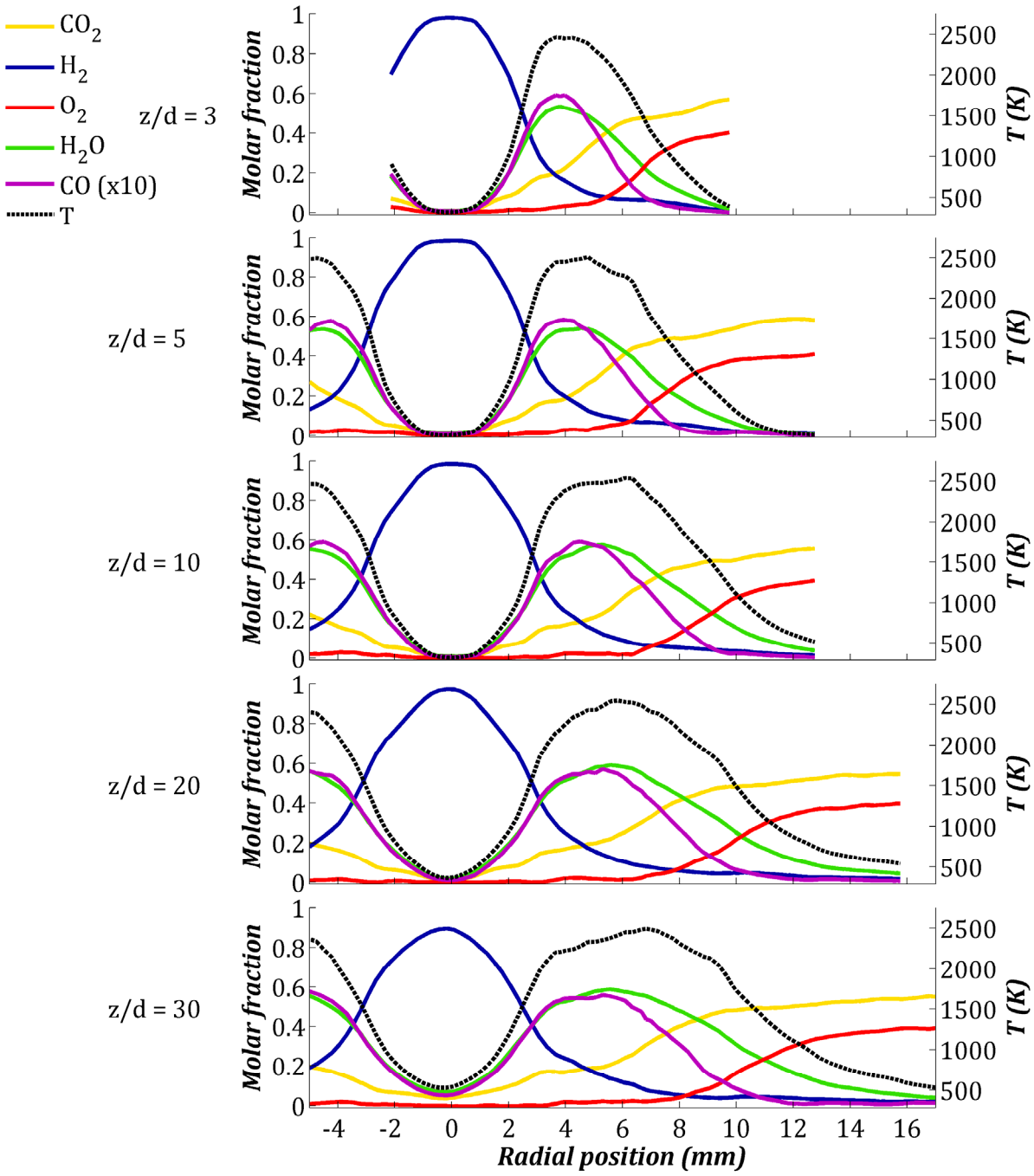

Figure C.4: Reynolds-averaged radial profiles of molar fractions of the main species and temperatures from NP-H_2-OF-4, measured by LRS at different heights above the fuel nozzle.

C.1.5. NP-H_2-OF-5

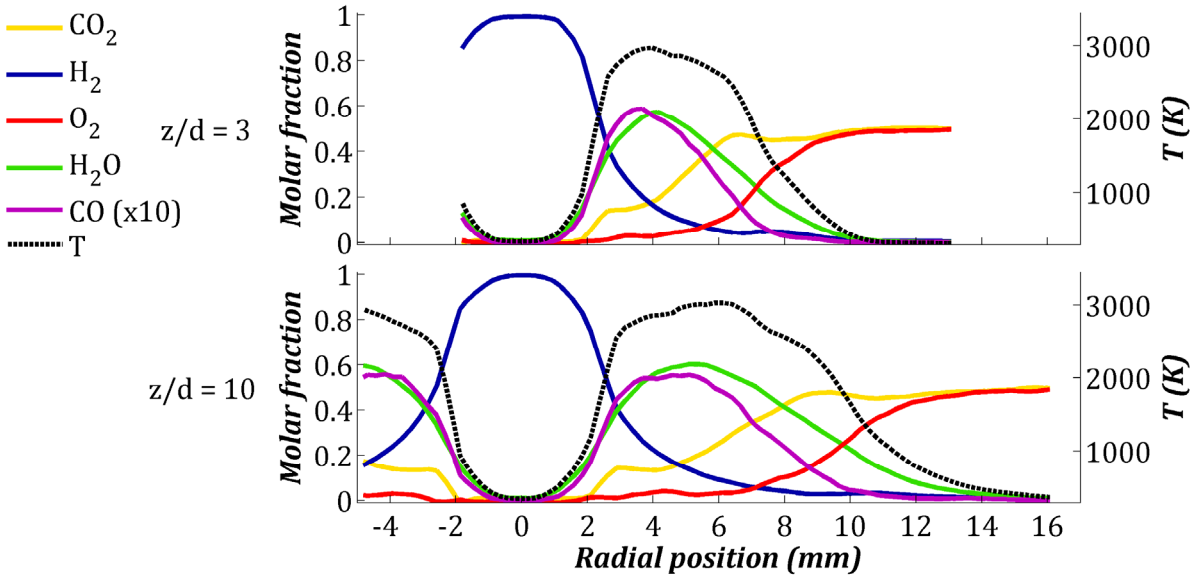

Figure C.5: Reynolds-averaged radial profiles of molar fractions of the main species and temperatures from NP-H_2-OF-5, measured by LRS at different heights above the fuel nozzle.

C.1.6. NP-H_2-OF-6

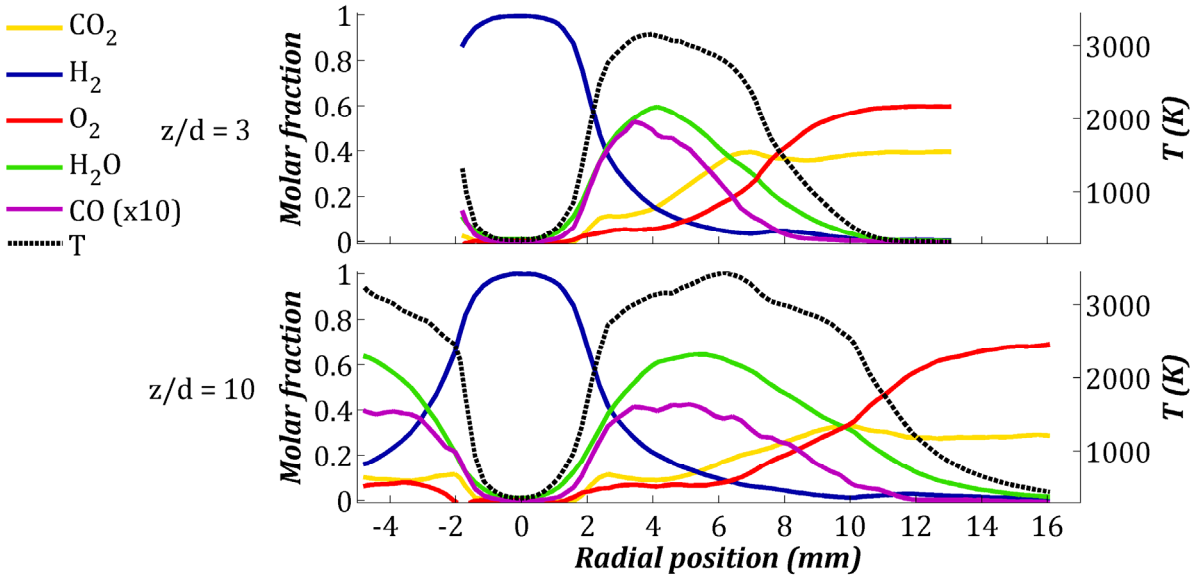

Figure C.6: Reynolds-averaged radial profiles of molar fractions of the main species and temperatures from NP-H_2-OF-6, measured by LRS at different heights above the fuel nozzle.

C.1.7. NP-H_2-OF-7

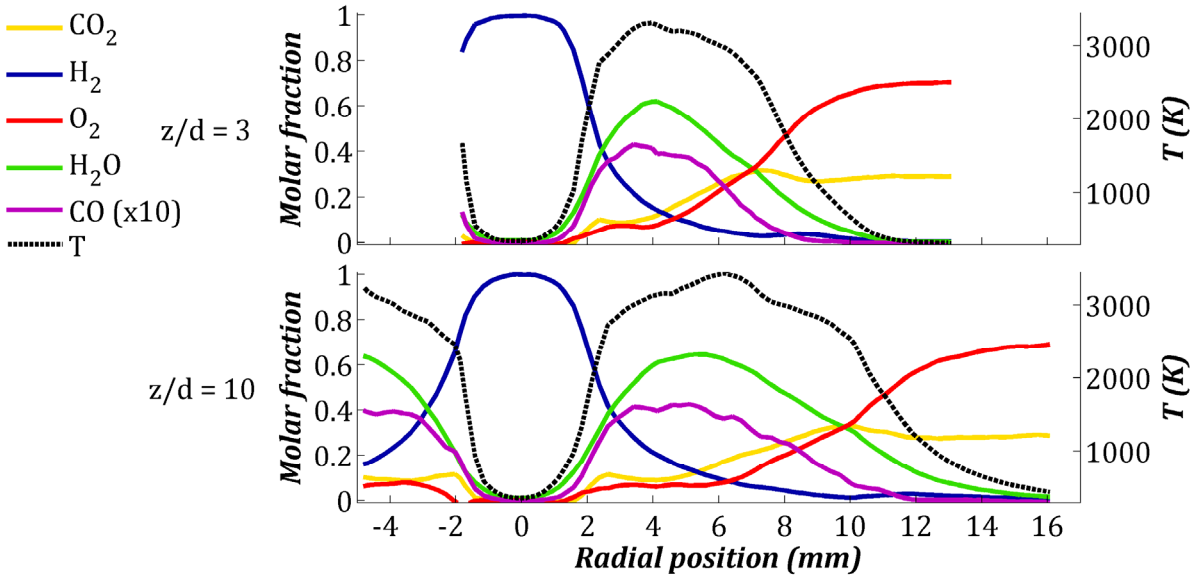

Figure C.7: Reynolds-averaged radial profiles of molar fractions of the main species and temperatures from NP-H_2-OF-7, measured by LRS at different heights above the fuel nozzle.

C.2. Scatter plots in mixture fraction space

The scatter plots of the temperature and the molar fractions of H_2, O_2, H_2O, CO_2 and CO are displayed in mixture fraction space at two different heights above the fuel nozzle. Other axial locations are not displayed since they present very similar trends to those shown here.

C.2.1. NP-H_2-OF-1

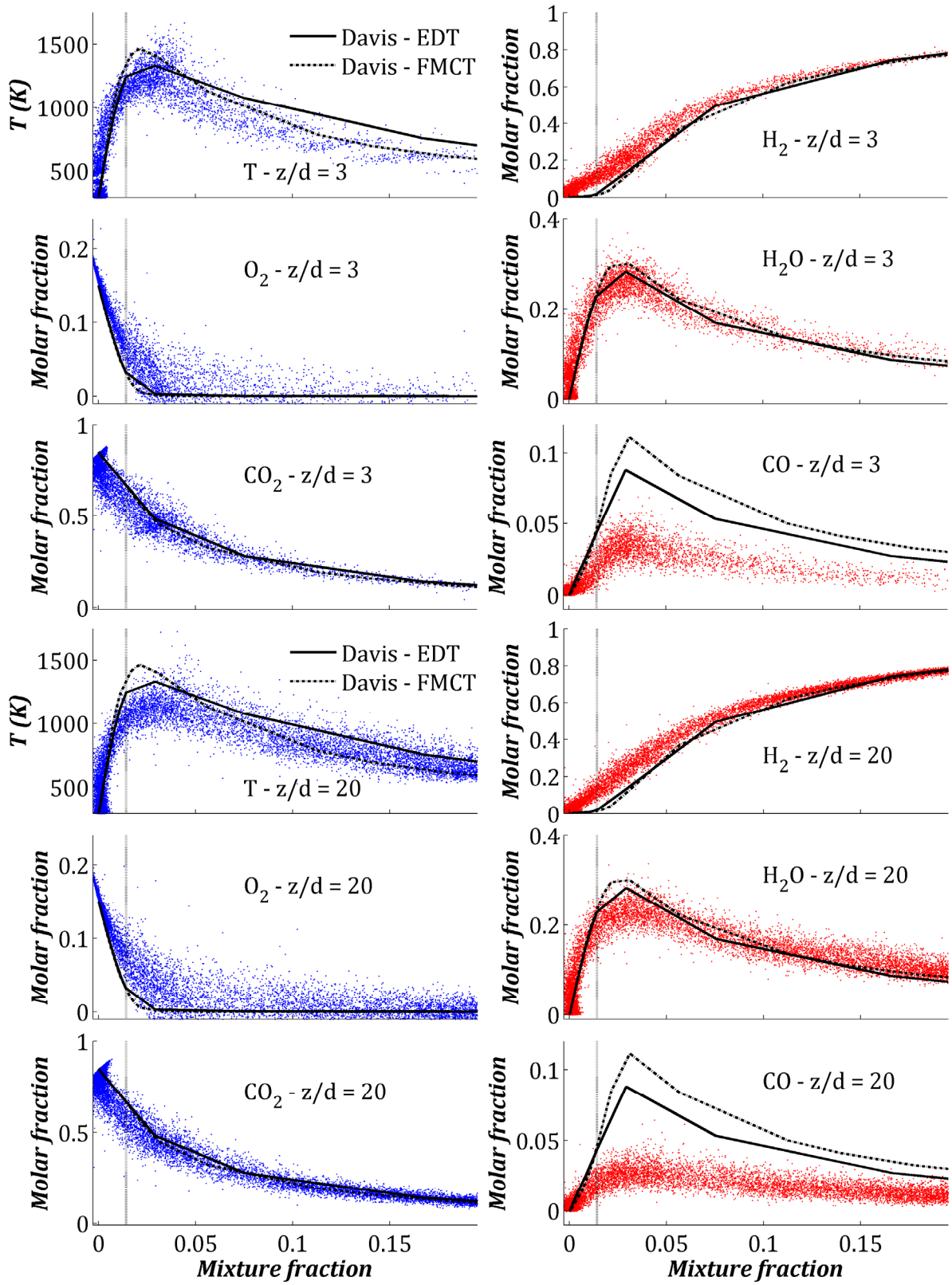

Figure C.8: Scatter plots in mixture fraction from NP-H_2-OF-1, measured by LRS at different heights above the fuel nozzle.

C.2.2. NP-H_2-OF-2

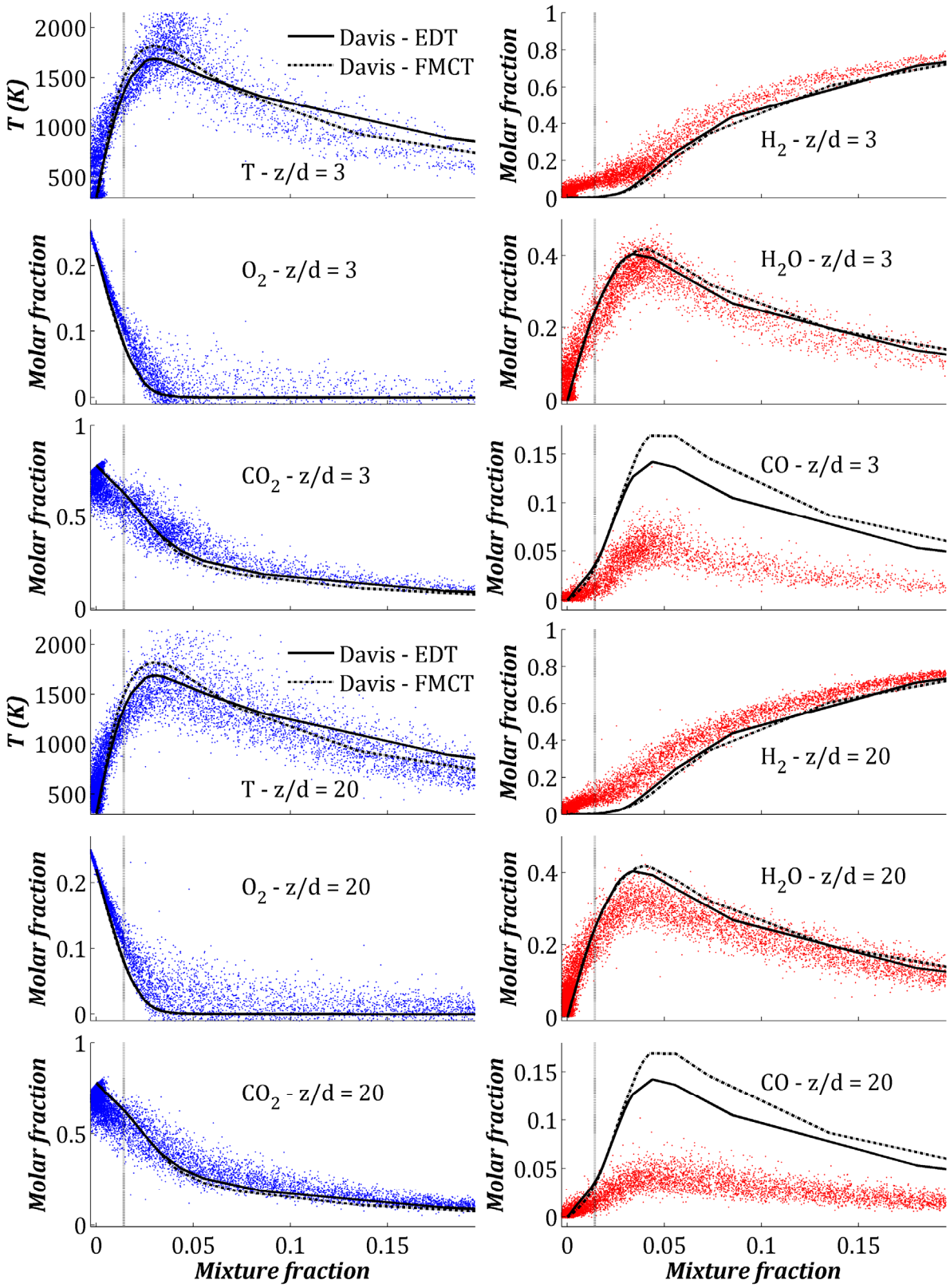

Figure C.9: Scatter plots in mixture fraction from NP-H_2-OF-2, measured by LRS at different heights above the fuel nozzle.

C.2.3. NP-H_2-OF-3

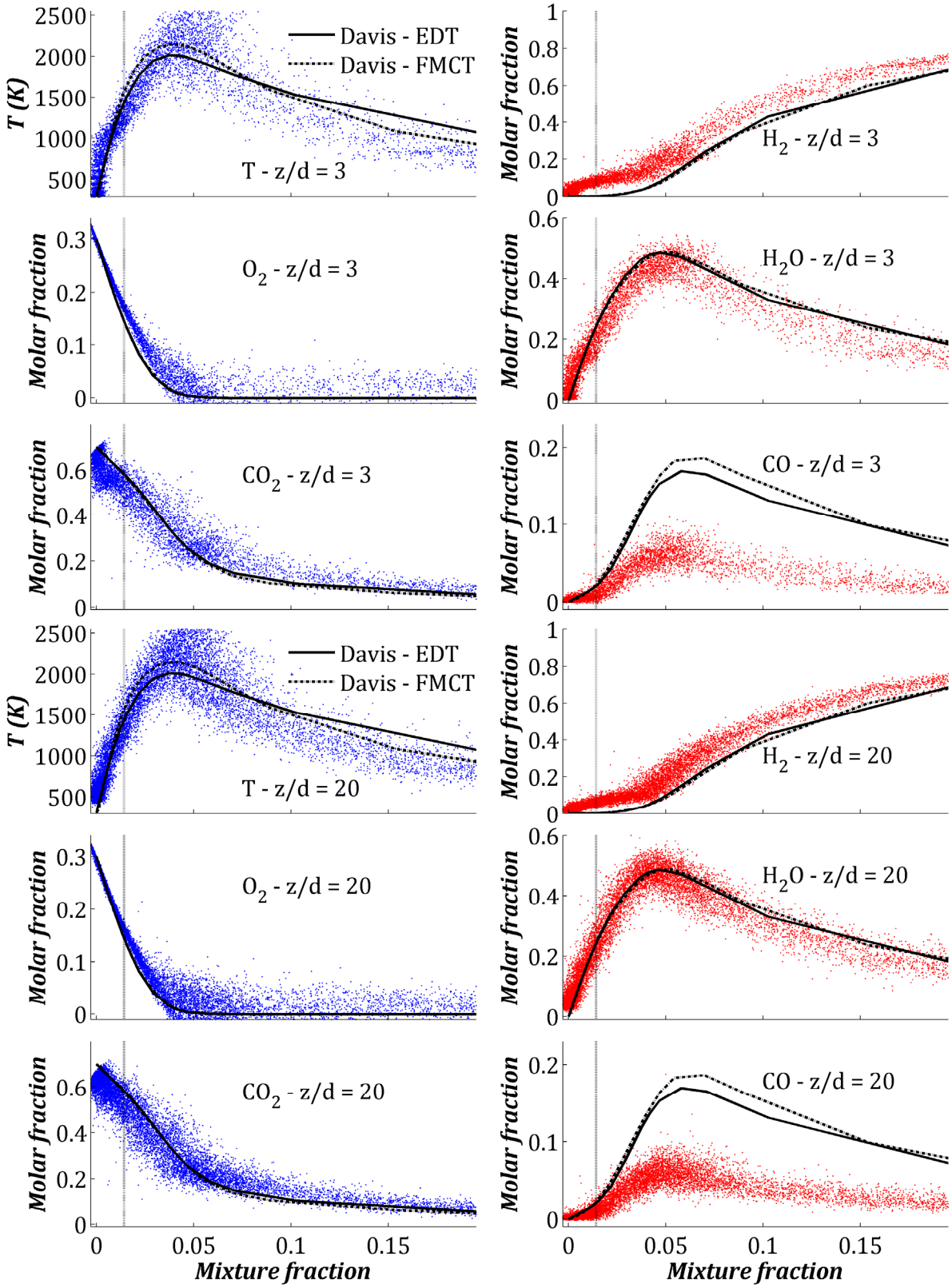

Figure C.10: Scatter plots in mixture fraction from NP-H_2-OF-3, measured by LRS at different heights above the fuel nozzle.

C.2.4. NP-H_2-OF-4

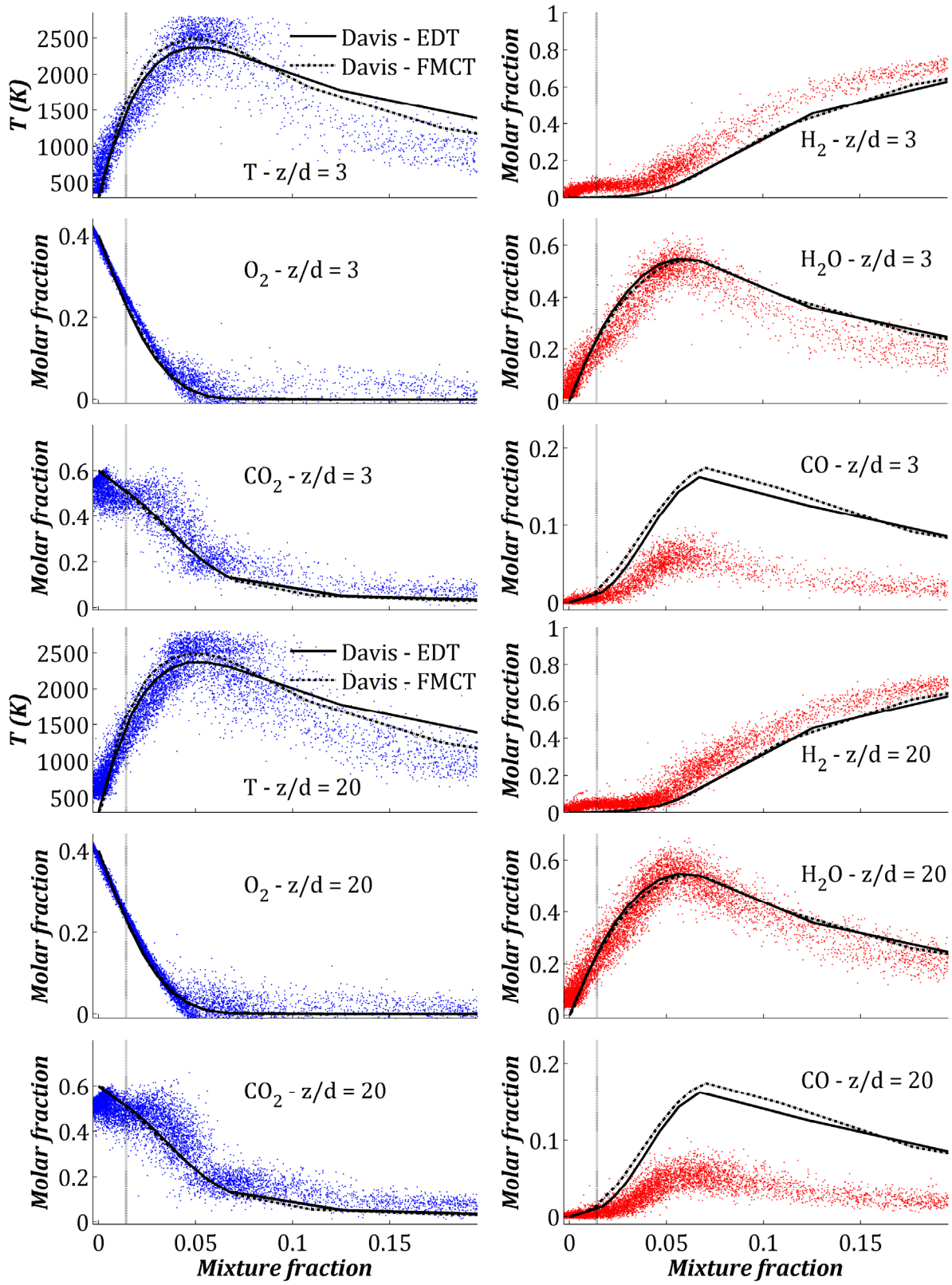

Figure C.11: Scatter plots in mixture fraction from NP-H_2-OF-4, measured by LRS at different heights above the fuel nozzle.

C.2.5. NP-H_2-OF-5

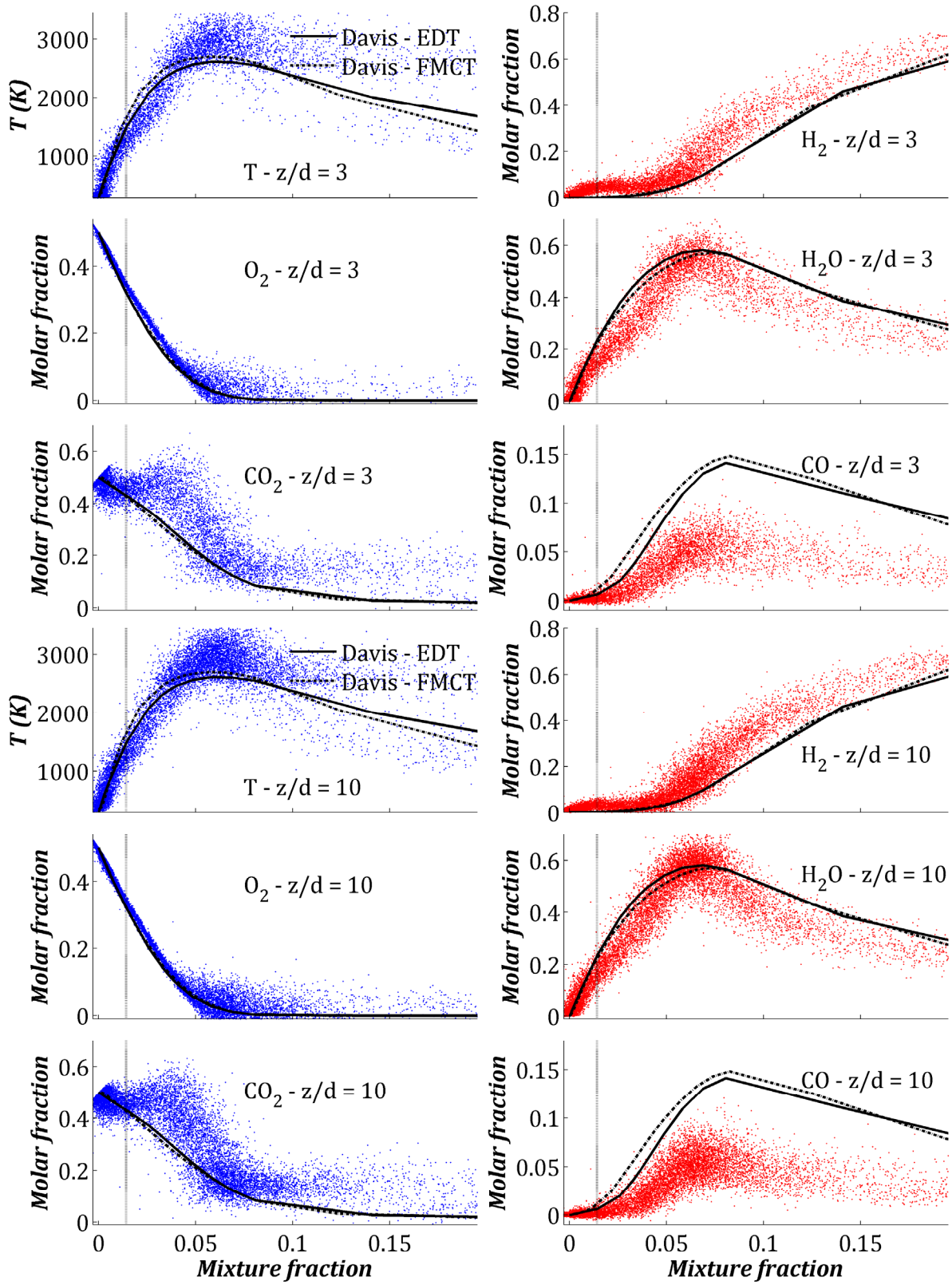

Figure C.12: Scatter plots in mixture fraction from NP-H_2-OF-5, measured by LRS at different heights above the fuel nozzle.

C.2.6. NP-H_2-OF-6

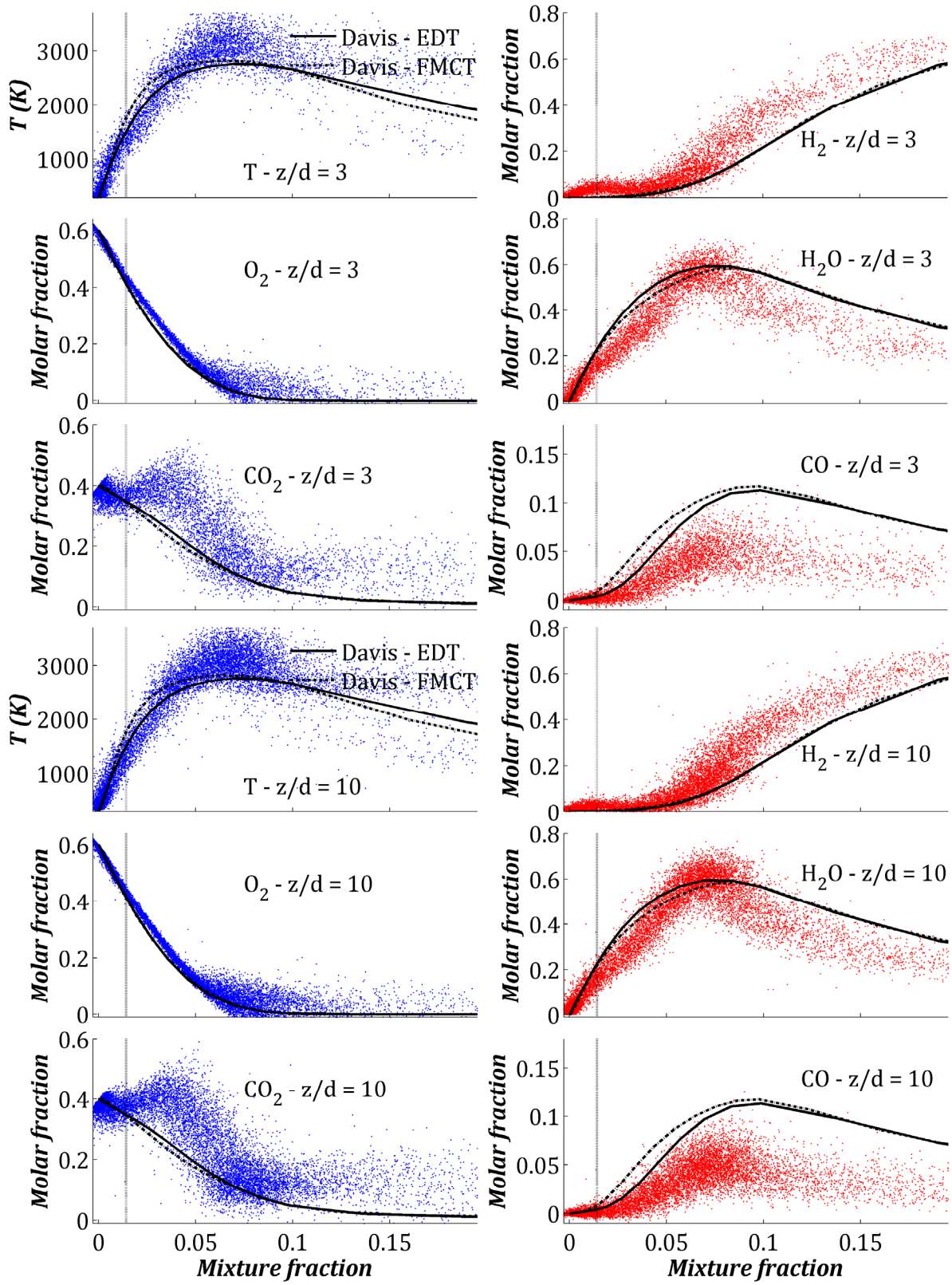

Figure C.13: Scatter plots in mixture fraction from NP-H_2-OF-6, measured by LRS at different heights above the fuel nozzle.

C.2.7. NP-H_2-OF-7

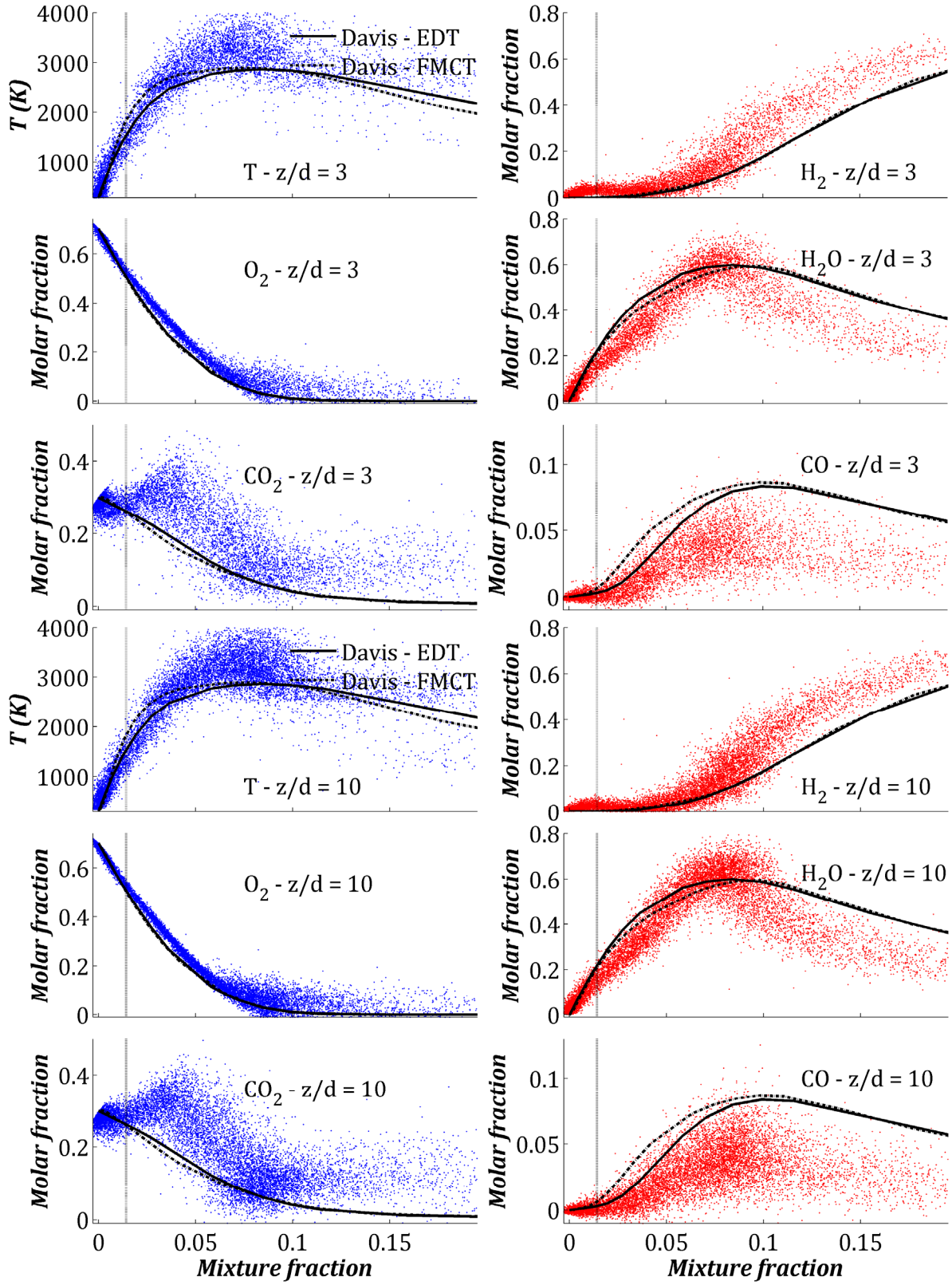

Figure C.14: Scatter plots in mixture fraction from NP-H_2-OF-7, measured by LRS at different heights above the fuel nozzle.

D. JOURNAL PUBLICATION

On the structure of the near field of oxy-fuel jet flames using Raman/Rayleigh laser diagnostics

Alexis Sevault, Robert S. Barlow, Matthew Dunn and Mario Ditaranto.

In press, to be published in Combustion and Flame.

The following publication is related to the experimental results achieved during a 6-month exchange at the Combustion Research Facility at Sandia National Laboratories (Livermore, CA, USA) (cf. Section 7).

Article history:

Received 12 December 2011
Received in revised form 25 June 2012
Accepted 25 June 2012
Available online 23 July 2012

Please cite this article in press as: A. Sevault et al., Combust. Flame (2012), http://dx.doi.org/10.1016/j.combustflame.2012.06.017

On the Structure of the Near Field of Oxy-Fuel Jet Flames Using Raman/Rayleigh Laser Diagnostics

Alexis Sevault[a], Matthew Dunn[b], Robert S. Barlow[b] and Mario Ditaranto[c]

[a]Energy and Process Engineering Department, Norwegian University of Science & Technology, 7491 Trondheim, Norway.
Corresponding author: E-mail: Alexis.Sevault@sintef.no, Tel: +47 735 93 089.

[b]Combustion Research Facility, Sandia National Laboratories, Livermore, CA 94551-0969, USA.
E-mails: Barlow@sandia.gov, Matthew.Dunn@sydney.edu.au.

[c]Department of Energy Processes, SINTEF Energy Research, 7465 Trondheim, Norway.
E-mail: Mario.Ditaranto@sintef.no.

Please cite this article in press as: A. Sevault et al., Combust. Flame (2012), http://dx.doi.org/10.1016/j.combustflame.2012.06.017

Abstract

An experimental study on turbulent non-premixed jet flames is presented with focus on CO_2-diluted oxy-fuel combustion using a coflow burner. Measurements of local temperatures and concentrations of the main species CO_2, O_2, CO, N_2, CH_4, H_2O and H_2 were achieved using the simultaneous line-imaged Raman/Rayleigh laser diagnostics setup at Sandia National Laboratories. Two series of flames burning mixtures of methane and hydrogen were investigated. In the first series, the hydrogen molar fraction in the fuel was varied from 37 to 55 %, with a constant jet exit Reynolds number Re_{Fuel} of 15,000. In the second series the jet exit Reynolds number was varied from 12,000 to 18,000, while keeping 55 % H_2 molar fraction in the fuel. Besides local temperatures and concentrations, the results revealed insights on the behaviour of localized extinction in the near-field**.** It was observed that the degree of extinction increased as the hydrogen content in fuel was decreased and as the jet Reynolds number was increased. Based on the distribution of the temperature, a fully burning probability index able to quantify the degree of extinction along the streamwise coordinate was defined and applied to the present flame measurements. A comparison of measured conditional mean of mass fractions and laminar flame calculations underlined the significant level of differential diffusion in the near-field that tended to decrease farther downstream. The results also showed high local CO levels induced by the high content of CO_2 in the oxidizer and flame products. A shift of maximum flame temperature was observed toward the rich side of the mixture fraction space, most likely as a consequence of reduced heat release in the presence of product dissociation. Main characteristics of laser Raman scattering measurements in CO_2-diluted oxy-fuel conditions compared to air-diluted conditions are also highlighted. Most data, including scalar fluctuations and conditional statistics are available upon request.

Keywords

Oxy-fuel, jet flame, CO_2-diluted, localized extinction, Raman, differential diffusion.

1. Introduction

Due to climate change and favourable policies aiming at reducing carbon dioxide emissions, carbon capture and storage (CCS) technologies are seen as an effective panel of solutions for a transition between today's mostly combustion-based energy production, generating undesirable emissions, and tomorrow's energy production mostly based on renewables. Based on the great advance in oxygen separation technologies, which leads to reduced costs and the absence of post-combustion constraints, oxy-fuel combustion stands for a potentially efficient solution among the available CCS processes. Bolland et al. [1, 2] and Tan et al. [3] studied the design of oxy-fuel gas turbines fired with natural gas as a CO_2 removal option. The authors concluded that using partial flue gas recirculation offers a great potential for short-term feasibility and provides better operating conditions for the CO_2 scrubber performance compared to a plant equipped with a CO_2 scrubber without recirculation. Using O_2/CO_2 mixtures instead of air for fuel combustion ideally results in exhaust gases composed of water, which can be easily separated by condensation, and relatively pure carbon dioxide that can be captured, used in the semi-closed power cycle, and stored.
An advantage of this technology is its potential to reduce nitric oxides (NO_x) emissions. Ditaranto et al. [4-6] investigated NO_x emissions from oxy-fuel flames without CO_2 dilution, as it is used in glass melting industry for instance. The authors observed that NO_x emissions are especially influenced by air leaks and residual N_2 present in either natural gas or oxygen stream. Indeed, small amounts of N_2 can lead to significant NO_x emissions due to the high-temperature characteristic of oxy-fuel flames and the induced predominance of the thermal mechanism. However, if CO_2 dilution is considered, flame temperatures can be significantly reduced and NO_x emissions are expected to be lower than in air-diluted conditions [7].

The heat transfer properties of CO_2 are radically different from those of N_2. Consequently, as Ditaranto et al. [8] observed, CO_2 molecules radiate much more than N_2 molecules and tend to locally quench the chemical reaction. It has been seen in different studies [8, 9] that the molar percentage of oxygen in the oxidant should be around 30 % to reach air flame like stability, depending on the mixing process. In the present study, the oxygen molar fraction is set to 32 % in the oxidizer mixture. It has been observed that turbulent jet flames barely sustain with less than 30 % oxygen using a coflow burner. However, optimizing the mixing enables to stabilize turbulent flames with lower oxygen content in the oxidizer. For instance, Kutne et al. [10] stabilized oxy-fuel flames with contents as low as 20 % oxygen in the oxidizer by using swirl and partial premixing. The choice of using a coflow in the present study has been motivated

by the interest in observing how the turbulent mixing is characterized in CO_2-diluted oxy-fuel flames.

Another phenomenon that may affect the flame structure is differential diffusion, which is especially likely to happen with high H_2 content in the fuel, though its magnitude in jet flames may progressively decrease as the Reynolds number and streamwise distance increase [11-13]. Computational codes do not necessarily take differential diffusion into account since they are most likely industry-oriented, where Reynolds numbers are much higher than at laboratory scale. Since one purpose of the present experiments is to provide data for validation of computational codes, the Reynolds numbers have been set to the highest achievable values in the laboratory conditions to minimize the effect of this phenomenon.

Besides limiting the flames series to stabilized conditions on a simple jet burner, laser Raman/Rayleigh scattering technique restricted the study to non-sooting flames, at least over most of their length. Indeed, hydrocarbon fluorescence from fuel-rich zones, where soot is likely to form locally, considerably affects Raman signals. The local soot level is very sensitive to the oxygen content in the oxidizer, as observed in previous studies on combustion in oxygen-enriched oxidizers [14, 15]. In the present case, due to the high H_2 content in the fuel, the level of fluorescence interferences coming from soot formation was at an acceptable level so that the Raman and Rayleigh signals could be confidently corrected.

2. Specific Objectives

Literature regarding CO_2-diluted oxy-fuel flame structure and composition is scarce. The objectives of this study were to investigate the detailed scalar structure of CO_2-diluted oxy-fuel jet flames, exhibiting strong effects of turbulence chemistry interaction, and thereby provide new insights and data that may be used for improvement or validation of combustion models. Another purpose was to highlight the main particularities of using laser Raman scattering technique in CO_2-diluted oxy-fuel flames compared to air-diluted conditions.

Five flames were investigated in order to parametrically determine the effects of fuel composition (CH_4/H_2 molar fraction) and jet exit Reynolds number on the degree of localized extinction measured in the flame. Localized extinctions have been recently studied by Barlow et al. [16] in piloted jet flames of CH_4/H_2/air, in comparable conditions. Accurate prediction of localized extinction is recognized as an important test of turbulent combustion models [17].

Two series of three flames were investigated (one flame is common to both series). Both series had a molar percentage of O_2 in the oxidizer of 32 %, based on

volumetric flow rates of the fuel and the CO_2/O_2 coflow. In the A-series, the molar percentage of H_2 in the fuel was varied from 37 to 55 % with a constant jet Reynolds number Re_{Fuel} = 15,000. In the B-series, Re_{Fuel} was varied from 12,000 to 18,000 with a molar content of 55 % H_2 in the fuel. The coflow temperature was kept at 294 K for each flame. Details are shown in Table 1.

Table 1. CO_2-diluted oxy-fuel jet flames properties.

Name	*$\%_{mol}$ H_2 in fuel*	*Re_{Fuel}*	*Jet speed (m/s)*	*Coflow speed (m/s)*	*Stoichiometric mixture fraction*	*Adiabatic temperature at stoichiometry (K)*
A-1	55	15,000	98.2	0.778	0.0535	2250
A-2	45	15,000	84.5	0.755	0.0553	2243
A-3	37	15,000	75.8	0.739	0.0565	2236
B-1	55	12,000	78.6	0.622	0.0535	2250
B-2	55	15,000	98.2	0.778	0.0535	2250
B-3	55	18,000	117.8	0.933	0.0535	2250

3. Experimental Setup

Measurements were performed using the simultaneous line imaging of Raman/Rayleigh scattering developed at Sandia National Laboratories. Details of the hardware configuration can be found in [18]. The setup enabled measurements of single-shot profiles of temperature and the mass fractions of all major species (CO_2, O_2, CO, N_2, CH_4, H_2O and H_2). The spatial resolution was 0.104 mm along a ~6 mm section of the focused beam. The total energy in the test section for the Raman/Rayleigh measurements was 1 J/pulse at 532 nm with an overall pulse duration of ~400 ns obtained from combining three frequency-doubled Nd:YAG laser pulses. Due to the high level of radiation emitted by CO_2 within the flames, heat-sensitive devices close to the flame were protected by reflective aluminium foil. The large collection lens in front of the Raman/Rayleigh setup was shielded by a 150-mm square, 1-mm thick window of infrared absorbing filter glass (Schott KG2).

The fuel nozzle was 5-mm inside diameter with 0.5 mm wall thickness and squared-off end, which helped to stabilize attached flames. The fuel nozzle was surrounded by a laminar coflow of 96.5 mm inside diameter. Thanks to the H_2 content in the fuel, the flame remained attached to the fuel nozzle. The nozzle had its tip 40 mm above the coflow and was long enough so that when the fuel mixture reached the nozzle tip the flow was considered fully developed. The oxidizer mixture first flowed through a series of perforated plates and then through a honeycomb to allow a uniform flow distribution. The burner was mounted at the top of a 25 cm x 25 cm square-section wind tunnel from where fresh air was flowing at 0.5 m/s to accompany the flow of

interest and prevent early mixing with ambient air. The setup allowed measurements from 1 to 20 diameters above the nozzle with no mixing with ambient air, and thus, no intrusion of nitrogen within the probe volume. Consequently, no combustion chamber was required for measurements in the near-field, which was most important for the present investigation of localized extinction in these flames.

The jet flames were axisymmetric, so radial profiles were measured from the central axis to the pure oxidizer region, to ensure capturing the full reaction zone. To obtain the profiles, the 6-mm probe was translated by steps of 3 mm, with a minimum of 500 shots systematically acquired for each step. When crossing the reaction zone, as many as 1500 shots were recorded to improve the quality of the data.

The calibration and data processing method used for laser Raman scattering was the recently developed hybrid method described in [19]. The method is based on the Ramses spectral simulation code [20], which generates Raman spectral libraries for the major species over temperatures ranging from 290 K to 2500 K, for optically well characterized detection setups. Coupled with a short series of calibration measurements (practically one per species), the main calibration coefficients required to process the Raman data can be known by integrating the spectral libraries over regions corresponding to the on-chip binning. However, not everything was solved by the Ramses code. Since the code is based on quantum mechanical models, reliable spectra simulations for methane, for instance, are not available over the whole temperature range of interest. Thus, the remaining calibration coefficients still had to be found through direct measurements over a large temperature range. For example, the temperature dependent calibration curves for CH_4 Raman response and CH_4 crosstalk onto other species were determined from measurements of an electrically heated CH_4/N_2 mixture between room temperature and about 950 K. Extrapolation to flame temperatures was tested by comparing measurements and Chemkin calculations of laminar partially premixed CH_4/air jets flames and opposed flow flames [11].

CO mass fraction could locally reach up to 0.18 in these oxy-fuel flames, and there is no crosstalk from N_2 onto the CO Raman channel in these flames, which are free of N_2. Consequently, CO-Raman measurements are of better quality in the present flames than in typical CH_4/air flames and are reported here in favour of the CO-LIF measurements. Additionally, measurements of pure cold CO were added to the calibration procedure to improve the accuracy of the calibration. The CO Raman response at higher temperature was calculated from Ramses libraries [19, 20] in reference to the cold calibration. In air-diluted flames, the CO-LIF measurements are used in favour of the CO-Raman measurements, and the CO calibration is done in a fuel-rich, premixed laminar flame in order to minimize uncertainty in the effects of collisional quenching.

Signals were corrected for CCD background, flat field, total Nd:YAG laser energy, interferences from laser induced fluorescence in Raman signals, broadband flame luminosity, beam steering through flames, and bowing effect through Raman optics [19]. Data were filtered for sparks and dusts particles altering Rayleigh and Raman signals, although such events were rare since in-line particle filters had been installed along the critical gas lines.

Table 2 lists the uncertainties calculated from laminar premixed CH_4/air flat flames, based on the standard deviation (precision) and the estimated accuracy of averaged measurements. The standard deviation is mostly higher than in [18], due to the lower laser energy (approximately 1 J/pulse instead of 1.8 J/pulse, limited by the availability of only three of four lasers and the need to avoid optical breakdown in the coflow mixture) and to about 15 % transmission loss through the Schott KG2 glass filter. The estimated accuracy is mostly the same as in [18], except for CO and H_2, whose Raman calibration is based on pure gas measurements at ambient temperature, leading to better accuracy. In non-premixed oxy-fuel flames, accuracy for CO is expected to be better, since CO levels are higher and there is no crosstalk from N_2, though this positive effect may be locally balanced by interferences from laser induced fluorescence (cf. Section 4.5). The accuracy at low temperatures for the reactants from the oxy-fuel flames is also expected to be better, since they are calibrated with pure gas measurements at ambient temperature. However, relative uncertainties in the mean values increase for all reactive species as their mass fractions decrease. All flows were measured using mass flow controllers which were calibrated (within 1 % of reading) against laminar flow elements. The mixture fraction was calculated from the measured mass fractions using the Bilger formulation [21]. The measurement limits are discussed in Sections 4.5 and 4.6, in the context of the reported results.

Table 2. Representative uncertainties of scalar measurements at flame conditions

Scalar	***Standard deviation (%)***	***Accuracy (%)***	***Premixed flame***
T	1.3	2	Φ = 0.97, T = 2185 K
N_2	1.1	2	Φ = 0.97, T = 2185 K
CO_2	4.5	4	Φ = 0.97, T = 2185 K
H_2O	4.1	3	Φ = 0.97, T = 2185 K
Φ	3.1	5	Φ = 0.97, T = 2185 K
CO	6.7	8	Φ = 1.28, T = 2045 K
H_2	9.2	8	Φ = 1.28, T = 2045 K

4. Results and Discussion

Most of the following analysis will deal with the progression of the flame structure in the A- and B-series of flames, and will rely on the analysis of Favre-averaged radial profiles of selected mass fractions, measured conditional scalar statistics in mixture fraction space, and results from laminar diffusion flame calculations. First, the focus will be set on the evolution of the localized extinction, followed by an investigation on the influence of differential diffusion. Then, the CO measurements and the shift of the maximum flame temperature from stoichiometry will be commented. Lastly, the measurement limits and the main particularities seen for CO_2-diluted oxy-fuel flames compared to air-diluted flames while using Raman/Rayleigh laser diagnostics will be discussed.

4.1. Localized extinction

Localized extinction occurs when turbulent mixing rates become competitive with critical rates of chemical reactions. The phenomenon induces local temperature drops due to increasing heat removal rates from convection and diffusion along with decreasing chemical reaction rates [22].

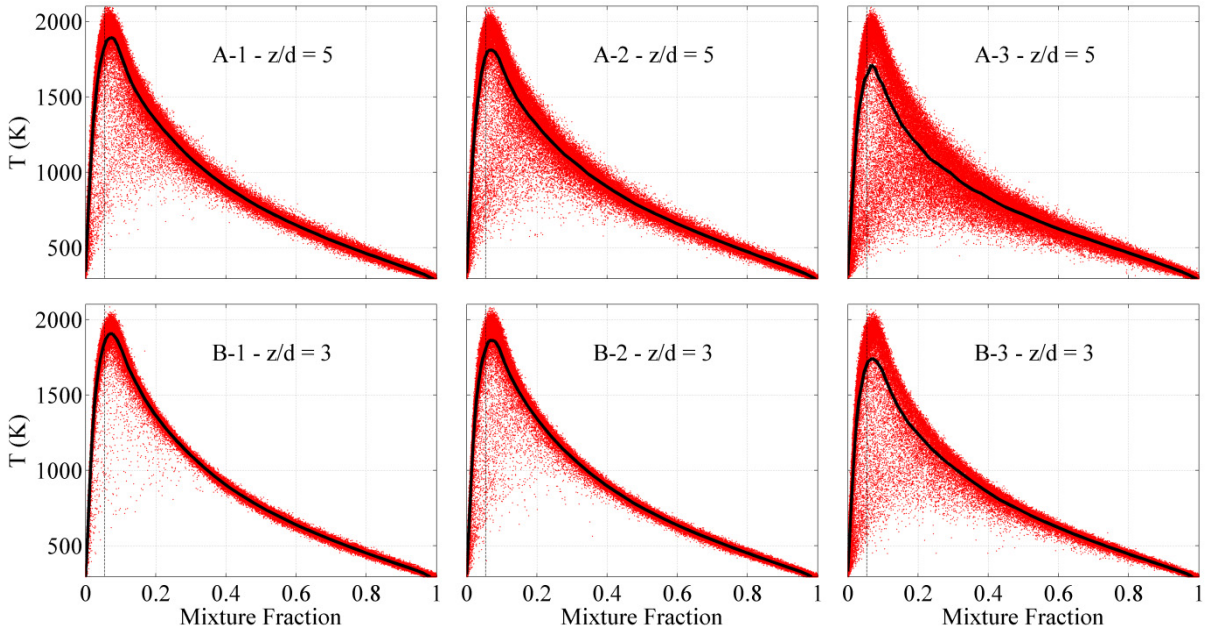

Fig. 1. Scatter plots of Rayleigh temperature at z/d = 5 for A-series and at z/d = 3 for B-series. The conditional mean temperature is plotted with a solid line. The stoichiometric mixture fraction is marked by a vertical dashed line.

Scattered plots of Rayleigh temperature versus mixture fraction for both flame series are shown in Fig. 1. Each dot represents the result of a single-shot measurement

from various locations along the radial axis. Dots scattered below the narrow, dense band of temperature indicate localized extinction. Barlow et al. [16] reported that extinction roughly took place around four diameters above the nozzle within the CH_4/H_2/air flames that were studied. Similarly, extinction tended to happen within this area in the present flame series. The probability of localized extinction gradually increased by lowering the H_2 content in fuel as seen with the A-series or by increasing Re_{Fuel} as seen with the B-series. This result was expected, as lowering the H_2 content in fuel decreases the chemical reaction rate, and increasing Re_{Fuel} increases the mean scalar dissipation rate, both rates being essential in the localized extinction mechanism.

Figure 1 shows that the samples deviating from the narrow band of temperature were especially located between 600 and 1700 K and the evolution of probability of localized extinction did not significantly affect the behaviour of the narrow band of temperature, representing fully reacting states or flamelets. The conditional mean of temperature, shown by the black solid lines, decreased only moderately for the observed levels of localized extinction.

Figure 2 shows pictures of the two series of turbulent jet flames, taken using a very low exposure time to help reveal patterns from the flame structure. Flames A-1 and B-1 visually appeared to be fully burning even though they displayed in Fig. 1 a non-negligible number of samples deviating from the narrow band of temperature. During the preliminary phase of defining the flame conditions, H_2 molar fraction of 60 % in fuel was tested and displayed even fewer samples out of the narrow band of temperature (not shown here), as expected since H_2 considerably improves the local stability of flames by increasing the chemical reaction rate.

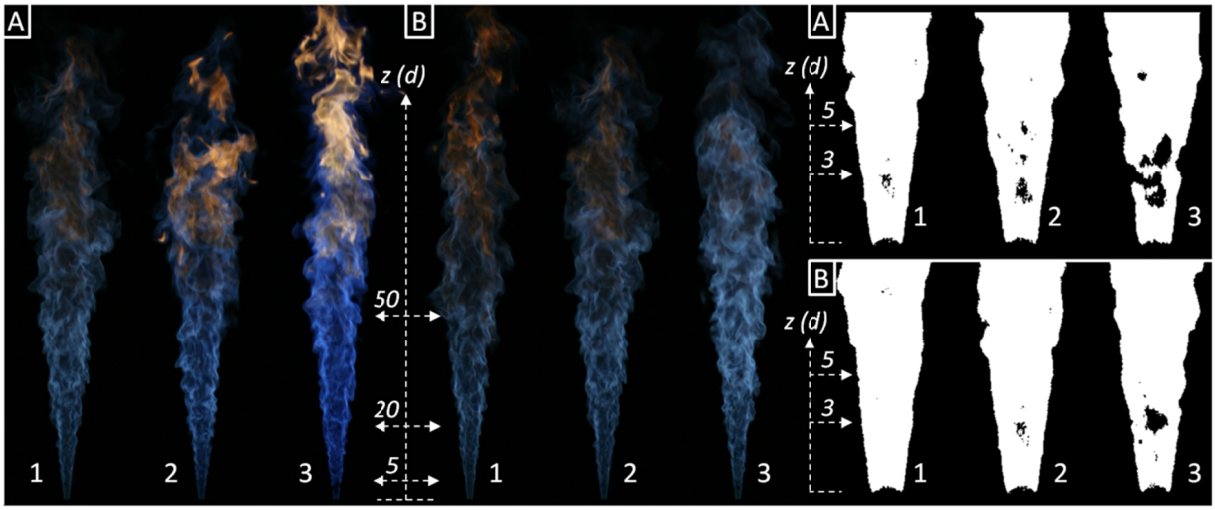

Fig. 2. Pictures of A-series flames (left), B-series flames (centre) and close-ups from the region of localized extinction for A-series (top-right) and B-series (bottom-right). Close-ups were post-processed by applying a threshold to highlight the localized extinction. Exposure time: 1/2500 s, ISO: 1600.

A chosen sample of flame pictures was binarized with a fixed threshold and allowed enhanced visualization of the localized extinction as areas of reduced visible luminosity (see Fig. 2, right). The shape and exact location were constantly changing, though the phenomenon tended to systematically appear between 3 and 5 diameters above the nozzle. Localized extinction events appeared very intense on Flame A-3, as shown in Fig. 2 (top-right). Note that, for a given flame, effects from localized extinction do not necessarily appear on every picture as clear as in the chosen sample, notably due to the line of sight visualization, though the chosen sample is quite representative.

By lowering the H_2 molar fraction in fuel below 37 %, localized extinction systematically became more frequent, leading to lift-off or flame blow-off. Similarly, increasing further Re_{Fuel} up to around 20,000 also lead to lift-off and instabilities. These conditions were certainly the threshold of the unbalanced competition between heat removal rate and chemical reaction rate.

Results from Raman/Rayleigh diagnostics brought systematic and reliable information. The conditional means of mass fraction for CO, H_2, O_2 and H_2O are plotted with the mixture fraction in Fig. 3 for both flame series, at three different axial positions, intercepting the region of localized extinction. Similarly, the Favre-averaged mass fractions of CO, H_2, O_2 and H_2O are plotted with the radial position in Fig. 4. Note that, measurements performed at 1 diameter above the nozzle revealed mass fraction profiles very similar for each series and thus, are not shown here. By looking at O_2 mass fraction at 3 or 5 diameters above the fuel nozzle in Fig. 3 and 4, it can be seen on the fuel-rich side that unburnt oxidizer penetrated into the fuel-rich part of the jet, with lower H_2 content in fuel or higher Re_{Fuel}. This was a direct consequence of localized extinction, which seemed to vanish out farther downstream.

In Fig. 3 and 4, the levels of H_2O and CO gradually decreased around the localized extinction zone, respectively with decreasing the H_2 content in fuel in the A-series, and with increasing the jet Reynolds number in the B-series. This variation was mostly induced by the increase of O_2 mass fraction in the reaction zone. However, this was slightly more intense in the A-series and could be explained by the variation of fuel composition, coupled with lower jet exit speeds. Farther downstream, far from the localized extinction, the decreased levels in H_2O and CO were still visible for the A-series. A slight increase in CO_2 mass fraction was also found but is not shown here. For the B-series, fuel and oxidizer compositions are the same for each flame, only the jet and coflow speeds were varied.

In Fig. 3 and 4, the root-mean square (RMS) fluctuations of CO mass fractions for Flame A-1 and B-1 are shown by grey areas. They enable to see the significant amplitude of the local fluctuations, which are mainly due to turbulent intensity. However, for Flame A-1, effects of localized extinction may have contributed to the amplitude of the RMS fluctuations, which appears larger than for Flame B-1.

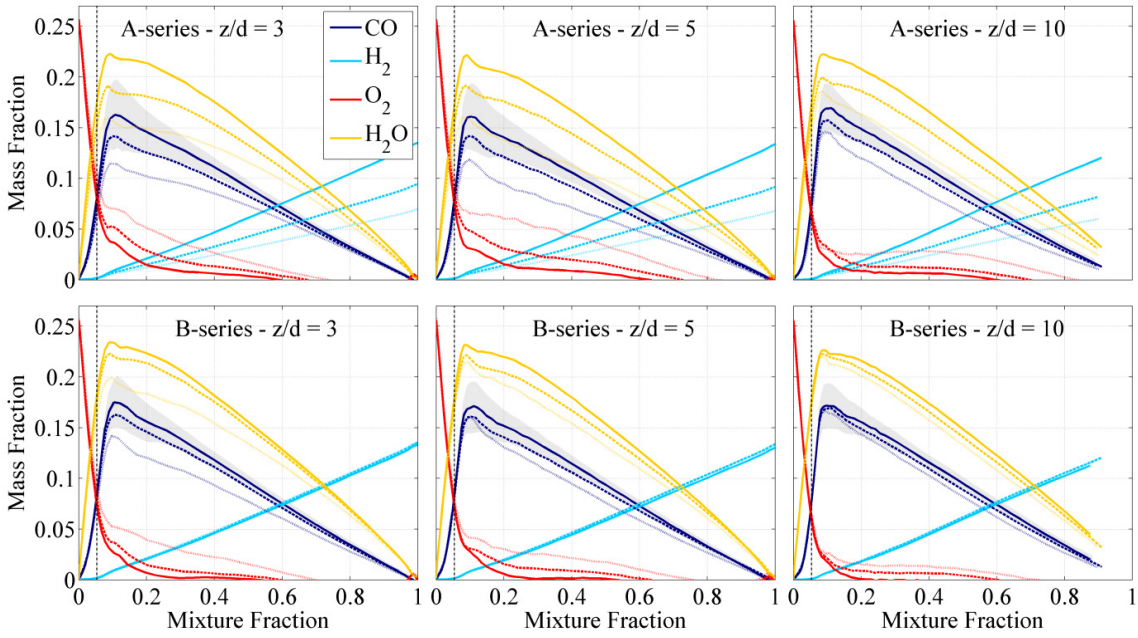

Fig. 3. Conditional means for CO, H_2, O_2 and H_2O mass fractions for both A- and B-series at z/d = 3, 5 and 10. Flames A-1 and B-1 are shown with solid lines, A-2 and B-2 with dashed lines, and A-3 and B-3 with dotted lines. The stoichiometric mixture fraction is marked by a dashed line. The grey area represents the conditional RMS fluctuations for CO mass fraction corresponding to Flames A-1 and B-1.

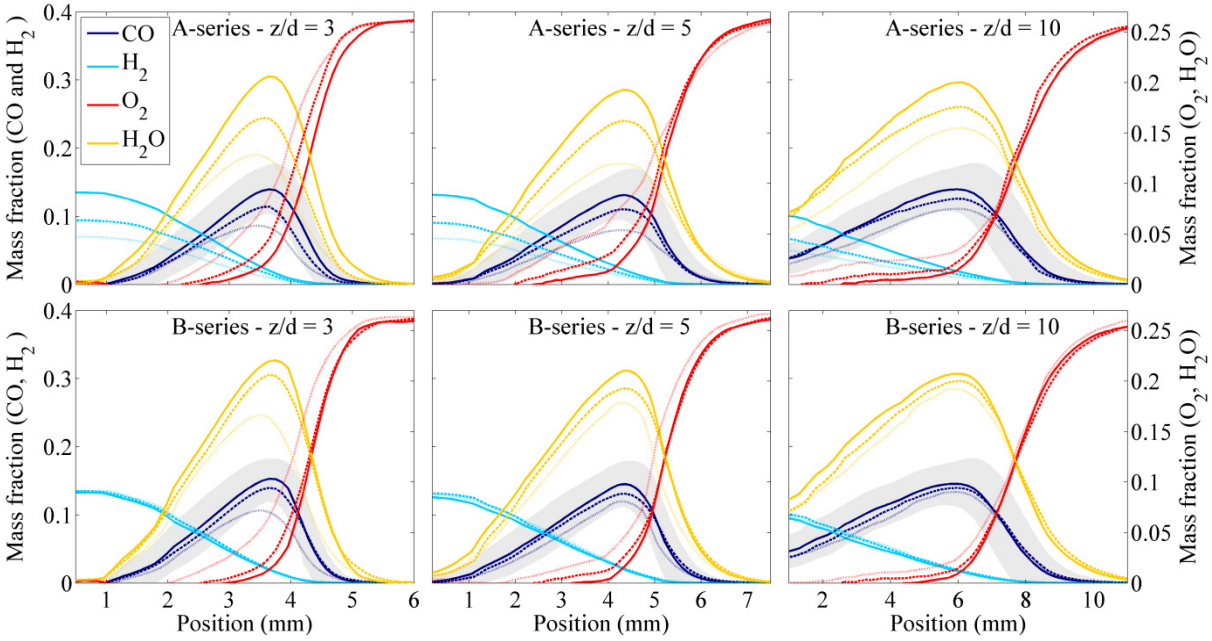

Fig. 4. Favre-averaged radial profiles for CO, H_2, O_2 and H_2O mass fractions for both A- and B-series at z/d = 3, 5 and 10. Flames A-1 and B-1 are shown with solid lines, A-2 and B-2 with dashed lines, and A-3 and B-3 with dotted lines. The grey area represents the RMS fluctuations (according to the Favre decomposition) for CO mass fraction corresponding to Flames A-1 and B-1.

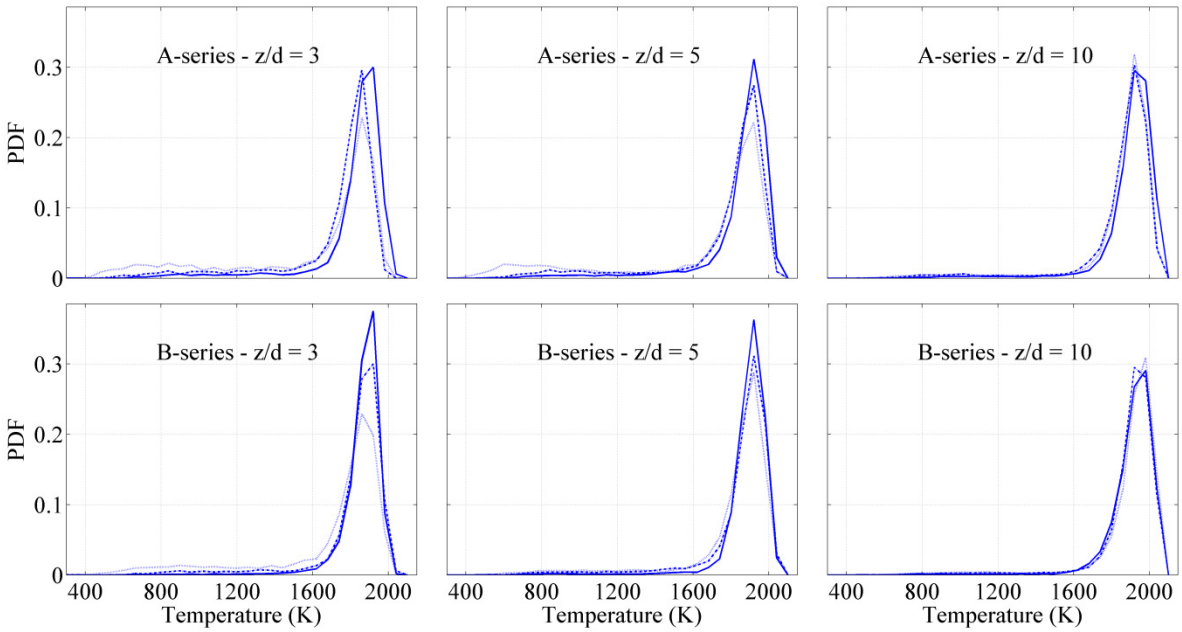

Fig. 5. PDF of the temperature within a narrow band in mixture fraction (total width 2 Δ = 0.04) centred on the locus of maximum temperature for both A- and B-series at z/d = 3, 5 and 10. Flames A-1 and B-1 are shown with solid lines, A-2 and B-2 with dashed lines, and A-3 and B-3 with dotted lines.

Figure 5 shows the probability density function (PDF) of the temperature for both flame series at 3, 5 and 10 diameters above the nozzle. The PDF of the temperature is calculated for each profile only on a narrow band, 2Δ, of mixture fraction centred on the locus of maximum temperature. In the present study, Δ is chosen equal to 0.02 to include a representative number of temperature measurements in the PDF calculation. The number of temperature measurements used for the PDF is about the same for each flame at a given axial location, from about 6000 measurements at z/d = 3 to about 13,000 at z/d = 10. Within each plot, only one parameter is varied: hydrogen content in the fuel for the A-series and jet Reynolds number in the B-series. In addition, the adiabatic flame temperature is similar from one flame to another. Thus, any variation of the PDF of the temperature for a given axial location can be mostly attributed to a variation of the degree of localized extinction inducing local temperature drops. At 10 diameters above the nozzle, above the region of localized extinction, all flames display very similar profiles of PDF of the temperature. At 3 and 5 diameters above the nozzle, lower and higher temperatures can be clearly distinguished into two zones. Higher temperatures correspond to the fully burning mixtures and systematically display a peak. For the A-series, the PDF of the temperature within this range decreases with the H_2 content in the fuel. For the B-series, the same trend can be observed while increasing the jet Reynolds number, though it is clearer at 5 diameters above the nozzle than at 3 diameters. The decreased contribution from the higher temperatures is balanced by an increased contribution from the lower temperatures, and especially from the very low temperatures, suggesting an increased content in fresh gases. These observations can

be correlated to the corresponding higher presence of oxygen and lower presence of flame products in the flame region, as seen in Fig. 3 and 4.

One further way to quantify the degree of localized extinction is to define a fully burning probability (*FBP*), based on the same definition of the PDF of the temperature above. FBP is calculated as the PDF within a 2Δ narrow band of mixture fraction centred on locus of maximum temperature, corresponding to the temperatures above a threshold temperature, T_{lim}, and plotted with the measured axial locations (see Fig. 6). T_{lim} should be reasonable, well below the calculated adiabatic temperatures (~2250 K for all the present flames) and still relatively high. As seen in Fig. 5, T_{lim} = 1700 K appears as a good trade-off to capture localized extinction effects on temperature within the present flames.

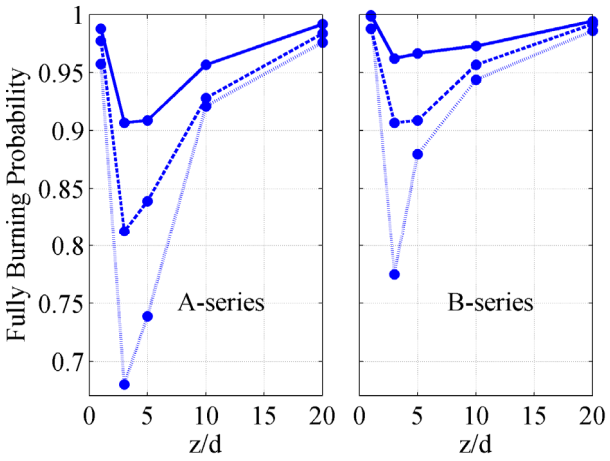

Fig. 6. Fully burning probability plotted with axial location for both flame series, based on the PDF of the temperatures above T_{lim} = 1700 K, within a narrow band in mixture fraction (total width 2Δ = 0.04) centred on the locus of maximum temperature. A-1 and B-1 are shown with solid lines, A-2 and B-2 with dashed lines, and A-3 and B-3 with dotted lines.

FBP is equal to 1 when all measured temperatures from the sample are above T_{Lim}, thus the sample is considered as in a fully burning state. On the other hand, *FBP* is equal to 0 when those temperatures are all below T_{Lim}, meaning that locally, the flame is supposedly close to blow-off. A flame showing an axial profile with constant *FBP* equal to 1 would be considered as fully burning over its whole measured length.

It can be seen in Fig. 6 that, according to the *FPB* criterion, none of the present flames was fully burning, though Flame B-1 was reasonably close. Fig. 6 also shows that localized extinction happened systematically between 1 and 5 diameters above the nozzle and its effect vanished out downstream since all profiles seemed to tend to *FBP* = 1. As expected, Flame A-3 appeared to have the most dramatic *FBP* of the two series. At 1 diameter above the nozzle, the *FBP* criterion gradually decreased for the A-series as the molar fraction of H_2 in the fuel decreased, showing a more dramatic effect on the

very near field than for the B-series. Only a few axial locations have been measured and a finer resolution would be required to draw further conclusions.

Another way to quantify the degree of extinction is to calculate the burning index based on temperature (BI_T). Details and limits about it can be found in the literature [16, 23-25]. BI_T is generally calculated as the ratio of the difference between local instantaneous temperature and room temperature, and the difference between reference temperature and room temperature. For hydrocarbon flames, the reference temperature represents a fully burnt state at a given mixture fraction, and is typically taken a laminar flame calculations at low strain rate from an arbitrary chosen flame composition. BI_T is then usually plotted with the mixture fraction.

FBP has been used in the present study in favour of BI_T since it enables to integrate the whole set of temperature measurements into one comprehensive plot against the streamwise location. It enables to spatially bound the localized extinction zone and to compare its streamwise influence on flames from series of similar composition. However, *FBP* has the disadvantage of being sensitive to two arbitrary-defined parameters and requires a certain number of measurements in the streamwise direction to be properly resolved.

4.2. Influence of differential diffusion

In turbulent non-premixed flame calculations, to greatly simplify the mixing problem, it is often assumed that energy diffuses at the same rate for all species, i.e. the diffusivities are set equal for all species [22], giving the so-called equal diffusivities transport model. However, in the near field of simple jet flames at low to moderate Reynolds number, this assumption is known to be inaccurate as diffusion effects tend to strongly influence the mixing process. The phenomenon has been especially seen at low Reynolds numbers and with high H_2 content in the fuel [11-13]. Thus, changes in the relative importance of molecular diffusion and turbulent transport were expected in the near-field of the present flames.

To evaluate the influence of differential diffusion, laminar diffusion flame calculations were performed with CHEMKIN-PRO [26] using the opposed-jet reactor with the GRI 3.0 mechanisms [27]. Considering non-premixed flames as an ensemble of laminar non-premixed flamelets, results from those calculations could be locally comparable to the experimental results. The purpose was not to simulate the investigated flames but simply to bring into the light underlying physics from the results by isolating some cases locally close to flamelet calculations. Results were compared to the present flames using similar fuel and oxidizer compositions and the two different transport models: full multi-component transport and equal diffusivities. The full multi-component transport model takes into account the effect of differential

diffusion, whereas the equal diffusivities assumption sets all species diffusivities equal to the thermal diffusivity (Lewis number equal to 1). Note that radiation effects were included in the calculations and the strain rate was defined as in [28].

In turbulent non-premixed jet flames, one could expect to match a location in the near-field with a relatively high strain rate, whereas a location farther downstream would rather match with a lower strain rate [29]. Focusing especially on Flame B-1, more relevant in this case since closer to a fully burning state (see Fig. 6), and on CO mass fraction, a good match was found with a strain rate a = 800 s^{-1} at z/d = 1 and a = 15 s^{-1} at z/d = 20, with full multi-component transport model, as shown in Fig. 7.

In turbulent non-premixed jet flames, the shear layer develops downstream by forming larger-scale turbulent structures until stirring the whole reaction zone, so that those structures control the local mixing rates. Thus, the effects of differential diffusion are expected to be more significant closer to the nozzle, as reported from different flames burning hydrogen [30, 31]; whereas equal diffusivities transport model would rather match far downstream zones where the upstream effects of differential diffusion have been washed out through a process of re-entrainment and turbulent mixing over the development length of the jet [29].

Figure 7 shows the scatter plots of CO, O_2, H_2, H_2O, CO_2 and CH_4 mass fractions compared to the laminar flame calculations. At 1 diameter above the nozzle, most results agree well with the full multi-component transport model, even though CH_4 and H_2 mass fractions seem to rather agree with the equal diffusivities assumption. At 20 diameters above the nozzle, the results are settled between the two different models. However, after only a few diameters above the nozzle, products start to be present on both sides of the flame region, leading to unclear conclusions for the relative importance of differential diffusion in the mixing process.

One way to quantify the degree of differential diffusion is to calculate the differential diffusion parameter, Z, defined as the difference between the elemental mixture fractions of hydrogen atoms (F_H) and carbon atoms (F_C); see details in [29]. Fig. 8-9 show the results for A- and B-series of flames at 1, 3 and 20 diameters above the nozzle compared to the laminar flame calculations corresponding to similar fuel and oxidizer compositions. RMS fluctuations for A-1 and B-1 are also shown.

Figures 8 and 9 show that the maximum of differential diffusion parameter close to stoichiometric mixture fraction considerably decreased with the axial location, showing good agreement with the expectations. A second observation, especially seen at z/d = 1, is that the differential diffusion parameter agrees well with the full multi-component transport model on the lean side of the reaction zone and then shows a major departure from this model toward the equal diffusivities transport model on the rich side. Indeed, close to the nozzle, the reaction zone and lean side of the flame were

in a laminarized part of the flow, so that there, the mixing was mostly controlled by molecular diffusion. However, the rich inner part of the mixing layer was still relatively cold and strongly affected by the pipe flow turbulence. This is likely to explain the behaviour of H_2 and CH_4 mass fractions in Fig. 7 and the major departure from the full multi-component transport model toward the equal diffusivities transport model in the rich side of the flame in Fig. 8-9.

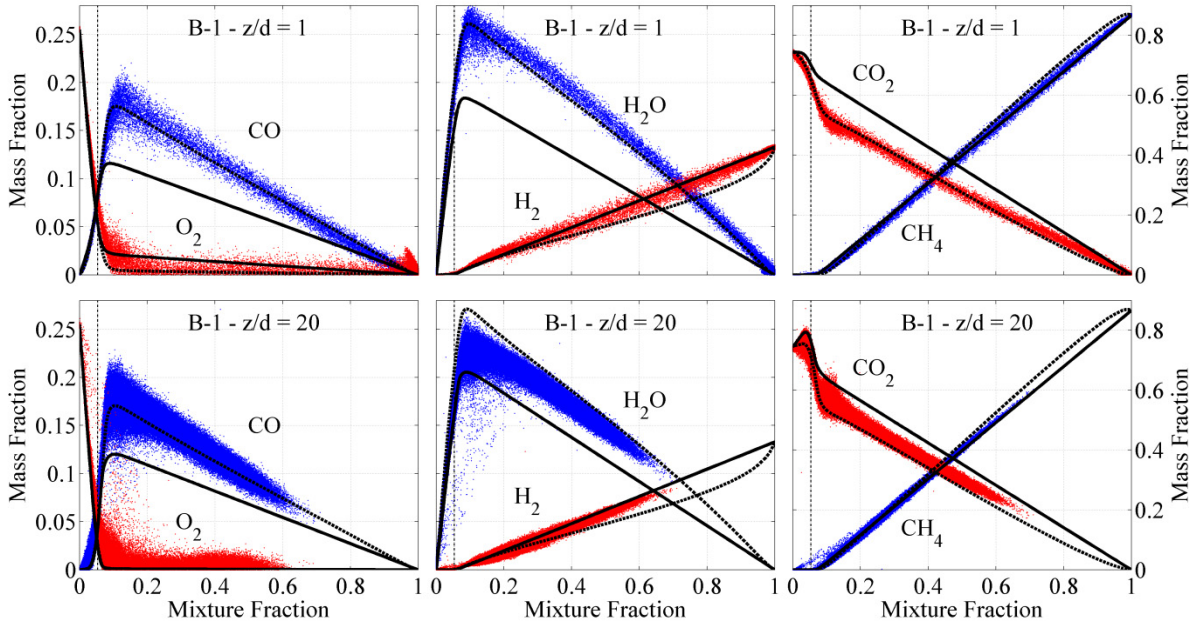

Fig. 7. Scatter plots of mass fractions plotted versus the Bilger mixture fraction for Flame B-1 at z/d = 1 and 20. Corresponding results from laminar flame calculations for strain rates of 800 s^{-1} (top) and 15 s^{-1} (bottom) are plotted using the two different transport models: full multi-component transport (dashed lines) and equal diffusivities (solid lines). The stoichiometric mixture fraction is marked by a vertical dashed line.

The differential diffusion parameter was determined by subtracting two uncertain values. In Fig. 8 and 9, the difference between the measurements was not significant compared to the corresponding RMS fluctuations. Despite the high level of uncertainty of *Z*, Fig. 8 seems to show a dependence of the differential diffusion with the CH_4/H_2 ratio. This is confirmed with the laminar flame calculations using A-1, A-2 and A-3 fuel and oxidizer compositions showing that the maximum of the differential diffusion parameter seems to decrease while decreasing the hydrogen molar fraction in the fuel. This result underlines the relative importance of differential diffusion effects in flames where H_2 is mixed with a heavier gas in the fuel stream. Nevertheless, no clear conclusions can be made about the jet Reynolds number dependence of the differential diffusion effects in the B-series flames in Fig. 9.

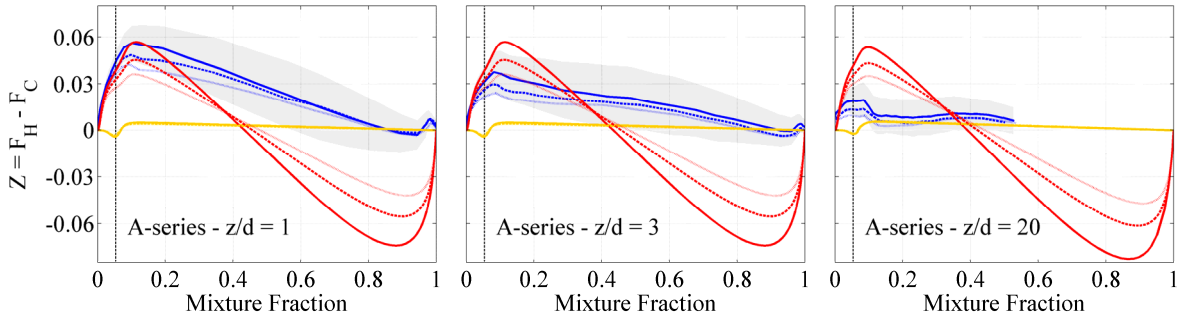

Fig. 8. Differential diffusion parameter Z plotted with the Bilger mixture fraction for A-series flames at z/d = 1, 3 and 20. A-1 is shown with blue solid lines, A-2 with blue dashed lines, and A-3 with blue dotted lines. Corresponding results from laminar flame calculations using A-1 (solid lines), A-2 (dashed lines) and A-3 (dotted lines) fuel and oxidizer compositions with strain rates of 800 s^{-1} (left and centre) and 15 s^{-1} (right) are plotted using the two different transport models: full multi-component transport (red lines) and equal diffusivities (orange lines). The grey area represents the conditional RMS fluctuations for Z corresponding to Flame A-1. The stoichiometric mixture fraction is marked by a vertical dashed line.

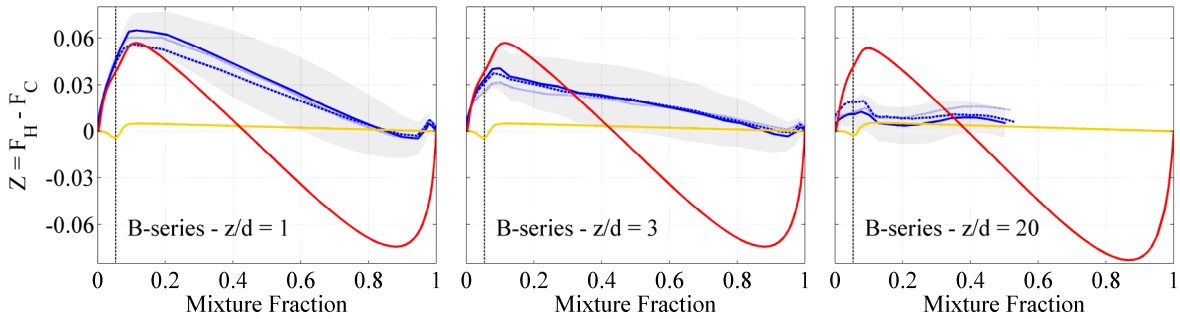

Fig. 9. Differential diffusion parameter Z plotted versus the Bilger mixture fraction for B-series flames at z/d = 1, 3 and 20. B-1 is shown with blue solid lines, B-2 with blue dashed lines, and B-3 with blue dotted lines. Corresponding results from laminar flame calculations using B-series fuel and oxidizer compositions with strain rates of 800 s^{-1} (left and centre) and 15 s^{-1} (right) are plotted using the two different transport models: full multi-component transport (red solid line) and equal diffusivities (orange solid lines). The grey area represents the conditional RMS fluctuations for Z corresponding to Flame B-1. The stoichiometric mixture fraction is marked by a vertical dashed line.

4.3. High CO levels

The conditional mean CO mass fraction could locally reach up to 0.18 (see Fig. 3, Flame B-1 and $z/d = 3$). Such high CO mass fractions result from high CO_2-dilution levels. Previous investigations with CO_2-dilution [32, 33] have concluded that CO_2 was not inert but competed primarily with O_2 for atomic hydrogen and lead to formation of CO through the reaction $CO_2 + H <-> CO + OH$. CO concentration is then expected to be locally higher than with air-dilution. Another conclusion was that the rate of the

reaction converting CO_2 into CO would decrease as the turbulent mixing rates increase up to reaching the forward rate of this reaction. The conditional mean of CO mass fraction showed in Fig. 3 for the B-series seems to agree with this trend, though it remains unclear because of the effects of localized extinction.

Heil et al. [34], who performed measurements in CO_2-diluted oxy-fuel flames in a furnace for flameless combustion, showed that high CO levels in the products are very sensitive to the O_2/CO_2 ratio. In low dilution oxy-fuel flames, high flame temperature would also contribute to increased local CO concentration through CO_2 dissociation. CO levels up to 30 % were found in pure oxygen flames [4]. In the present study, the O_2/CO_2 ratio was kept constant. Further investigation with a varying O_2/CO_2 ratio would be of great interest.

4.4. Shift of maximum temperature from stoichiometry

Figure 10 shows the scatter plots of temperature in mixture fraction space and the corresponding results from laminar flame calculations using the two transport models. A close-up was made on the flame region. Close to the nozzle, the temperature peak shows best agreement with the laminar flame calculation using full multi-component transport model, which tends to be slightly shifted toward the rich side compared to results with equal diffusivities transport model. This observation is verified for both Flame B-1 and Flame A-3, in spite of their significantly different CH_4/H_2 ratio. From z/d = 1 to z/d = 5, the temperature peak is greatly shifted back toward the lean side. Then, it seems to remain at a constant location in mixture fraction space until z/d = 20. The laminar flame calculations also show a similar trend when reducing considerably the strain rate from 800 s^{-1} to 15 s^{-1}. However, the shift for the laminar flame calculations using full multi-component transport model appears to be more dramatic than with the equal diffusivities transport model.

This trend can be explained by the relative importance of differential diffusion when the reaction zone is still very thin in the near field, which probably enhances the diffusion of small molecules such as H_2 through the reaction zone. As the reaction zone thickens farther downstream, the relative importance of differential diffusion decreases. This phenomenon is seen in Fig. 10 over the development length of the jet until a region between z/d = 5 and z/d = 10, where differential diffusion does not seem to interact any more with the location of the temperature peak.

Law et al. [35] investigated the cause for the shifting of the maximum adiabatic flame temperature from stoichiometry. The authors concluded that the phenomenon is a consequence of reduced heat release in the presence of product dissociation. Thus, in the present case, there would be more dissociation in the lean side, so that the heat release peaks on the rich side, inducing the rich shift of the maximum flame

temperature. The shift may be more pronounced than with air-dilution, due to the high CO_2 content on the lean side, characterized by higher heat capacity and lower heat release than N_2.

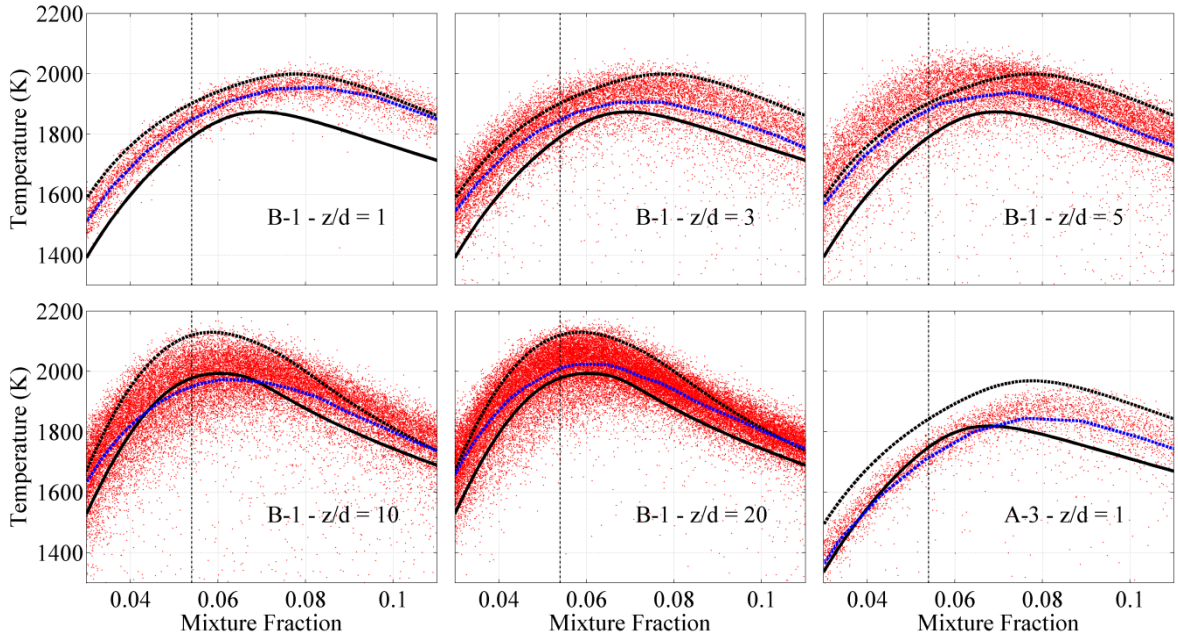

Fig. 10. Scatter plots of Rayleigh temperature with mixture fraction for Flame B-1 at z/d = 1, 3, 5, 10 and 20 and for Flame A-3 at z/d = 1. The conditional mean is plotted with a blue dashed line. Results from laminar flame calculations corresponding to fuel and oxidizer composition of displayed flame are plotted for strain rates of 800 s^{-1} (top row and bottom-right), and 15 s^{-1} (bottom-left and -centre). The two transport models were used in the calculations: full multi-component transport (dashed lines) and equal diffusivities (solid lines). The multi-component solution lies above the equal diffusivities solution in both cases. The stoichiometric mixture fraction is marked by a vertical dashed line.

Figure 11 gives another view of the results from the laminar diffusion flame calculations. Mixture fractions corresponding to the peak of adiabatic temperatures, $T_{Ad\text{-}Max}$ have been plotted within a range of strain rates from 10 to 1000 s^{-1}. Results show that, at very low strain rates, $T_{Ad\text{-}Max}$ peaks rather close to the stoichiometric mixture fraction for both transport models. However, at higher strain rates, the temperature peak tends to be shifted toward the rich region of the mixture fraction space. For strain rates from 500 to 1000 s^{-1}, this trend seems to get slightly attenuated with the equal diffusivities transport model but keeps on with the full multi-component transport model, for which the shift of $T_{Ad\text{-}Max}$ peak toward the rich region is more dramatic. In fact, the flame thickness is decreased as the strain rate is increased, which consequently acts on the residence time. Thus, at low strain rates, the mixing time is longer than the reaction time, so that the system is close to follow the ideal assumption of fast chemistry. In this case, $T_{Ad\text{-}Max}$ would peak at stoichiometric mixture fraction and the transport phenomena would not affect much the temperature peak shift. On the other

hand, at higher strain rates, the mixing time becomes shorter than the reaction time, potentially leading to incomplete reactions and stronger effects of the transport phenomena.

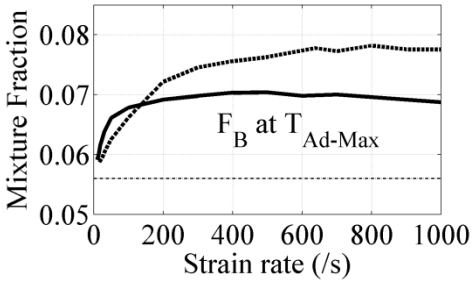

Fig. 11. Mixture fraction at maximum adiabatic flame temperature from laminar diffusion flame calculations corresponding to fuel and oxidizer composition of flames A-1, B-1, B-2 and B-3. Results are plotted with the strain rate. The two transport models were used in the calculations: full multi-component transport (dashed lines) and equal diffusivities (solid lines). The stoichiometric mixture fraction is shown by a horizontal dashed line.

4.5. Discussion of measurement challenges

During the measurements, flames displayed trends concerning soot formation at the flame tip (see Fig. 2). By reducing the H_2 content in fuel, A-series flames produced visible soot farther upstream, in part due to lower speeds at the jet exit for the same jet exit Reynolds number (see Table 1), the correspondingly longer residence time for soot formation, and the higher hydrocarbon species concentration. A similar trend was revealed with B-series flames while lowering Re_{Fuel}. As seen in Fig. 2, soot formation actually reached easily visible levels in Flame A-3.

The magnitude and spectroscopic distributions of hydrocarbon fluorescence interferences on the Raman measurements vary in these flames, depending on fuel composition, Reynolds number, and spatial location. Generally, measured interference levels increased with downstream distance in each flame, due to increasing residence time. At a given downstream location, hydrocarbon fluorescence interference decreased with increasing H_2 fuel fraction and with increasing Reynolds number.

Corrections for these hydrocarbon fluorescence interferences are not perfect and leave some residual errors, particularly in regions of high interference on the fuel-rich side of the reaction zone. These residual errors can be seen, for example, in O_2 and CO mass fraction results (see Fig. 3), which can be over- or under corrected by around 1 %, often appearing as a wrinkle in the plots. Similarly, an unrealistic wrinkle tended to appear for O_2 mass fraction in Fig. 3-4 and 7 and for Z in Fig. 8-9, corresponding to mixture fractions close to 1. These imperfections are most likely due to the Raman

cross-talk of CH_4 onto O_2, which is sensitive to very slight fluctuations where CH_4 is present in large quantities. This consequently affected other species mass fraction.

Localized extinction phenomena are extremely sensitive to the coflow temperature. A slight temperature variation can have a dramatic effect on flame structure close to blow-off conditions. While with air-diluted combustion, it is generally not a problem to supply large quantity of air at a stable temperature, supplying large quantities of CO_2 was challenging. CO_2 has a much larger Joule-Thomson coefficient than other supplied species, leading to a strong temperature dependence on upstream pressure conditions. An aluminium evaporator had to be coupled to liquid CO_2 tanks, followed by in-line gas heaters and a few dozens of meters of gas pipes, to keep the CO_2 temperature constant at 294 K at the coflow outlet.

More detailed investigation on differential diffusion could be of importance in both flame series since Re_{Fuel} remained close to transition of molecular transport models. An investigation at much higher Re_{Fuel} would have been even more beneficial, but remained physically unfeasible at laboratory scale due to the consequent supply of O_2 and CO_2.

4.6. Discussion of Raman/Rayleigh diagnostics in CO_2-diluted oxy-fuel flames

As for performing laser diagnostics, CO_2-diluted oxy-fuel flames remained very challenging due to their high CO_2 content. For instance, CO_2 has a higher refractive index than air, and this caused some steering of the laser beam when it passed through the unsteady interface between air and the CO_2/O_2 coflow. Another drawback is its high emissivity which creates a significant thermal load. Those two examples had to be taken into account while performing the experiments. Beam steering was not severe using the 32 % O_2 mixture, and the main effects of beam steering are accounted for automatically by the hybrid Raman/Rayleigh processing method [19].

Furthermore, the two Raman bands for CO_2 can reach high intensities relatively to the other species, due to their high Raman cross-section and the Raman scattering linearity with the concentration. Since the Raman spectrum of CO_2 overlaps the detection region of O_2, the induced crosstalk of CO_2 onto O_2 can lead to significant relative uncertainties in the measurement of O_2 if not correctly accounted for in the data processing, especially when the actual concentration of O_2 is low. Raman rotational bands of H_2, mostly neighbouring the CO_2 Raman bands, may also affect the latter when H_2 is present at large quantities, or at high temperatures. Both crosstalk effects are reasonably well handled by the hybrid method.

An important advantage compared to air-diluted conditions is the absence of N_2 in the Raman spectra, which limits the number of Raman species to be processed to six.

Besides, N_2 is very close to CO on the Raman spectra. N_2 induces a strong cross-talk onto CO, enhanced by the relatively high concentration of N_2 in air-diluted flames. As previously detailed, detection and quantification of CO could be confidently achieved by laser Raman scattering in favour of laser induced fluorescence techniques.

Varying the oxygen molar fraction in the oxidizer can lead to very high temperatures, for which the radical pool may represent a non-negligible concentration and cannot be ignored any more in the Raman/Rayleigh resolution. In the present flames, a molar fraction of 32 % oxygen in the oxidizer limited the radical pool to a negligible concentration compared to the uncertainties of the diagnostics.

5. Concluding remarks

Measurements of the temperature and mass fractions of main species were performed in turbulent non-premixed CO_2-diluted oxy-fuel jet flames, using the simultaneous line imaging of Raman/Rayleigh scattering. Two series of three flames burning mixtures of hydrogen and methane in a coflow burner were studied. The objective was to investigate the influence of CH_4/H_2 ratio and jet Reynolds number on localized extinction and flame structure in CO_2-diluted oxy-fuel jet flames.

Consequences of localized extinction in the flame composition could be captured, notably by the scatter plots of temperature in mixture fraction space, at different axial locations. Additionally, higher contents of oxygen on the rich side of the flame front could be observed in the conditional mean of O_2 mass fraction as one progress toward higher probability of localized extinction. Based on the PDF of the temperature, a fully burning probability index able to quantify the degree of extinction along the streamwise location was calculated.

Comparison of conditional mean mass fractions and laminar flame calculations using similar fuel and oxidizer compositions underlined the significant level of differential diffusion in the near-field, due to the very low levels of turbulence in the reaction zone so close to the nozzle. The relative importance of differential diffusion tended to decrease farther downstream as the large-scale turbulent structures tended to develop and control the local mixing rates by stirring the reaction zone.

Due to the high CO_2 content in the oxidizer, CO mass fraction was found to be effectively higher than in comparable air-diluted flames, especially in the near-field. This effect would be due to CO_2 competing primarily with O_2 for atomic hydrogen and leading to formation of CO through the reaction $CO_2 + H \leftrightarrow CO + OH$.

A shift of maximum flame temperature toward the rich side of the mixture fraction space was observed in the measurements. The shift appeared to be greater in

the near-field and tended to diminish until z/d = 5, from where the peak location seemed to remain constant. The phenomenon can be a consequence of reduced heat release in the presence of product dissociation, so that more dissociation in the lean side induces the heat release peak on the rich side and a rich shift of the maximum flame temperature.

Results on the whole displayed reasonable accuracy, from 1 up to 20 nozzle diameters above the nozzle. Though levels of hydrocarbon fluorescence were fairly high in some cases, the sensitivity of the detection system also allowed capturing precise hydrogen mass fractions which would make this data relatively interesting for validation of turbulent combustion models. Only a limited part of the results is shown in the present paper but most data, including scalar fluctuations and conditional statistics, are available upon request.

Acknowledgements

This publication forms a part of the BIGCO2 project performed under the strategic Norwegian research program Climit. The authors acknowledge the partners: Statoil, GE Global Research, Statkraft, Aker Kværner, Shell, TOTAL, ConocoPhillips, ALSTOM, the Research Council of Norway (178004/I30 and 176059/I30) and Gassnova (182070) for their support. Sandia National Laboratories is a multi-program laboratory operated by Sandia Corporation, a Lockheed Martin Company, for the United States Department of Energy under contract DE-AC04-94-AL85000. The authors also gratefully acknowledge R. Harmon for his contributions in these experiments.

References

[1] O. Bolland, S. Saether, Energ. Convers. Manage. 33 (5-8) (1992) 467-475.

[2] O. Bolland, P. Mathieu, Energ. Convers. Manage. 39 (16-18) (1998) 1653-1663.

[3] Y. Tan, M. A. Douglas, K. V. Thambimuthu, Fuel 81 (8) (2002) 1007-1016 Pii S0016-2361(02)00014-5.

[4] M. Ditaranto, J. C. Sautet, J. M. Samaniego, Exp. Fluids 30 (3) (2001) 253-261.

[5] J. C. Sautet, M. Ditaranto, J. M. Samaniego, O. Charon, Int. Commun. Heat Mass 26 (5) (1999) 647-656.

[6] J. C. Sautet, L. Salentey, M. Ditaranto, Int. Commun. Heat Mass 28 (2) (2001) 277-287.

[7] E. Croiset, K. V. Thambimuthu, Fuel 80 (14) (2001) 2117-2121.

[8] M. Ditaranto, J. Hals, Combust. Flame 146 (3) (2006) 493-512 DOI 10.1016/j.combustflame.2006.04.015.

[9] F. H. V. Coppens, A. A. Konnov, Fuel 87 (13-14) (2008) 2866-2870 DOI 10.1016/j.fuel.2008.04.009.

[10] P. Kutne, B. K. Kapadia, W. Meier, M. Aigner, Proc. Combust. Inst. 33 (2) (2011) 3383-3390.

[11] R. S. Barlow, J. H. Frank, A. N. Karpetis, J. Y. Chen, Combust. Flame 143 (4) (2005) 433-449 DOI 10.1016/j.combustflame.2005.08.017.

[12] M. C. Drake, R. W. Bilger, S. H. Stårner, Proc. Combust. Inst. 19 (1982) 459-467.

[13] L. L. Smith, R. W. Dibble, L. Talbot, R. S. Barlow, C. D. Carter, Combust. Flame 100 (1-2) (1995) 153-160.

[14] L. Wang, N. E. Endrud, S. R. Turns, M. D. D'Agostini, A. G. Slavejkov, Combust. Sci. Technol. 174 (8) (2002) 45-72 10.1080/00102200290021245.

[15] M. Ditaranto, T. Oppelt, Exp. Therm. Fluid Sci. 35 (7) (2011) 1343-1350.

[16] R. S. Barlow, H. C. Ozarovsky, A. N. Karpetis, R. P. Lindstedt, Combust. Flame 156 (11) (2009) 2117-2128 DOI 10.1016/j.combustflame.2009.04.005.

[17] D. C. Haworth, Prog. Energ. Combust. Sci. 36 (2) (2010) 168-259 DOI 10.1016/j.pecs.2009.09.003.

[18] R. S. Barlow, G. H. Wang, P. Anselmo, M. S. Sweeney, S. Hochgreb, Proc. Combust. Inst. 32 (2009) 945-953 DOI 10.1016/j.proci.2008.06.070.

[19] F. Fuest, R. S. Barlow, D. Geyer, F. Seffrin, A. Dreizler, Proc. Combust. Inst. 33 (1) (2011) 815-822.

[20] D. Geyer, 1D-Raman/Rayleigh Experiments in a Turbulent Opposed-Jet, PhD Thesis, TU Darmstadt, VDI-Verlag, Düsseldorf (2005) ISBN 3-18-353306-5.

[21] R. W. Bilger, S. H. Starner, R. J. Kee, Combust. Flame 80 (2) (1990) 135-149.

[22] J. Warnatz, U. Maas, R. W. Dibble, Combustion, Springer 3rd Edition (2000).

[23] R. R. Cao, S. B. Pope, Combust. Flame 143 (4) (2005) 450-470 10.1016/j.combustflame.2005.08.018.

[24] A. R. Masri, P. A. M. Kalt, Y. M. Al-Abdeli, R. S. Barlow, Combust. Theor. Model. 11:5 (2007) 653-673.

[25] J. Xu, S. B. Pope, Combust. Flame 123 (3) (2000) 281-307.

[26] CHEMKIN-PRO, Reaction Design: San Diego, 2008.

[27] G. P. Smith, D. M. Golden, M. Frenklach, N. W. Moriarty, B. Eiteneer, M. Goldenberg, C. T. Bowman, R. K. Hanson, S. Song, W. C. Gardiner, V. V. Lissianski, Z. Qin, http://www.me.berkeley.edu/gri_mech/.

[28] Z. Cheng, J. A. Wehrmeyer, R. W. Pitz, Combust. Sci. Technol. 178 (12) (2006) 2145-2163 Doi 10.1080/00102200600616745.

[29] R. S. Barlow, G. J. Fiechtner, C. D. Carter, J. Y. Chen, Combust. Flame 120 (4) (2000) 549-569.

[30] W. Meier, A. O. Vyrodov, V. Bergmann, W. Stricker, Appl. Phys. B-Lasers O. 63 (1) (1996) 79-90.

[31] V. Bergmann, W. Meier, D. Wolff, W. Stricker, Appl. Phys. B-Lasers O. 66 (4) (1998) 489-502.

[32] A. R. Masri, R. W. Dibble, R. S. Barlow, Combust. Flame 91 (3-4) (1992) 285-309.

[33] P. Glarborg, L. L. B. Bentzen, Energ. Fuels 22 (1) (2008) 291-296 Doi 10.1021/Ef7005854.

[34] P. Heil, D. Toporov, M. Forster, R. Kneer, Proc. Combust. Inst. 33 (2011) 3407-3413 DOI 10.1016/j.proci.2010.05.047.

[35] C. K. Law, A. Makino, T. F. Lu, Combust. Flame 145 (4) (2006) 808-819 DOI 10.1016/j.combustflame.2006.01.009.